Title
SKS Splitting from Ocean Bottom Seismometer Data in Offshore Southern California

Author
Ramsay, Joseph

Publication Date
2014

Peer reviewed|Thesis/dissertation

UNIVERSITY OF CALIFORNIA

Los Angeles

SKS Splitting from Ocean Bottom Seismometer Data in Offshore Southern California

A thesis submitted in partial satisfaction
of the requirements for the degree Master of Science
in Geophysics and Space Physics

by

Joseph Ramsay

2014

ABSTRACT OF THE THESIS

SKS Splitting from Ocean Bottom Seismometer Data
in Offshore Southern California

by

Joseph Ramsay

Master of Science in Geophysics and Space Physics
University of California, Los Angeles, 2014
Professor Paul M. Davis, Chair

SKS arrivals from OBS data of the ALBACORE experiment (Asthenospheric and Lithospheric Broadband Architecture from the California Offshore Region Experiment) offshore Southern California are analyzed for shear wave splitting. In a region several hundred kilometers from the Pacific Plate, splitting directions are similar to on-land directions WSW-ENE and with similar delays 1.1-1.4 seconds. Three measurements give higher delays and also W-E directions. The directions are at 45 degrees to APM of the Pacific plate suggesting that either frozen-in anisotropy from paleo-spreading dominates over APM effects in the asthenosphere or that deeper mantle shearing has occurred unrelated to APM. A toroidal flow around slab rollback presents one such possibility.

The thesis of Joseph Ramsay is approved.

Lingsen Meng

Gilles Peltzer

Paul M. Davis, Committee Chair

University of California, Los Angeles

2014

Contents

List of Figures

List of Tables

1 Introduction

While the surface motions of tectonic plates are well-known, the nature of mantle flow and its relationship to plate motions is still an enigma. One way to detect the finite strain associated with mantle flow is by measuring the effects of anisotropy on seismic waves that pass through it (Silver and Chan, 1991; Silver and Holt, 2002). This thesis examines splitting of SKS and SKKS waves recorded on an OBS network offshore Southern California to infer flow in the underlying mantle.

Currently there is controversy on the origin of the anisotropy that gives rise to SKS splitting. Away from subduction zones there is a tendency for splitting to align with absolute plate motions (APM) (Montagner et al., 2000). This has led to the belief that SKS splitting is associated with regions shallower than 400 km (Becker et al., 2006). Previous SKS analyses in Southern California by Kosarian et al. (2011) and Becker et al. (2012), however, found that SKS splitting directions align with the North America APM (SWS-ENE) even to the west offshore across the plate margin as expressed by the San Andreas fault (SAF), where one might have expected a transition to Pacific APM(Kosarian et al., 2011; Becker et al., 2006, 2012). This seems to suggest that anisotropy is not due to lithospheric drag on the asthenosphere(Kosarian et al., 2011). It was proposed that the Pacific APM west of the SAF simply has not yet had time to overprint the effects of North American APM. In central California, however, a tendency to align with Pacific plate motion west of the San Andreas Fault was observed suggesting that if APM is the cause, the effective plate margin in southern California is affected by the big bend of the San Andreas Fault and may be offshore. Thus measurements on an offshore OBS array might detect the transition. However, we conclude here that this is not the case. The OBS splitting directions continue in a WSW-ENE direction several hundred km out onto the Pacific plate.

2 Tectonic Setting

Given that any explanation of SKS splitting results will involve the tectonic setting of a region, it is important to establish the tectonic history of Southern California. Though the

western edge of California was once simply a passive margin, today it is a massively complex geologic area.

Near the end of the Precambrian (750 Ma) the supercontinent Rodinia began breaking into several pieces. One of these segments is called Laurentia. At this point in time a rift zone comprised the western edge of Laurentia and California was just offshore from it. As rifting progressed the region transformed into a passive continental margin(DeCourten, 2013). This allowed sediment to accumulate over time to form a shallow continental shelf.

During the mid-Paleozoic period (300 Ma) the masses that Rodinia had broken up into started to come together to form Pangaea which led to western North America becoming a convergent plate boundary. In the late Triassic period, the mid-Atlantic ridge opened and the North American plate began to move west. Meanwhile subduction continued along the western coast of modern North America as the Farallon plate was driven eastward from the Pacific-Farallon Ridge. At this point (mid Jurassic) the Pacific plate was moving north-west as the Farallon plate was moving south-east towards North America.

About 30 million years ago the western edge of the North American plate overran the Pacific-Farallon Ridge. This led to the collision of North America with the Pacific plate. Due to the collision of Pacific-Farallon spreading center and the North American continent, this ended subduction in the region and initiated the transform boundary we see today. A modern remnant of the Farallon plate, the Juan de Fuca plate, exists on the western edge of North America where the plate did not overtake the Pacific-Farallon Ridge before subduction stopped. Numerous fracture zones exist off the coast of Soutern California as a result of the seafloor spreading during this time. As the transform boundary progressed pieces of the North American plate were stripped away and joined onto the Pacific plate. Baja California is a notable example of this. Today, as seen in Figure 1 the entirety of California west of the San Andreas fault system is part of the Pacific plate and moving towards the north-west relative to North America(DeCourten, 2013).

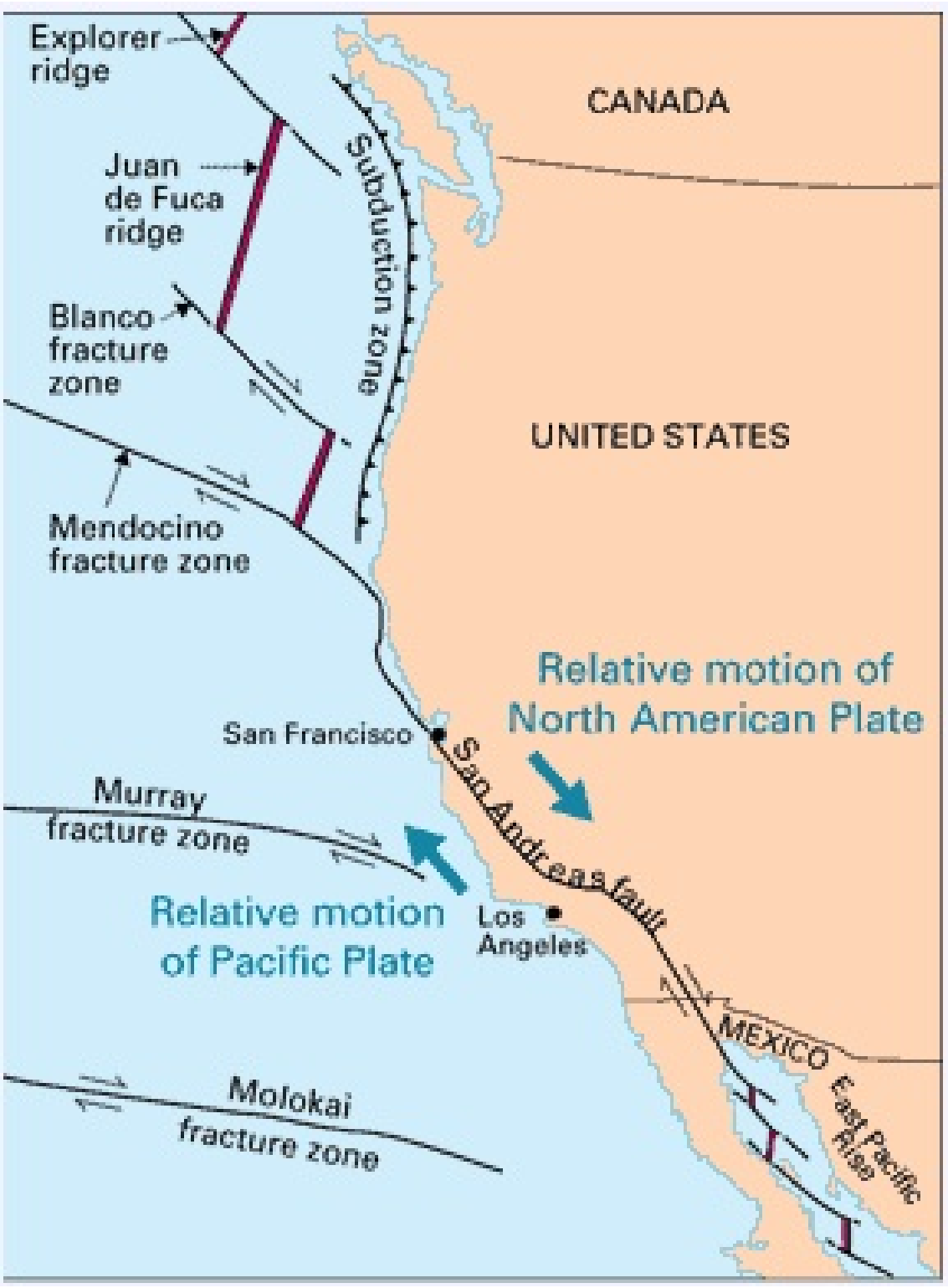

Figure 1: Current state of affairs concerning western North American tectonics.

3 Anisotropy

Although most seismic models of the Earth assume isotropy, many crystals and common materials of the Earth (and specifically the mantle) are anisotropic with elastic properties that vary with orientation. The effects of anisotropy are seen in the propagation of seismic waves.

The mathematical basis for anisotropy is seen by examining Hooke's Law:

$$\sigma_{ij} = c_{ijkl}\epsilon_{kl} \tag{1}$$

Stress and strain are both second-order tensors. By necessity, any elastic constant that relates the two is a fourth-order tensor. This leads to 81 independent values. This number is reduced by arguments of symmetry (of the stress and strain tensors) to 21 for a general material and still further for various geometries (Stacey, 1977). For example, whereas isotropic materials only have two independent elastic constants, olivine ($(Mg^{+2}, Fe^{+2})2SiO_4$), the predominant mineral of the upper mantle, is highly anisotropic with an orthorhombic symmetry leading to nine constants.

Anisotropy in the upper mantle causes numerous effects detected in seismic data:

1. Shear wave splitting - the two polarizations of S waves arrive at different times.
2. Azimuthal anisotropy - Arrival times of seismic waves at a given distance depend on the azimuth of approach.
3. Love and Rayleigh wave dispersion curves not explained by isotropic models(Anderson and Isaak, 2013).

The first of these, shear wave splitting, is the subject of this project.

3.1 Causes of Anisotropy in the Upper Mantle

There are two fundamentally different ways in which anisotropy can arise in rocks.

1. Shape-Preferred Orientation (SPO) in which a heterogenous material that is isotropic at can nevertheless exhibit anisotropy based on cumulative effects of alignment of shapes with contrasting velocities.

2. Lattice-Preferred Orientation (LPO) in which anisotropy exists due to a preferred orientation of anisotropic mineral crystals (Ribe and Yu, 1991).

The first type is chiefly of importance in layering of fast and slow materials, such as sedimentary rocks. It can, however, also be caused by preferred crack orientation (aligned cracks in a certain direction).

Of importance to this project is the second type, lattice-preferred orientation. Individual crystals can be highly anisotropic and, indeed, olivine is. If randomly oriented it is possible that anisotropy in olivine "cancels out." But if even a small fraction of crystals are aligned then anisotropy is produced Etchecopar (1977). How then are olivine crystals aligned? The answer to this question is why anisotropy is of such interest.

3.2 Causes of Olivine Alignment

It has been shown that plastic flow induces a preferred orientation in minerals such as olivine (Carter, 1976). This occurs primarily by dislocation slip and climb. A simple shear (the dominant regime in the upper mantle) applied to a crystal will rotate that crystal so that all slip lines except those in the slip plane will align with the flow line. Since crystals are required to remain in contact in an aggregate, this results in a bulk rotation of crystals. This means that plastic strain from mantle flow can cause anisotropy, and seismic anisotropy can be used to study mantle flow. One explanation for olivine alignment in the upper mantle is absolute plate motion (APM) or, in other words, lithospheric drag (Silver and Chan, 1991). In many instances it appears that anisotropy and APM agree nicely (Kosarian et al., 2011; Long and Silver, 2008).

As shown in seismic refraction experiments (Wolfe and Solomon, 1998; Harmon et al., 2004) P_n azimuthal anisotropy due to olivine alignment can be imposed on a material due to seafloor spreading. These measurements, however, only reflect properties just beneath the Moho. Other studies which utilize long-period surface wave azimuthal anisotropy extend the analysis to several hundred kilometers depth (Beghein et al., 2014). It appears that the alignment of fast direction with seafloor spreading breaks down for seafloor of greater age. Subsequently, a two layer model of anisotropy with anisotropy inherited from seafloor

spreading existing in the lithosphere with another layer in the direction of absolute plate motion existing in the asthenosphere has been proposed (Wolfe and Silver, 1998; Barruol et al., 2009). The relative influence of APM and seafloor spreading on the fast direction of anisotropy remains a subject of debate.

3.3 SKS Splitting

The effect of anisotropy can easily be seen in SKS arrivals. These are waves that start as S waves and travel through the mantle into the outer liquid core. Since a shear wave cannot propagate through a liquid or gas, it must become a P wave during this portion of its journey. Once this wave hits the core-mantle boundary (CMB) on its way back up to the surface, it converts to a shear wave again. The trip throughout the inner core, seen in Figure 2, acts as a sort of filter because it guarantees that the polarization of the emerging S wave is SV (or radially polarized), because it came from a P wave that only had radial motion.

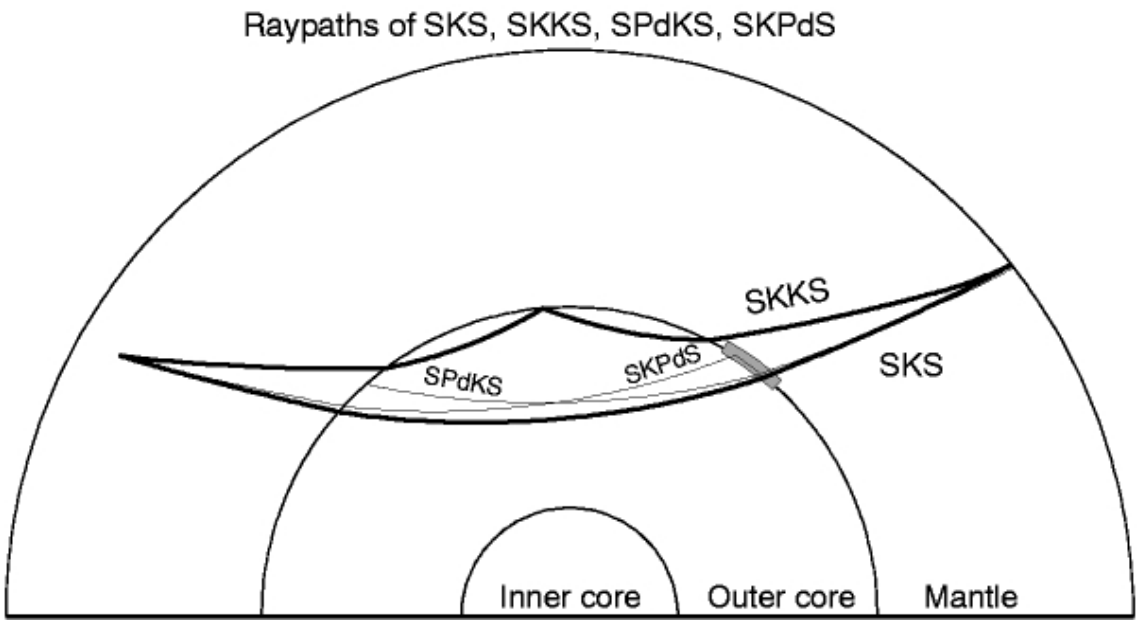

Figure 2: SKS ray paths typically used for splitting. (D. V. Helmberger, 1998)

As this wave encounters azimuthally anisotropic material it is split into 'fast and 'slow components based on the materials anisotropic orientation (Figure 3. The fast and slow components arrive at the surface out of phase (something that would not happen with-

out anisotropy). These components can then be analyzed bearing in mind that the initial polarization of the wave at the CMB should be almost purely SV.

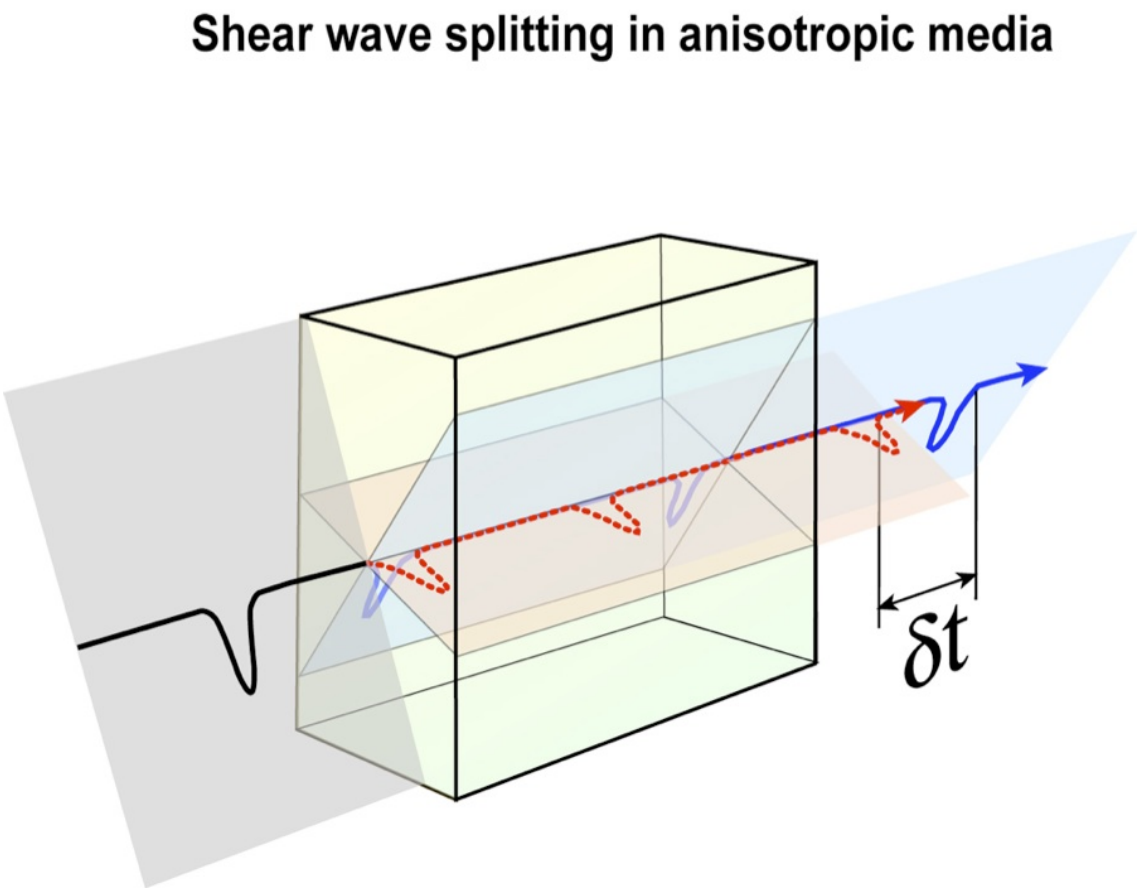

Figure 3: Shear wave splitting in anisotropy.

Once an SKS signal is recognized in a seismogram, two variables are sought: the phase shift between fast and slow signals δt and the fast direction ϕ. The process involves removing the effects of anisotropy using different values for ϕ and δt with the goal of minimizing energy along the transverse axis. This is all based on the presumption that without anisotropy somewhere along the ray path that energy of the transverse component would be zero. Knowing that the initial polarization is radial allows us to reconstruct the waveform prior to its encounter with anisotropy and gives us a way to infer the direction and strength of anisotropy. Note that this method ensures that the depth of the anisotropy detected is somewhere between the CMB and the surface but cannot indicate exactly where.

After correction for orientation, the horizontal axes of the seismogram are rotated by

some ϕ into trial 'fast' and 'slow' directions.

$$\begin{bmatrix} fast \\ slow \end{bmatrix} = \begin{bmatrix} \cos\phi & \sin\phi \\ -\sin\phi & \cos\phi \end{bmatrix} \begin{bmatrix} N \\ E \end{bmatrix} \tag{2}$$

A δt between the two phase arrival times is then used to advance the slow arrival. For this analysis a Fast Fourier Transform (FFT) was preformed on the slow component and was multiplied by a $e^{-iw\delta t}$ (where δt is a trial time shift in attempt to remove the delay). The signals are then rotated back into the geographic axes.

$$\begin{bmatrix} N \\ E \end{bmatrix} = \begin{bmatrix} \cos -\phi & \sin -\phi \\ -\sin -\phi & \cos -\phi \end{bmatrix} \begin{bmatrix} fast \\ slow' \end{bmatrix} \tag{3}$$

And finally into radial and transverse components. Here $\theta = BAZ - \pi$. A diagram of the various angles involved in this process are seen in Figure 4.

$$\begin{bmatrix} R \\ T \end{bmatrix} = \begin{bmatrix} \cos\theta & \sin\theta \\ -\sin\theta & \cos\theta \end{bmatrix} \begin{bmatrix} N \\ E \end{bmatrix} \tag{4}$$

The energy in the transverse direction can then be analyzed for a minimum.

For this project, ϕ directions every 1 degree between 0° and 180° and δt shifts every 0.1 seconds between 0 and 4 seconds were attempted. A subsequent contour plot of energy for each of these combinations reveals the set of parameters that minimizes energy in the transverse direction.

Key to recognizing split seismograms is the knowledge that the splitting process separates the waveform such that the transverse component is the time derivative of the radial component. To show this, we again use a standard rotation matrix. Here $B = BAZ - \pi - \phi$.

$$\begin{bmatrix} R \\ T \end{bmatrix} = \begin{bmatrix} \cos B & \sin B \\ -\sin B & \cos B \end{bmatrix} \begin{bmatrix} fast \\ slow \end{bmatrix} \tag{5}$$

Which gives us

$$R = f(t + \delta t/2)\cos^2 B + f(t - \delta t/2)\sin^2 B \tag{6}$$

and

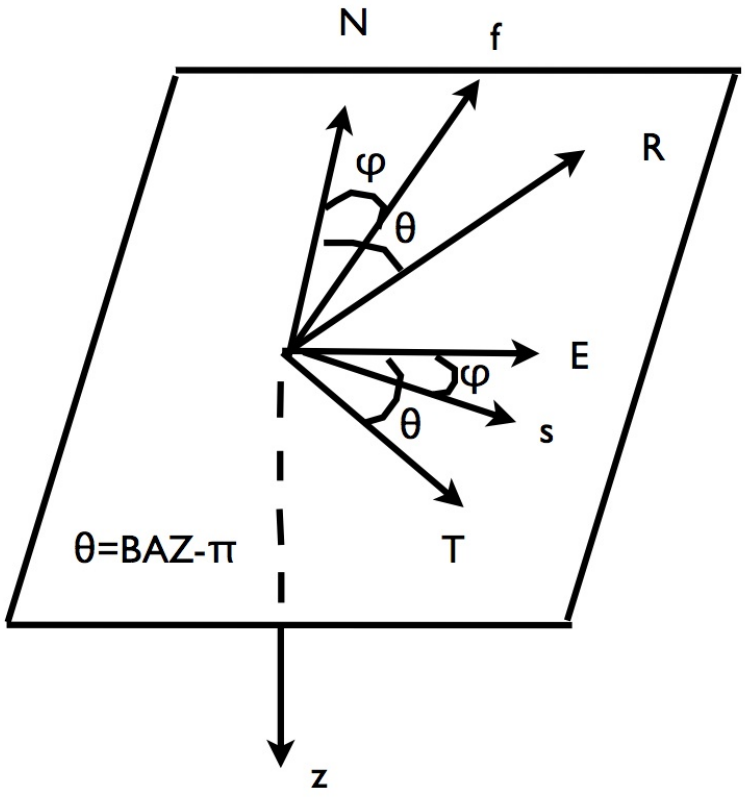

Figure 4: Diagram of Angles Used

$$T = f(t + \delta t/2) \sin B \cos B - f(t - \delta t/2) \sin B \cos B \tag{7}$$

If we rearrange the transverse component and exploit the trig identity $\sin 2u = 2 \sin u \cos u$, we arrive at:

$$T = [f(t + \delta t/2) - f(t - \delta t/2)](1/2) \sin 2B \tag{8}$$

Which is equivalent to:

$$T \approx (1/2)\delta t \sin 2B \frac{dR}{dt} \tag{9}$$

Shear-wave splitting is excellent for this task because it is very difficult to produce the observed effect (two S pulses of similar shape orthogonal to each other, arriving at slightly different (<3 s) times, and with the derivative of the radial component equivalent to the tangential component) without anisotropy somewhere along the ray path. One concern, however, is that a thin highly anisotropic layer can produce the same delay time as a thick weakly anisotropic layer. Other considerations such as tectonic history must be brought to bear.

SKS splitting has no depth resolution in and of itself and therefore the depth of generation of anisotropy is uncertain since Rayleigh wave anisotropic studies generally see smaller effects than detected by splitting(Kosarian et al., 2011; Yuan and Romanowicz, 2010; West et al., 2009). The ALBACORE project presents a new opportunity in that it is the first SKS splitting study to extend across the plate boundary between the North American plate and the Pacific plate. Measurements across this boundary will shed new light on the possible causes of anisotropy and the interpretation of these results (Kosarian et al., 2011).

4 The ALBACORE Experiment

Between August 14, 2010 and August 27, 2010 the ALBACORE (Asthenospheric and Lithospheric Broadband Architecture from the California Offshore Region Experiment) cruise deployed 34 ocean bottom seismometers (OBSs) in a 150-km (north-south) by 400-km (east-west) region off the coast of Southern California. In the Continental Borderland region

station spacing was approximately 50-km while in the oceanic plate region spacing was approximately 75-km. The OBSs remained in place for 12 months before a recovery cruise which took place between September 7, 2011 and September 16, 2011. The locations of each seismometer can be seen in Figure 5. The purposes of ALBACORE were numerous (Kohler, 2012) and this project is one of them.

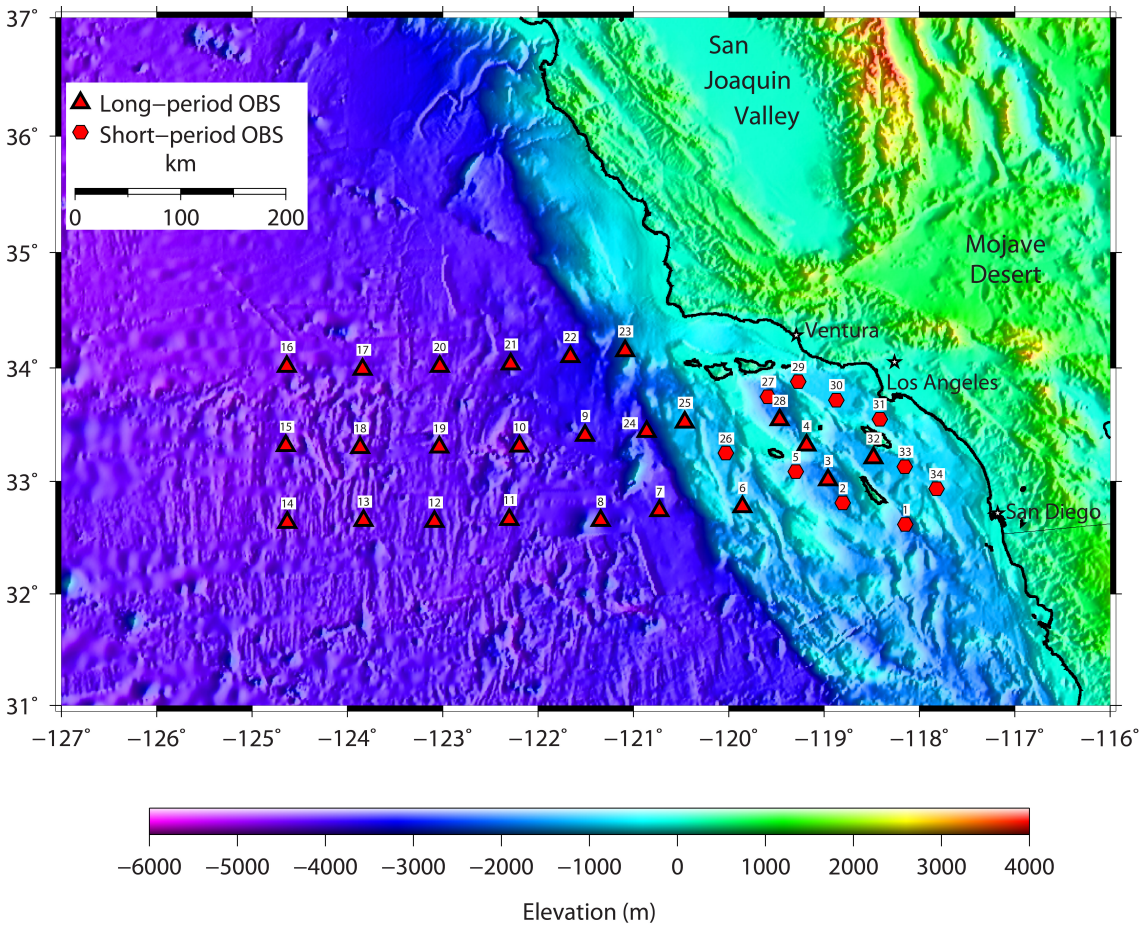

Figure 5: OBS Deployment Map (Kohler, 2012)

The OBSs fall into three categories: 21 three-component long-period Nanometrics Trillium 240 sensors with differential pressure gauges (DPGs), 3 three-component long-period Nanometrics Trillium T-40 sensors with DPGs, and 10 three-component short-period Sercel L-28 sensors with hydrophones. The data loggers on each OBS were the same: a Scripps-developed instrument that consisted of four channels (three directions and a differential pressure gauge), solid state memory, and a temperature-compensated oscillator.

During the ALBACORE projects deployment 24 long-period and 10 short-period seis-

mometers continuously recorded data at 50 samples per second. Due to the bandwidth requirement of filtering for SKS arrivals the short-period sensors were not useful for this analysis.

Since sensor orientations cannot be known due to twisting during deployment, Rayleigh wave vertical to horizontal amplitude ratios were analyzed. Rayleigh waves have retrograde elliptical particle motion which should only be visible on the vertical and radial components. Synthetic wave-forms for a variety of back azimuths are correlated with the observed Rayleigh wave. The maximum positive correlation coefficient indicates the azimuth of maximum correlation (Stachnik, 2012).These orientations were computed by Dr. Dayanthie Weeraratne and her graduate student Brian Clements of California State University, Northridge.

5 Data Analysis

For observing high signal-to-noise ratio (SNR) SKS and SKKS phases, we sought events of magnitude greater than 6.5 in the great circle distance of 90°-110°. Of the 98 events that fell in this range, 7 events showed coherent SKS or SKKS arrivals across the network. These signals were band-pass filtered between 0.06 and 0.1 hertz to obtain the best SNR. Noise due to microseism limited usable frequencies to under 0.1 hertz(Wolfe and Solomon, 1998). See Table 1 for each event used for analysis. The back azimuth range is illustrated in Figure 6 by plotting each event's great circle path.

The method of Silver and Chan (1991) was followed to minimize energy in the transverse component in order to obtain the azimuth of the fast direction ϕ and the delay time δt between the fast and slow components. Once north and east orientations are established, various fast directions and delay times are tested and energy in the transverse component for each SKS and SKKS arrival is measured. The direction and time delay that produces the minimum energy in the transverse component can be assumed to have removed the affects of anisotropy.

Due to the nature of anisotropy, it is assumed that an arrival for a certain event is a usable signal if three criteria are met: 1) that the event is seen across the network, 2) a time delay is seen between the radial and transverse components, and 3) that the derivative of the

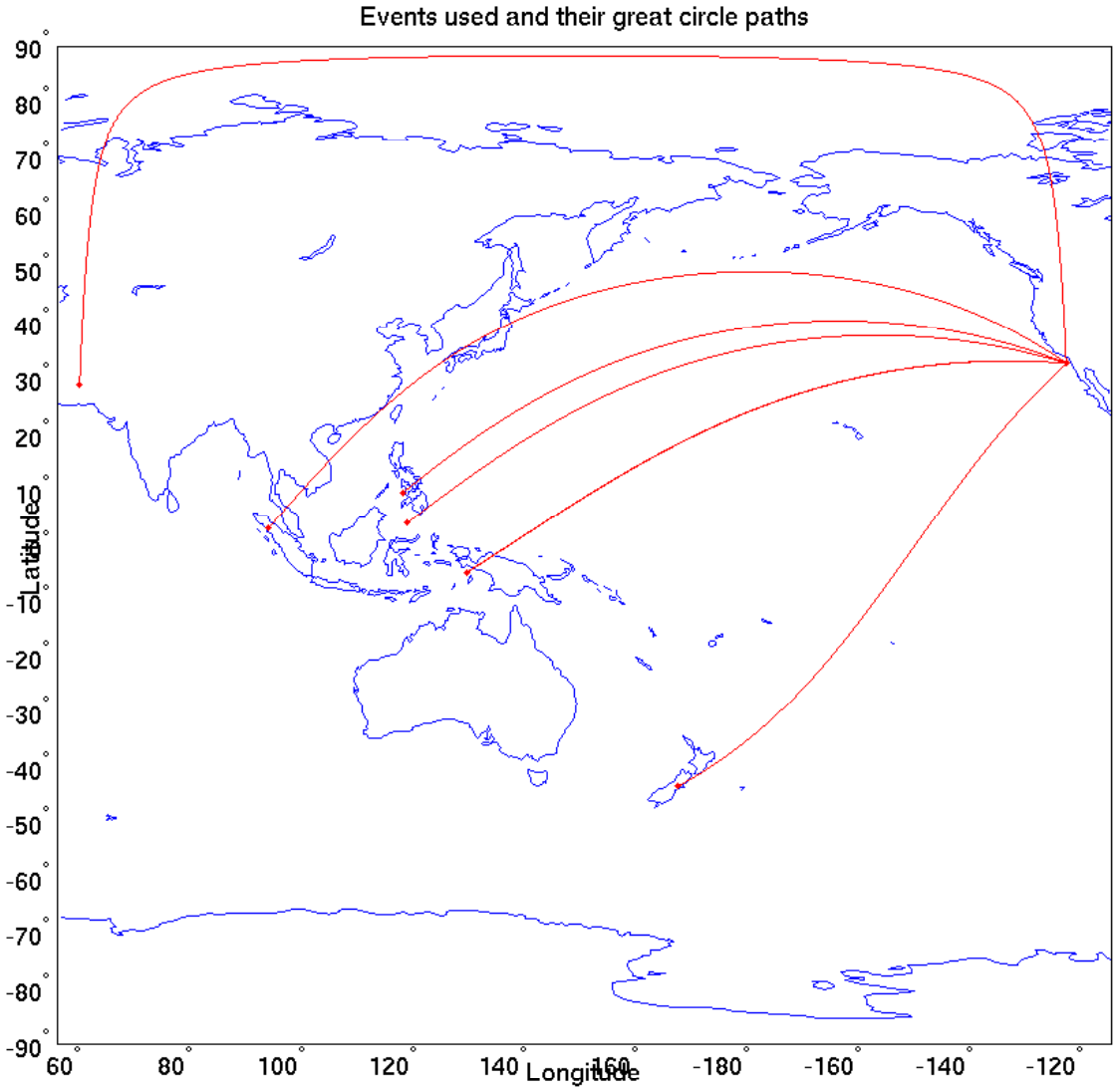

Figure 6: Great Circle Paths of Events Used

Table 1: Earthquakes used. BAZ is the back azimuth clockwise from north.

Event No.	Date	Origin Time	Latitude (°N)	Longitude (°E)	Depth (km)	BAZ	M
1	09/04/2010	16:35:47	-42.52	171.83	12	223	7
6	09/29/2010	17:10:51	-4.91	133.71	10	275	6.2
7	09/29/2010	17:11:25	-4.96	133.76	26	275	7
35	01/18/2011	20:23:23	28.78	63.95	68	358	7.2
42	02/10/2011	14:41:58	4.08	123.04	525	290	6.6
77	07/11/2011	20:47:04	9.51	122.18	19	295	6.4
98	09/05/2011	17:55:11	2.96	97.89	91	309	6.7

radial matches the transverse component. These requirements restricted our usable events greatly. With data as noisy as ocean bottom seismometer data we saw it necessary to ensure that we were truly analyzing SKS/SKKS arrivals and nothing else such as microseisms that displayed similar characteristics but were incoherent between stations. These strict requirements proved to prevent some stations from having any usable events. We succeeded in making reliable measurements on 11 of the 22 broadband OBS's. A sample seismogram of an acceptable signal for analysis is seen in Figure 43 and results are seen in Table 2.

Stacking methods similar to Wolfe and Silver (1998) were also used to obtain more robust results. This was especially useful due to the low number of usable events. Multiple events for the same station were stacked and SKS splitting methods were used on the resultant records. Stacking results for the network are encouragingly similar with little variation in between the majority of stations as seen in Table 3 and Figure 8.

6 FK Filtering

Many events under 90° were unusable due to interference of the S waves arrival. As such we attempted to remove the S wave arrival with a velocity filter technique. The Fourier transform was taken of a time window of the entire network that contained both the S wave and the SKKS arrival (as was typically the case of interference). Since velocity in the

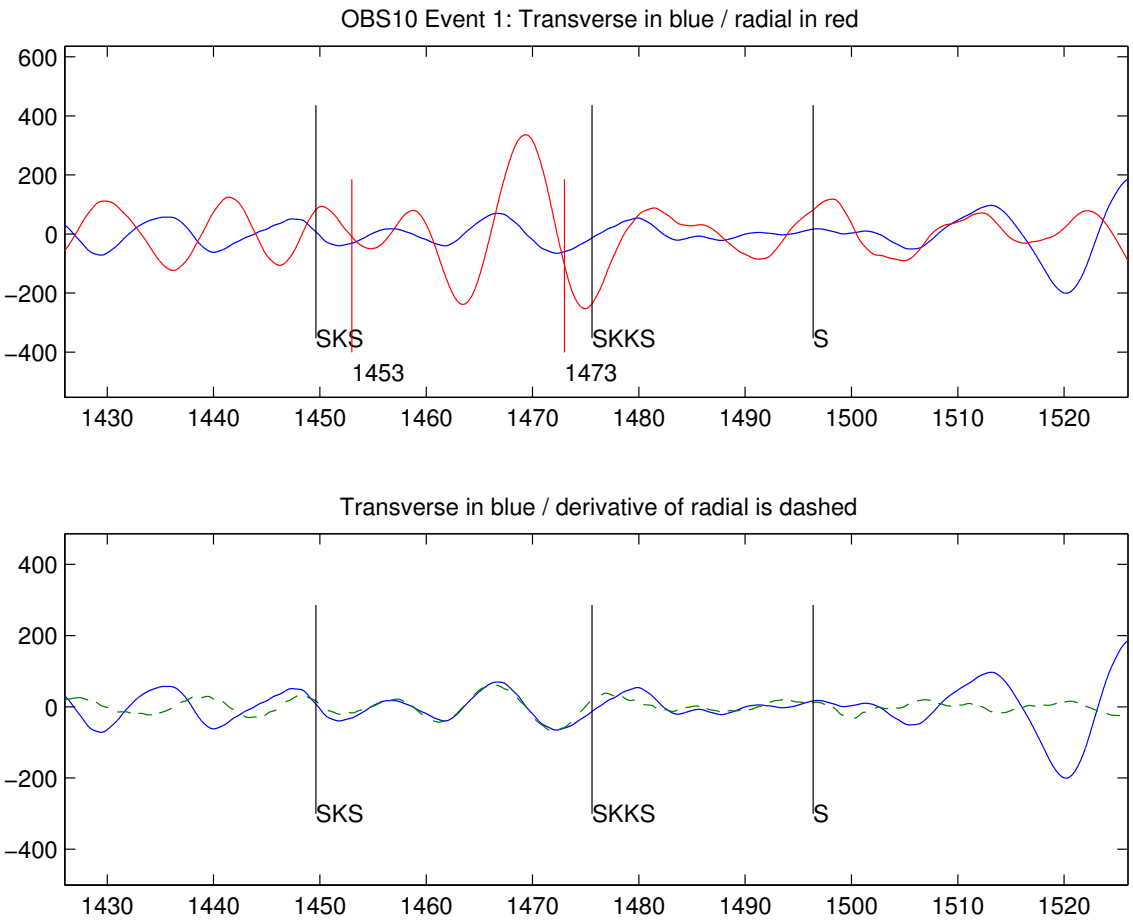

Figure 7: OBS10 Time Window

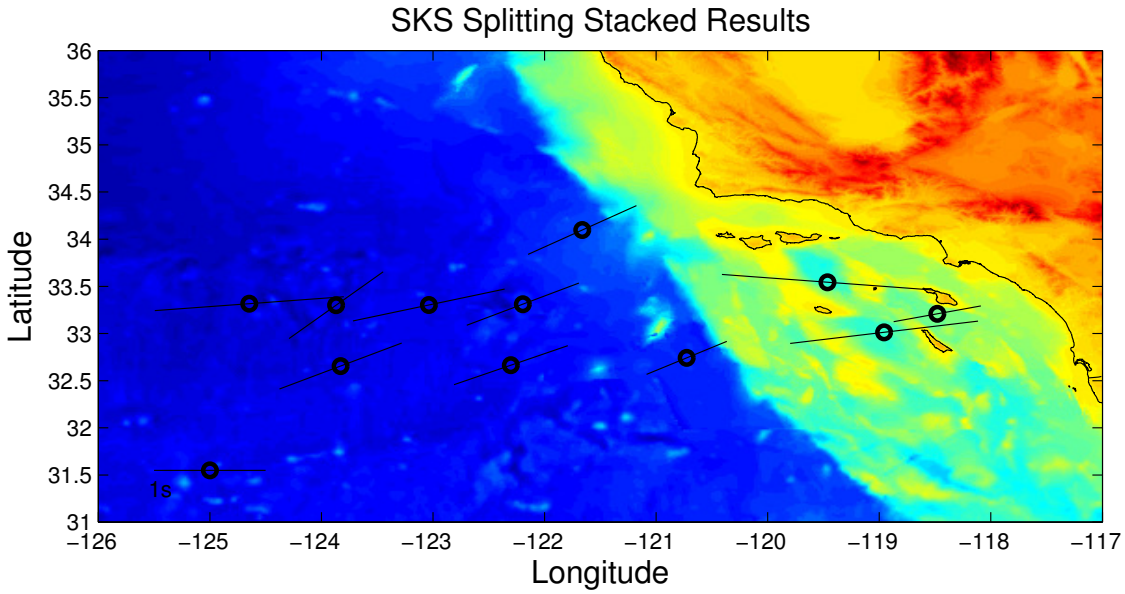

Figure 8: Stacking Results

Table 2: Single shear-wave splitting parameters at OBS sites. The direction ϕ of shear-wave polarization is measured clockwise from north.

Station	Event	ϕ (degrees)	δt (s)
3	1	81	1.8
	77	95	2.2
	98	73	1.9
7	98	84	1.8
8	98	89	1.8
10	1	71	1
	7	85	2.5
11	1	73	0.8
	98	78	1.8
13	77	79	1.2
15	1	81	1.7
	7	82	0.5
	77	86	2.1
	98	84	1.7
19	1	72	2
22	1	89	1.1
24	42	79	0.8
28	1	95	2.3
	98	85	1.8
32	1	94	2.8
	98	66	1.7

Table 3: Stacked shear-wave splitting parameters at OBS sites. The direction ϕ of shear-wave polarization is measured clockwise from north.

Station	Latitude (°N)	Longitude (°E)	ϕ (degrees)	δt (s)	Earthquakes Used
3	33.0129	-118.9574	82	1.7	1, 77, 98
7	32.7422	-120.7265	64	0.8	1, 98
10	33.3109	-122.1951	66	1.1	1
11	32.6645	-122.3016	68	1.1	1, 77, 98
13	32.655	-123.8286	66	1.2	1, 7, 77, 98
15	33.3157	-124.6472	85	1.7	1, 42, 77, 98
18	33.2999	-123.8685	50	1.1	6
19	33.3021	-123.0373	76	1.4	1, 6, 7, 42, 77, 98
22	34.0978	-121.6617	62	1.1	35
28	33.5433	-119.4645	95	1.9	1, 42, 98
32	33.2085	-118.4802	78	0.8	77

frequency domain is w/k, the velocity of the S wave could be zeroed out in f-k space. After the inverse Fourier transform was taken to get back into the time domain the S arrival should have been removed.

Figures 9 through 12 illustrate a synthetic test of this method. Two Ricker wavelets are sent across an arbitrary network at two different velocities. These waves can be seen traveling across the "network" with different apparent velocities in Figure 9.

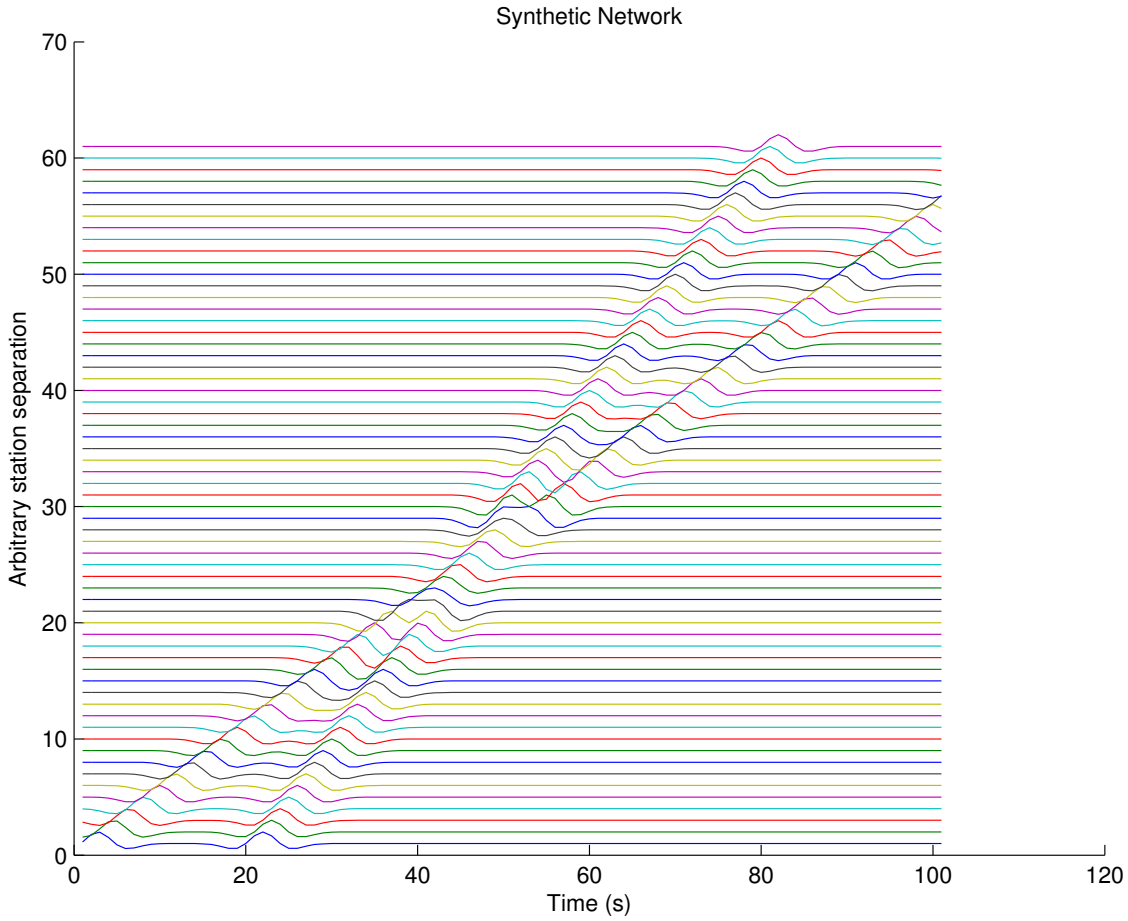

Figure 9: Synthetic Network with Two Arrivals

The 2D Fourier transform is taken of this synthetic data. In this ideal situation (in which the SNR is exceptionally good) we can see how the energy of the two waveforms shows up as two distinct groups of signal in Figure 11. These are easily selected and either can be filtered out.

This method works exceptionally well with synthetic data. The targeted arrival was

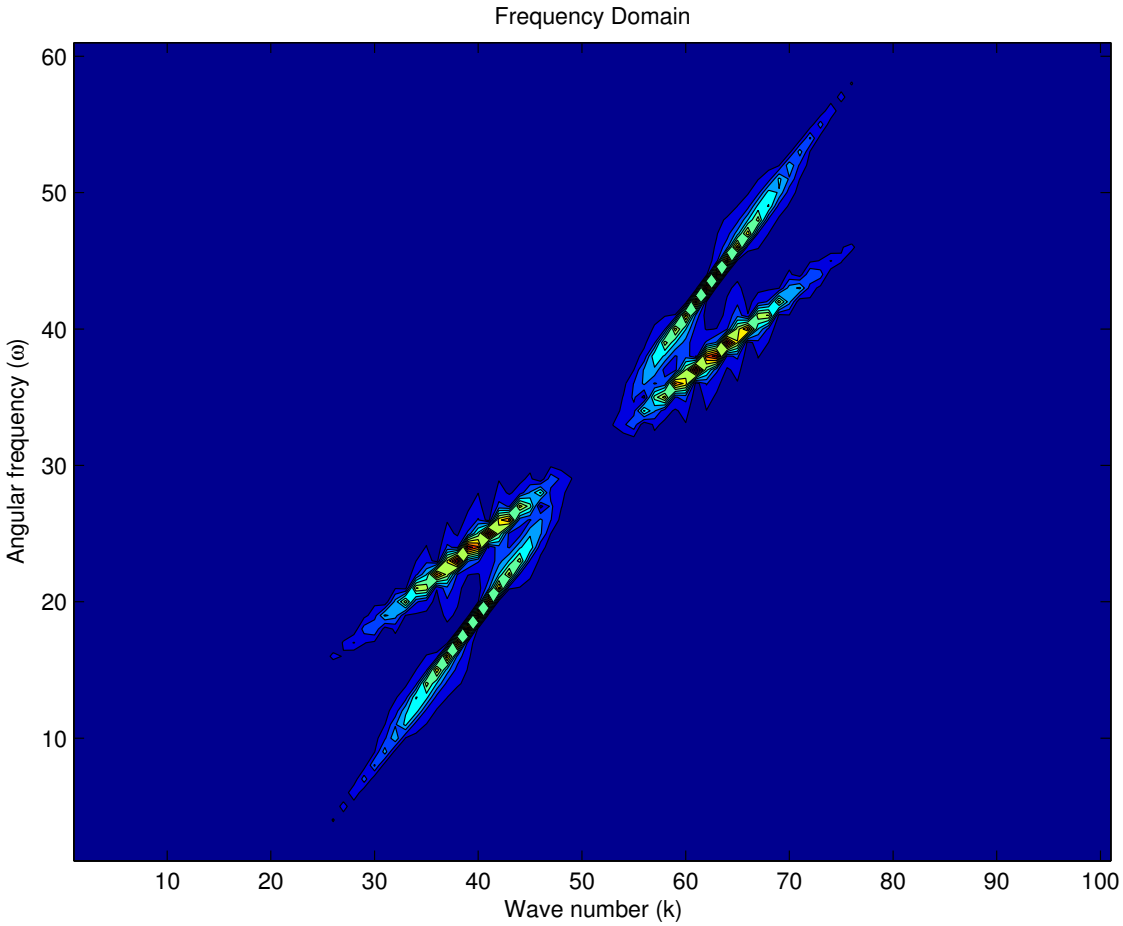

Figure 10: FFT of Synthetic Network

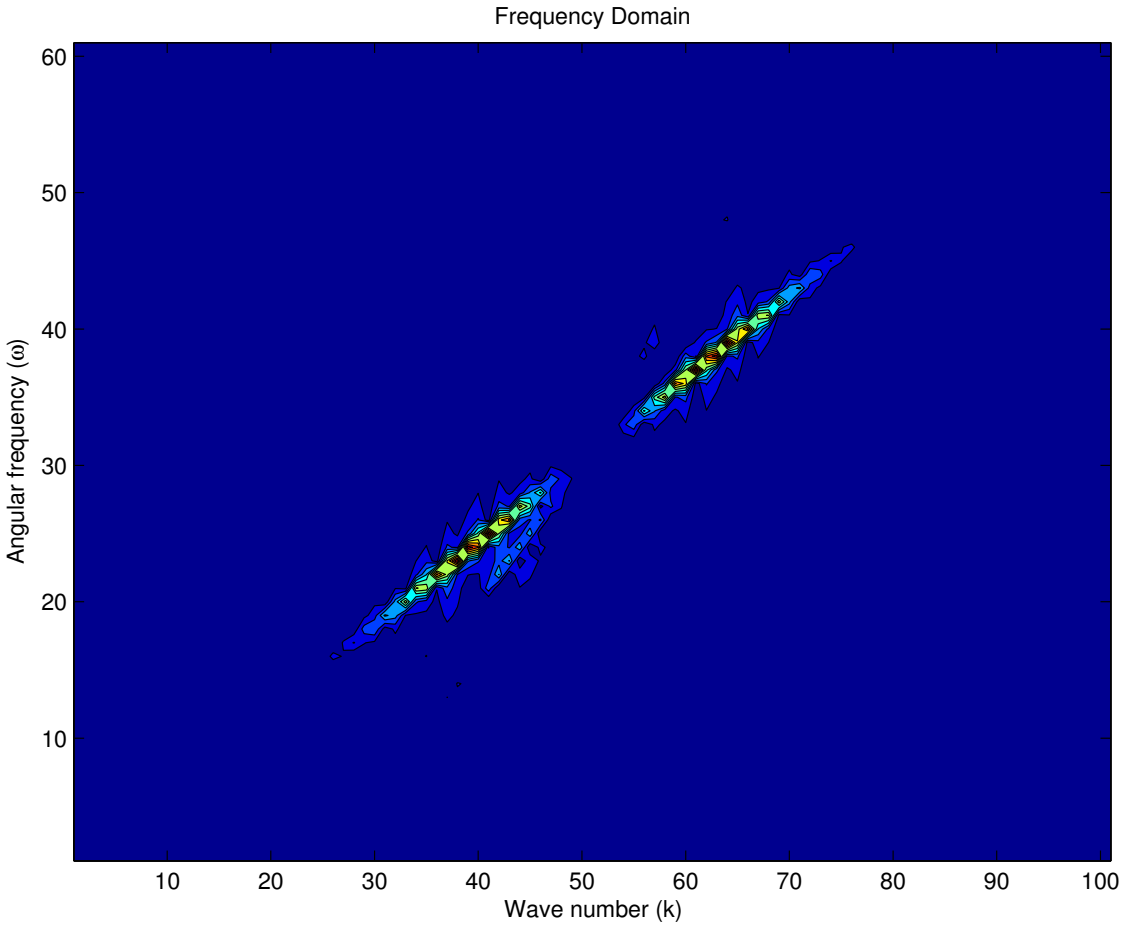

Figure 11: Post-Cutting FFT of Synthetic Network

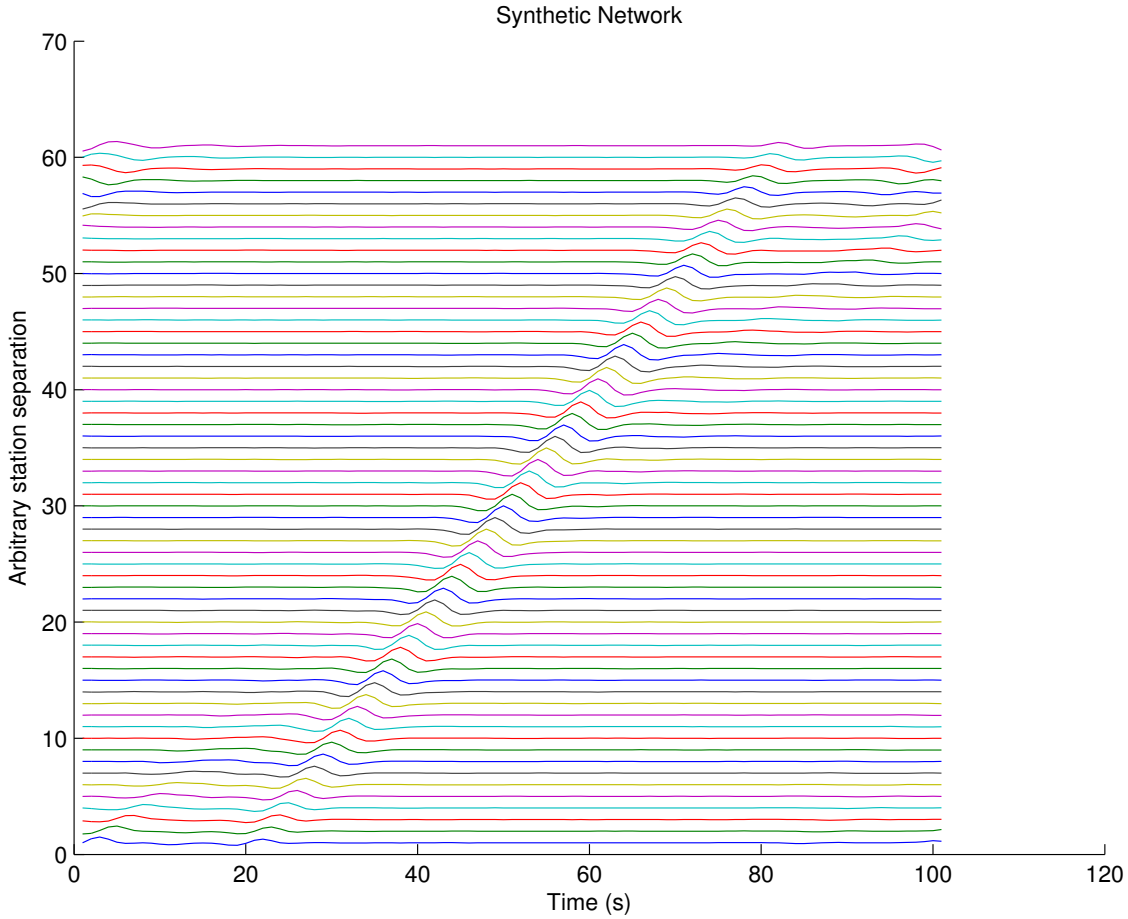

Figure 12: iFFT of Synthetic Network

removed with minimal influence on the remaining data as seen in Figure 12. With real data, however, it is unclear if the method is entirely effective. In Figure 13 we see an example event (#33) from the OBS data. This shows each station sorted by great circle arc path. Due to the requirement of evenly spaced data in time and space for an FFT it is necessary to interpolate for an evenly divided great circle path. This also means that the back azimuth of each station must be interpolated (since the back azimuth is necessary for splitting measurements). This situation is not ideal since any SKS splitting measurements done would not be for each actual station but merely give an interpolated trend of anisotropy. Signals are lined upon the SKS or SKKS arrival so that it is clear that the S wave has a different apparent velocity. In this way an SKS or SKKS wave is seen (especially in the stations further from the event). Figure 13 shows signals lined up on an SKS arrival so as to show the different apparent velocities of the SKKS and S arrivals. Since the SNR is not nearly as high as in the synthetic case the FFT of the data does not have as distinct patches of energy as seen in Figure 14.

Once the S energy is removed, the resultant data looks as seen in Figure 16.

While the S arrival with moveout to the right in Figure 13 does appear to be attenuated the SKKS arrival has a similar velocity and therefore it is difficult to eliminate S completely. Furthermore, SKS splitting measurements both before and after the velocity filter process produce similar results which suggests that the process does not have a great effect (see Table 4). The pre-FK filter splitting results show a median of 96° whereas the post-FK filter results show a median of 97°. In the end we determined that the velocity filter idea would be more useful for less noisy data, but removing interfering S energy makes the splitting analysis more reliable.

Table 4: SKKS splitting results of interpolated stations both before and after FK filtering. Stations are listed in receding great circle arc distance.

ϕ pre-filter	δt pre-filter	ϕ post-filter	δt post-filter
115	1.3	99	0.8
117	1.2	105	0.7
105	0.9	112	0.7
110	0.8	120	0.7

131	1.5	128	0.7
102	0.9	88	0.7
96	1.1	81	1.2
93	1.5	86	1.4
99	1.6	92	2
99	1.6	93	1.6
93	1.7	92	1.6
104	1.8	90	1.6
99	1.5	97	1.5
99	1.4	91	2.2
96	1.5	91	2.5
94	1.6	92	2.8
88	2.3	92	2.8
93	1.4	92	2.7
92	1.7	89	2.8
89	1.7	83	2.9
124	0.8	115	0.7
78	1.6	121	0.8
82	1.7	120	0.7
96	1.2	112	0.9
98	1.3	102	1.1
98	1.4	97	1.3
93	1.2	97	1.3
78	2.3	84	2.1
79	2.3	88	1.9
82	2.1	96	1.4
85	1.7	97	1.3
87	1.6	99	1.1
87	1.6	100	1.4
95	1.7	94	2.1

100	1.4	85	1.4
105	1	113	0.9
103	0.8	102	0.8
100	1	67	3.2
104	0.9	94	0.9
177	2.8	35	1.9
111	1.7	90	1.5
95	1.4	107	1
96	1.6	98	1.2
90	1.3	100	1.2
90	1.3	103	1.1
94	1.2	103	1.1
92	1.4	100	1.3
83	1.1	100	1.3
99	1.3	101	1.4
92	1.3	91	1.3
89	1.5	84	1.8
114	1.8	98	1.3
136	2.6	96	1.3
51	3.4	108	1.1
50	3.5	97	1.4
100	1	96	1.5
101	1.1	111	1.1
98	1.1	127	1
92	1.3	119	1.1
87	1.6	106	1.3

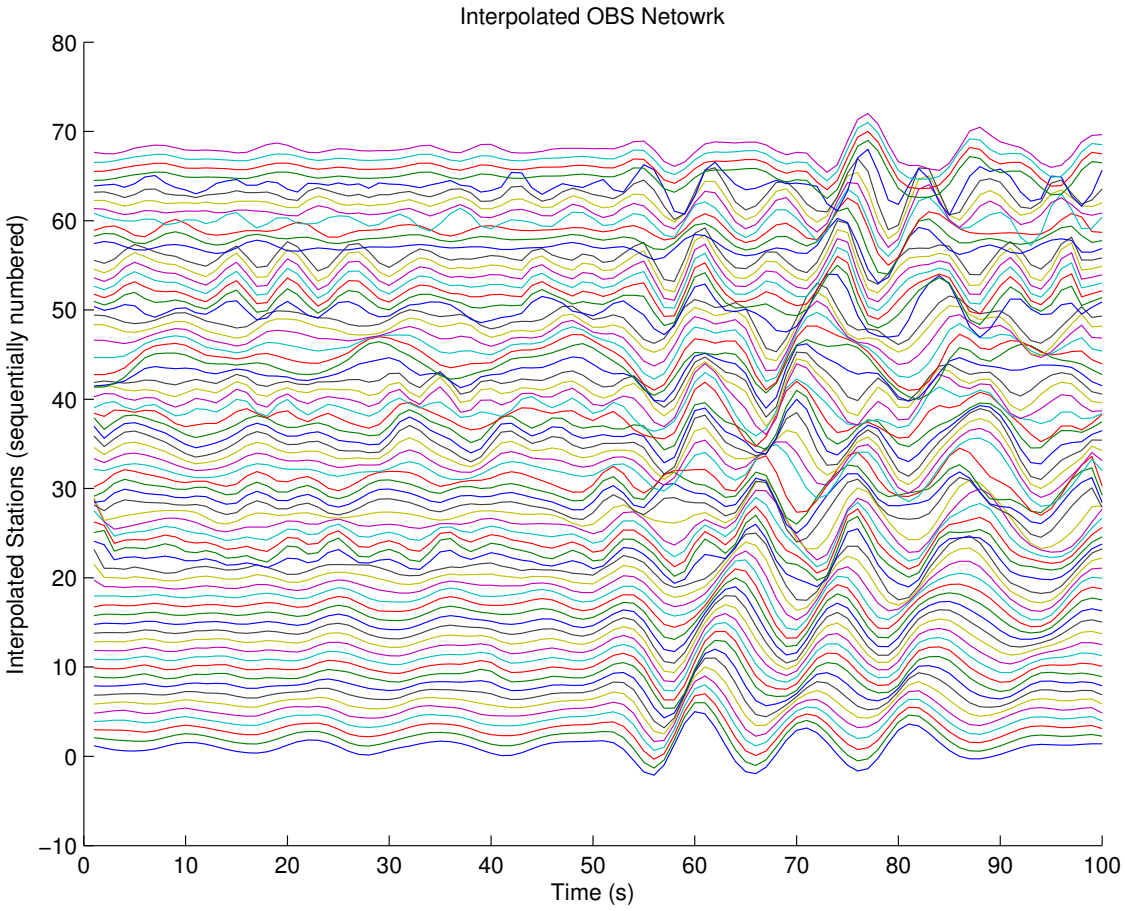

Figure 13: OBS Network with Interpolated Stations

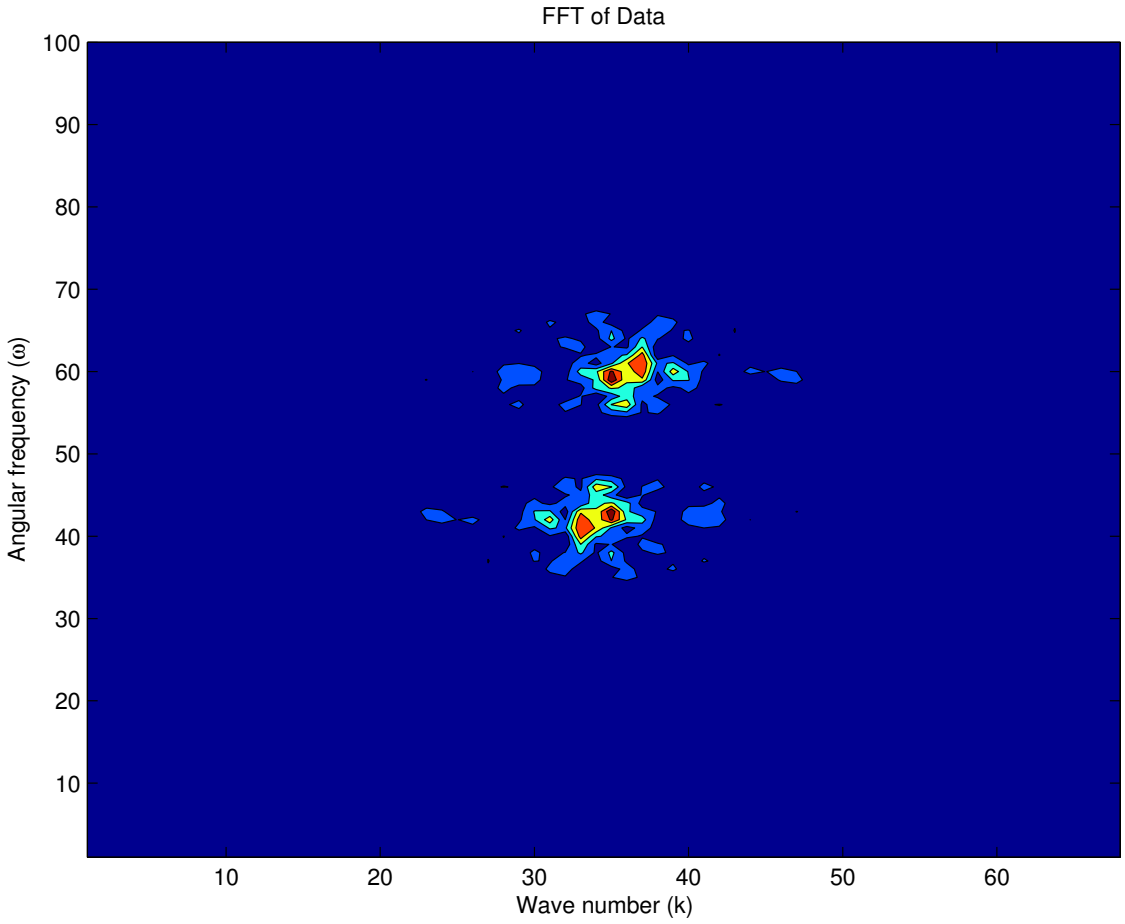

Figure 14: FFT Of Interpolated Network

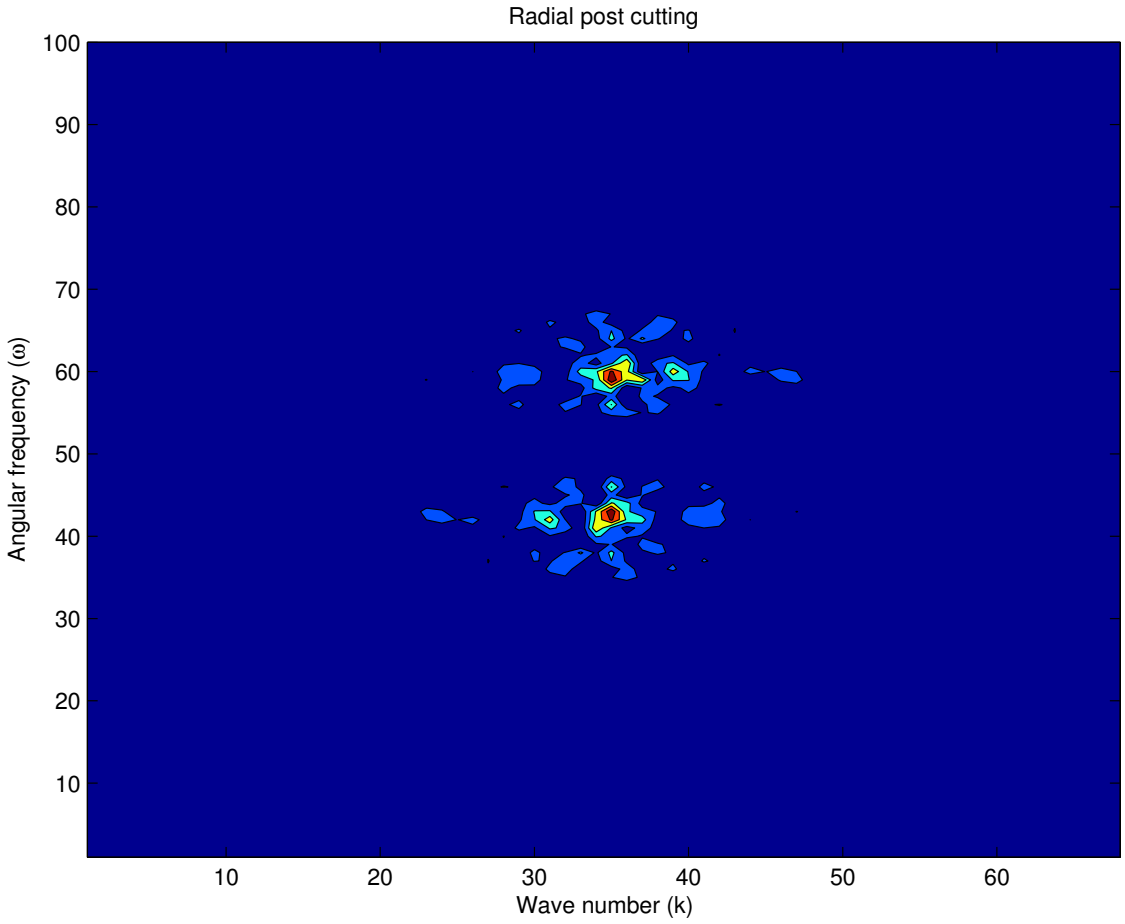

Figure 15: Post-Cutting FFT Of Interpolated Network

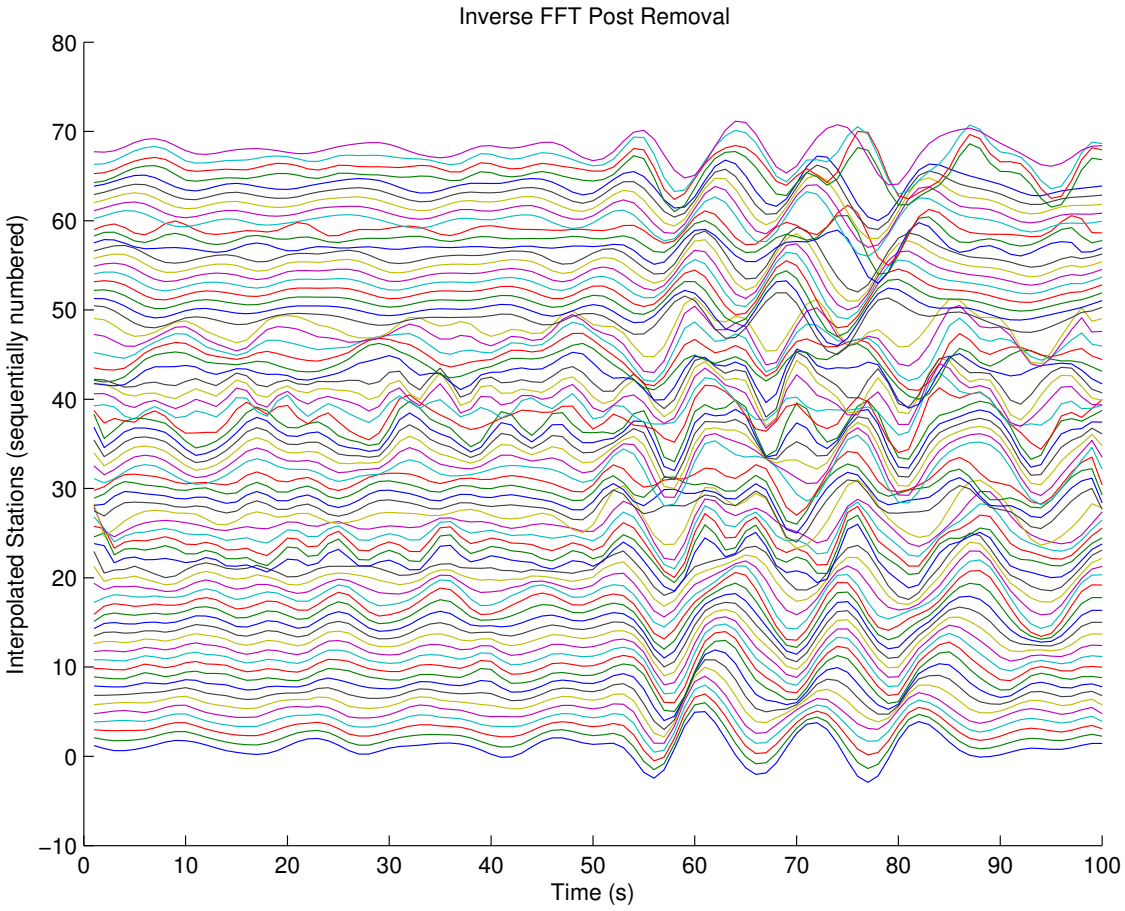

Figure 16: iFFT Of Interpolated Network

7 Discussion and Conclusion

Both the splitting and F-K filtering results show the fast direction of anisotropy out on the Pacific Plate does not align with APM, which was the original conjecture. These measurements extend the trend of anisotropy in Southern California well onto the Pacific Plate (˜500km). The results require a different explanation than simple lithospheric drag. It could be that a battle of influence between fossil seafloor spreading and APM is in play(Harmon et al., 2004). Given that our SKS splitting results align so well with the various fracture zones in the region, it seems possible that the seafloor age is young enough that we are still looking at fossil spreading. The seafloor is simply too young (<40My) for APM to have imprinted its direction on anisotropy in a complete sense. This hypothesis is supported by previous research which found that, while anisotropy in French Polynesia was oriented in APM, observations in the North Pacific indicated that fossil seafloor spreading still prevailed (Wolfe and Solomon, 1998).

When more recent studies are brought to bear, however, this seems unlikely. Kosarian et al. (2011) found E-W SKS splitting results on both sides of the Big Bend of the SAF whereas surface waves gave azimuthal anisotropy aligned with the SAF. These differences suggest that most of SKS splitting is generated deeper than the lithosphere. If this is the case, frozen in fossil spreading is an unlikely candidate.

Mantle flow could be the cause. Research by Zandt and Humphreys (2014) into the circular pattern of anisotropy in the western United States (see Figure has proposed the explanation that it is caused by slab rollback due to the Juan de Fuca plate. Mantle flow around the edge of the sinking Juan de Fuca plate causes a torroidal pattern of anisotropy as seen in Figure 18. If this is the case, a similar but counter flowing pattern could be predicted for the Cocos plate. Stubailo et al. (2012) found a similar circular pattern of anisotropy near the Trans-Mexican Volcanic Belt. A slab rollback story leading to torroidal mantle flow was proposed. Our results would fit in nicely with such a theory. The SWS-ENE pattern of SKS splitting would fit on the NW edge of such a circular pattern as seen in Figure 19.

Furthermore, our SKS splitting measurements do not agree with predicted splitting via azimuthal anisotropy models such as Yuan and Beghein (2013) except at a depth of 200km

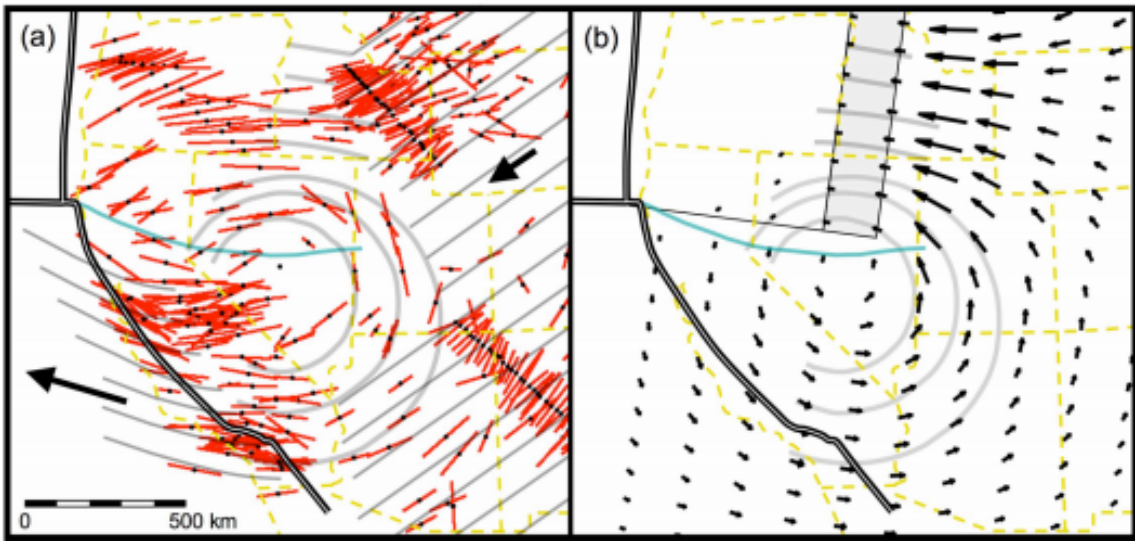

Figure 17: (a) SKS splitting from Zandt and Humphreys (2014) (b) mantle flow from numeric simulation given by rollback of a narrow slab (shaded rectangle)

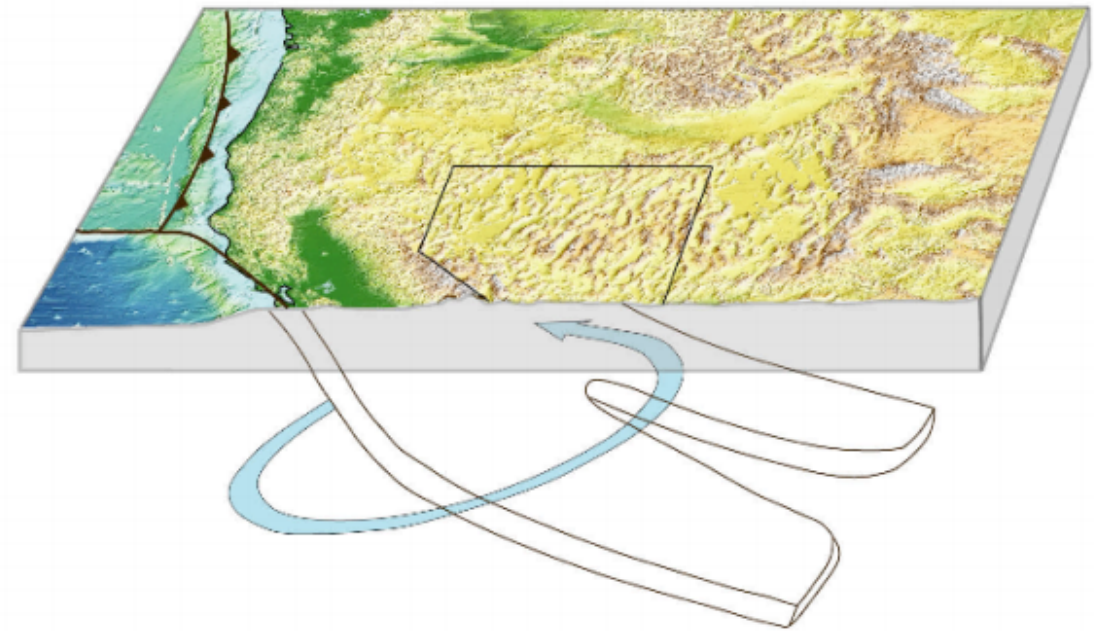

Figure 18: Schematic from Zandt and Humphreys (2014) showing flow around the edge of the Gorda-Juan de Fuca slab

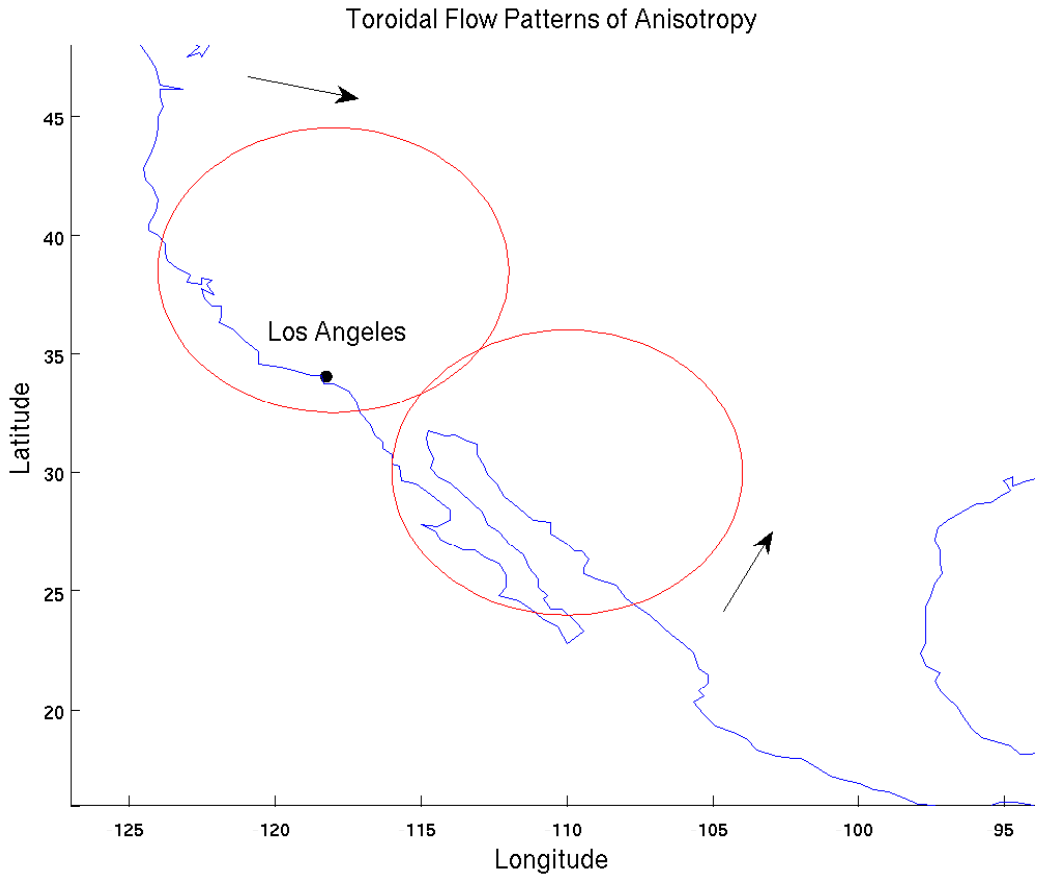

Figure 19: Proposed toroidal flow pattern of anisotropy

as seen in Figure 20. This would be an appropriate depth at which slab rollback influenced mantle flow would occur.

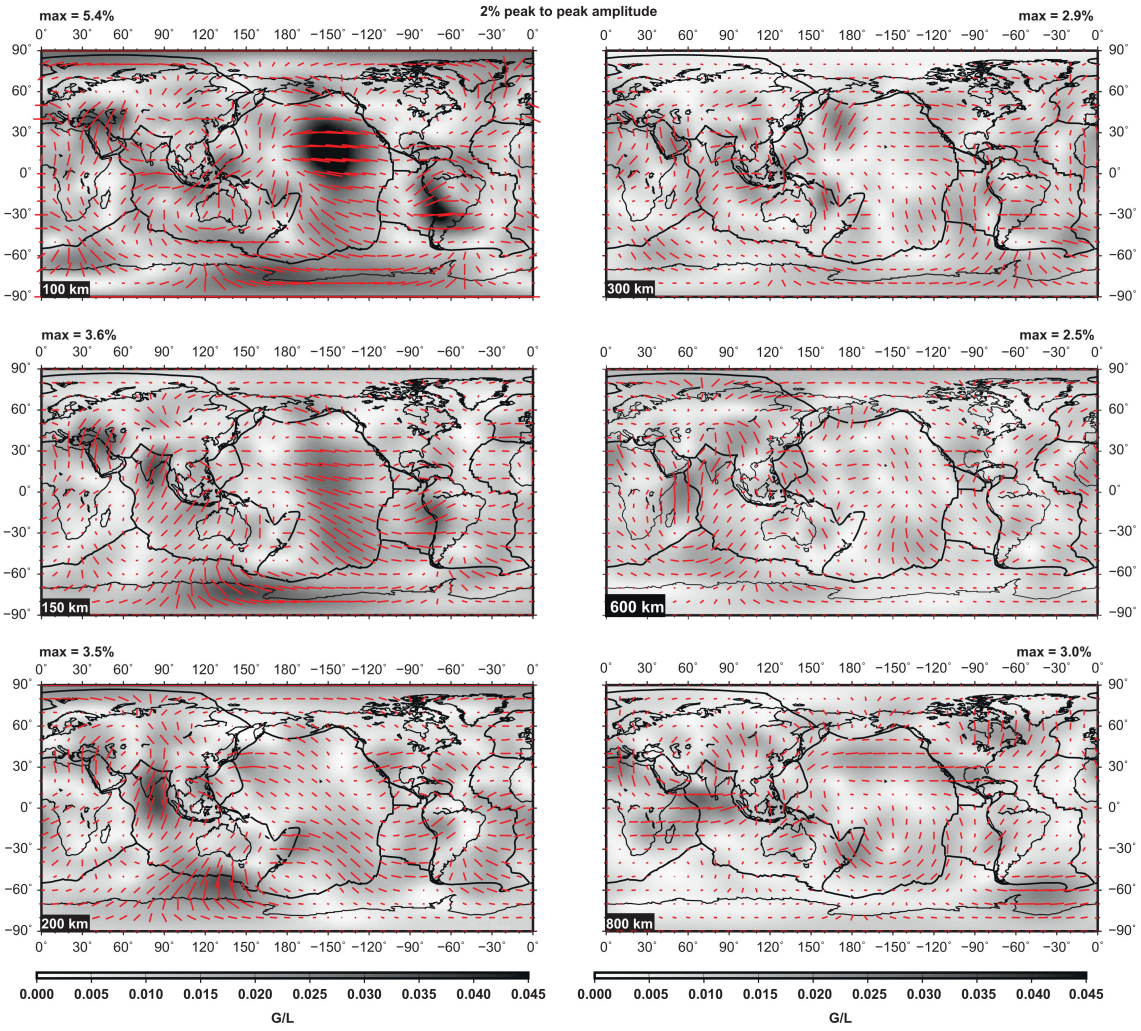

Figure 20: Global 3-D azimuthal anisotropy model from Yuan and Beghein (2013). Depth at 200km coincides with SKS splitting torroidal flow hypothesis.

Appendices

This appendix includes figures from every splitting measurement used for these results. They are formatted in the following way: data used complete with time window, contour map of tangential energy, particle motion of subsequent correction, time window showing the tangential component minimized. After this, if multiple events are used, will be a contour map of stacking energy. These measurements are listed sequentially for each station, starting with OBS03.

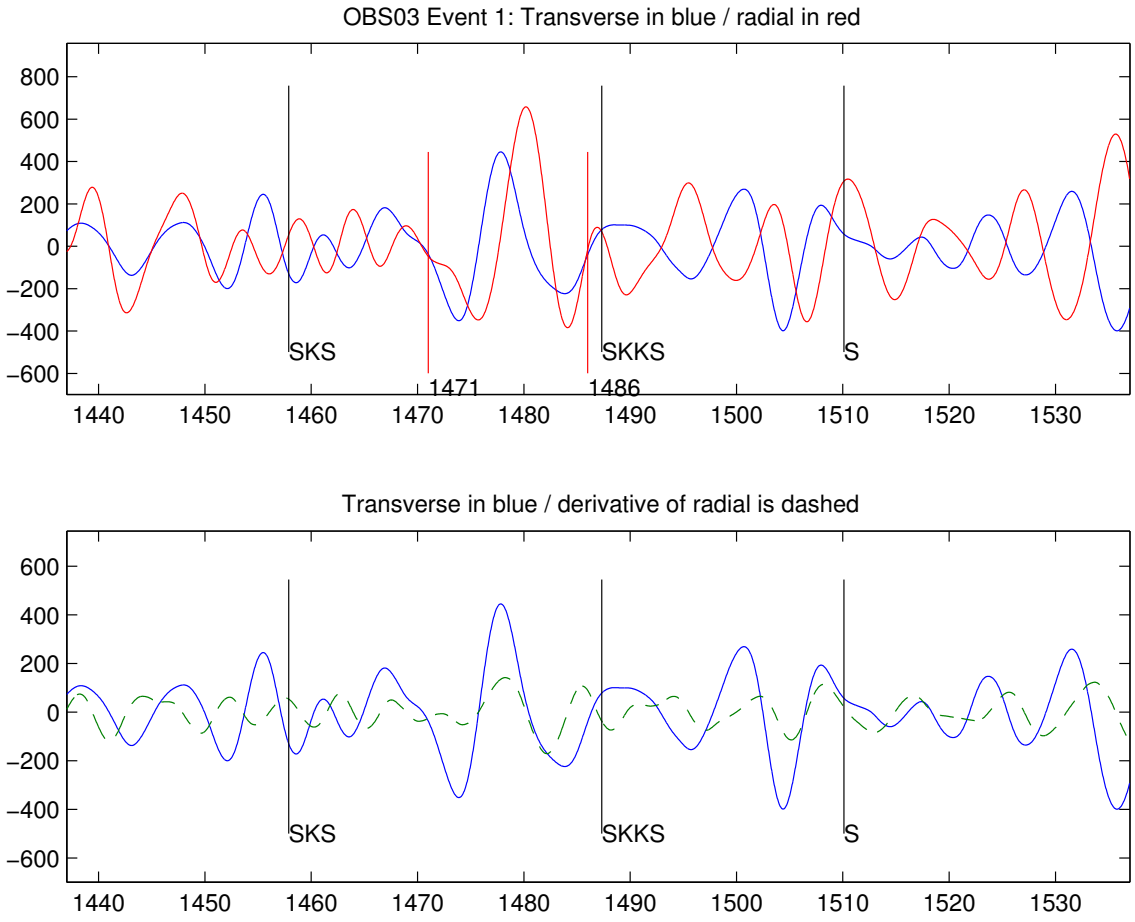

Figure 21: OBS03 Time Window

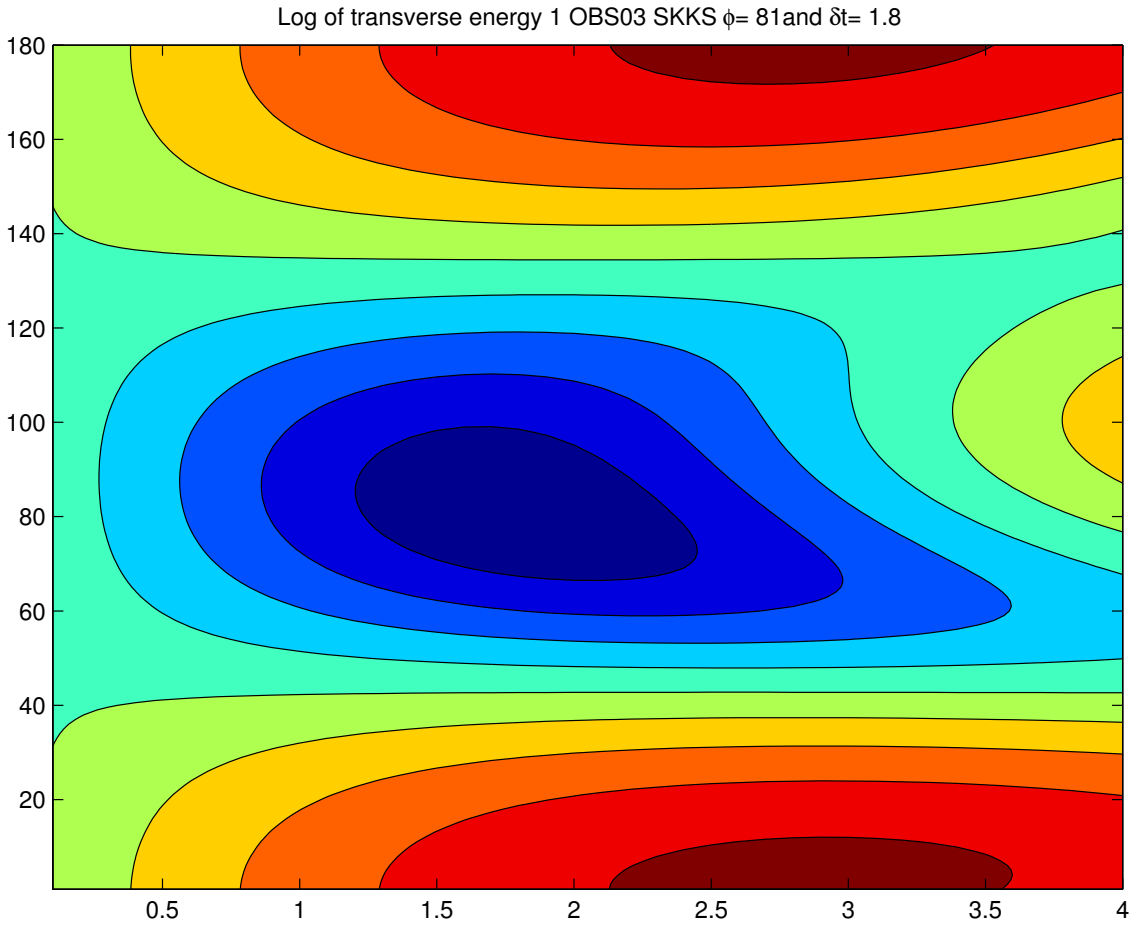

Figure 22: OBS03 Contour

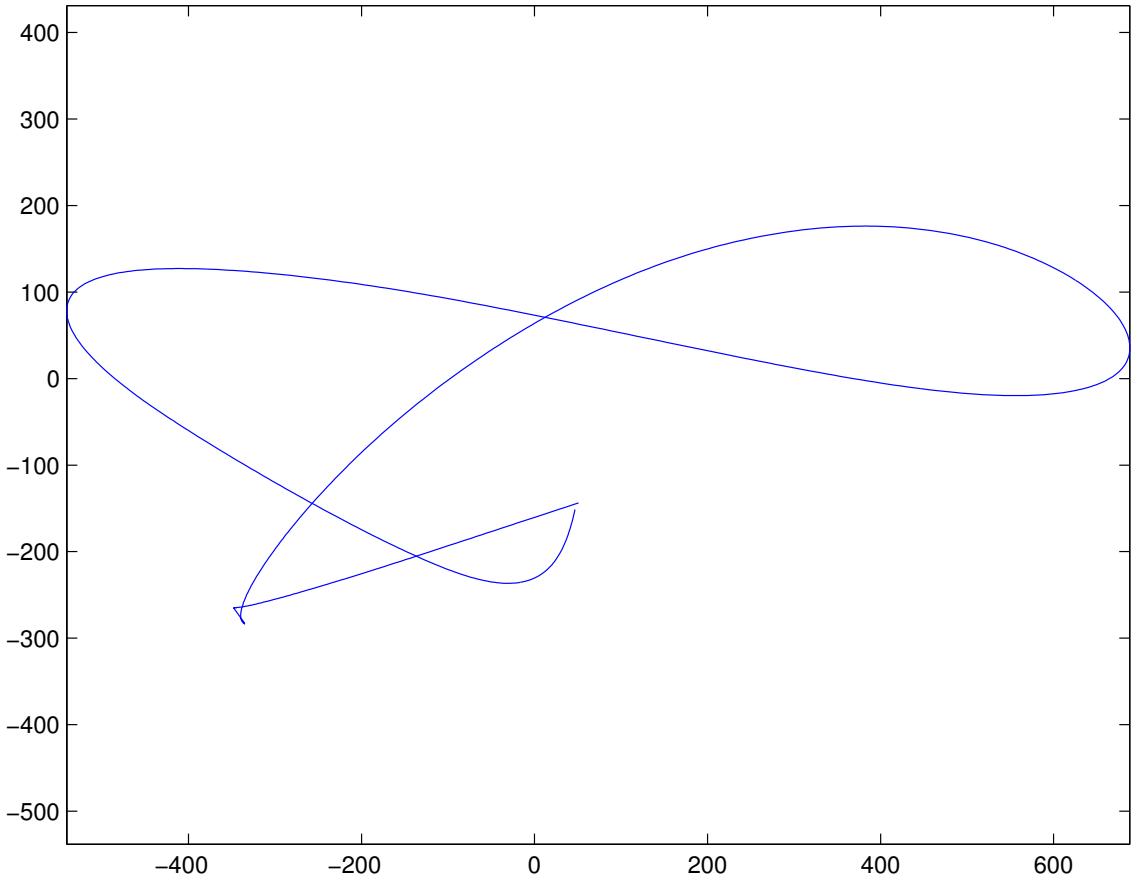

Figure 23: OBS03 Particle Motion

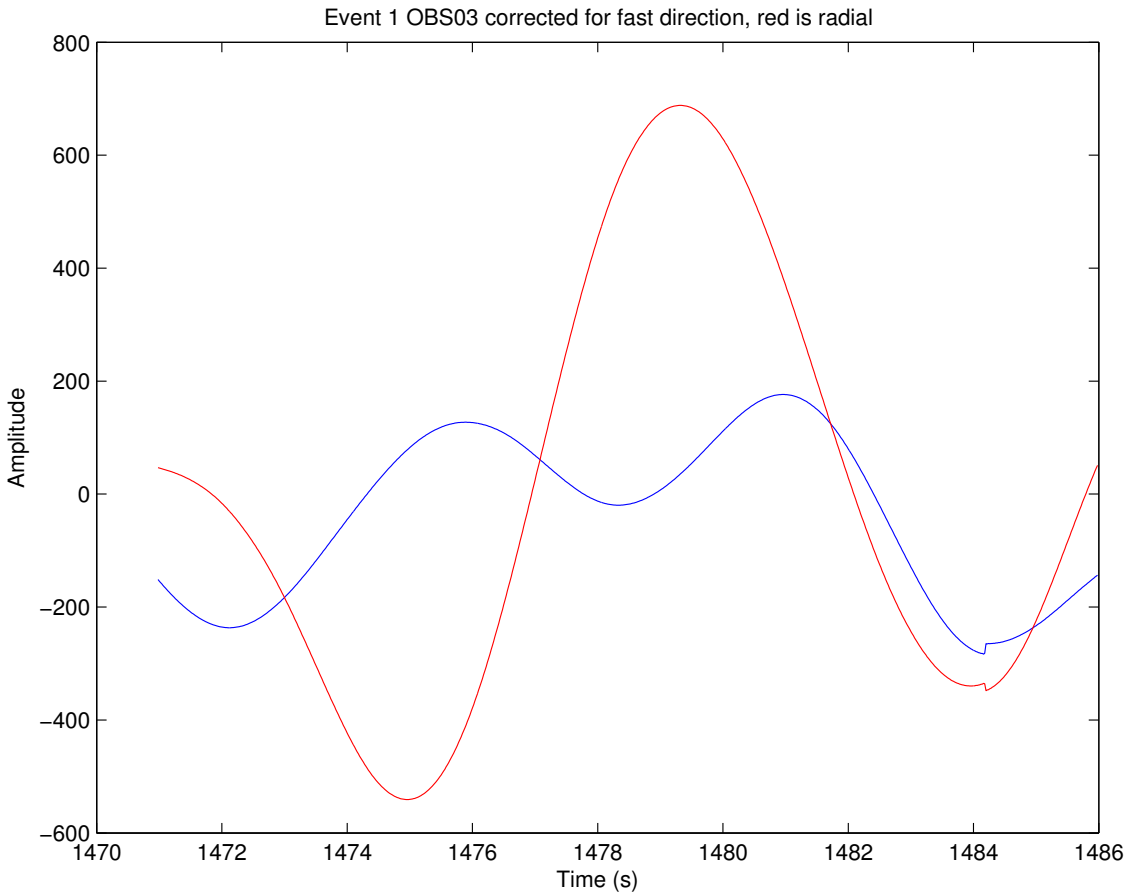

Figure 24: OBS03 Corrected

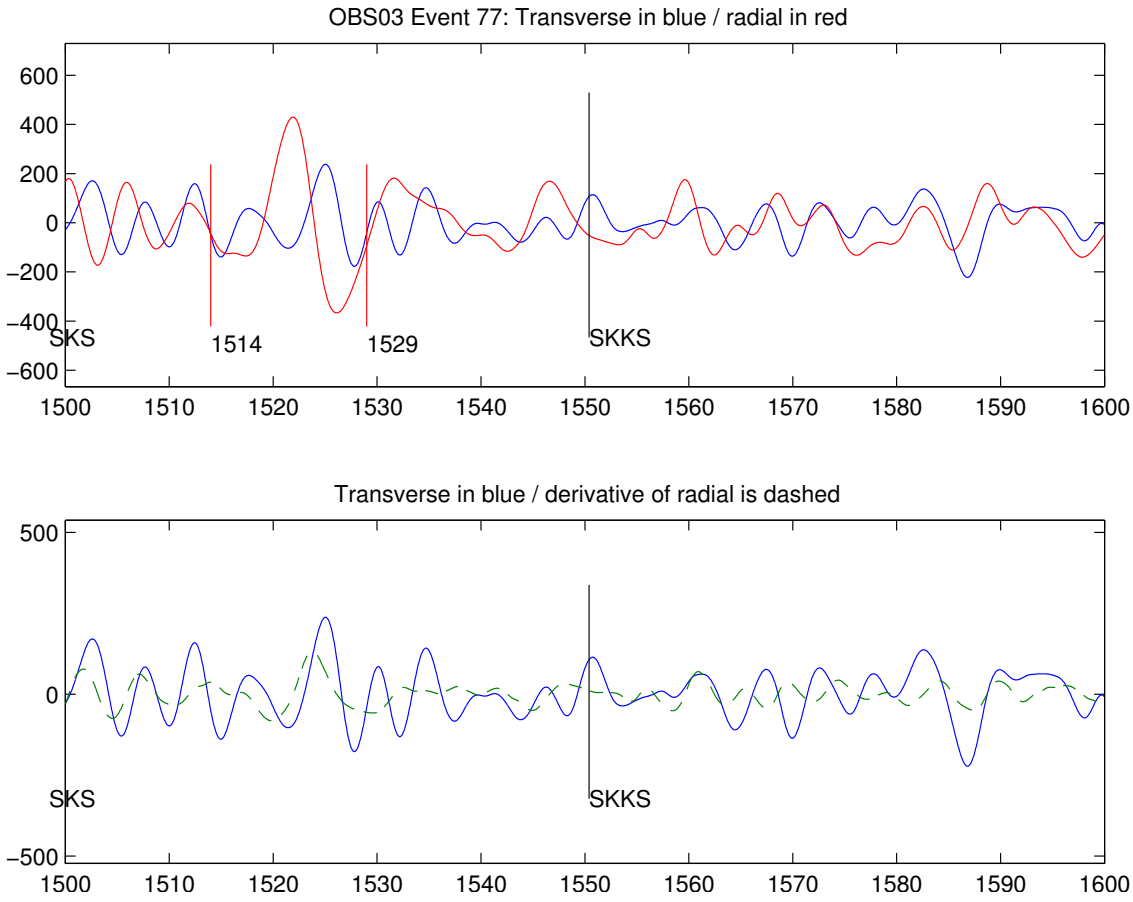

Figure 25: OBS03 Time Window

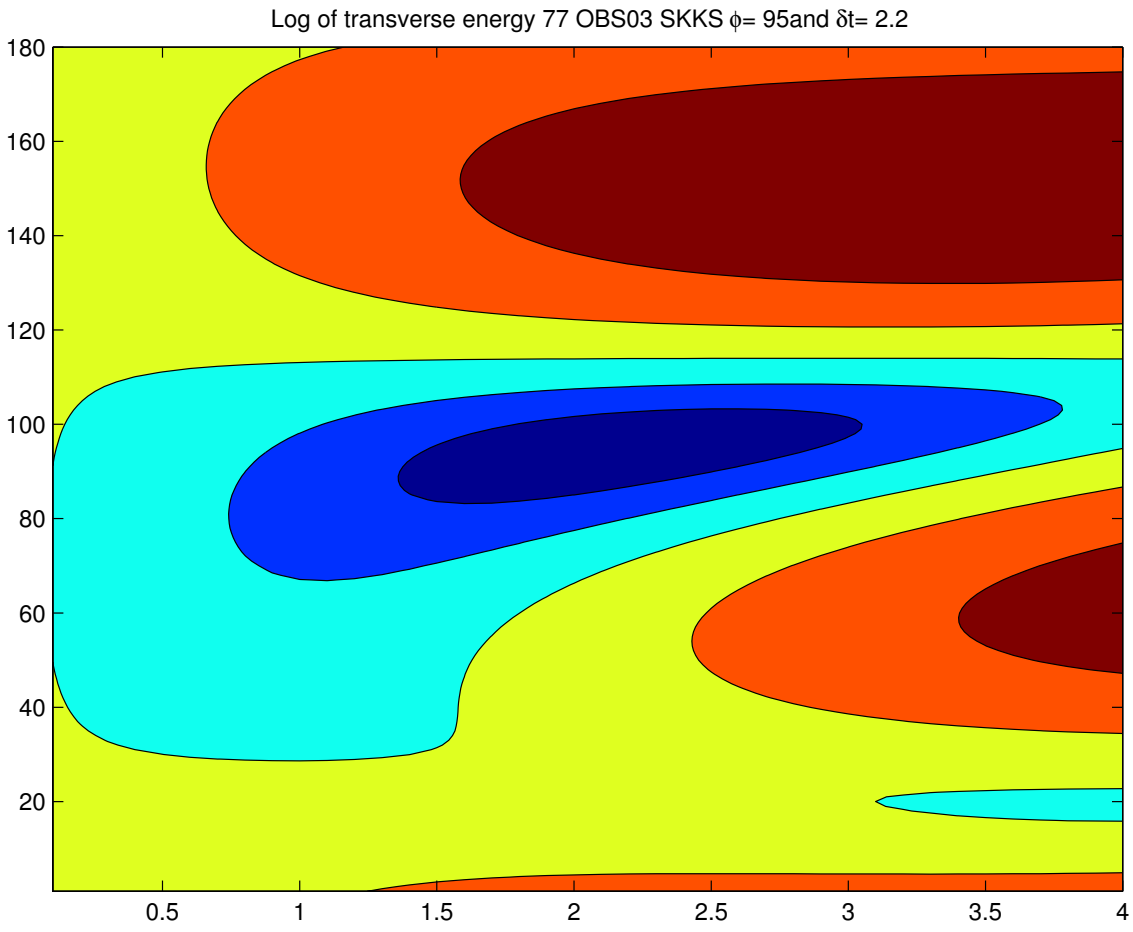

Figure 26: OBS03 Contour

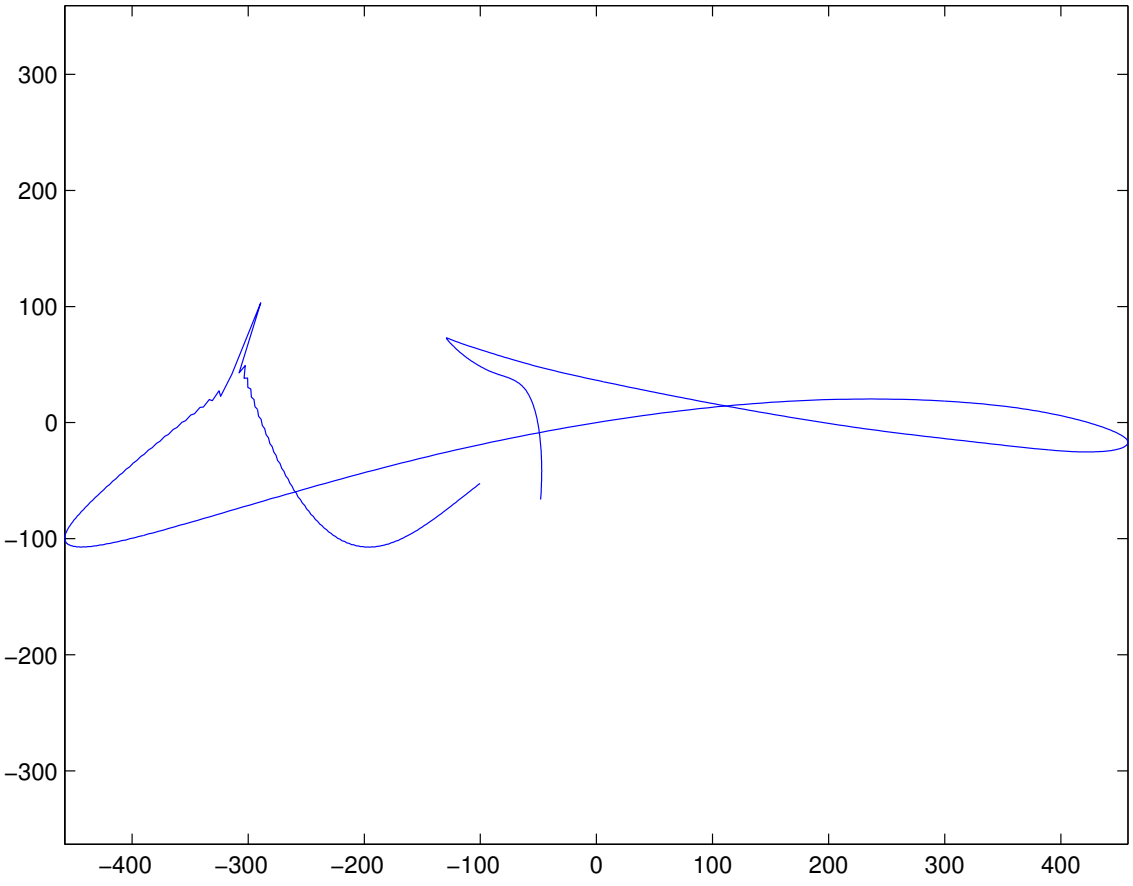

Figure 27: OBS03 Particle Motion

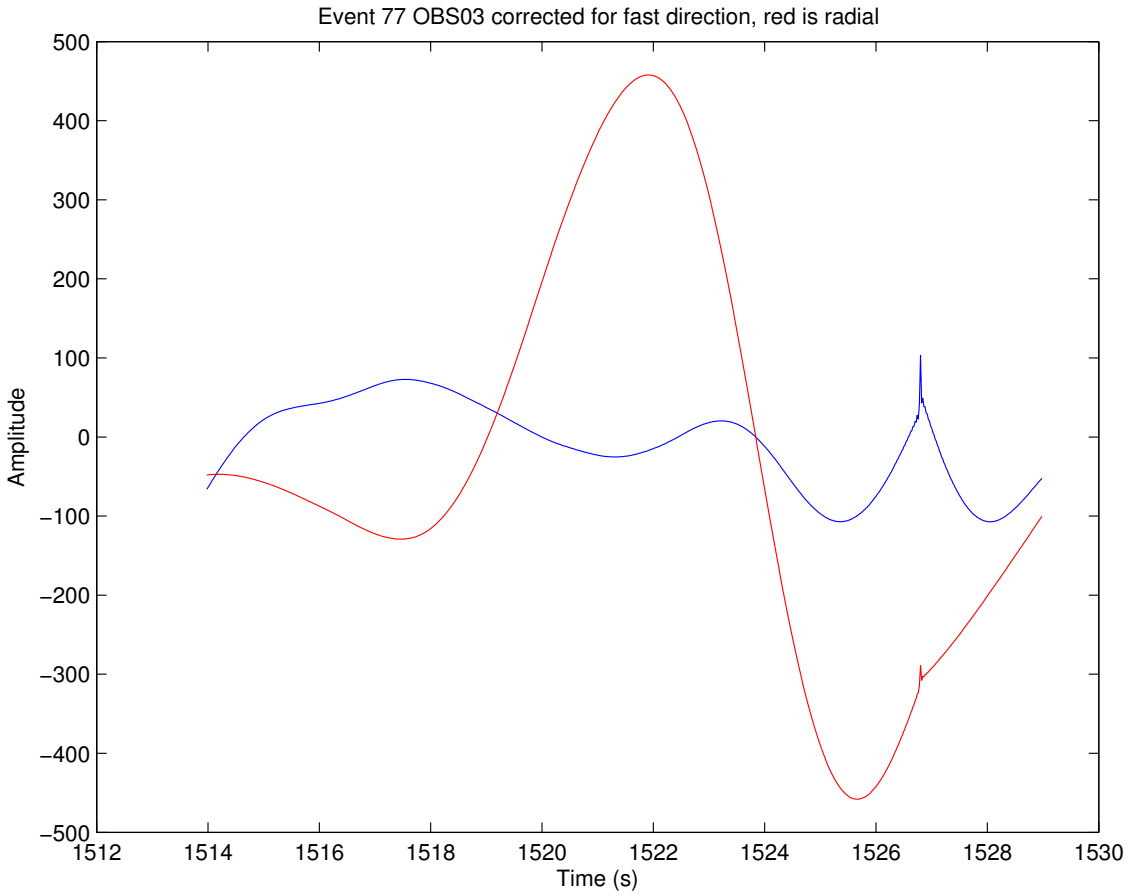

Figure 28: OBS03 Corrected

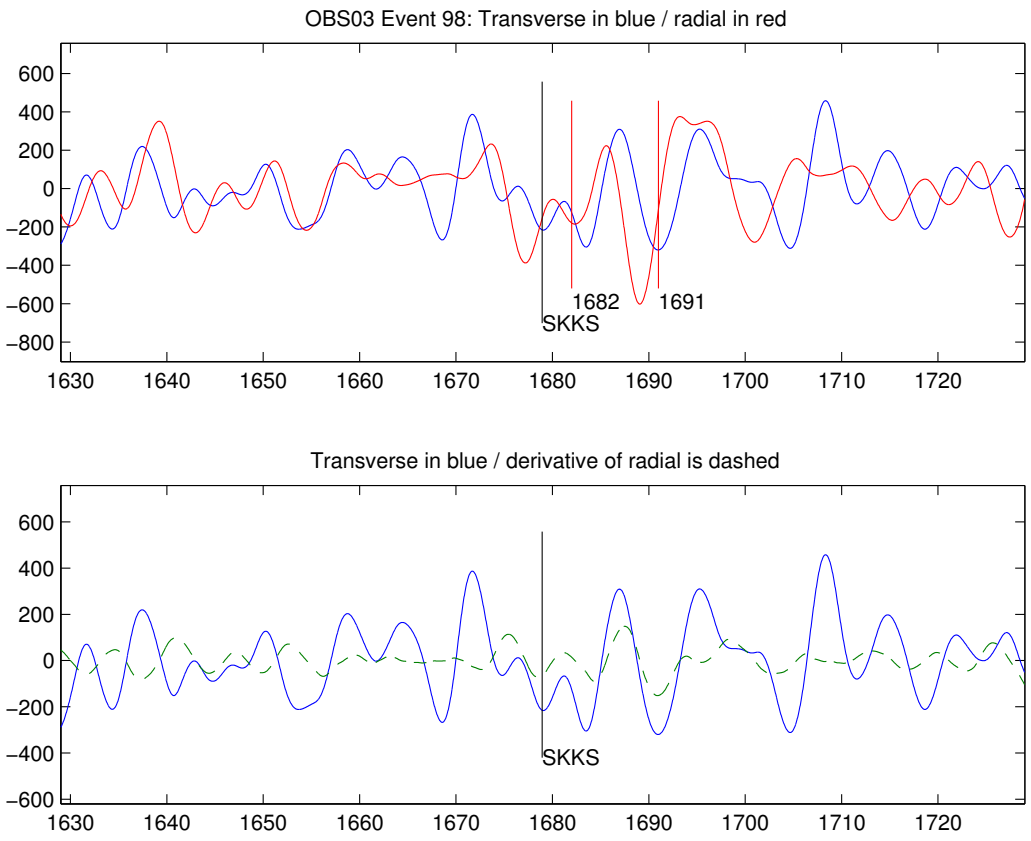

Figure 29: OBS03 Time Window

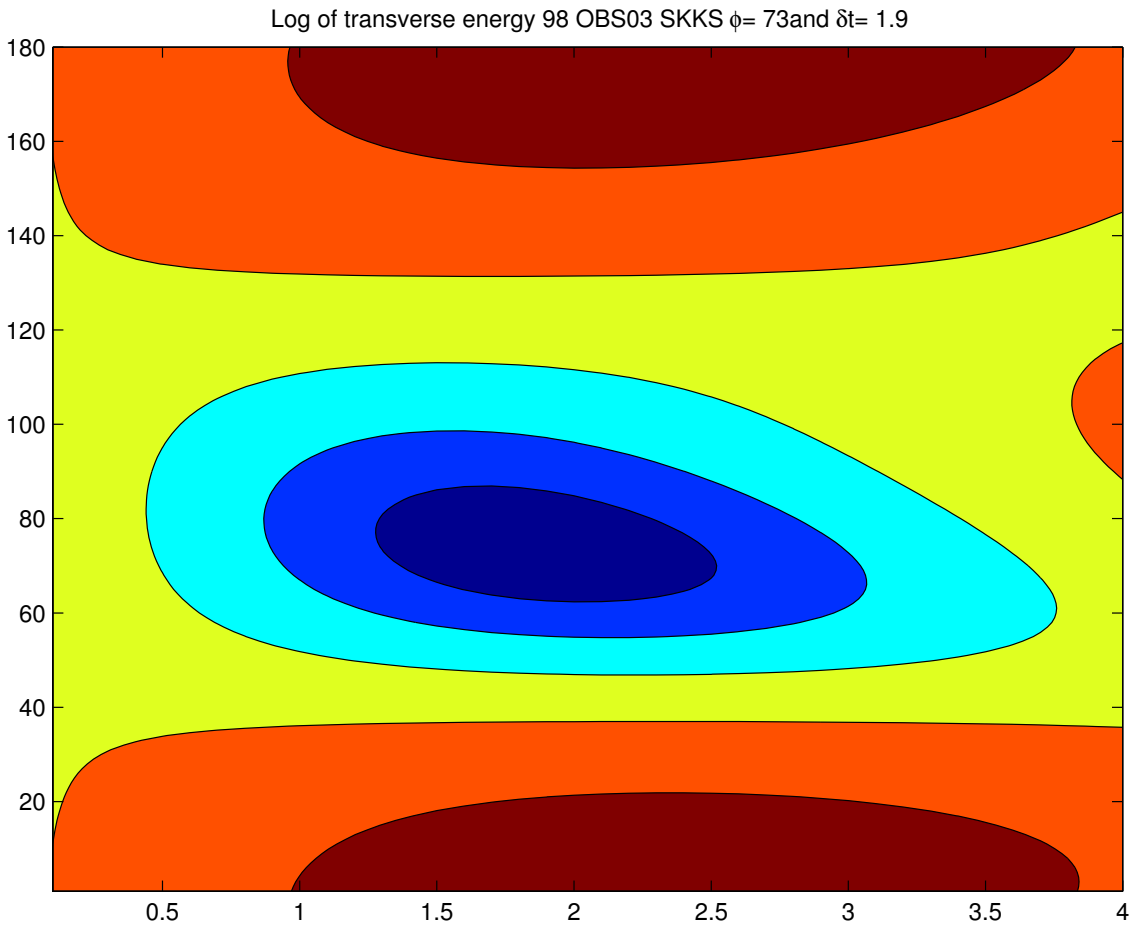

Figure 30: OBS03 Contour

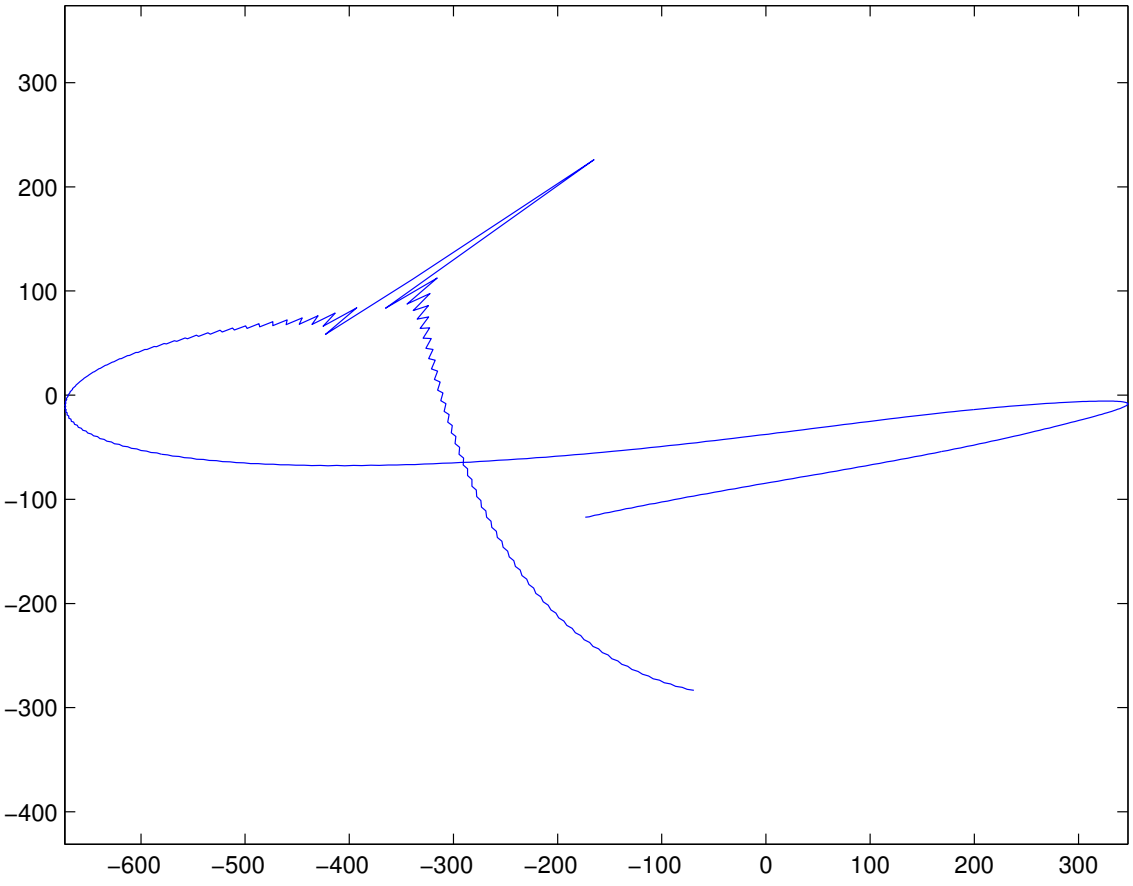

Figure 31: OBS03 Particle Motion

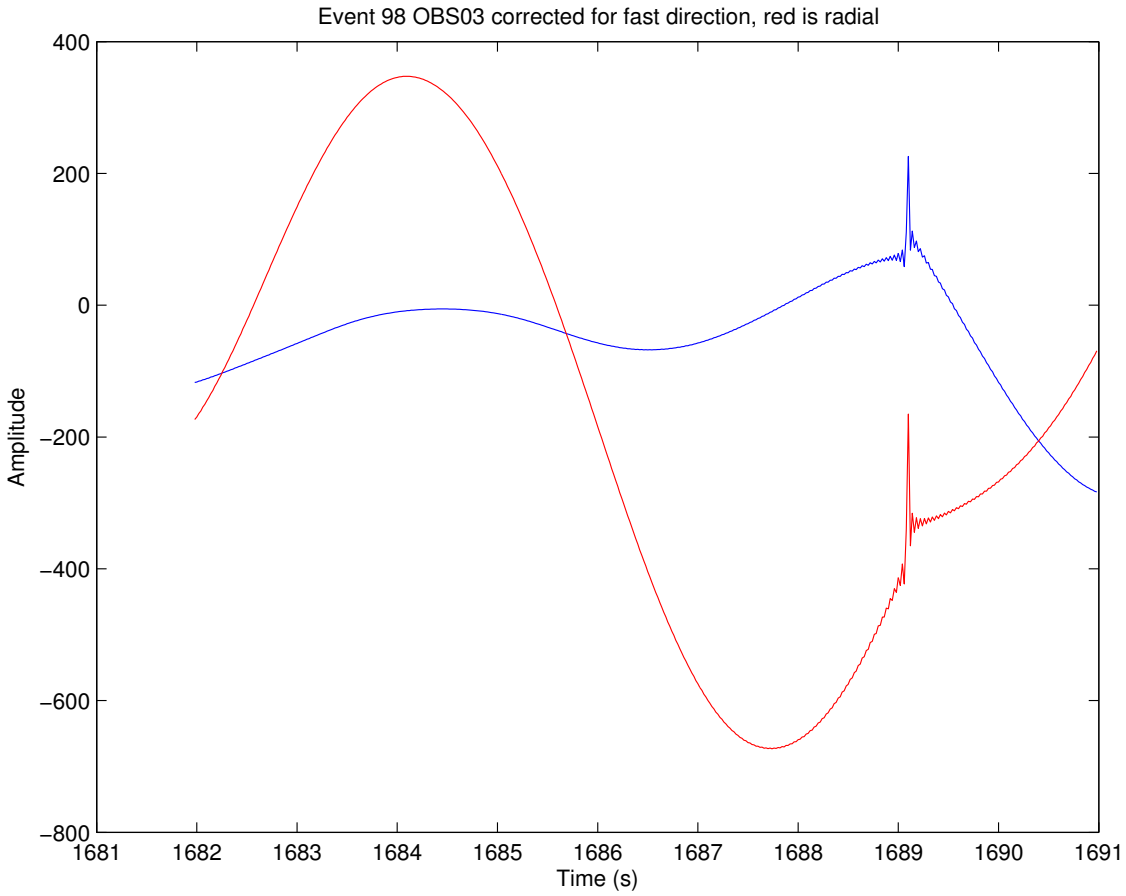

Figure 32: OBS03 Corrected

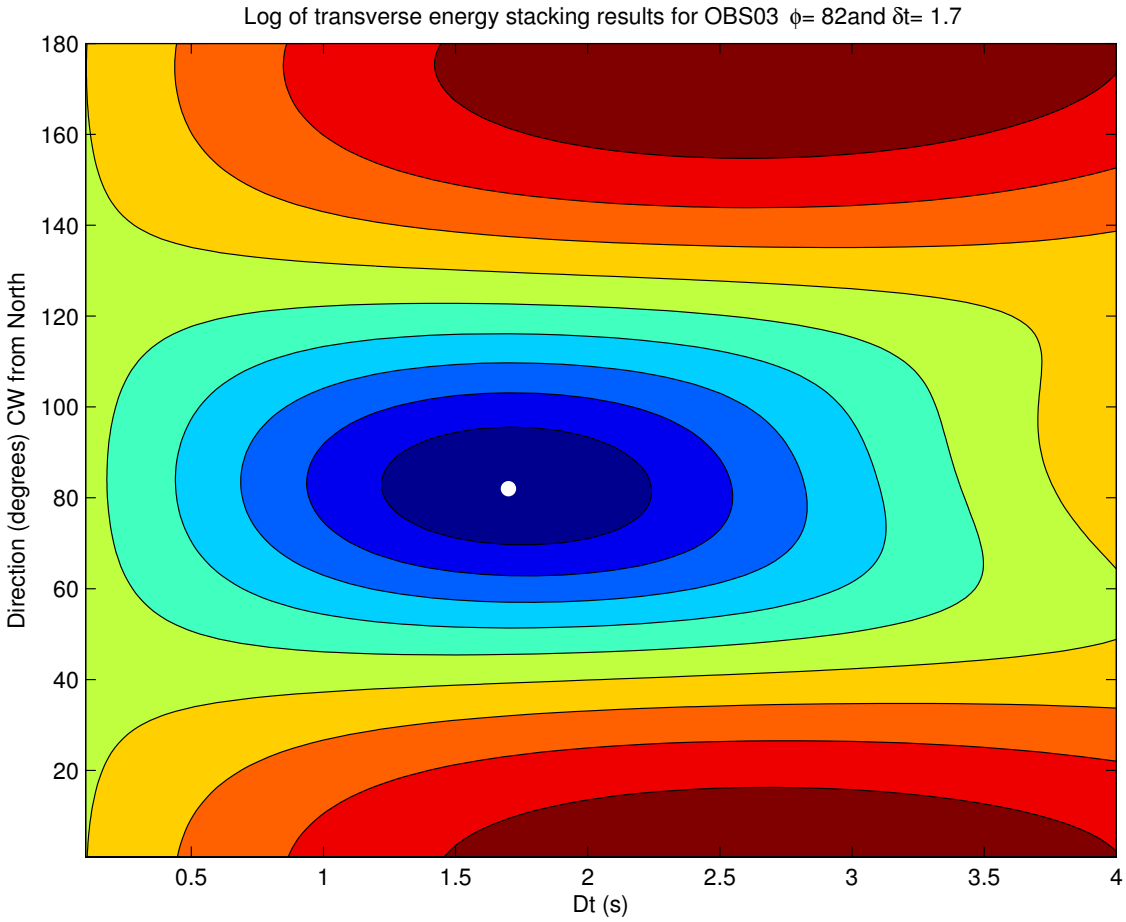

Figure 33: OBS03 Stacked Transverse Energy

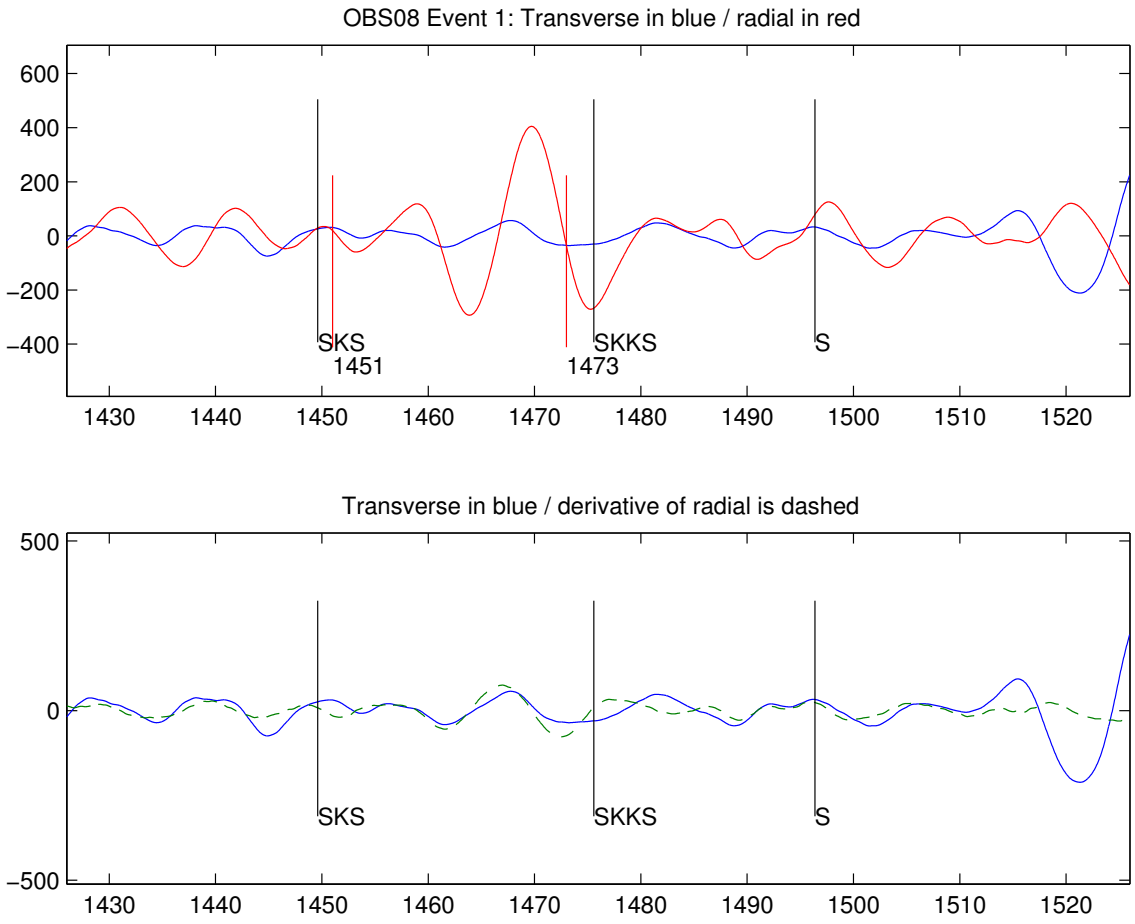

Figure 34: OBS08 Time Window

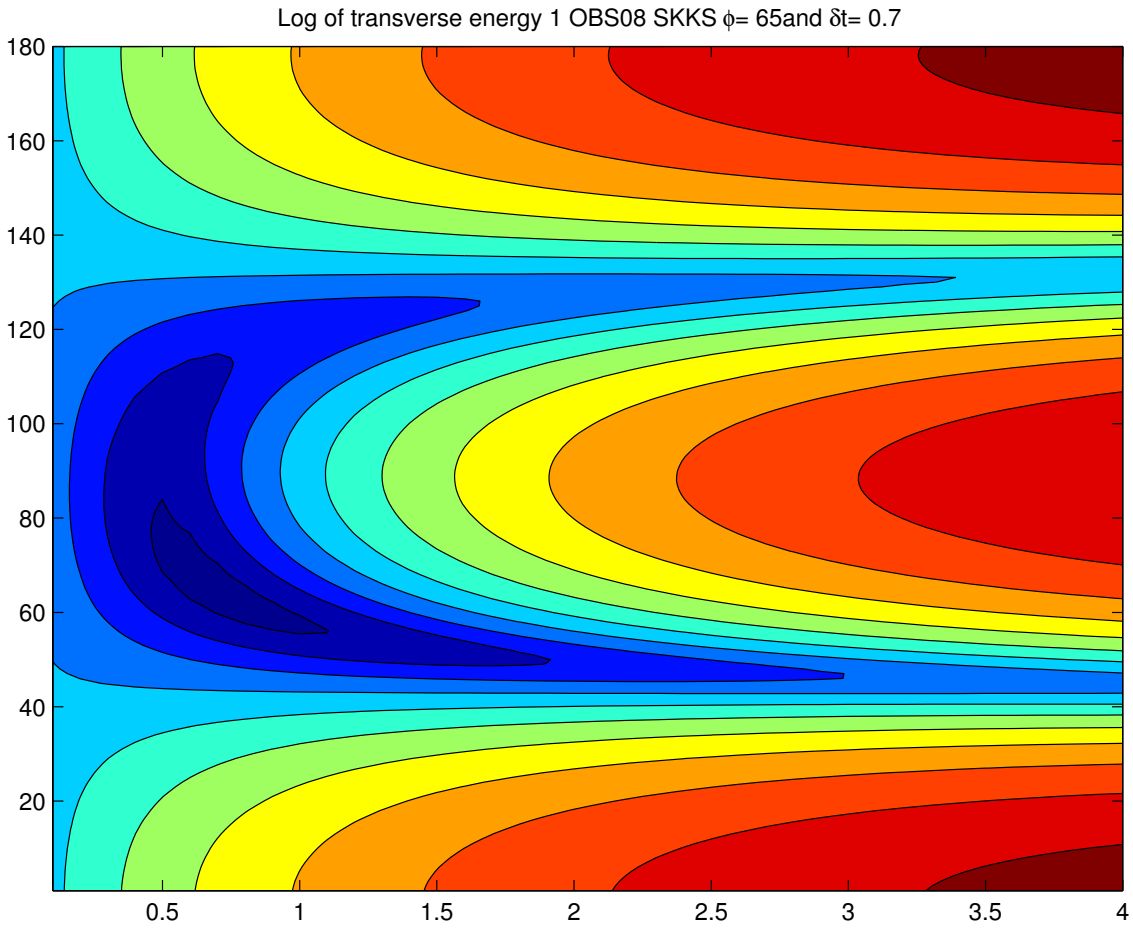

Figure 35: OBS08 Contour

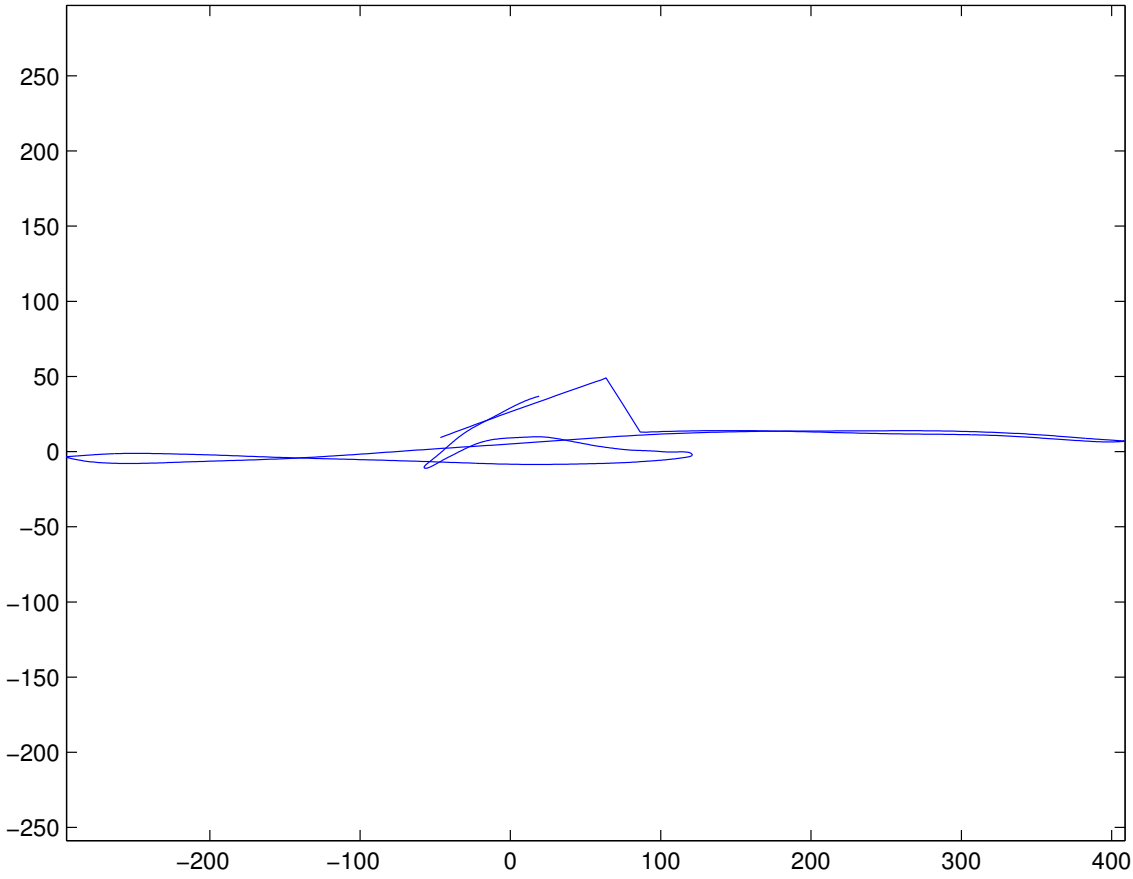

Figure 36: OBS08 Particle Motion

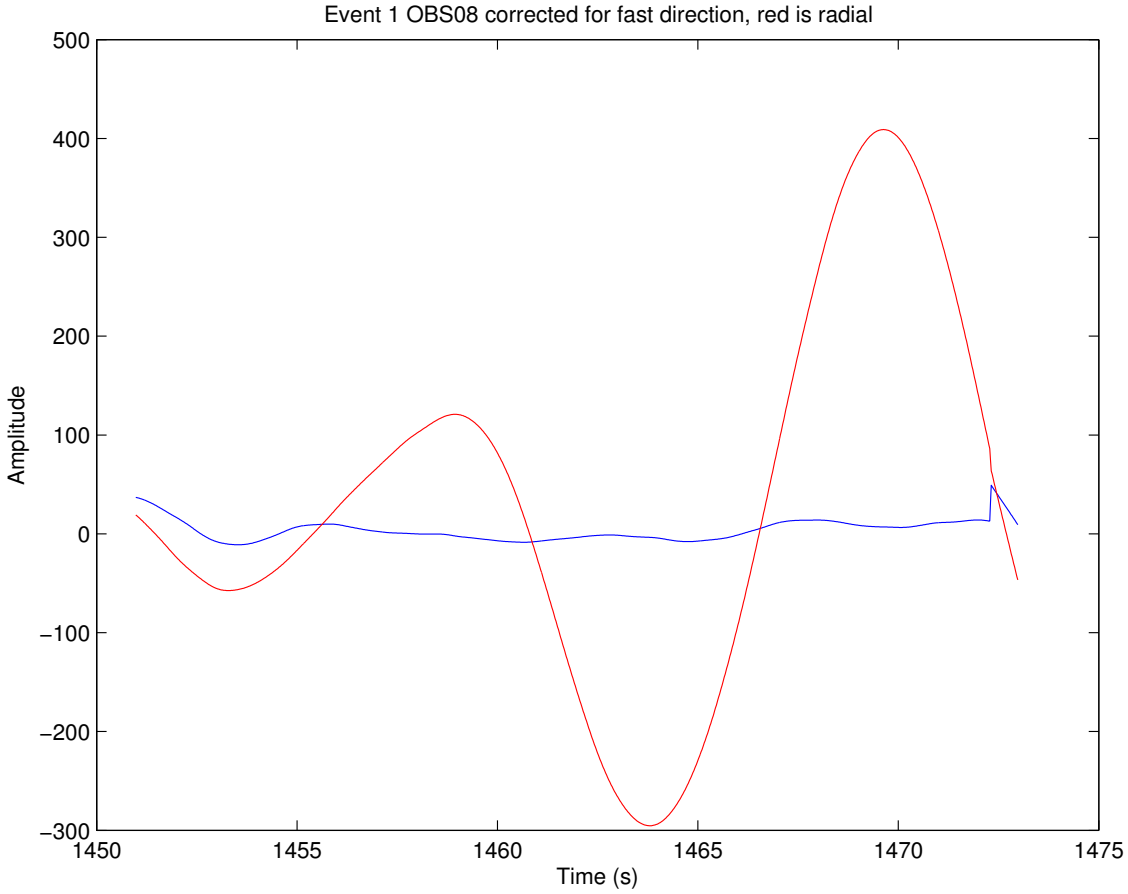

Figure 37: OBS08 Corrected

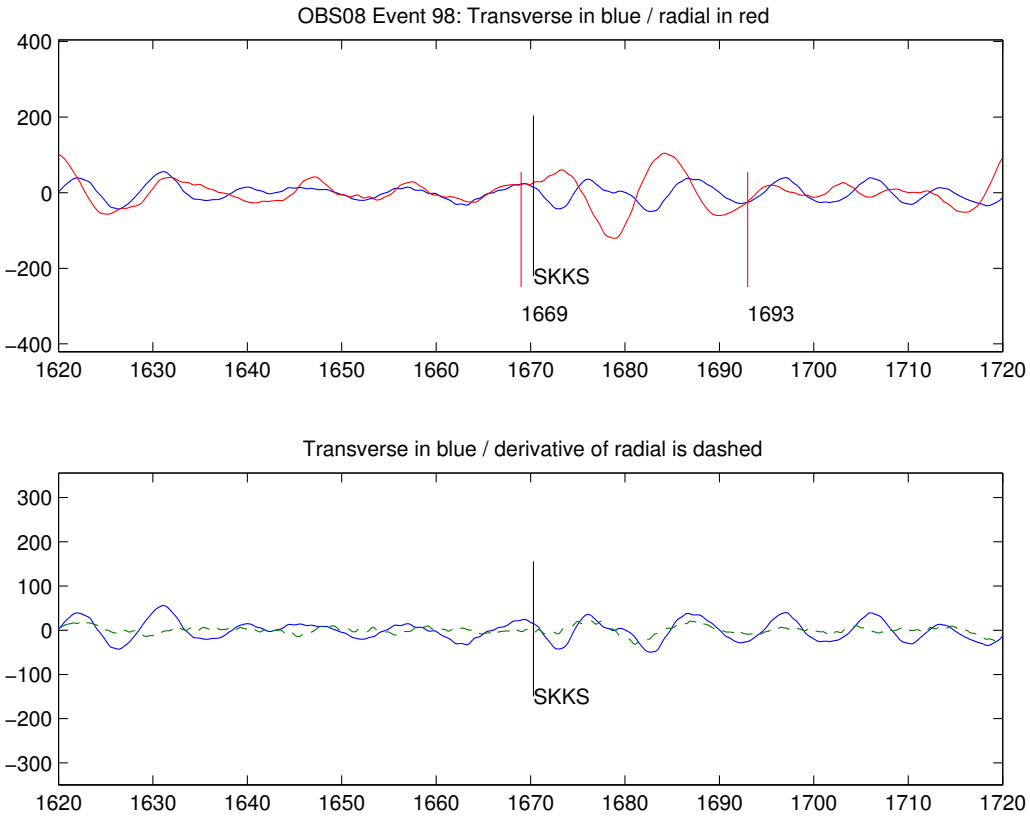

Figure 38: OBS08 Time Window

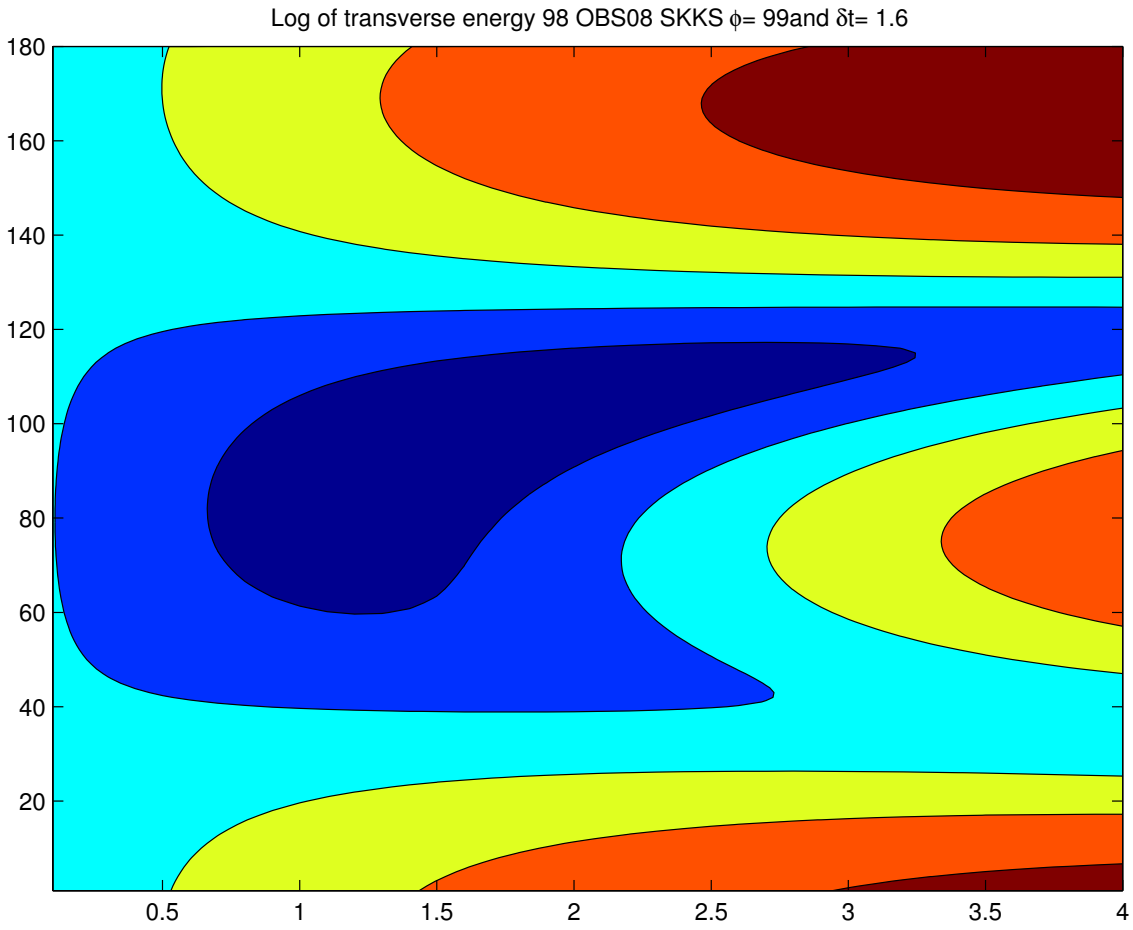

Figure 39: OBS08 Contour

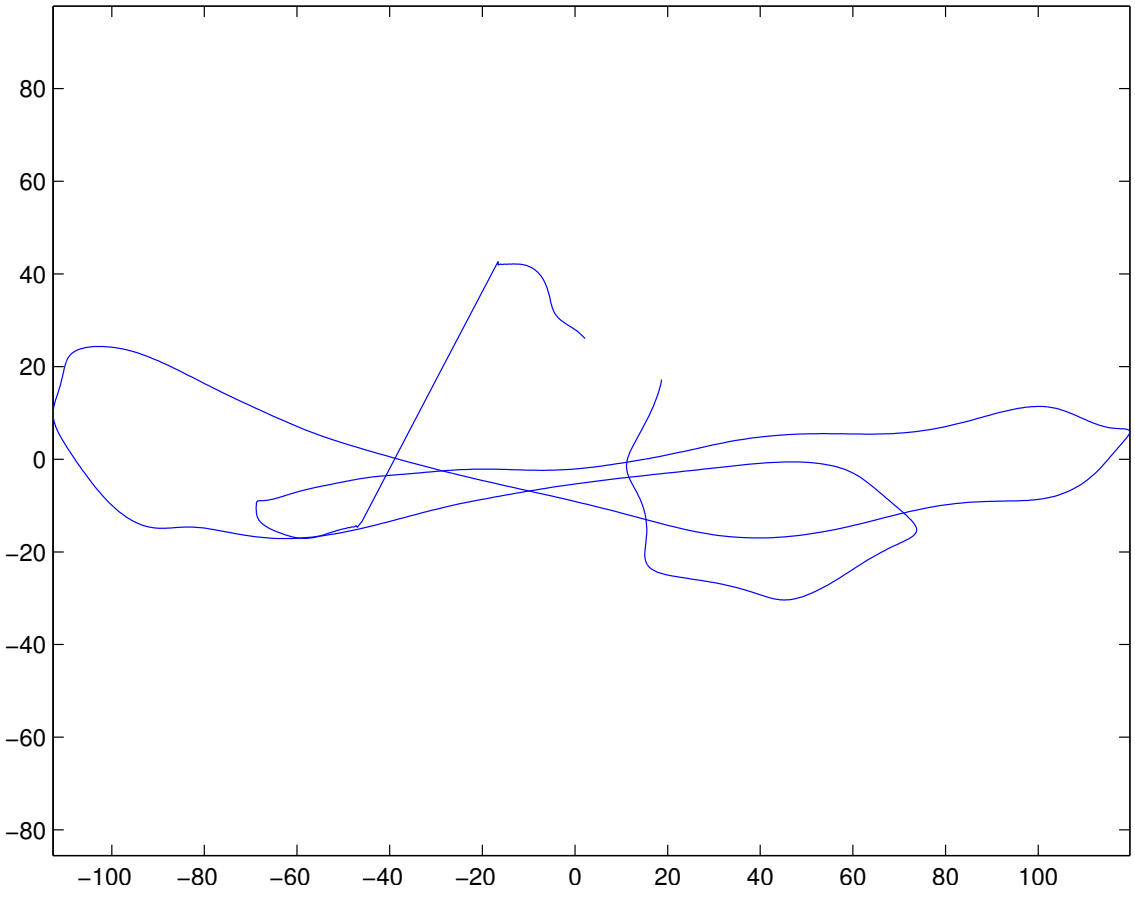

Figure 40: OBS08 Particle Motion

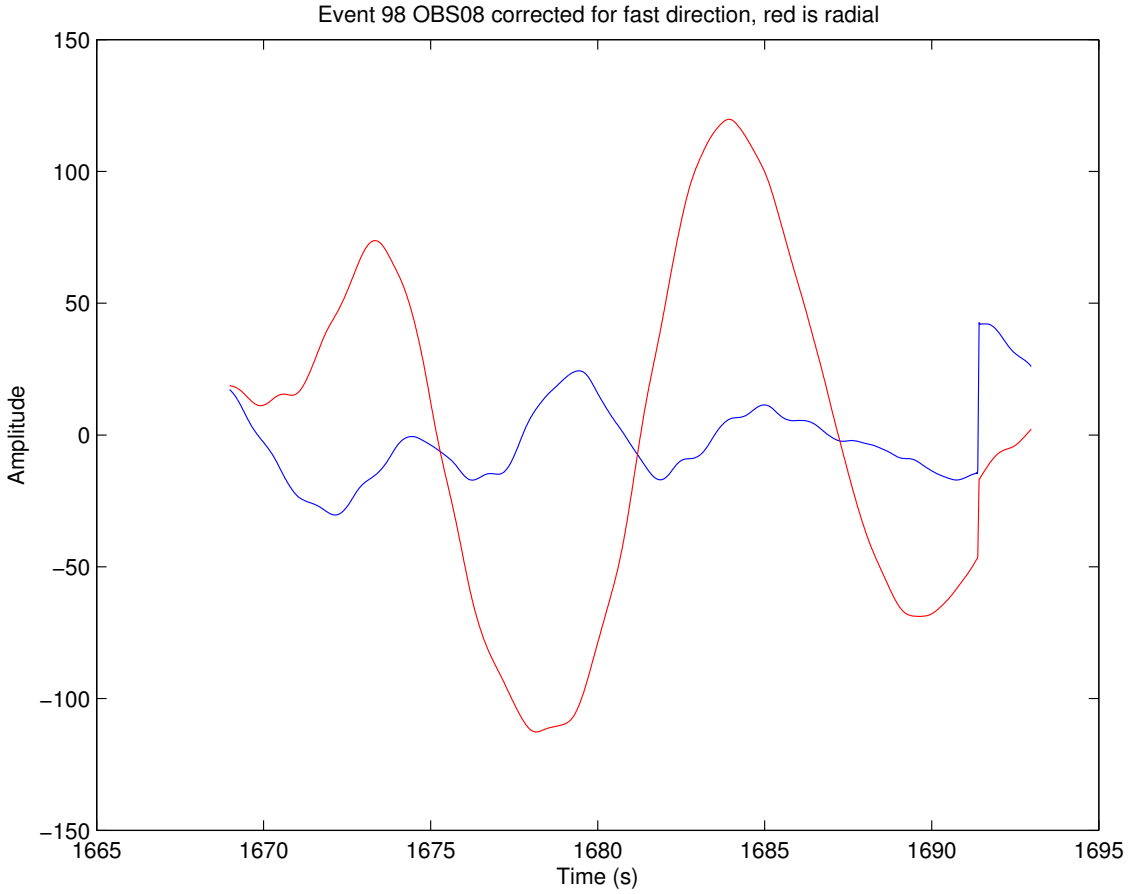

Figure 41: OBS08 Corrected

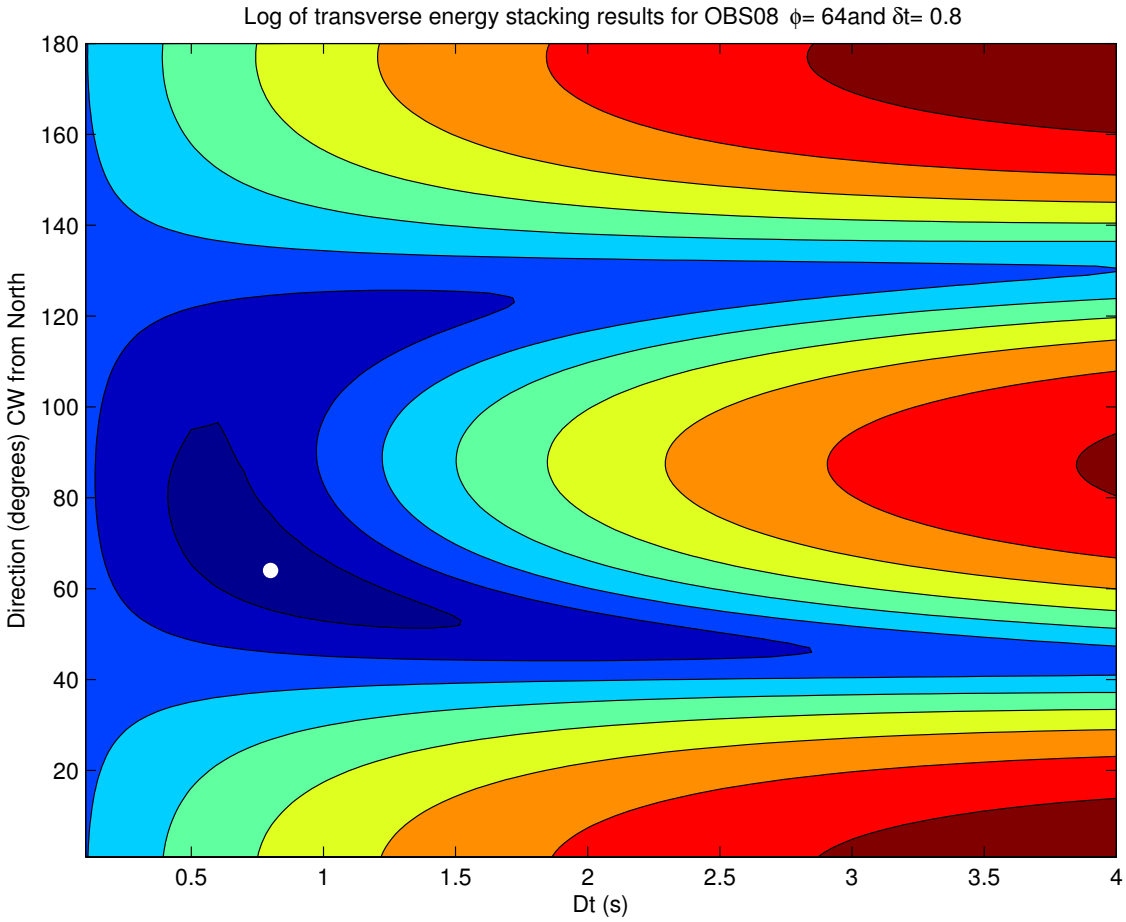

Figure 42: OBS08 Stacked Transverse Energy

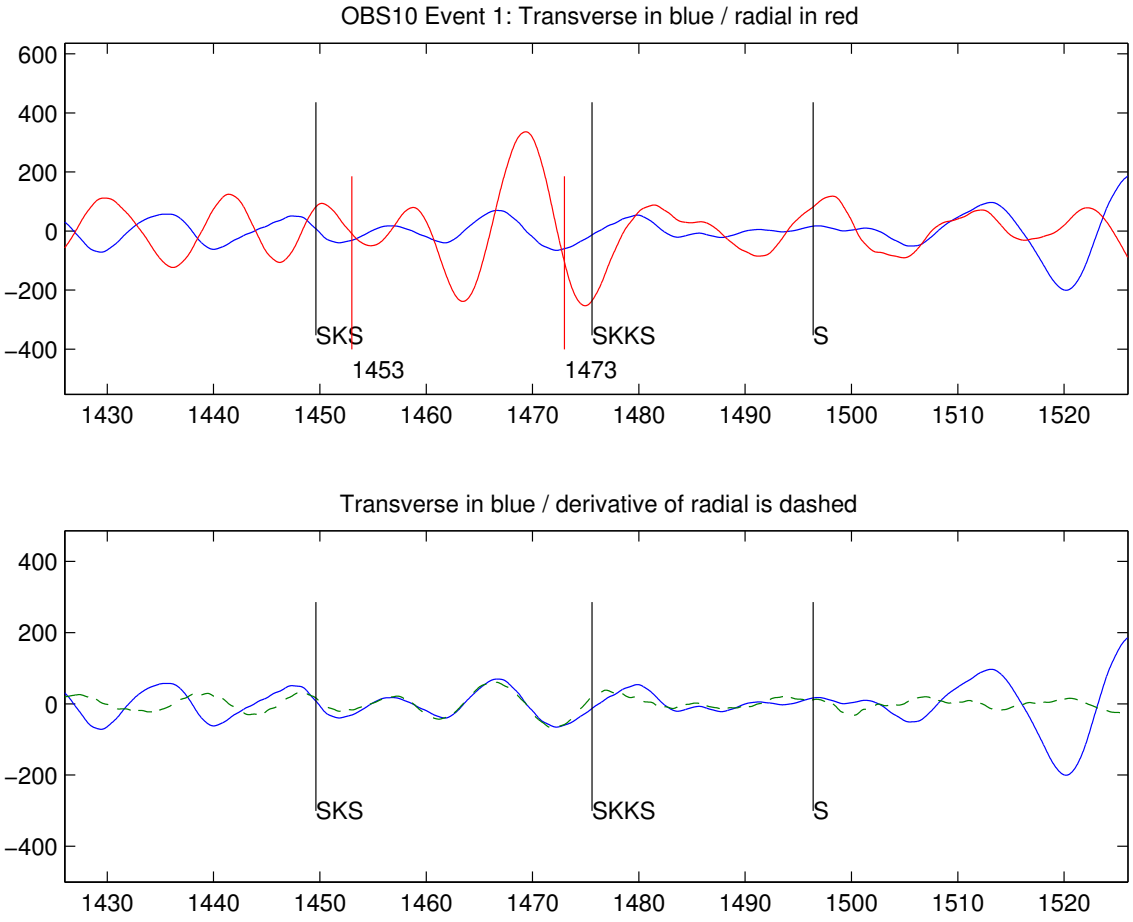

Figure 43: OBS10 Time Window

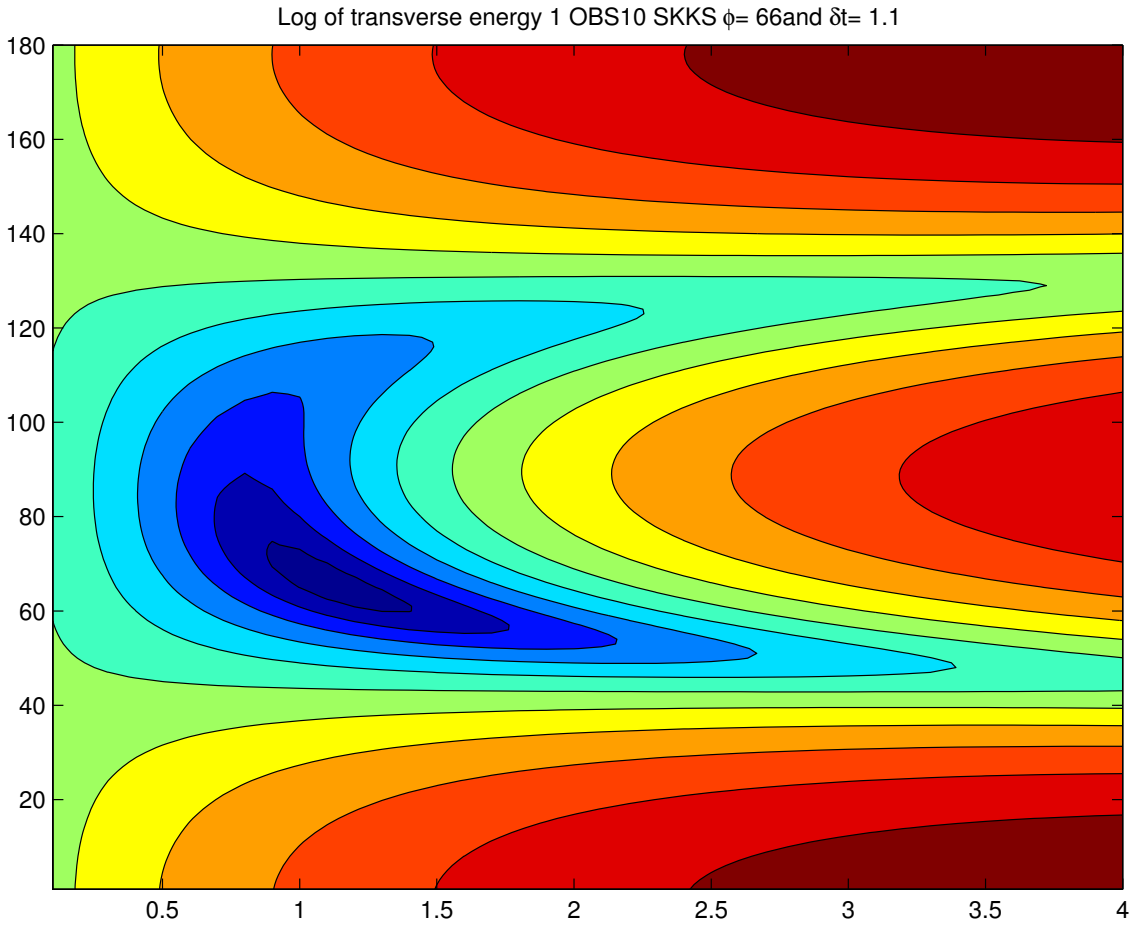

Figure 44: OBS10 Contour

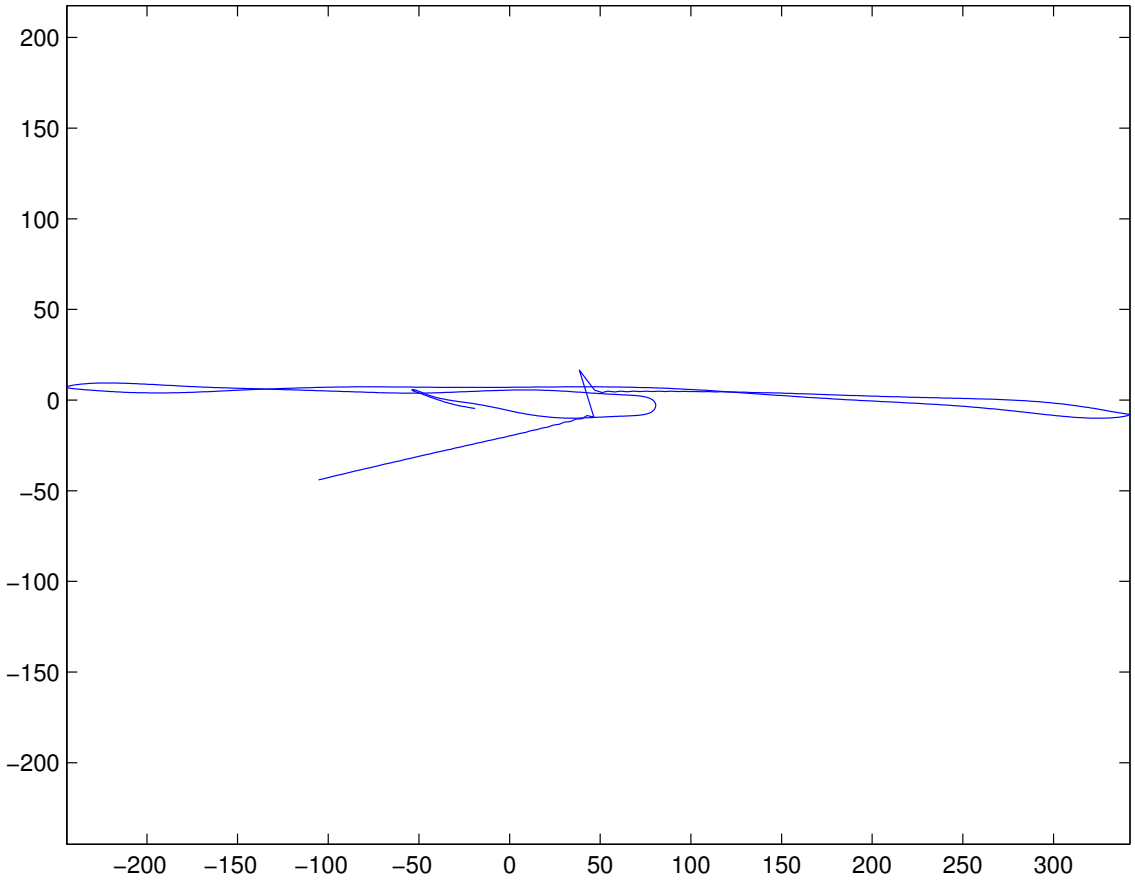

Figure 45: OBS10 Particle Motion

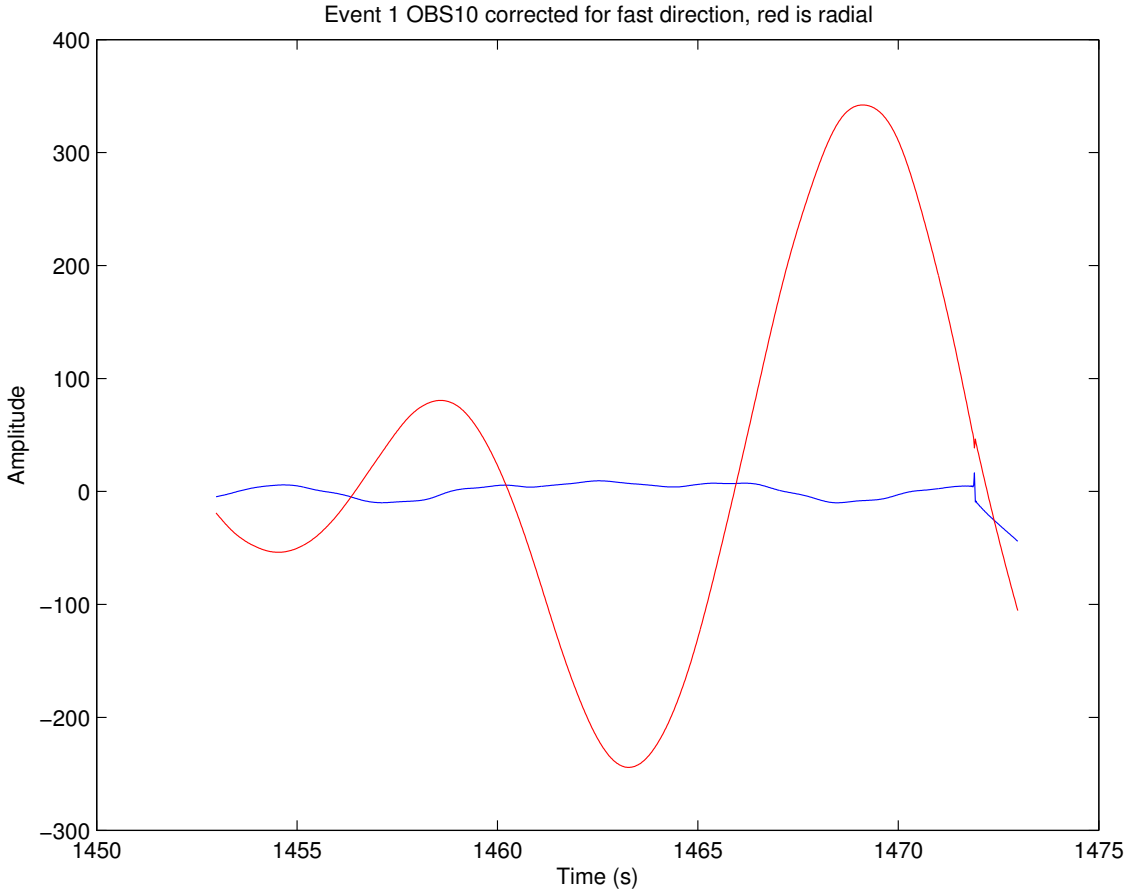

Figure 46: OBS10 Corrected

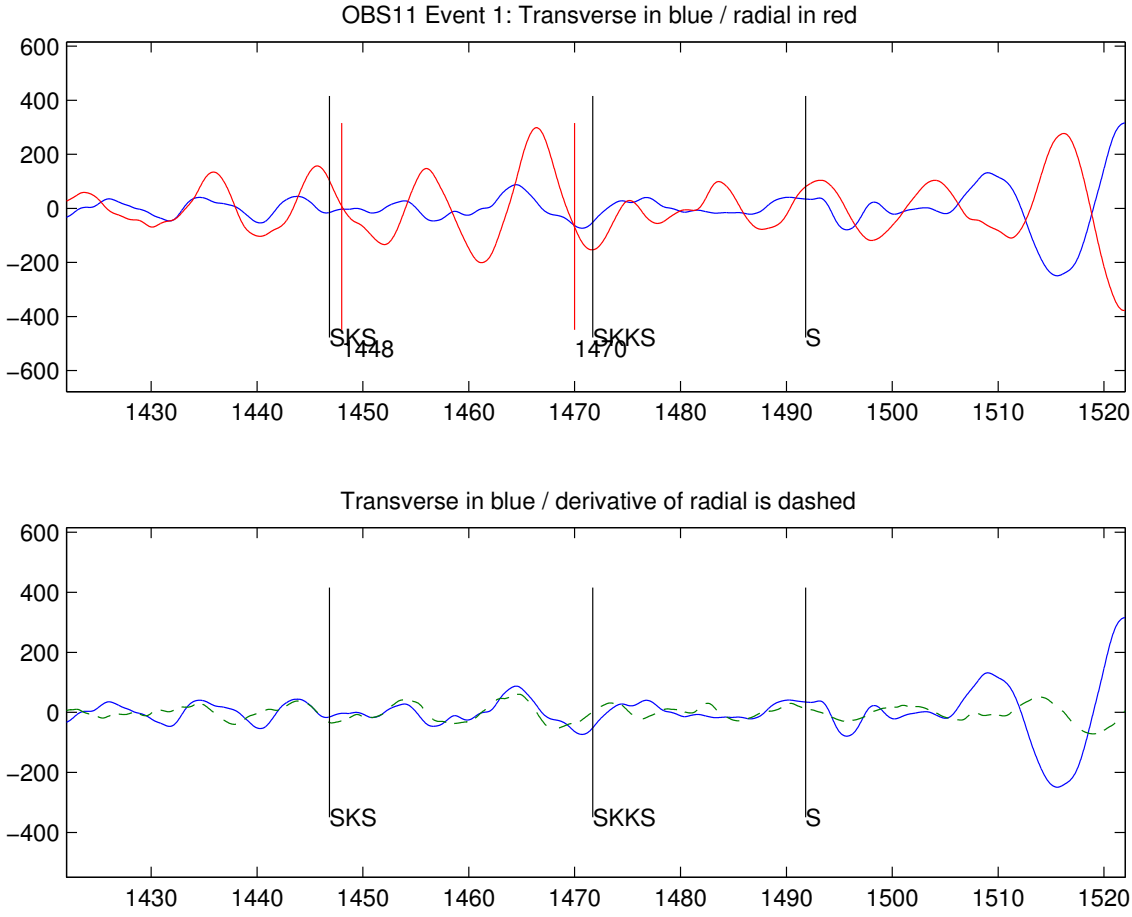

Figure 47: OBS11 Time Window

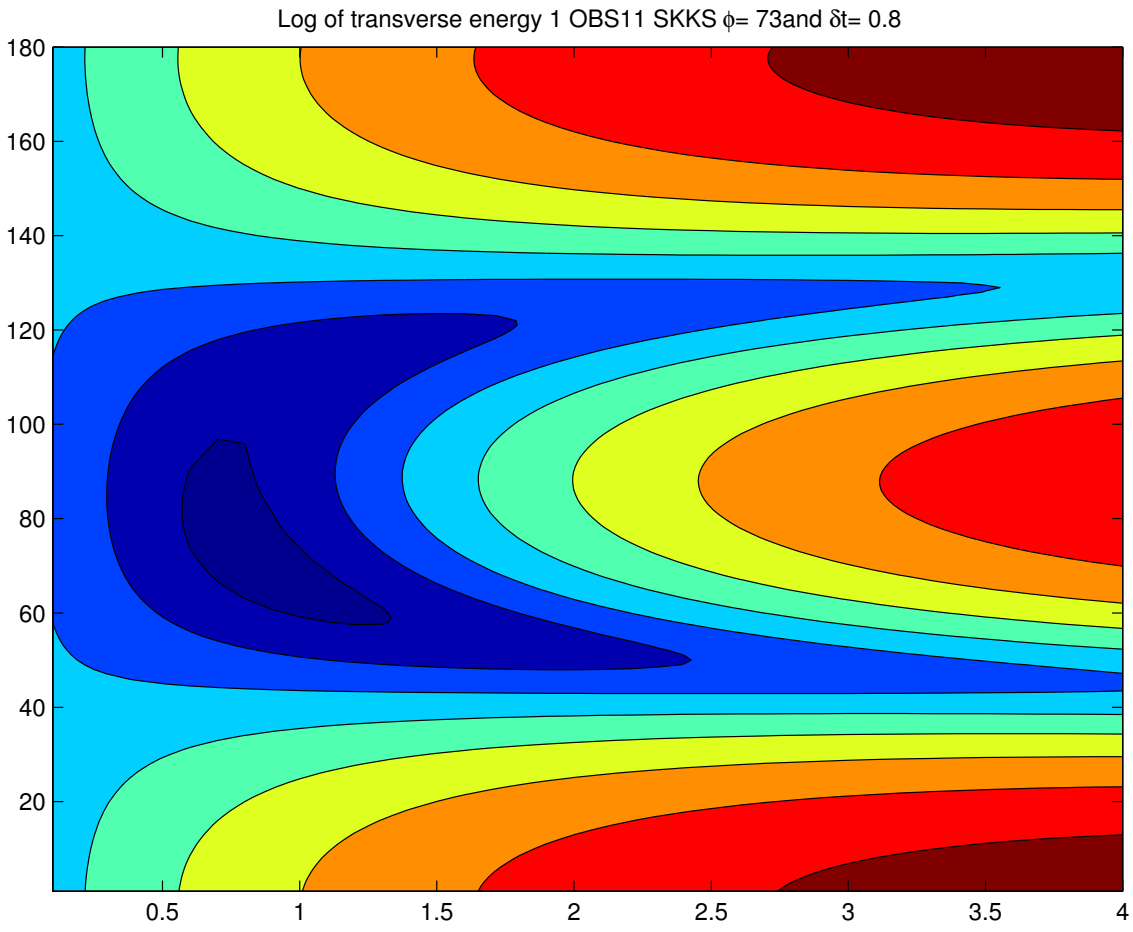

Figure 48: OBS11 Contour

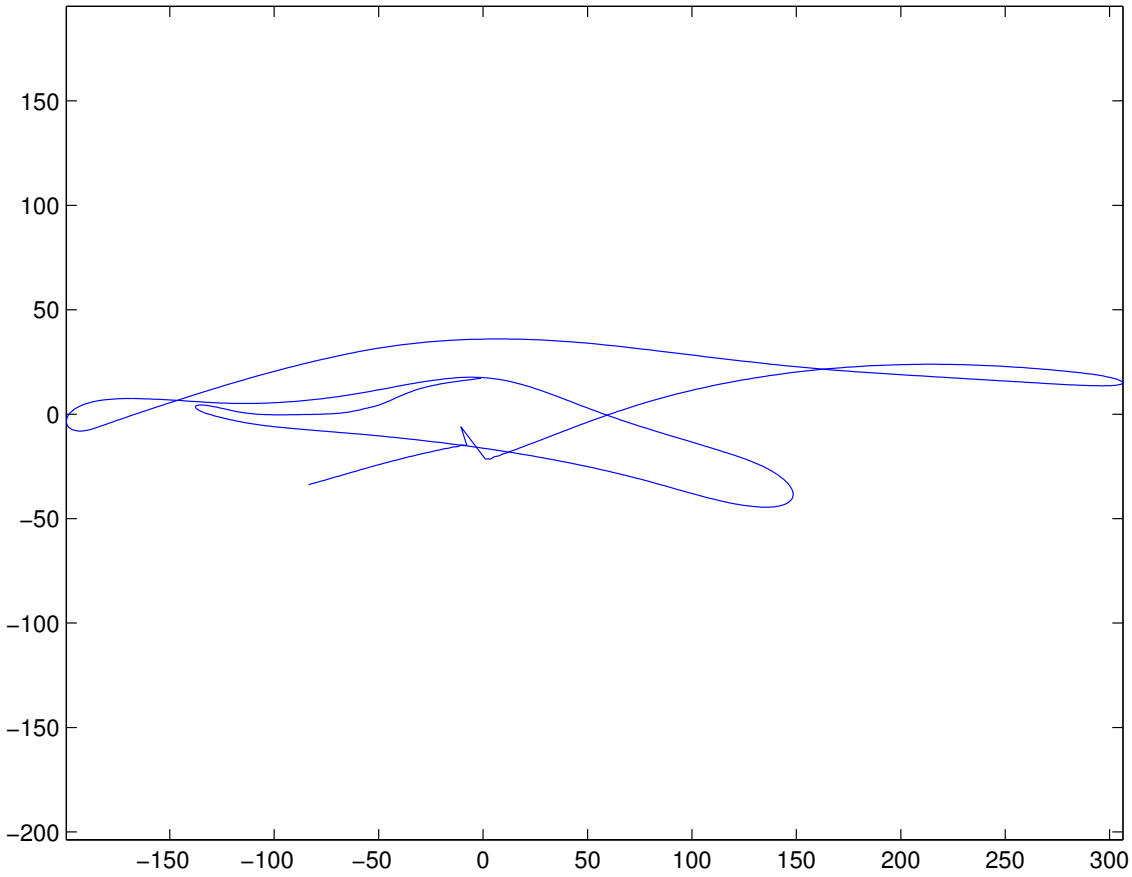

Figure 49: OBS11 Particle Motion

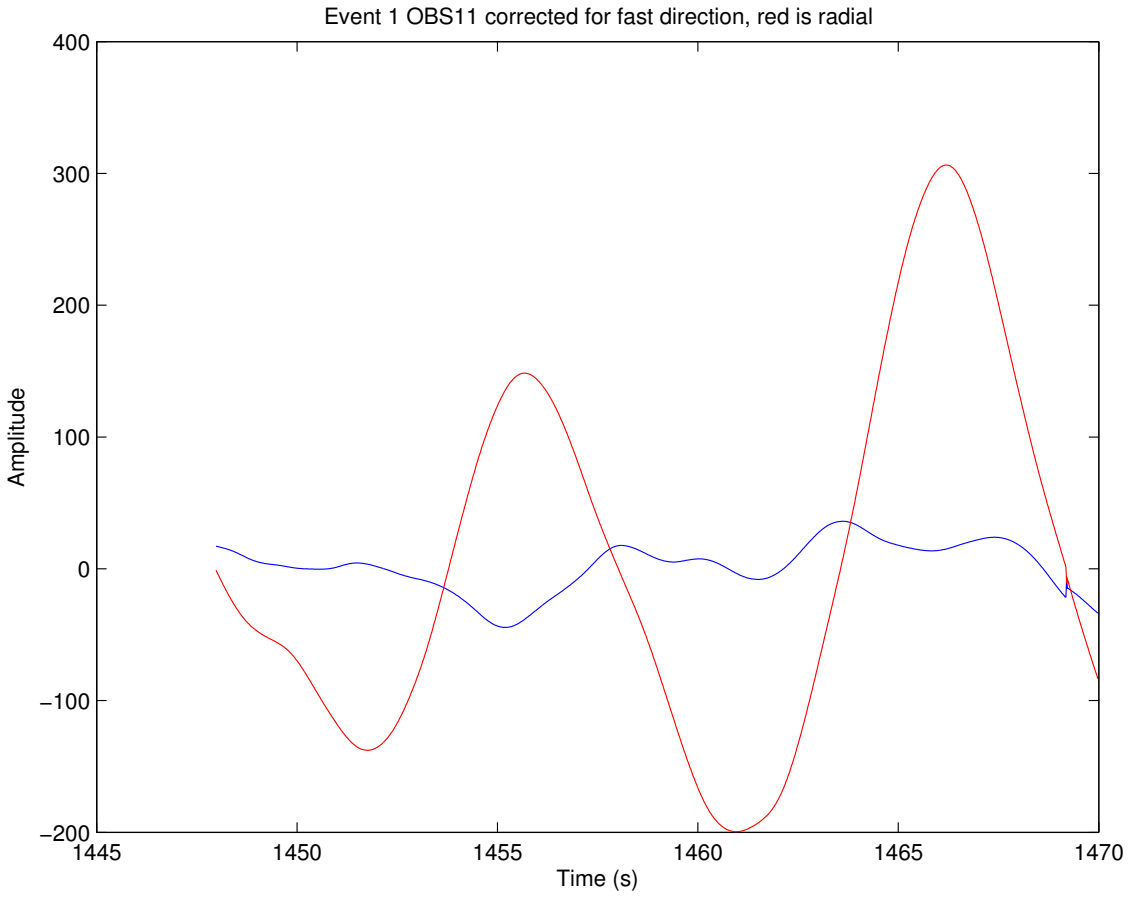

Figure 50: OBS11 Corrected

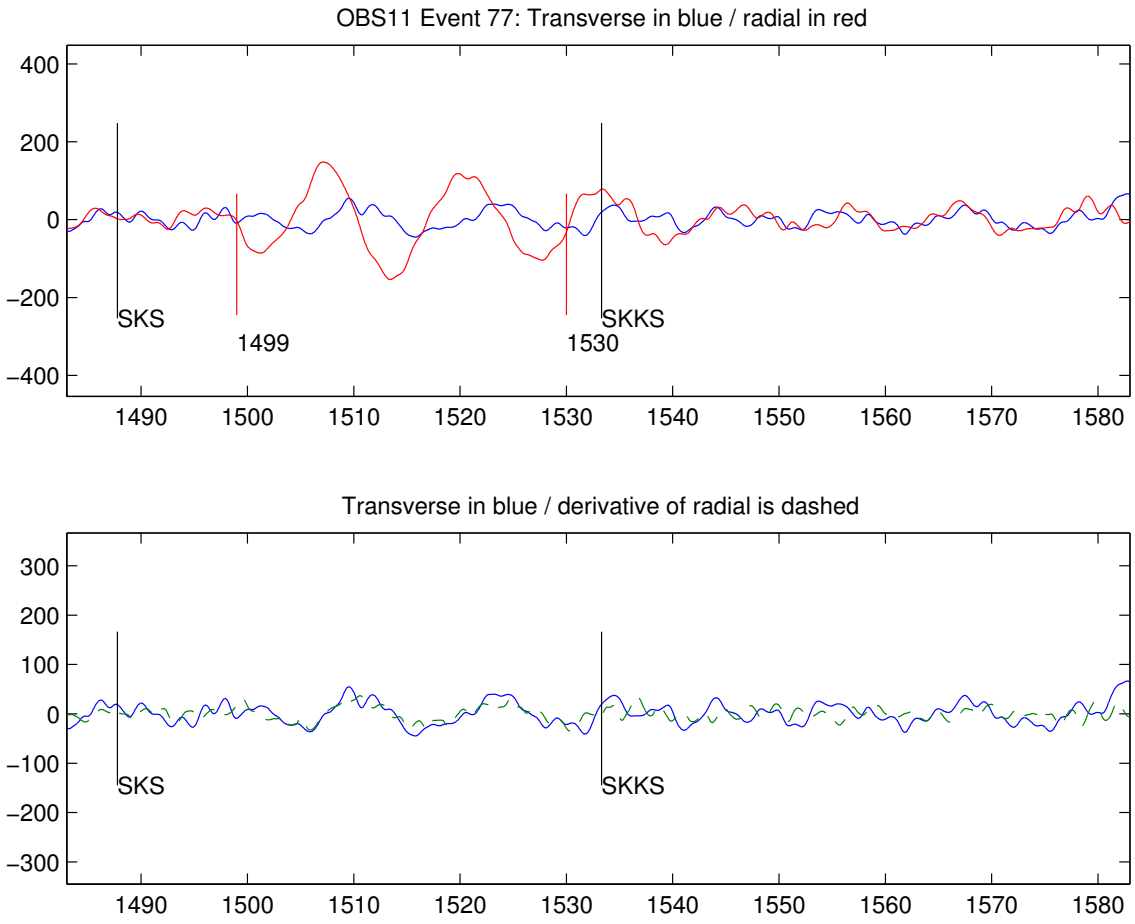

Figure 51: OBS11 Time Window

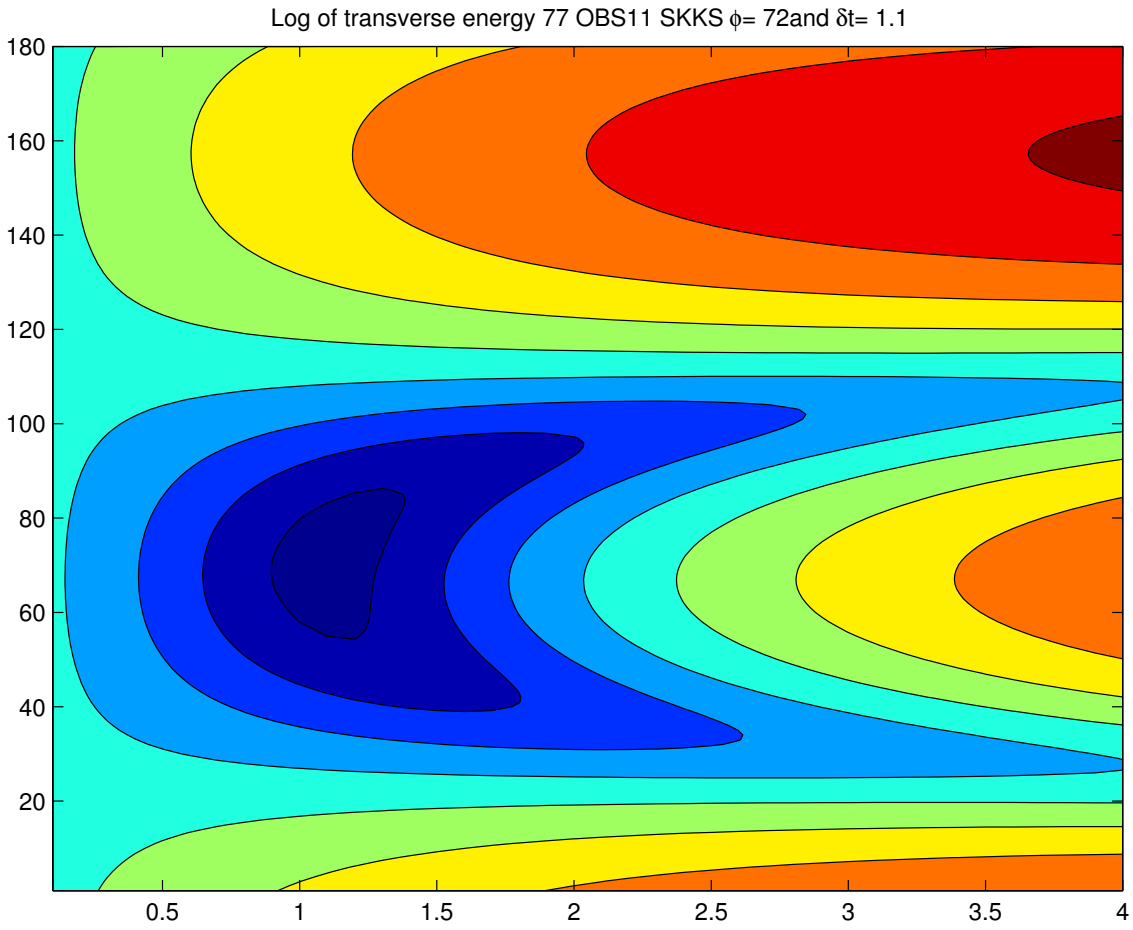

Figure 52: OBS11 Contour

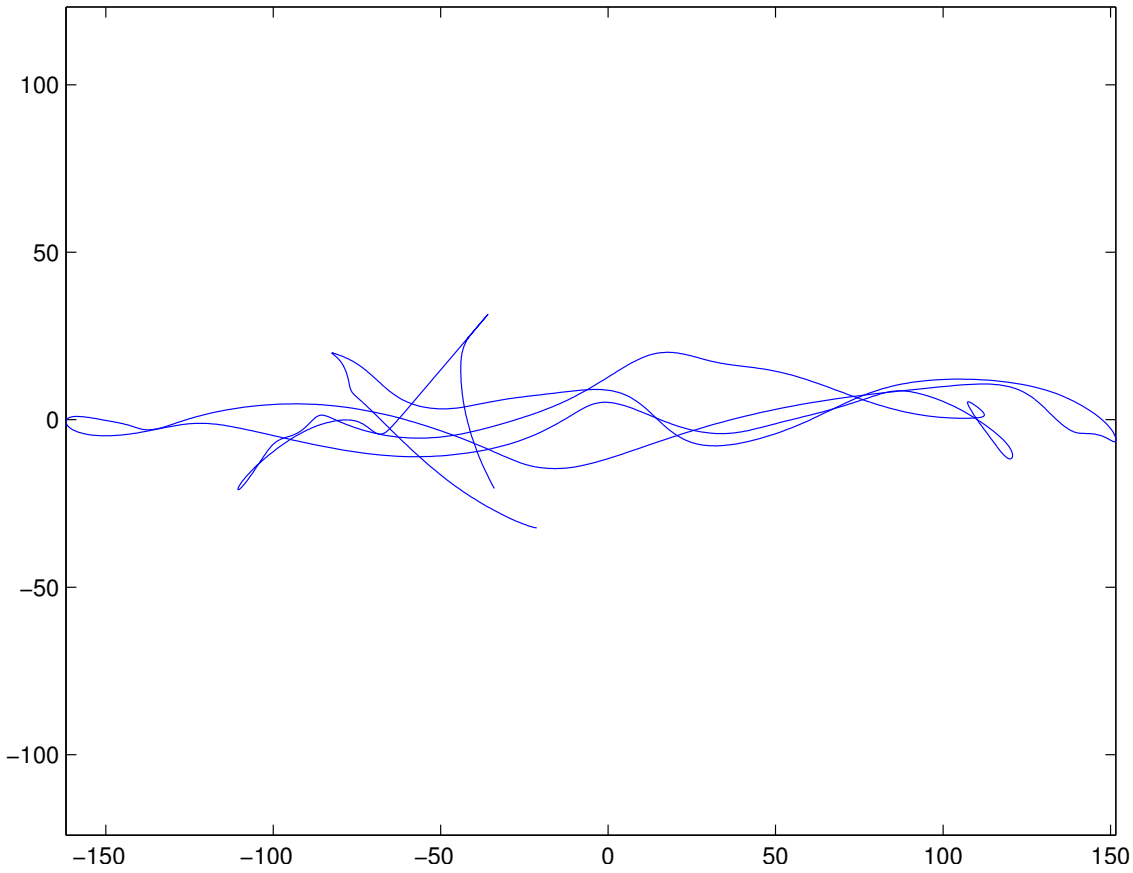

Figure 53: OBS11 Particle Motion

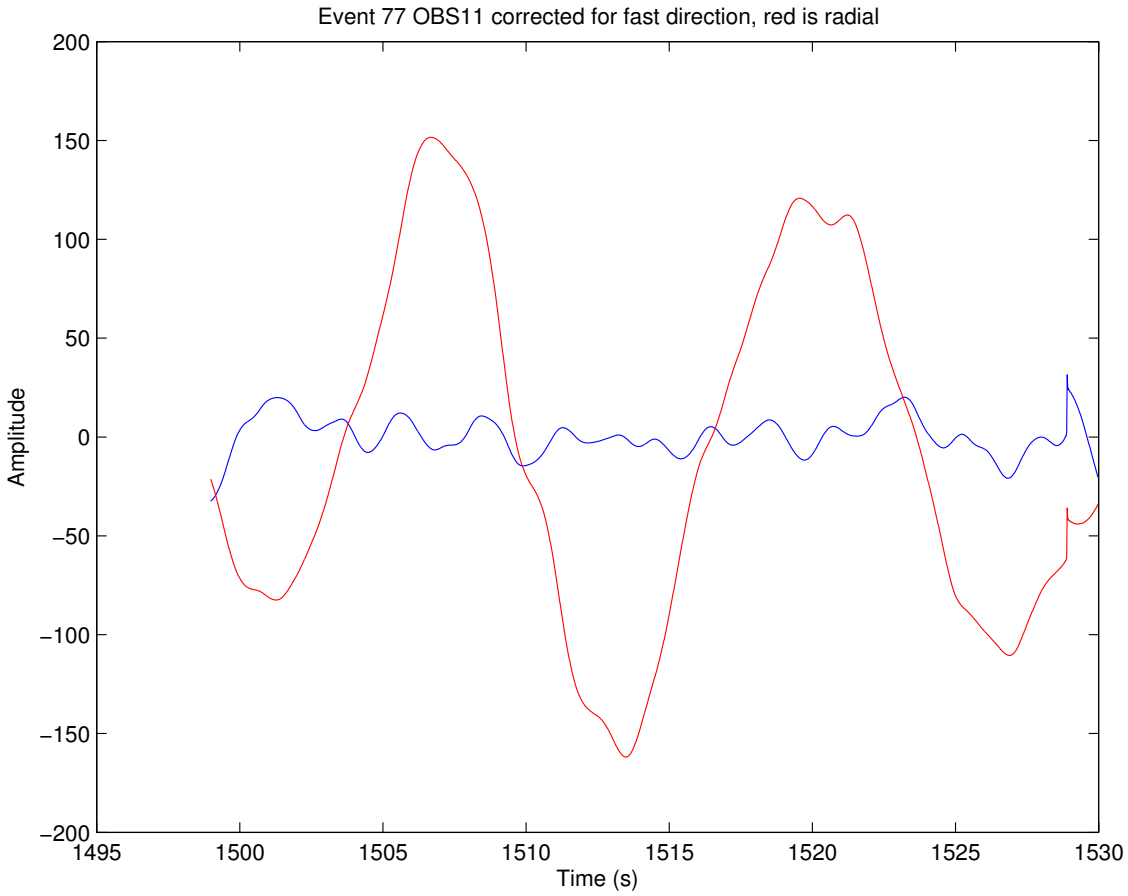

Figure 54: OBS11 Corrected

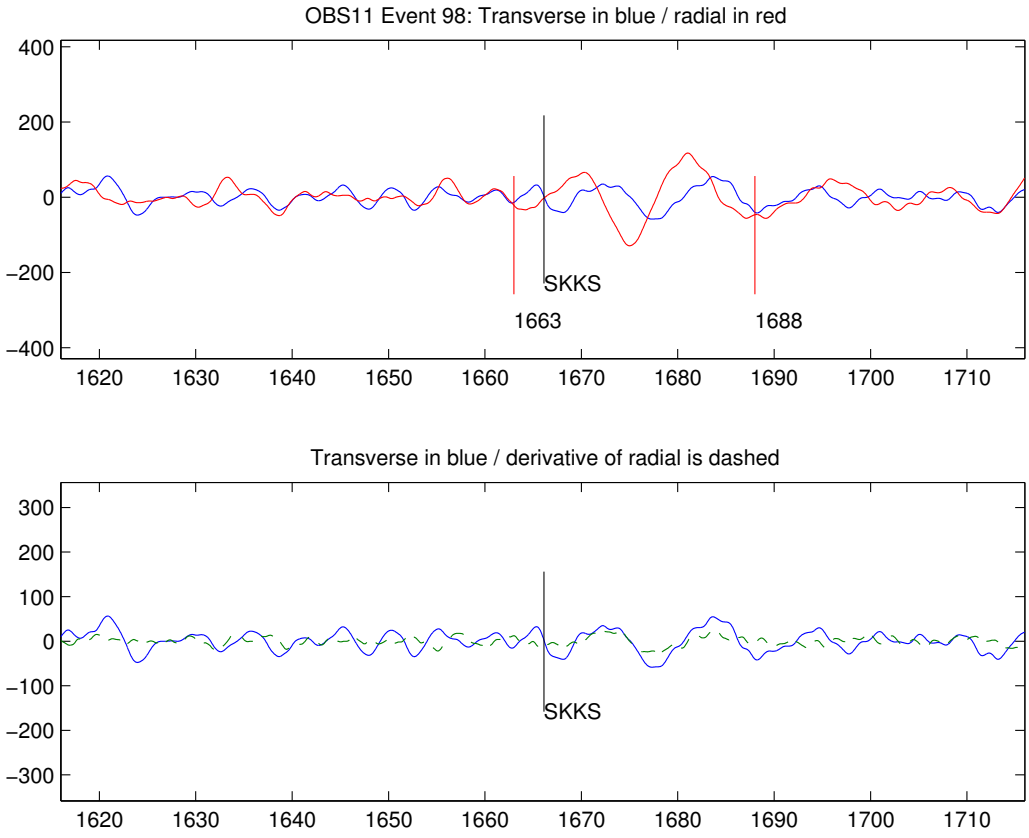

Figure 55: OBS11 Time Window

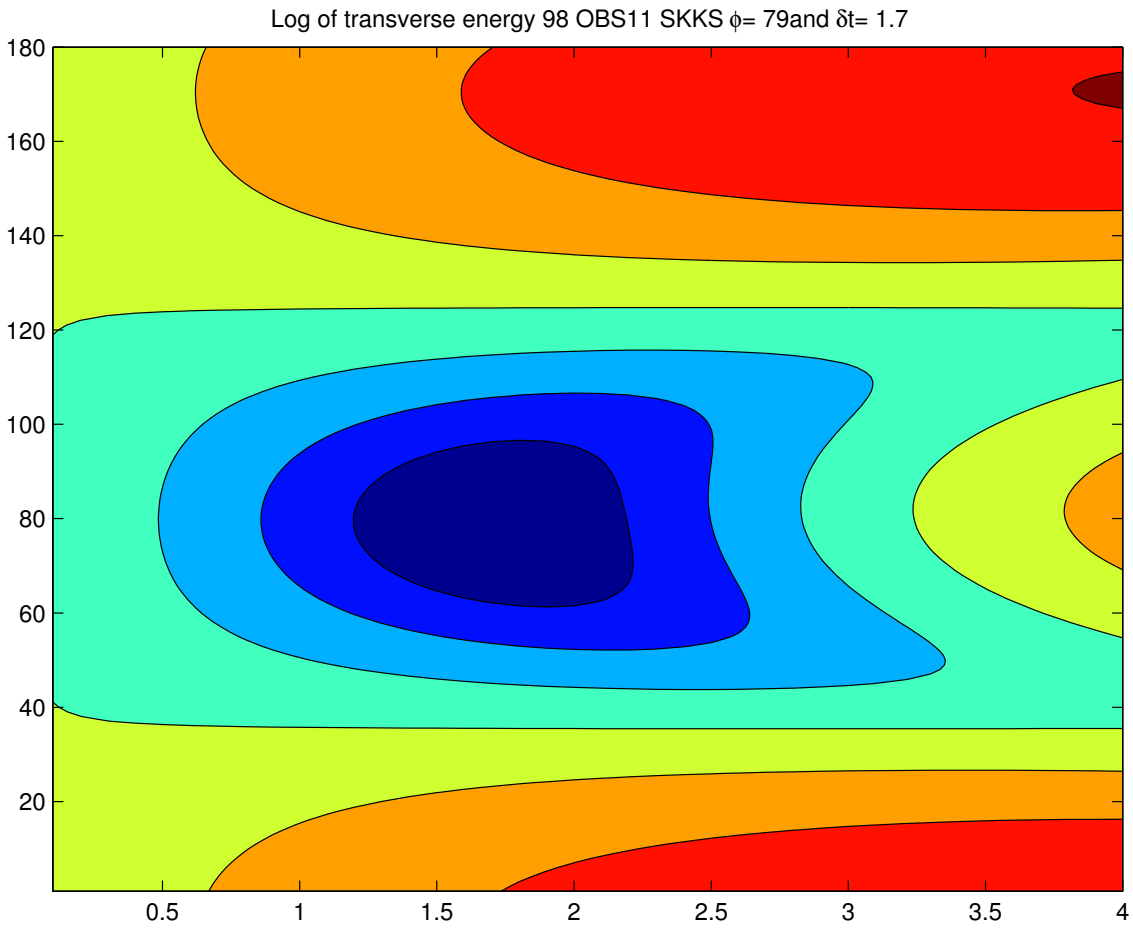

Figure 56: OBS11 Contour

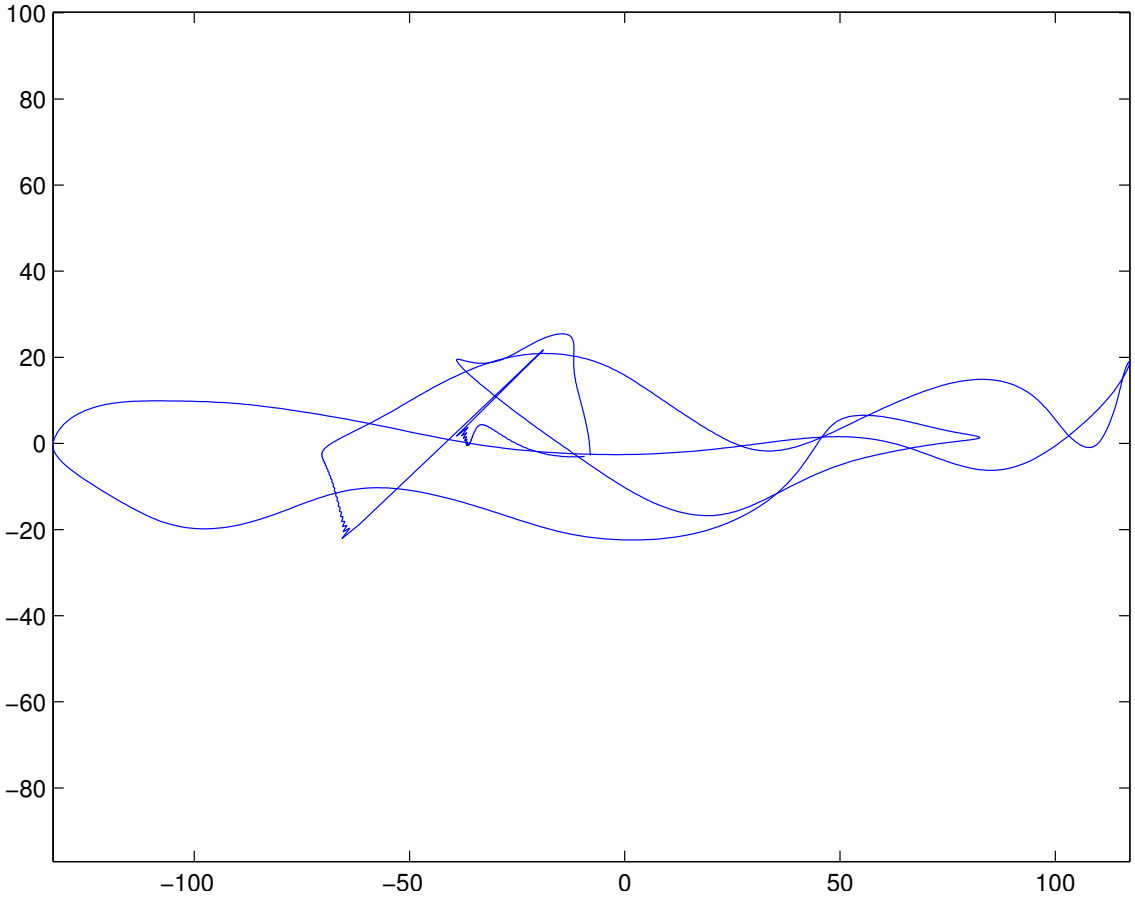

Figure 57: OBS11 Particle Motion

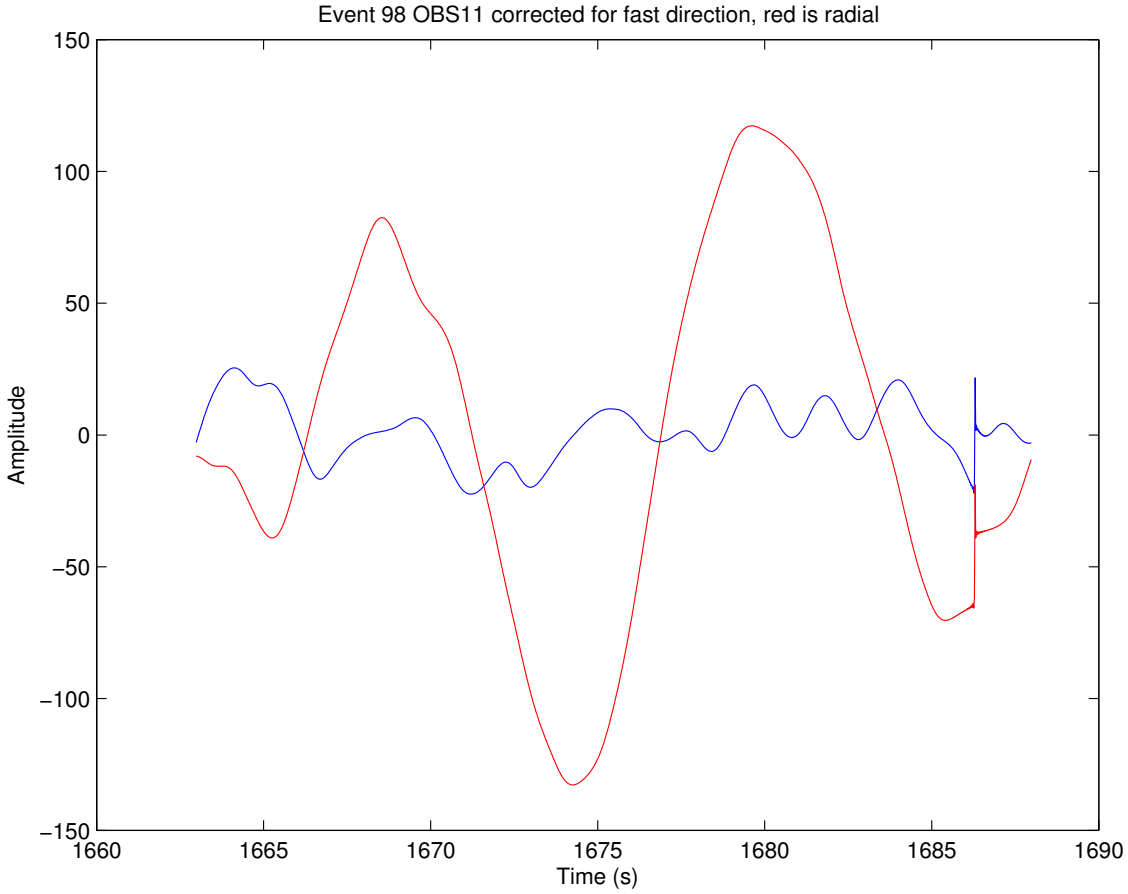

Figure 58: OBS11 Corrected

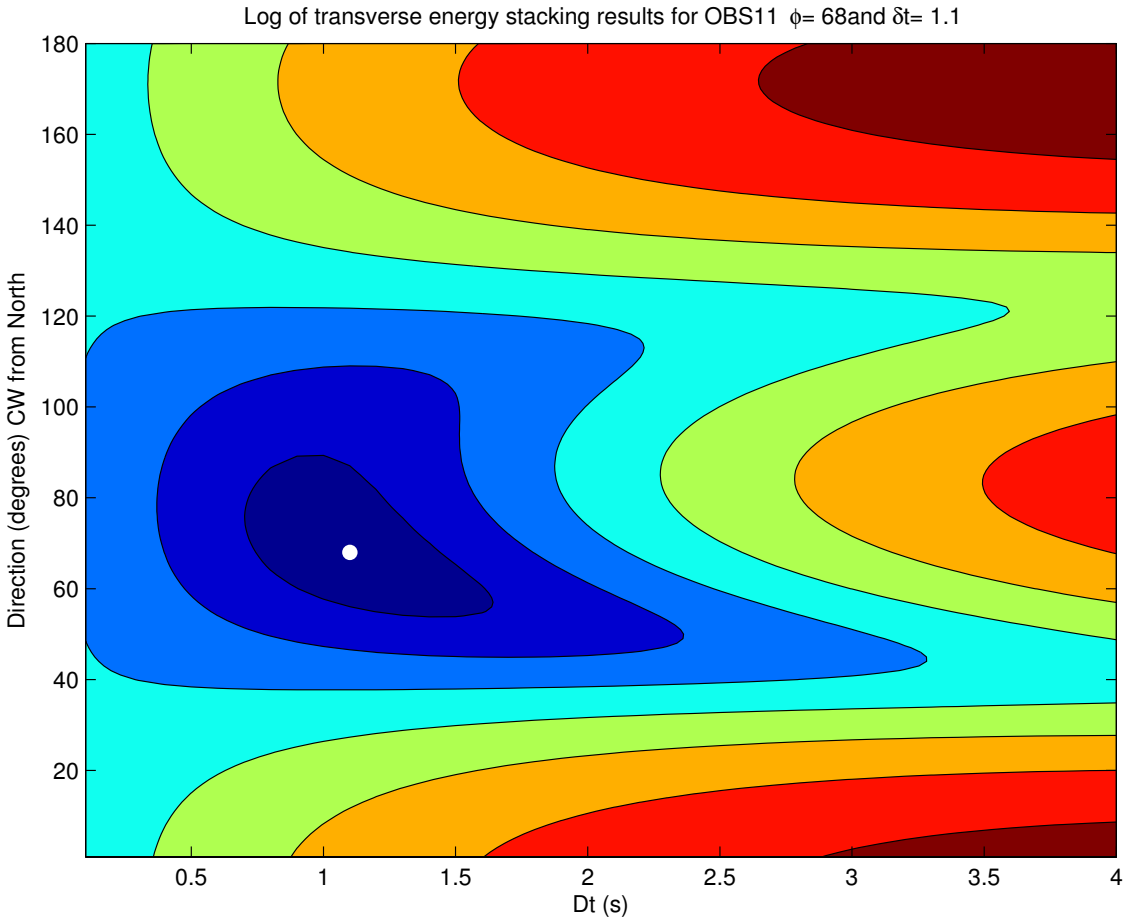

Figure 59: OBS11 Stacked Transverse Energy

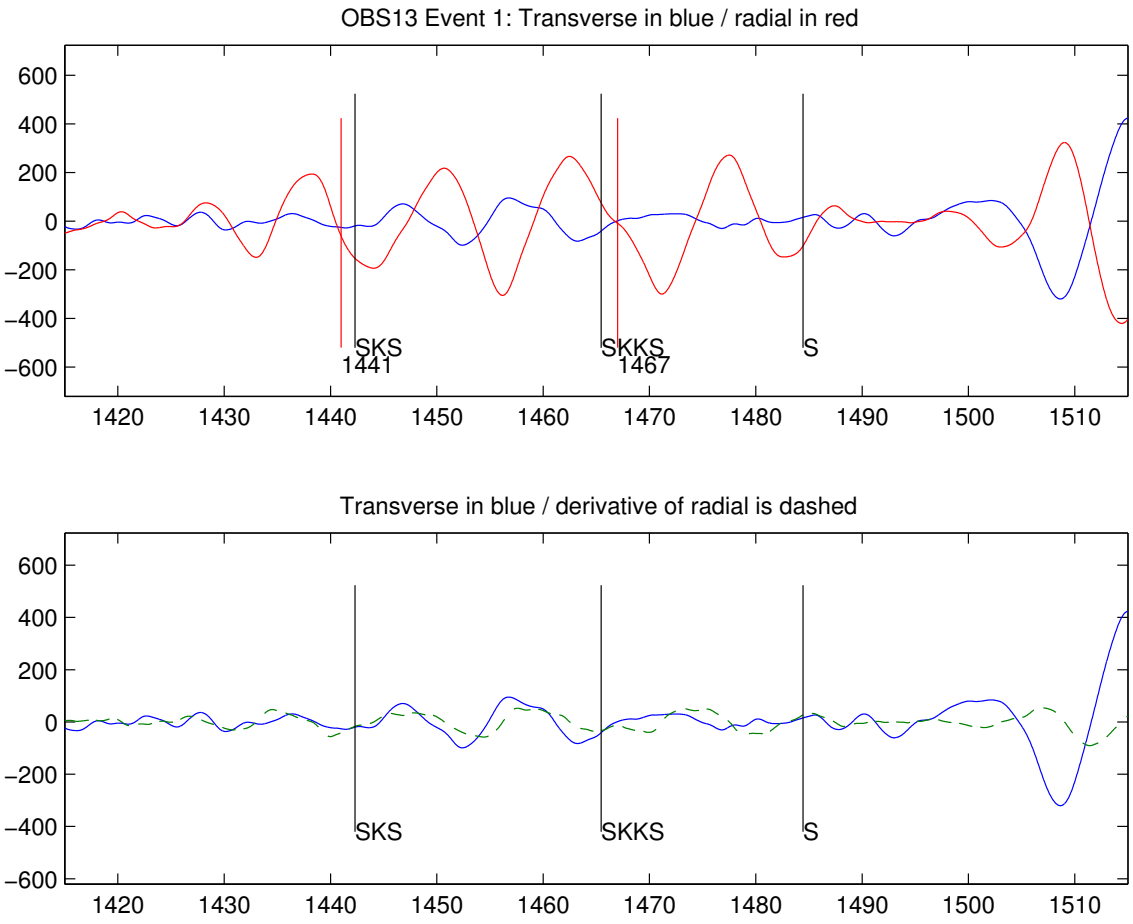

Figure 60: OBS13 Time Window

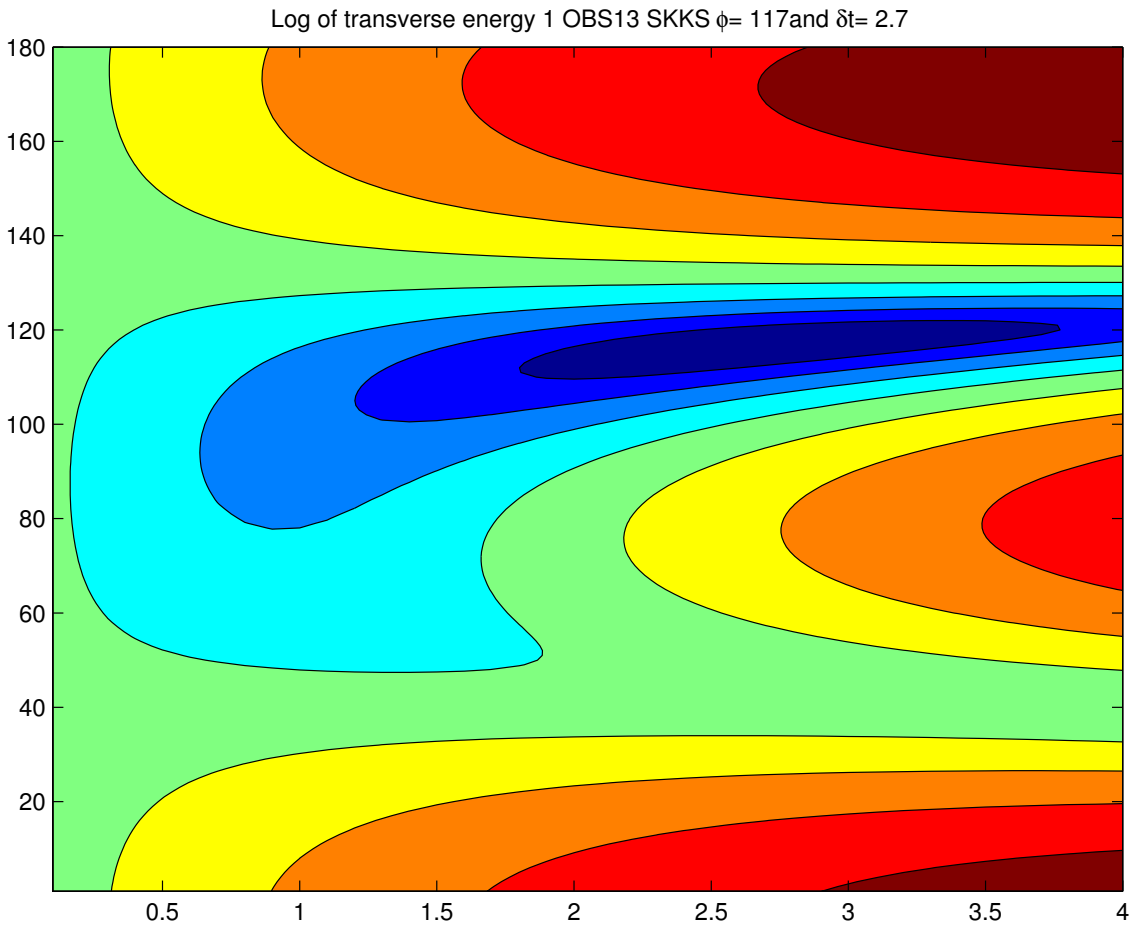

Figure 61: OBS13 Contour

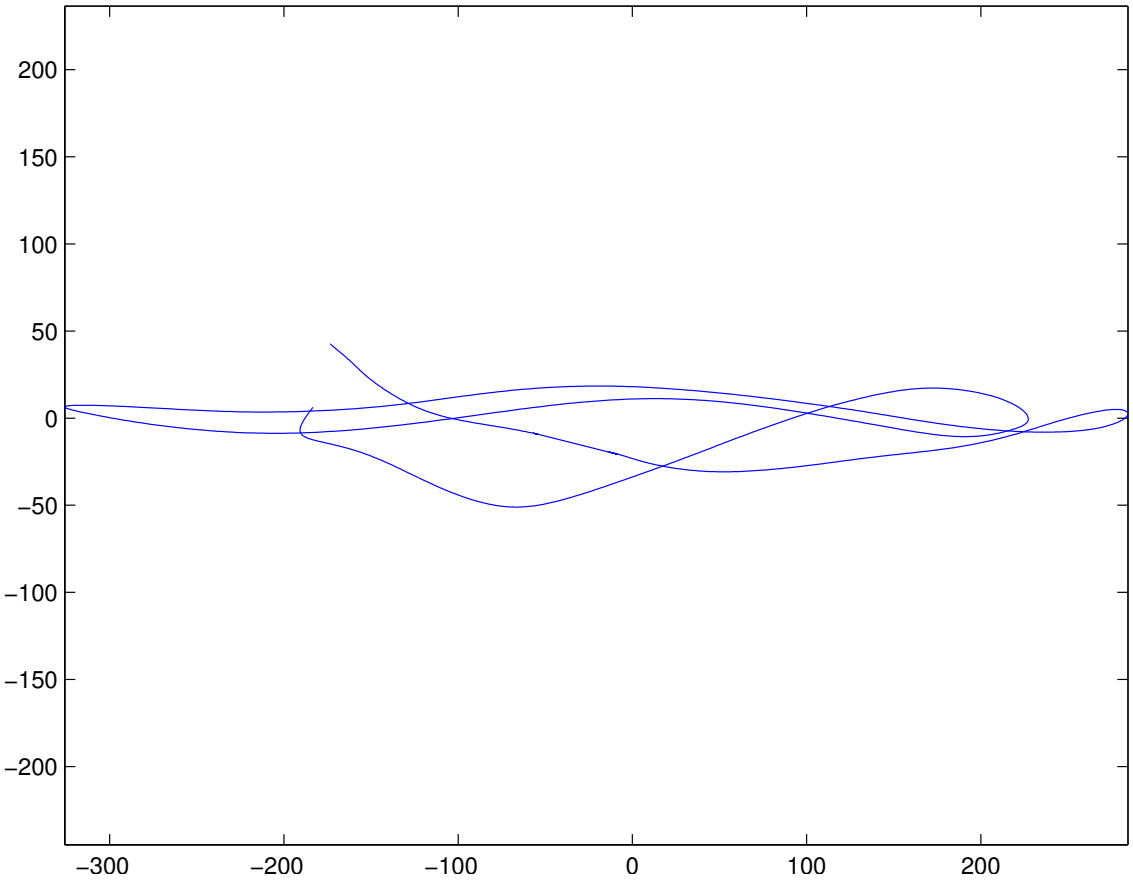

Figure 62: OBS13 Particle Motion

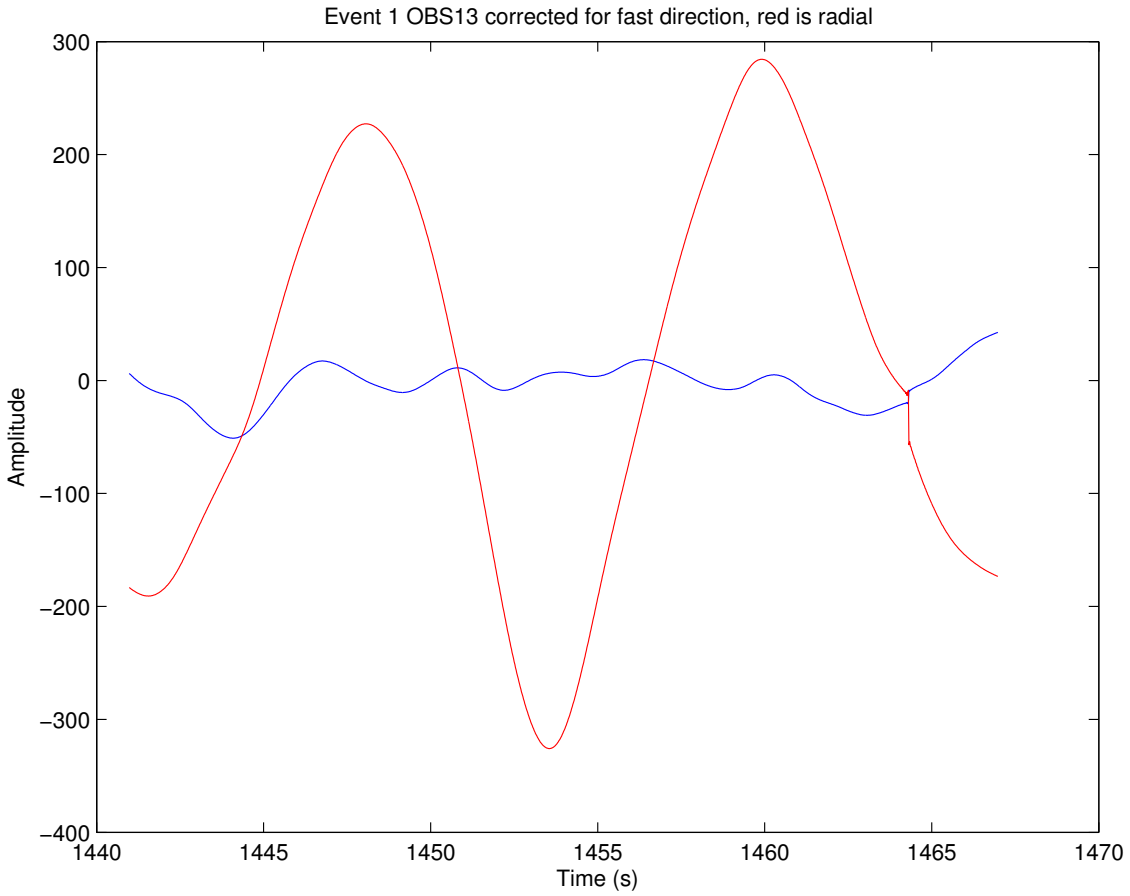

Figure 63: OBS13 Corrected

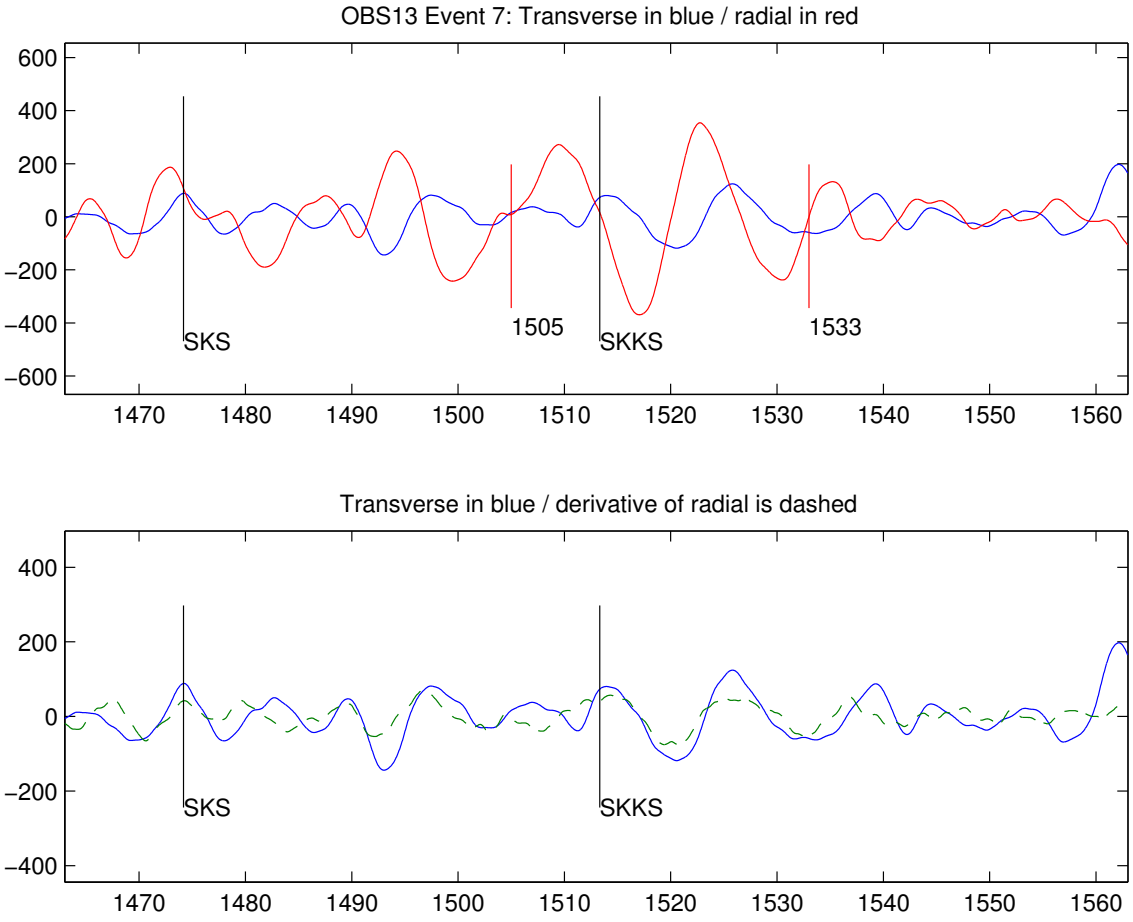

Figure 64: OBS13 Time Window

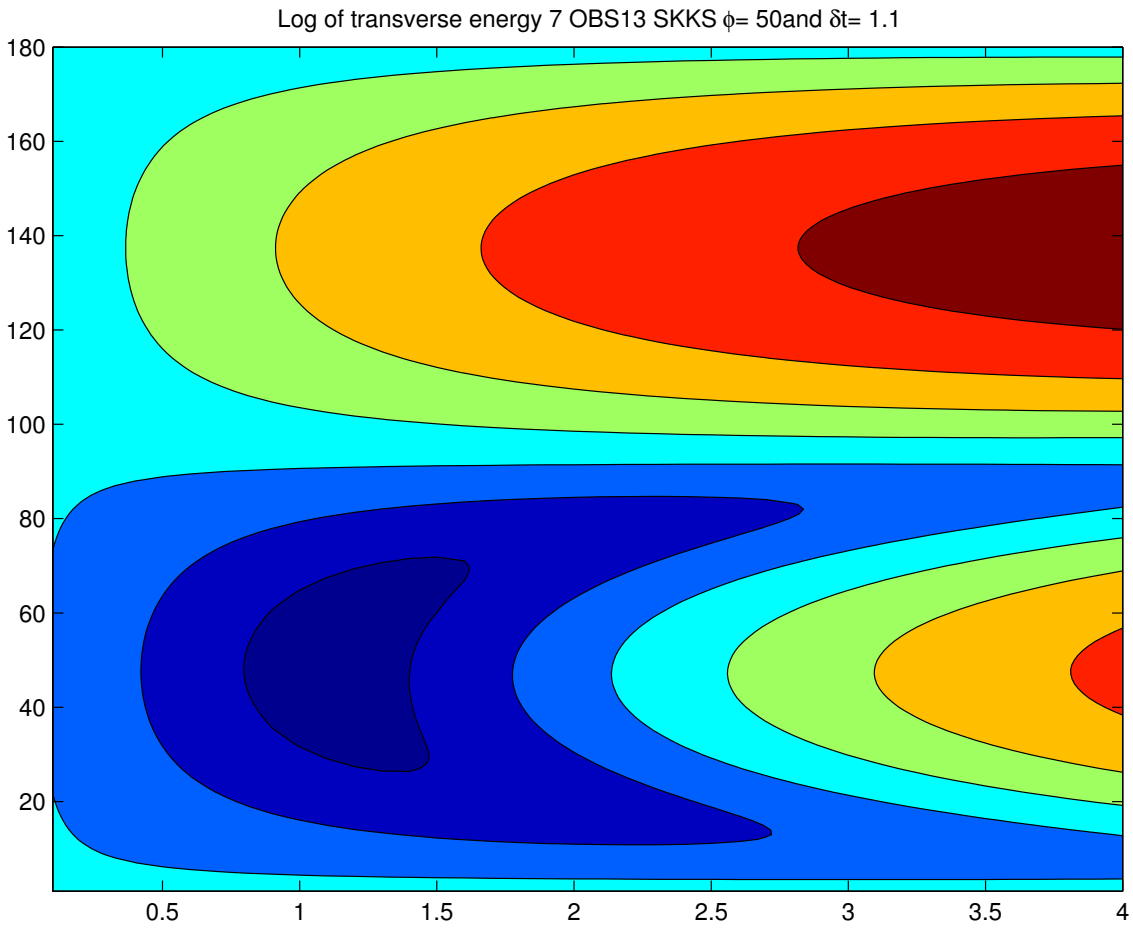

Figure 65: OBS13 Contour

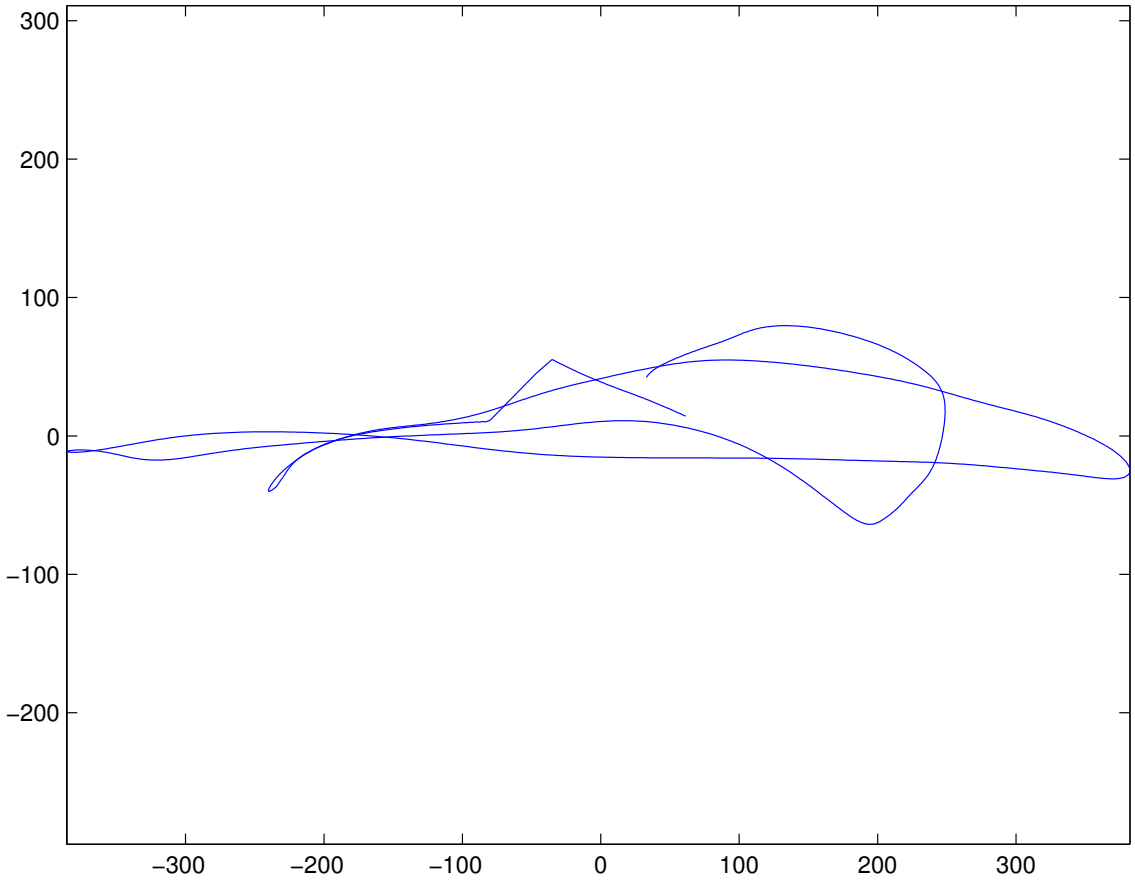

Figure 66: OBS13 Particle Motion

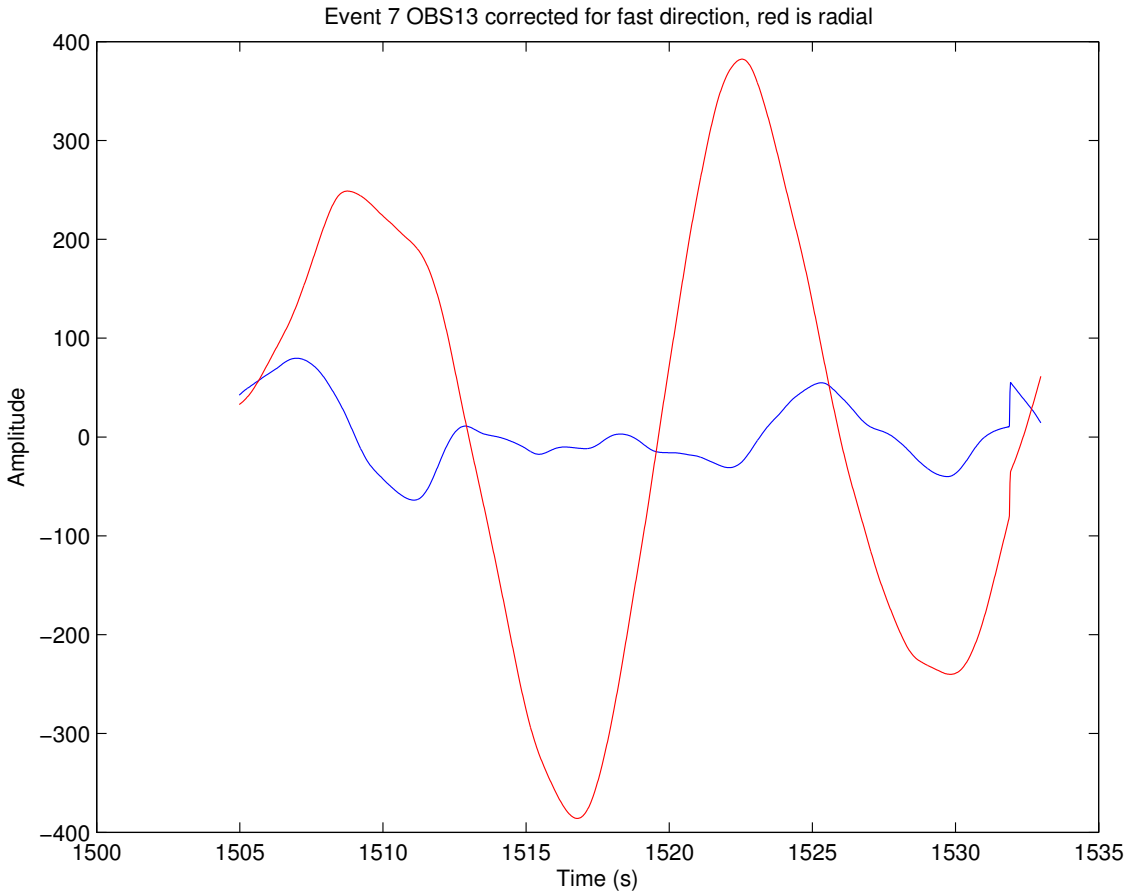

Figure 67: OBS13 Corrected

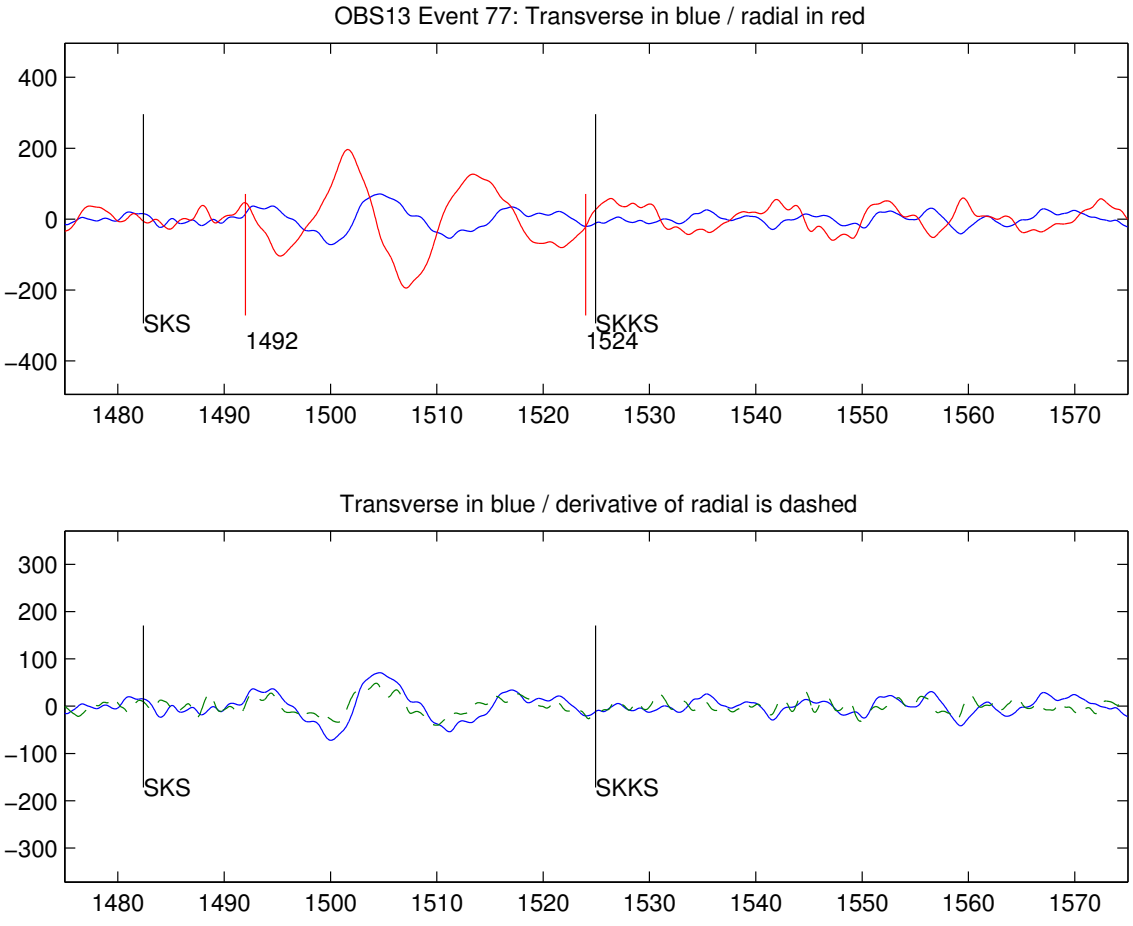

Figure 68: OBS13 Time Window

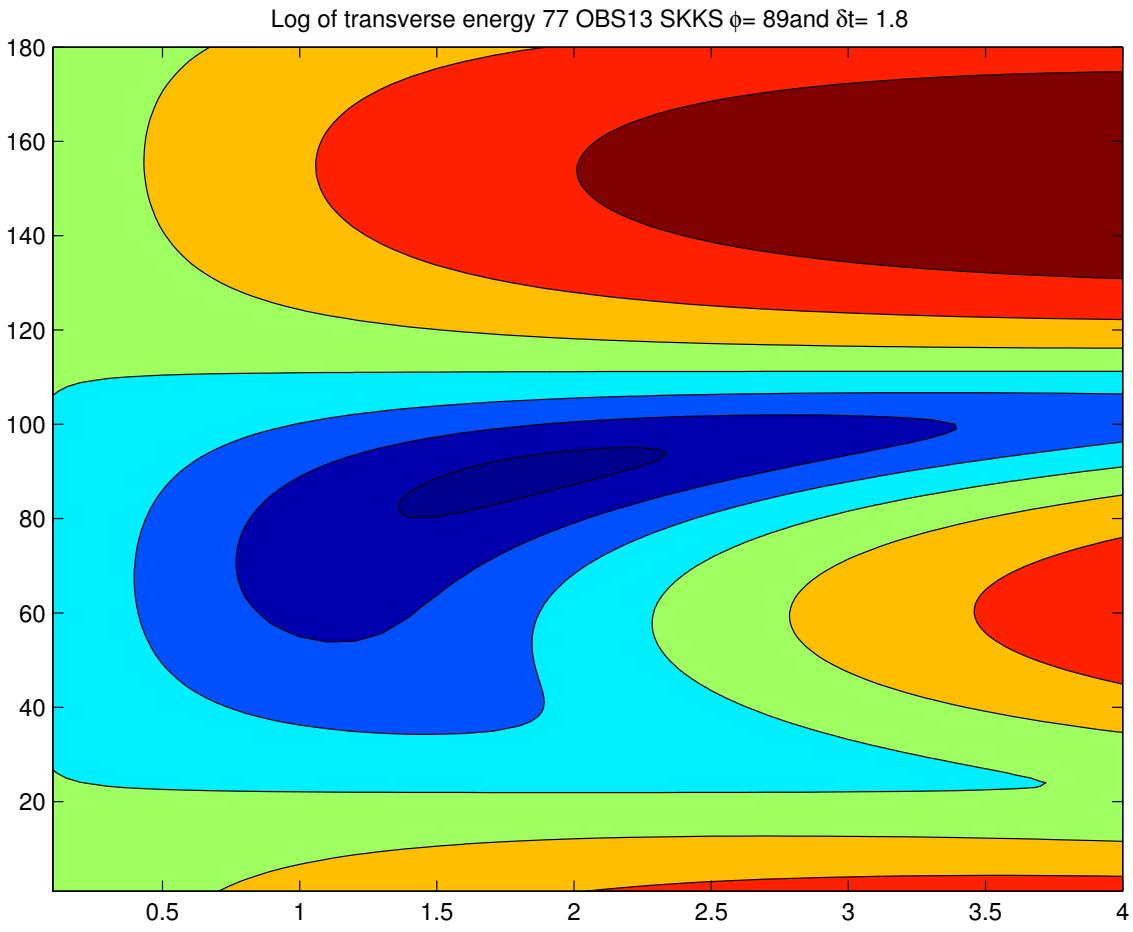

Figure 69: OBS13 Contour

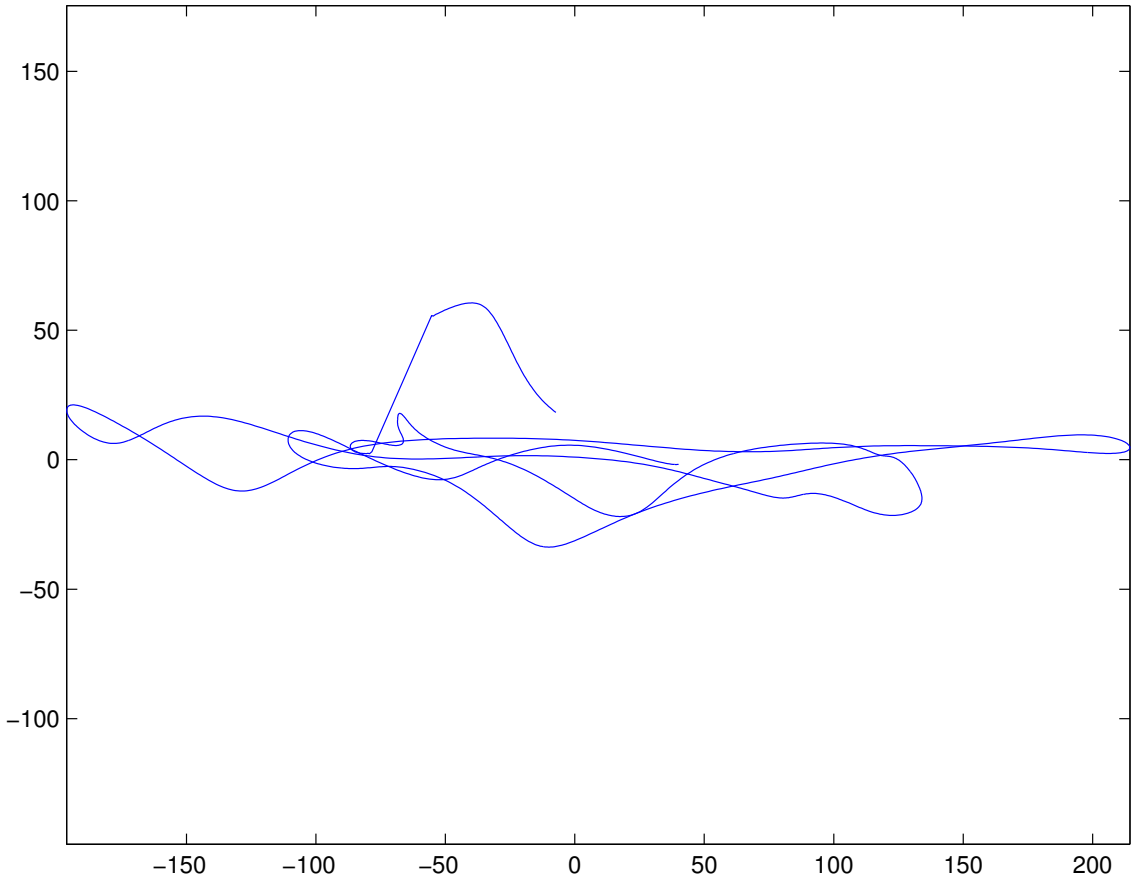

Figure 70: OBS13 Particle Motion

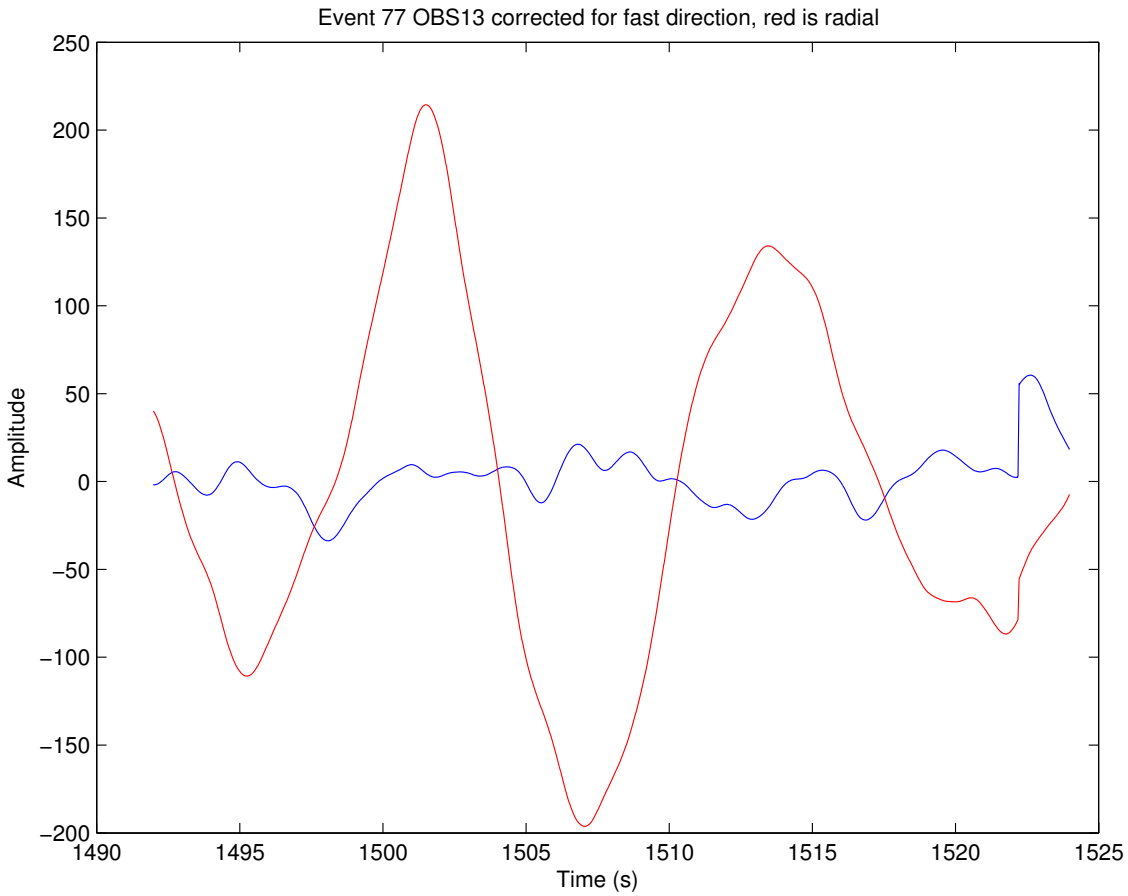

Figure 71: OBS13 Corrected

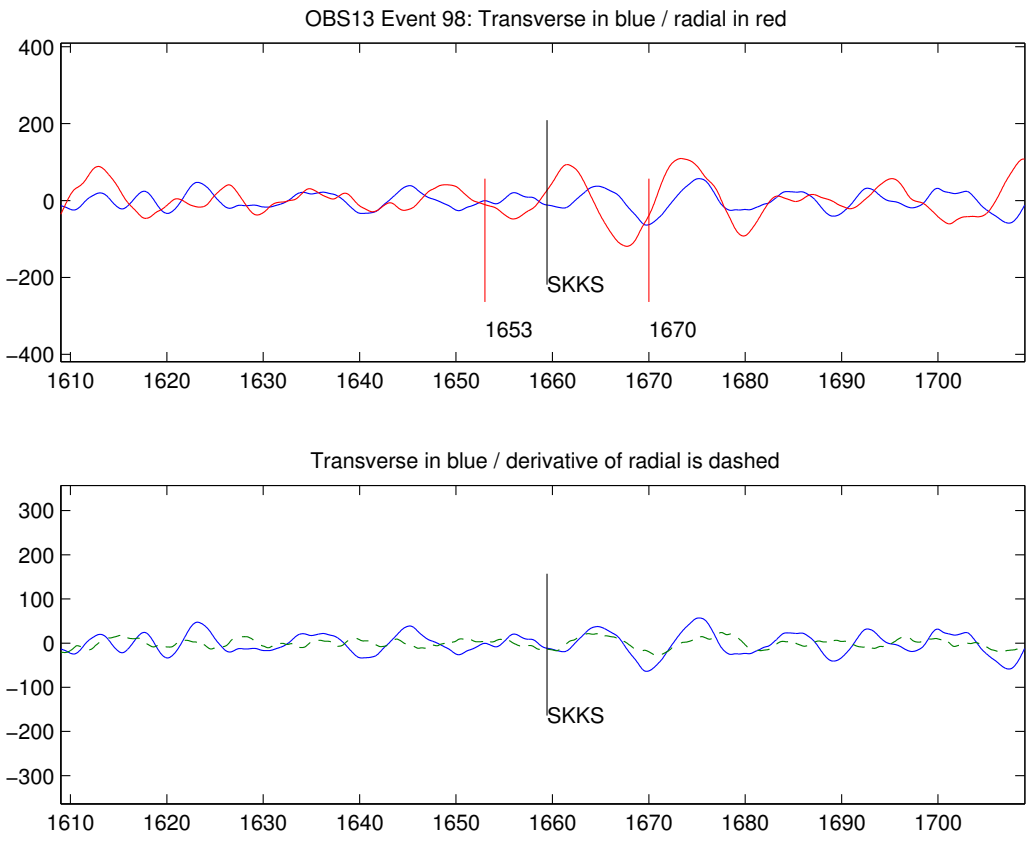

Figure 72: OBS13 Time Window

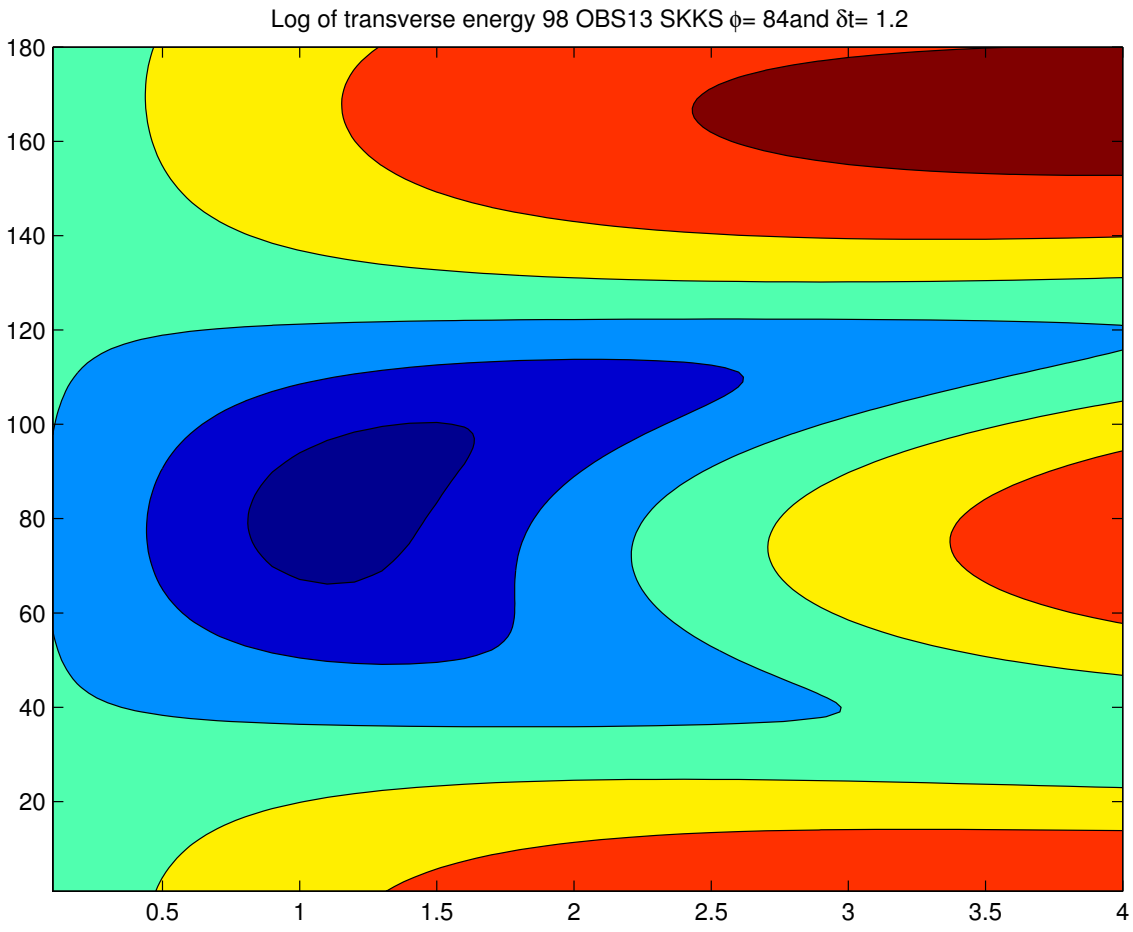

Figure 73: OBS13 Contour

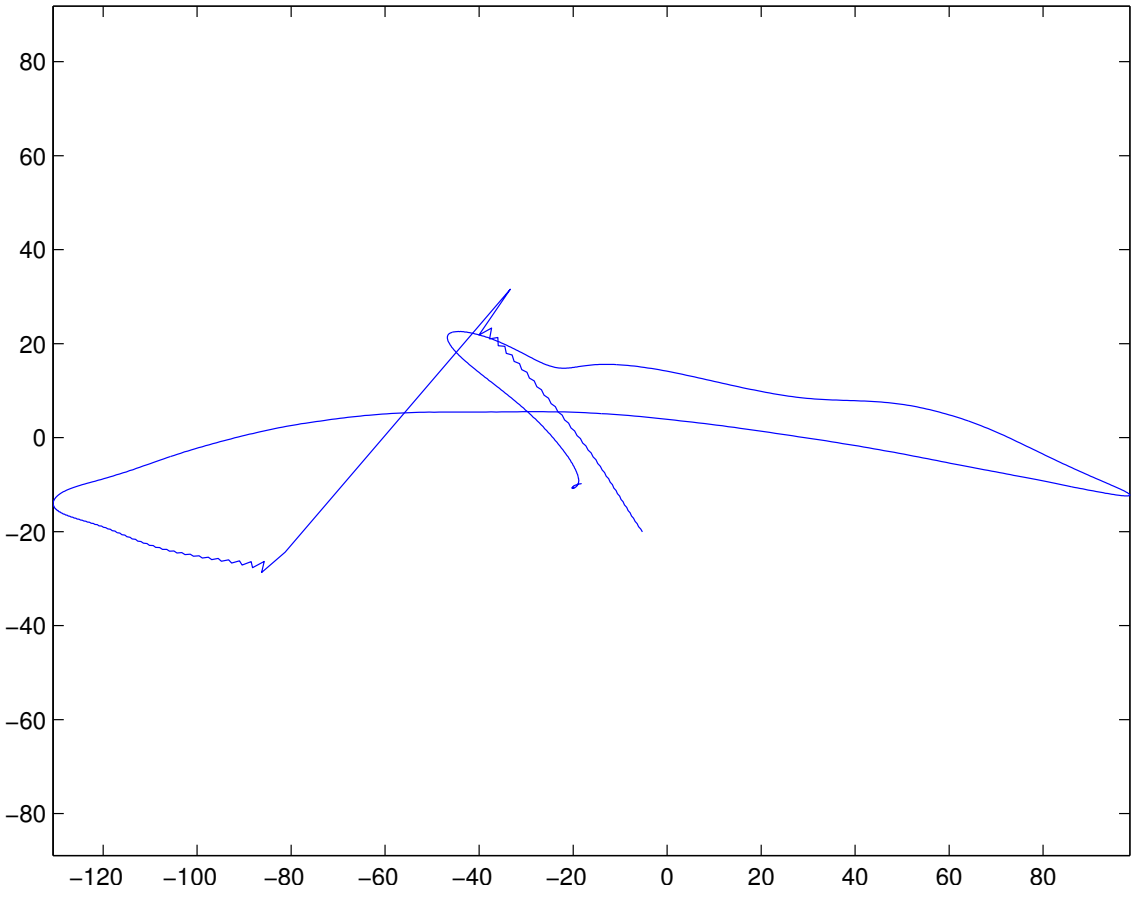

Figure 74: OBS13 Particle Motion

Figure 75: OBS13 Corrected

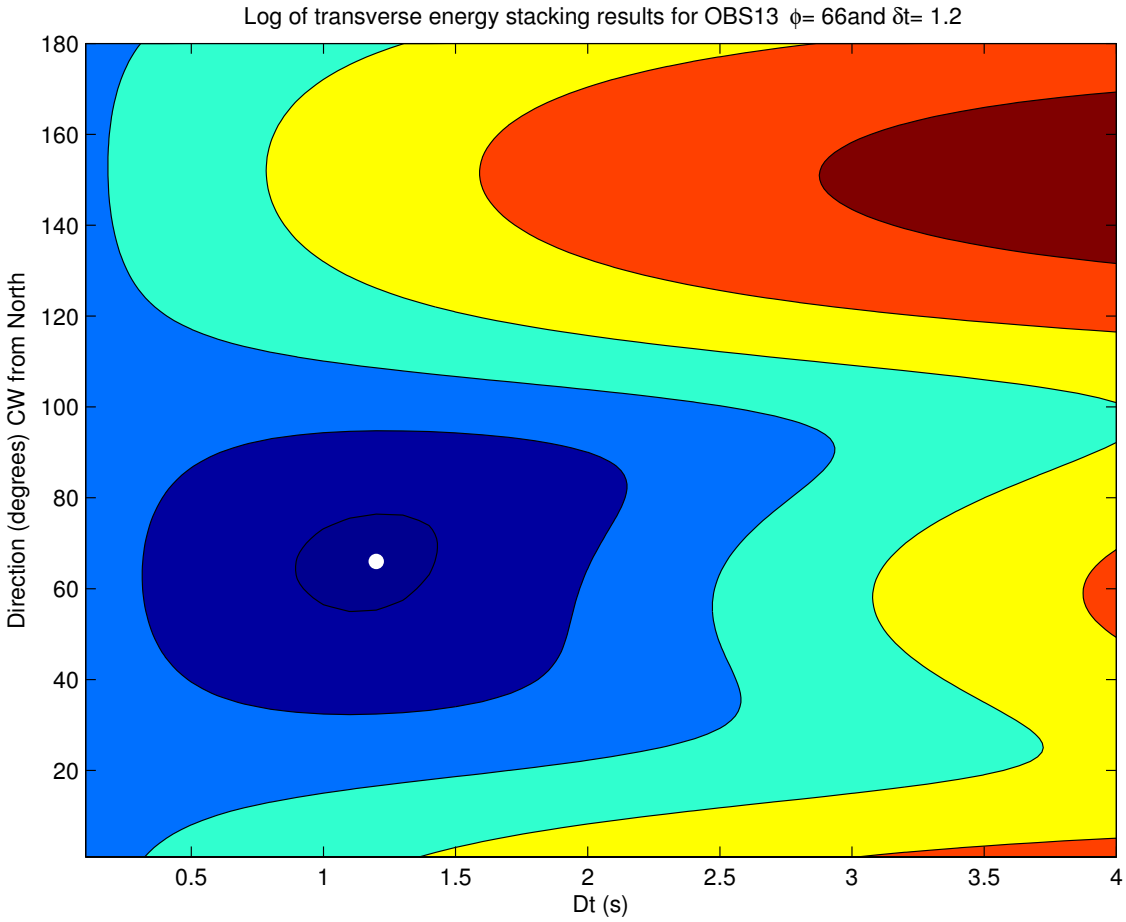

Figure 76: OBS13 Stacked Transverse Energy

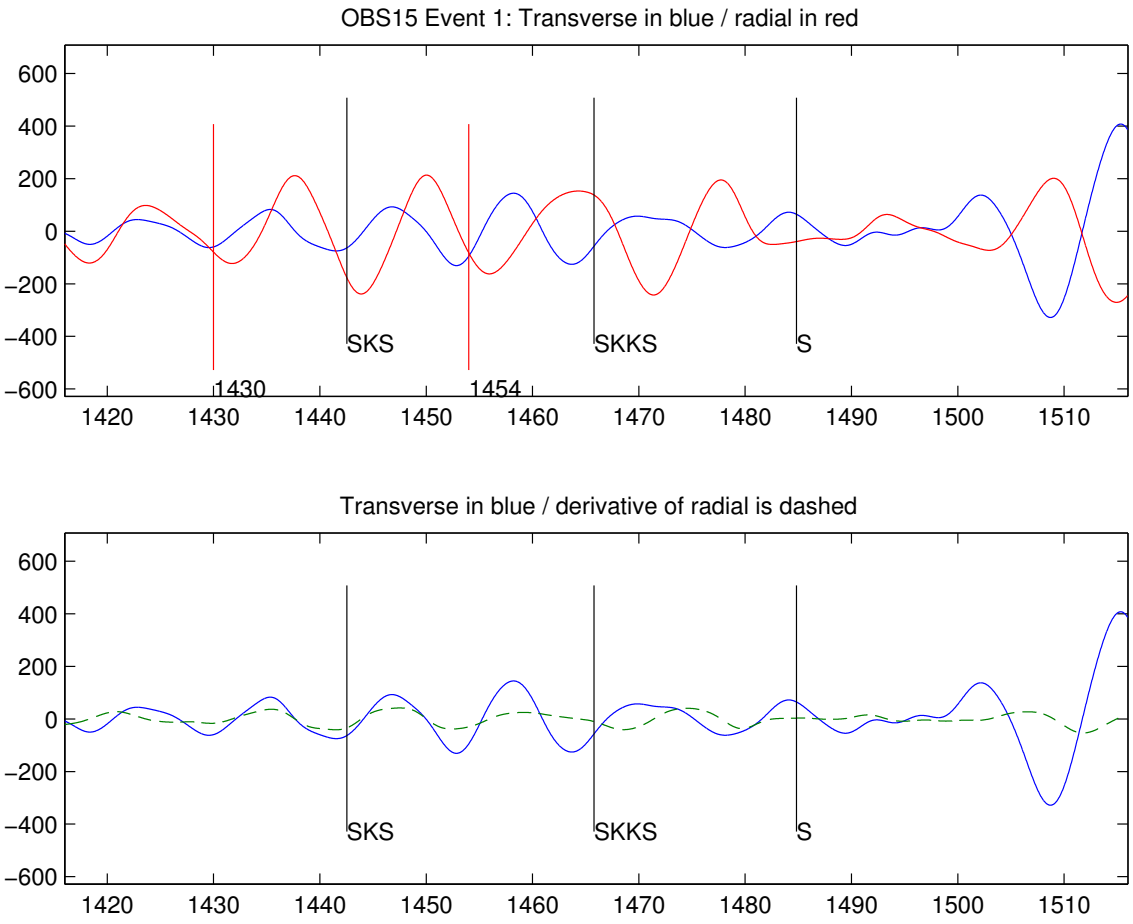

Figure 77: OBS15 Time Window

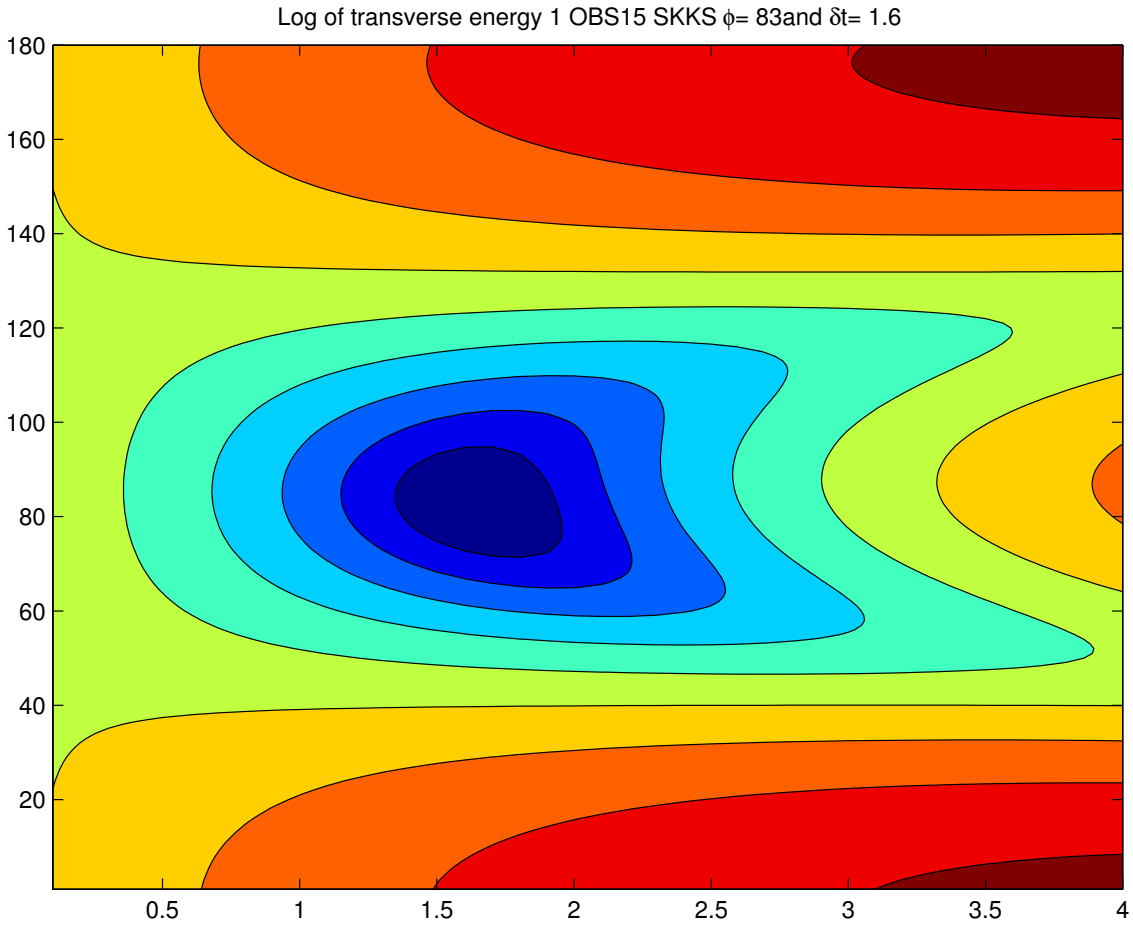

Figure 78: OBS15 Contour

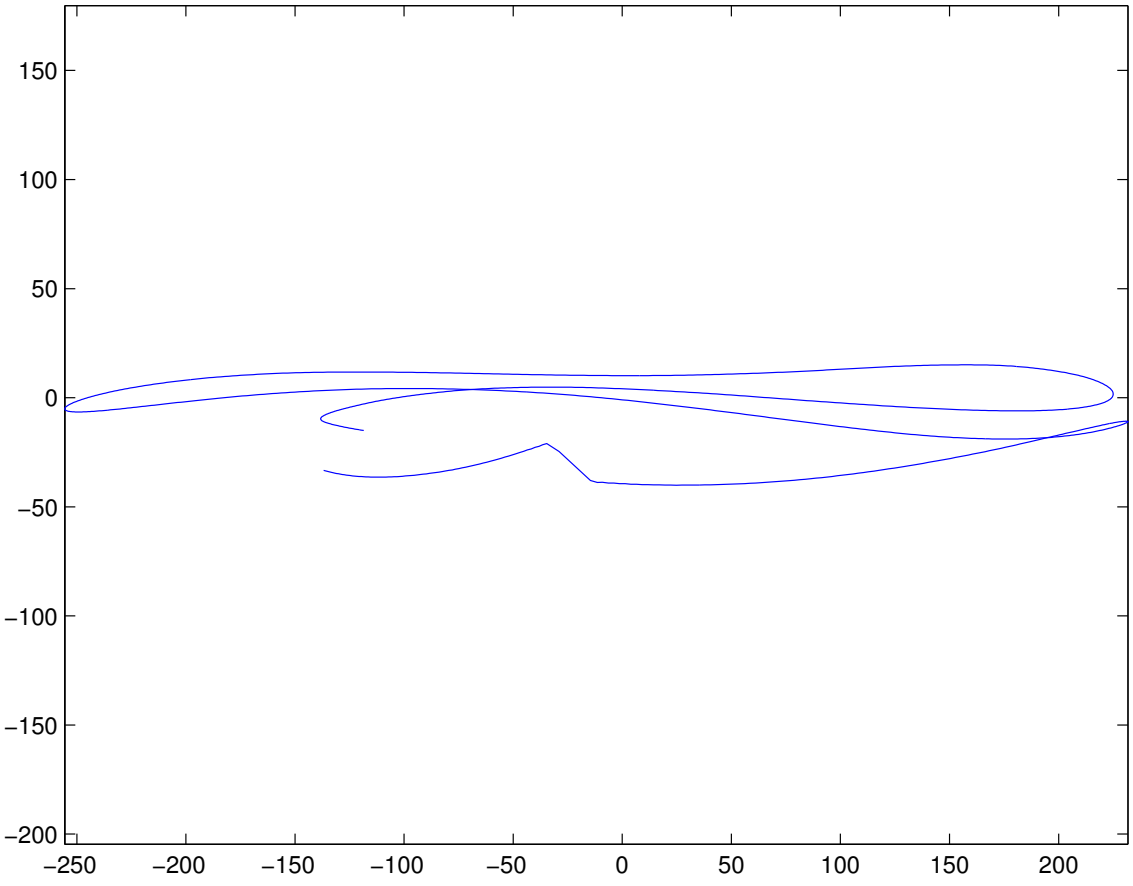

Figure 79: OBS15 Particle Motion

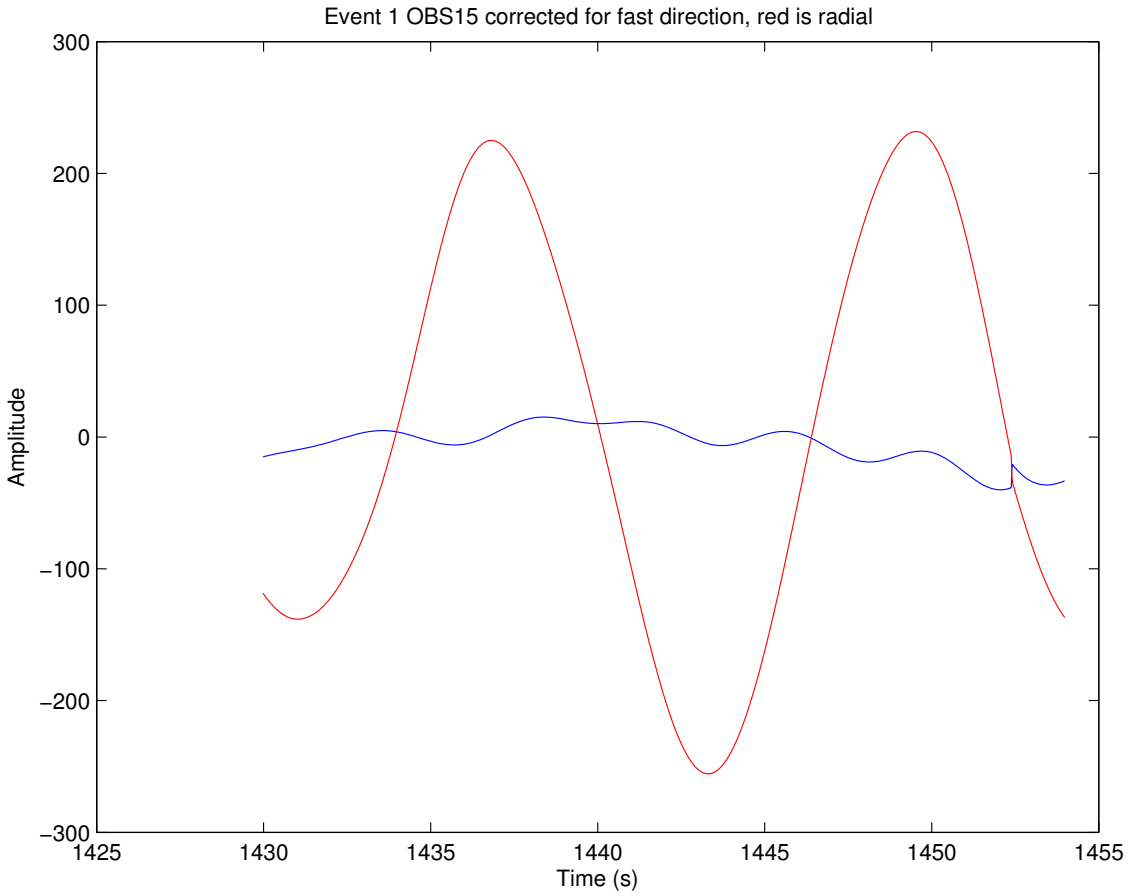

Figure 80: OBS15 Corrected

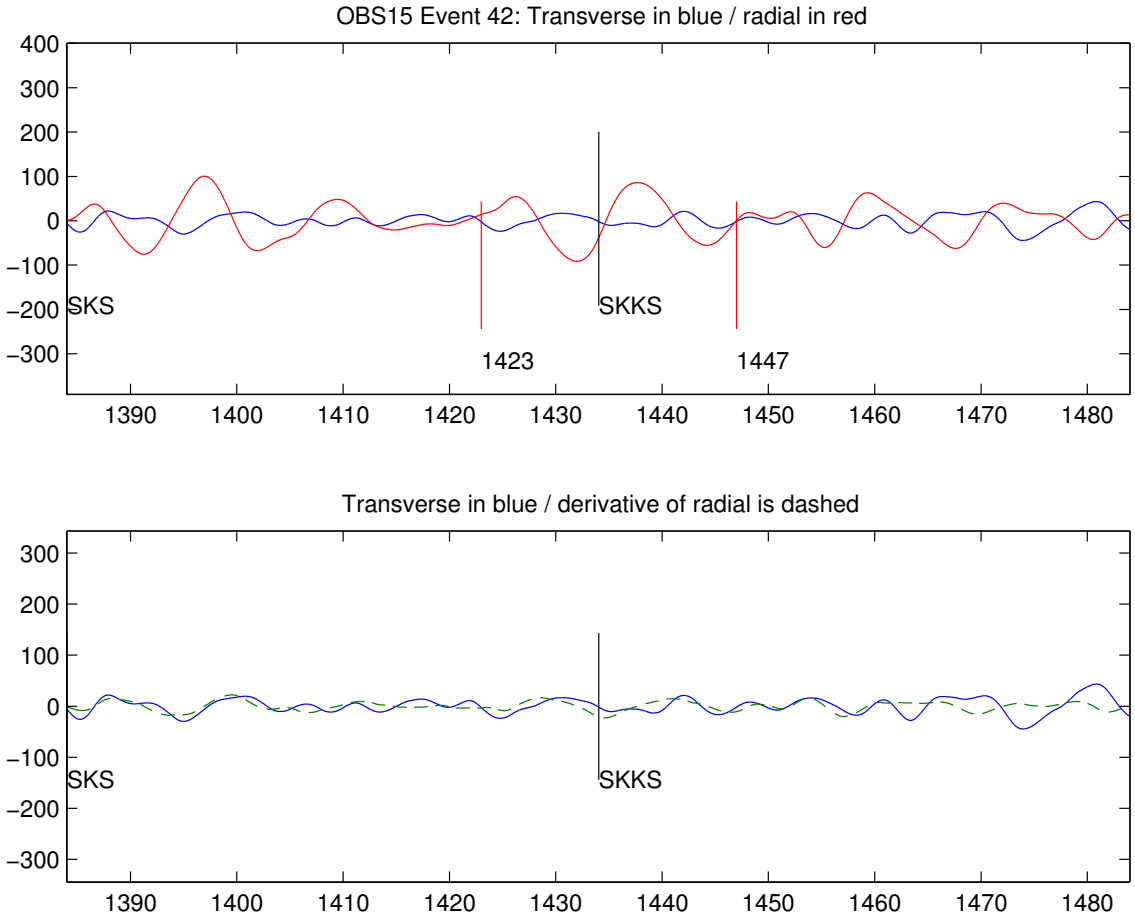

Figure 81: OBS15 Time Window

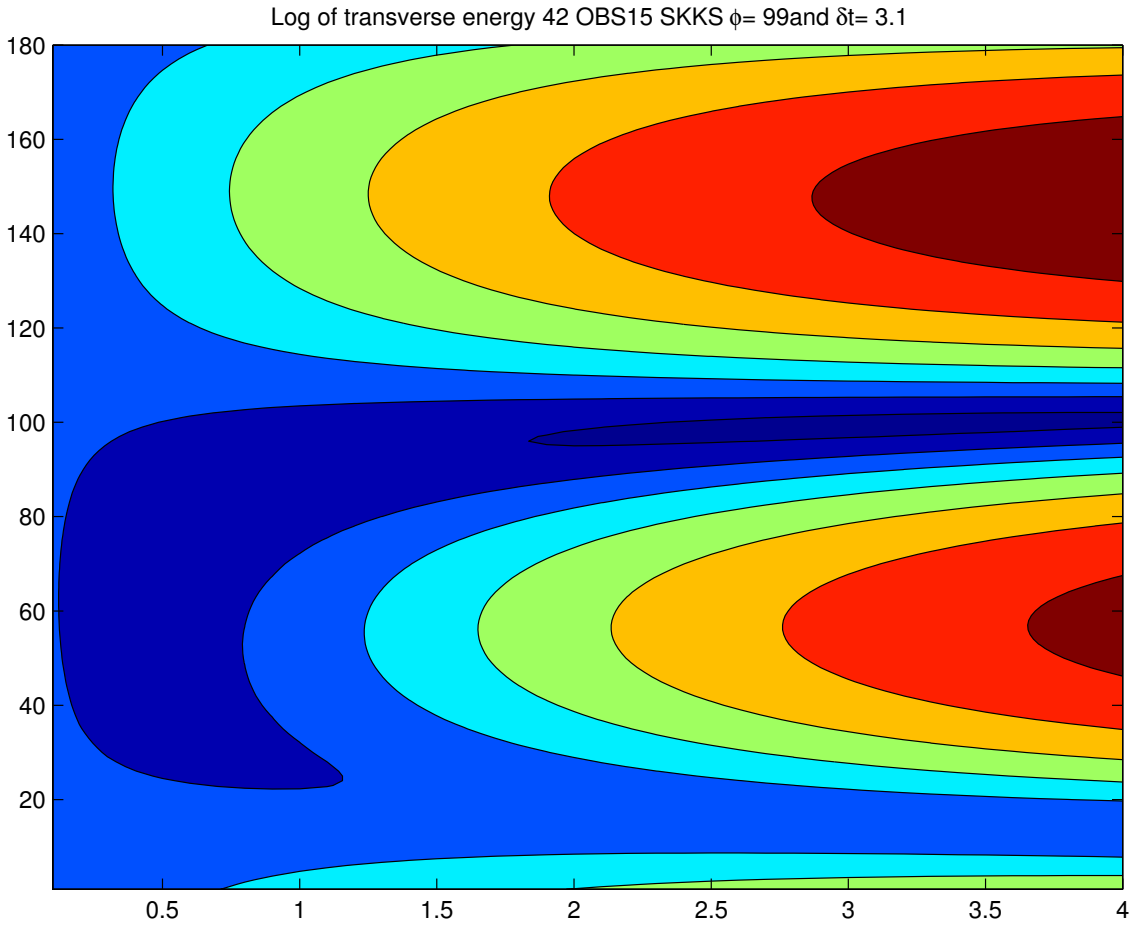

Figure 82: OBS15 Contour

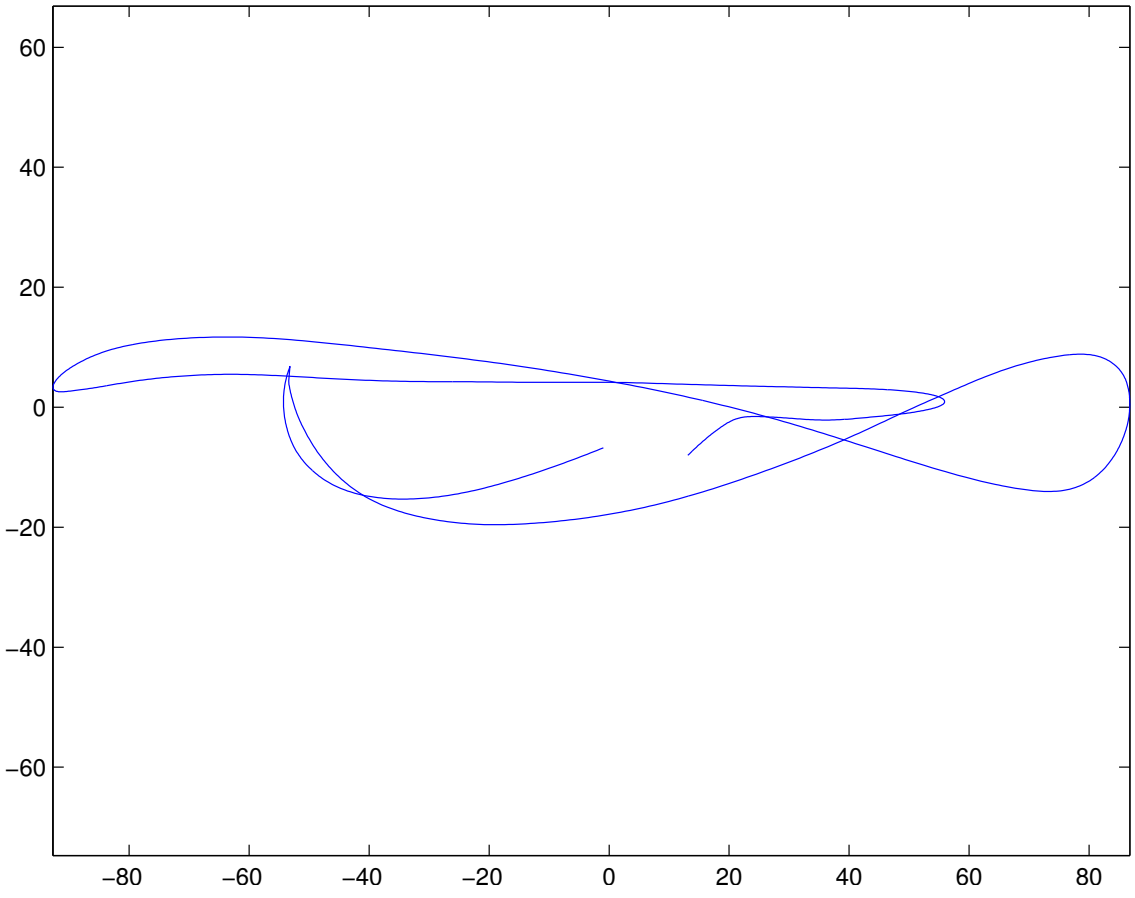

Figure 83: OBS15 Particle Motion

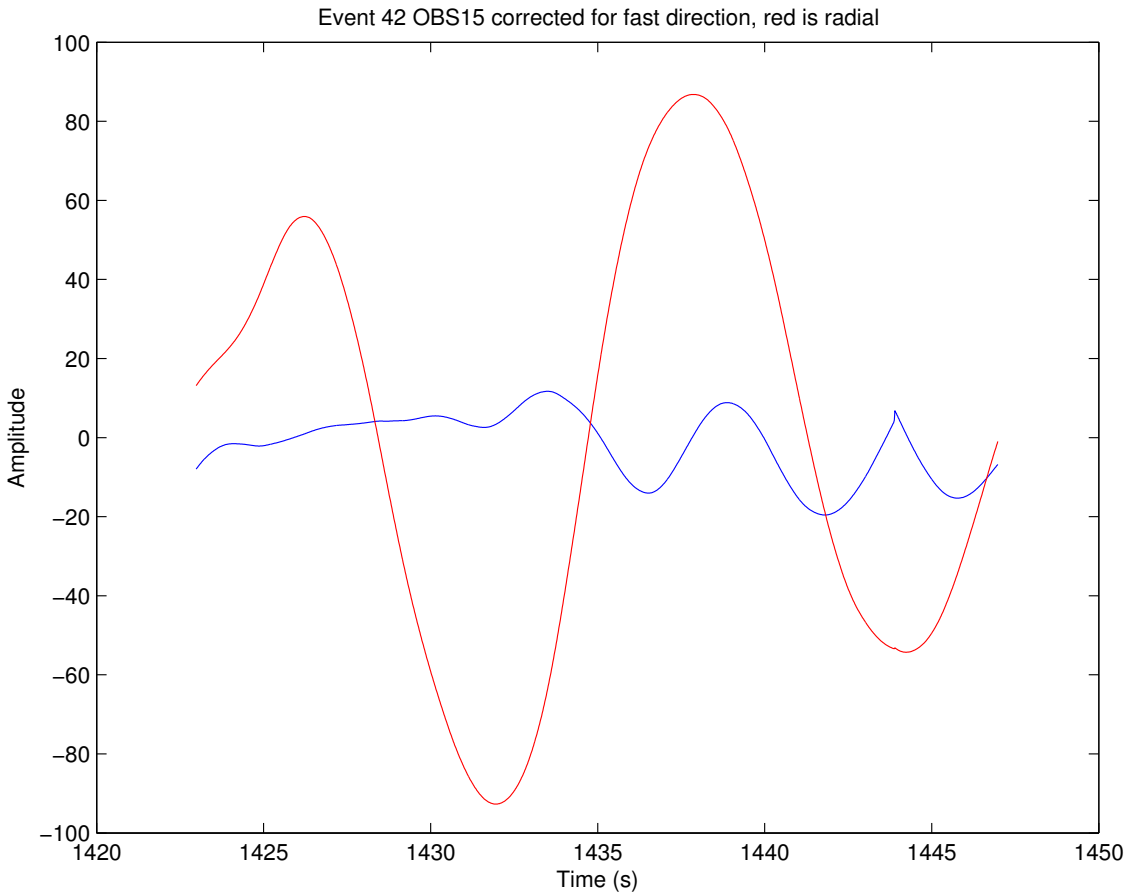

Figure 84: OBS15 Corrected

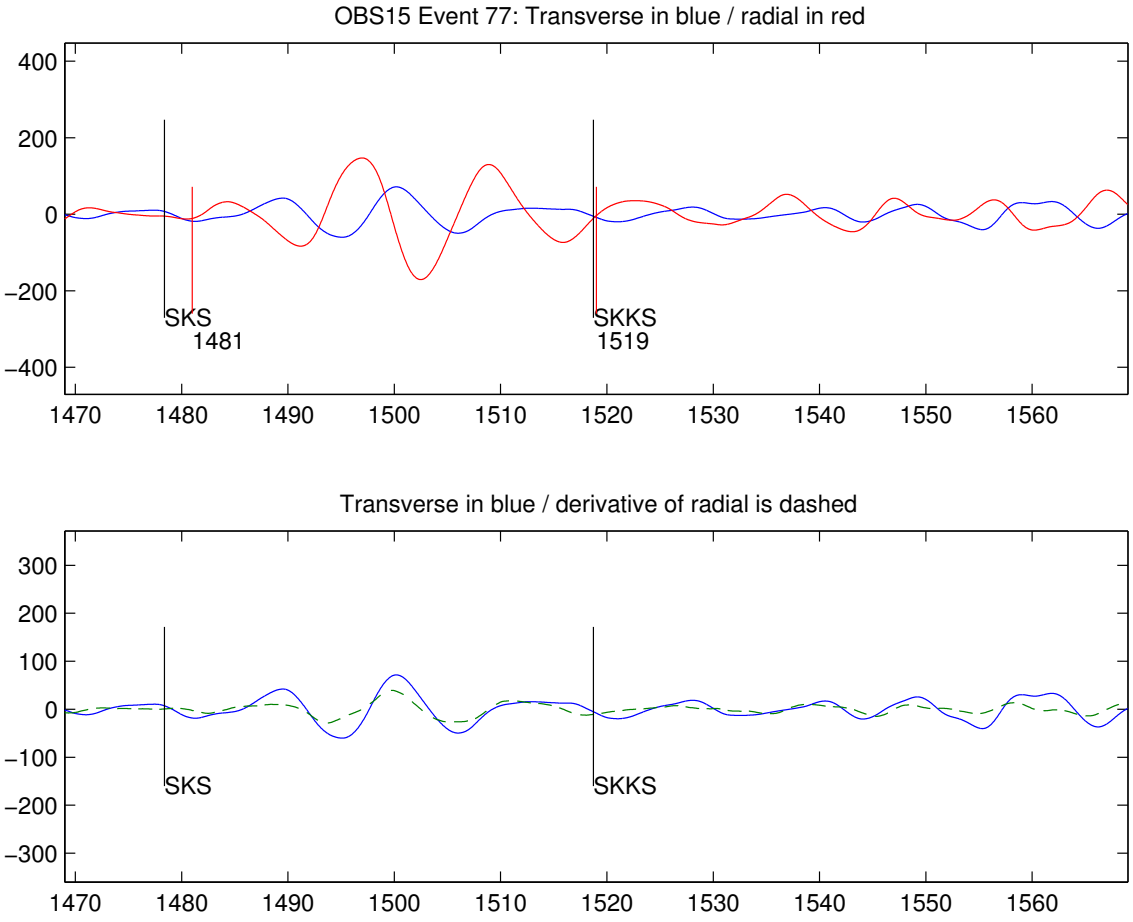

Figure 85: OBS15 Time Window

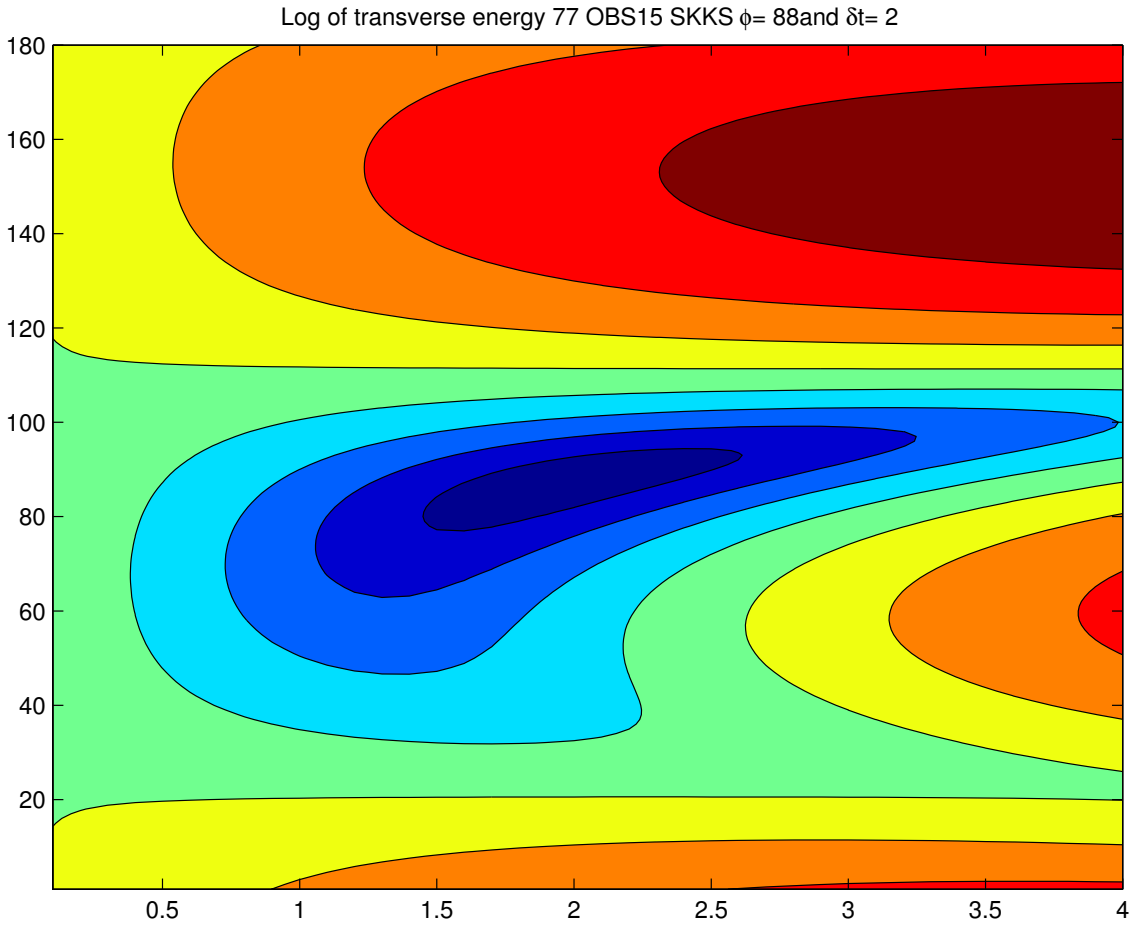

Figure 86: OBS15 Contour

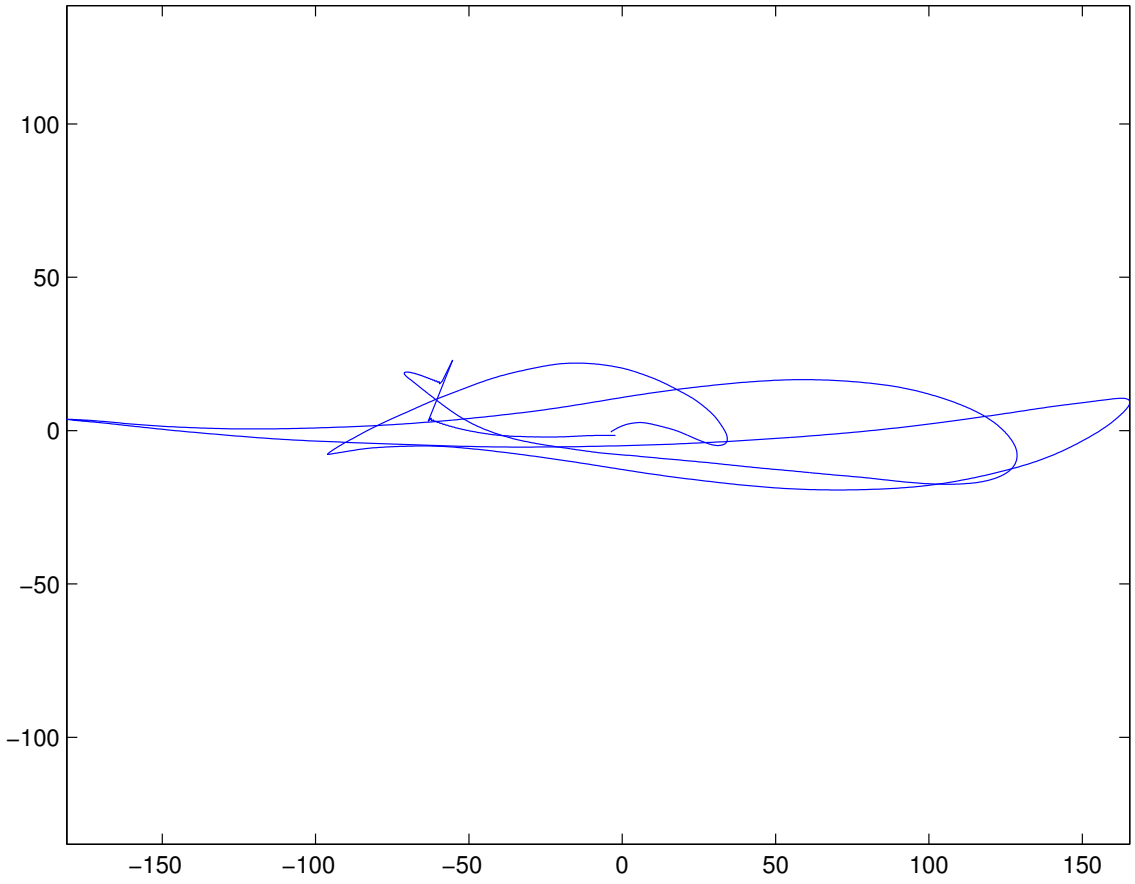

Figure 87: OBS15 Particle Motion

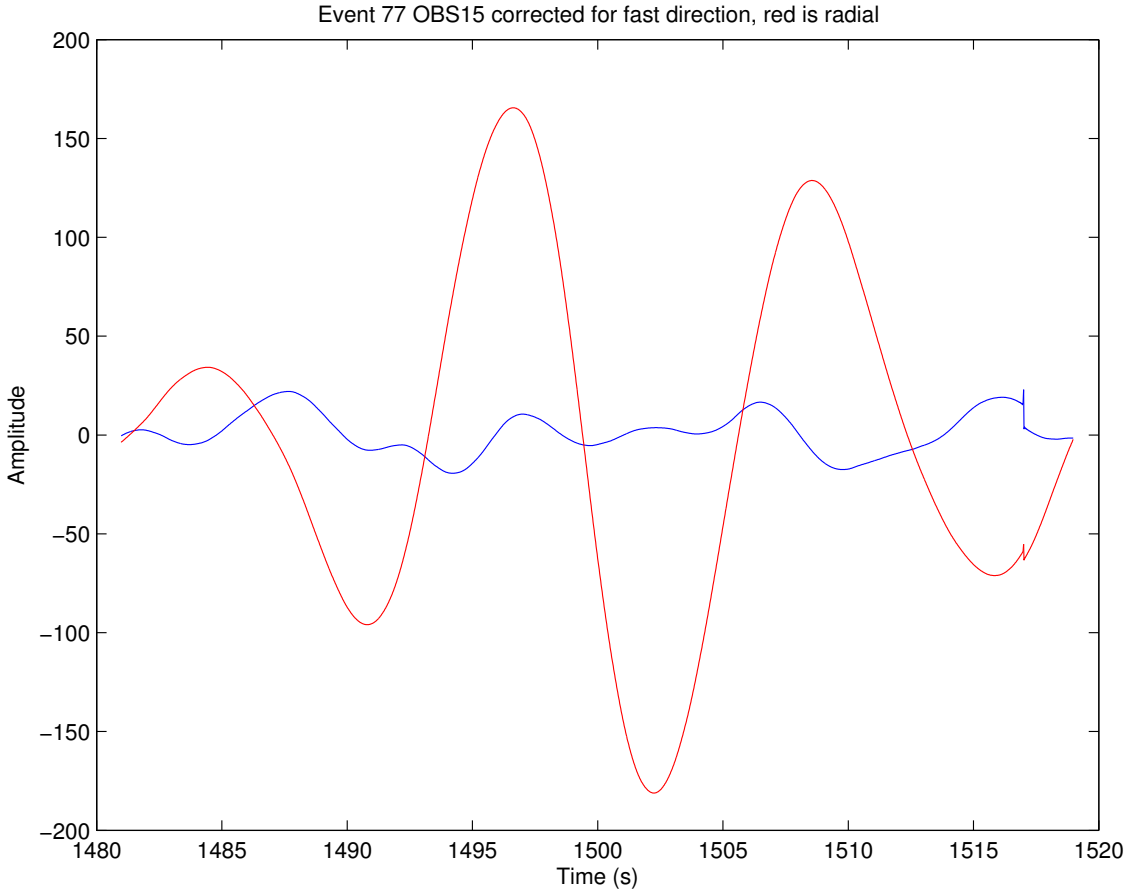

Figure 88: OBS15 Corrected

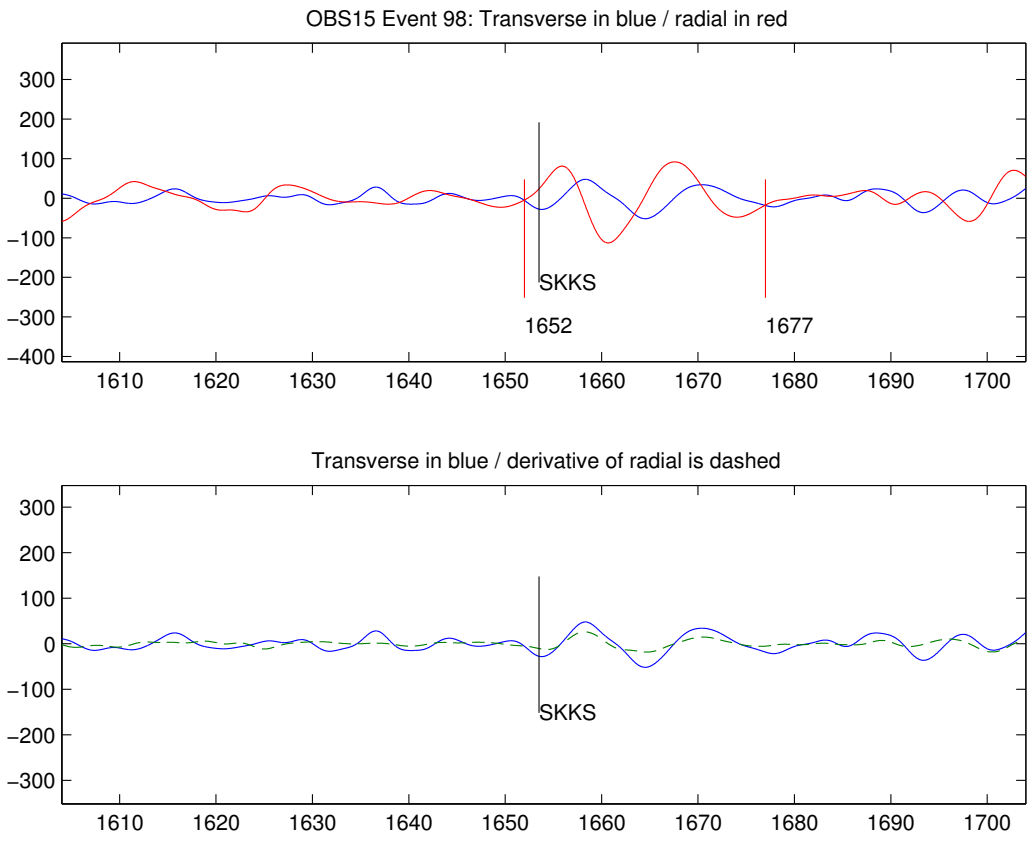

Figure 89: OBS15 Time Window

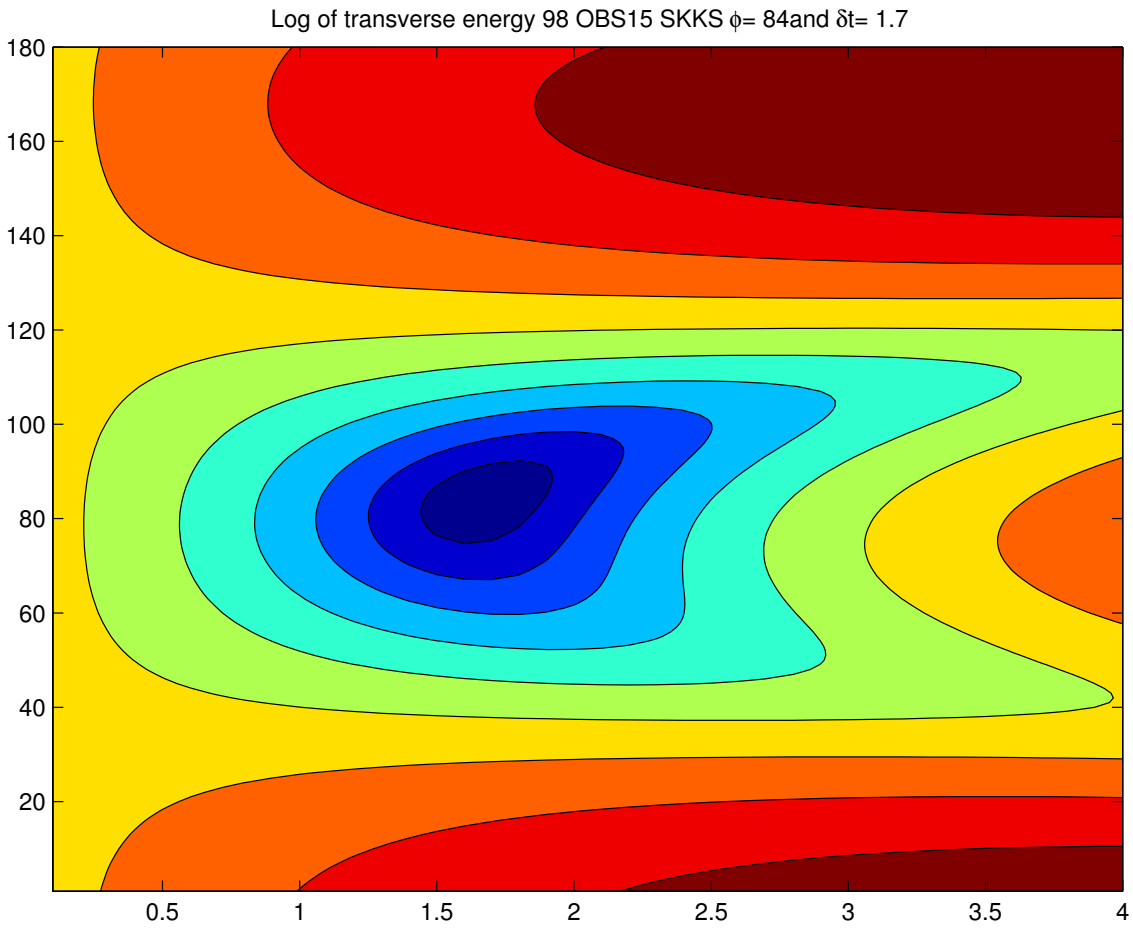

Figure 90: OBS15 Contour

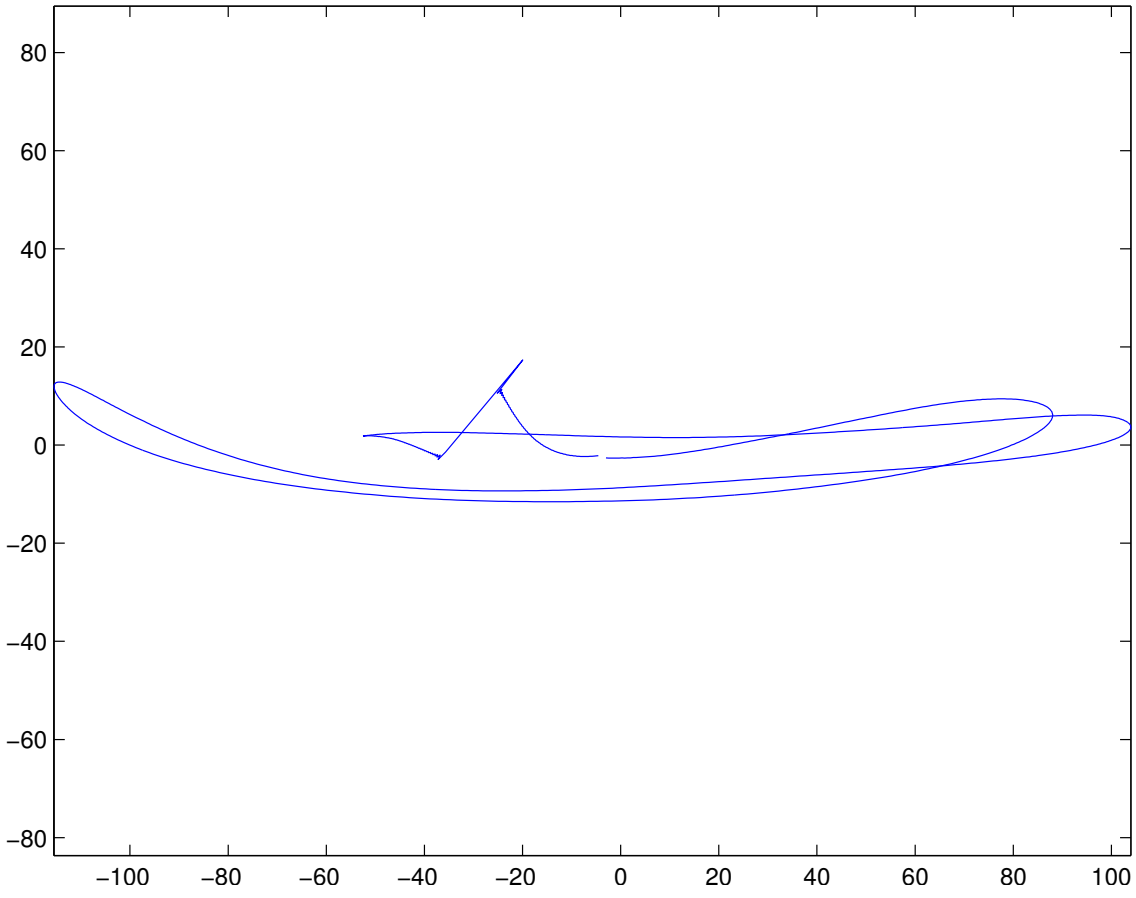

Figure 91: OBS15 Particle Motion

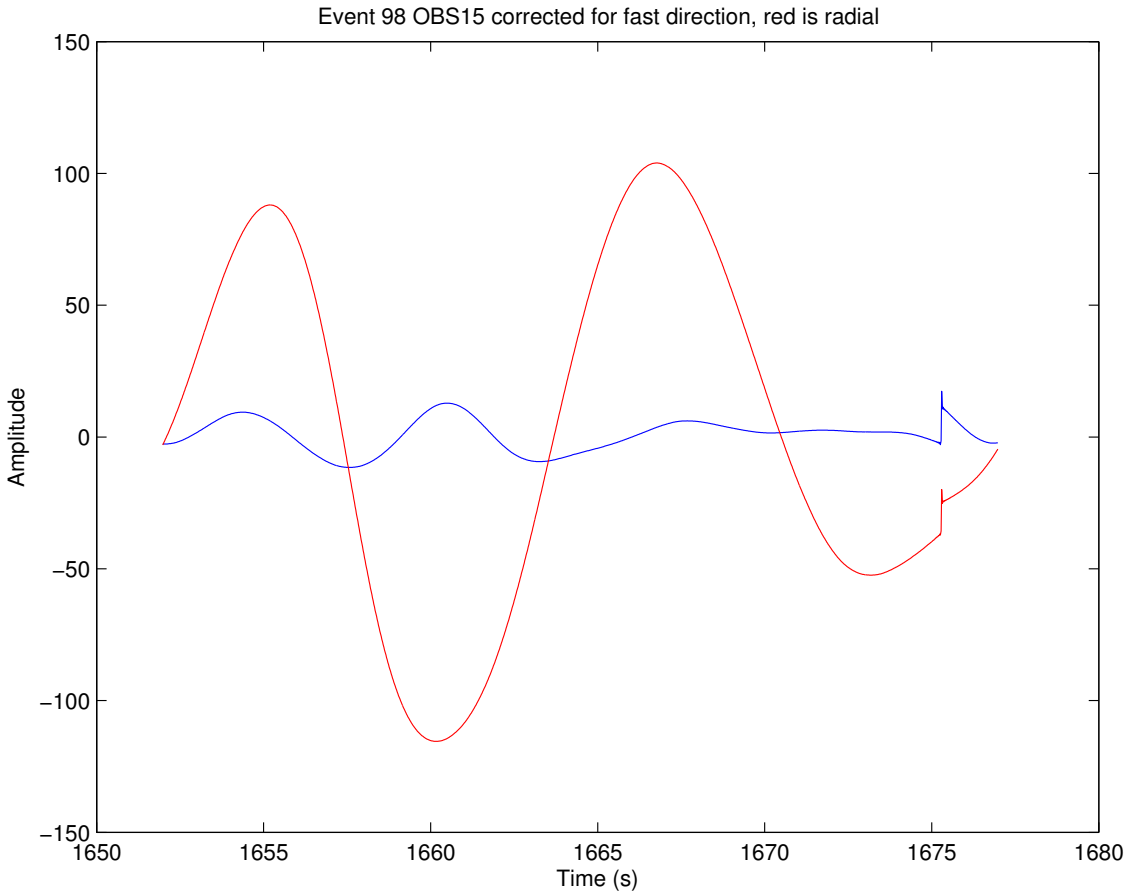

Figure 92: OBS15 Corrected

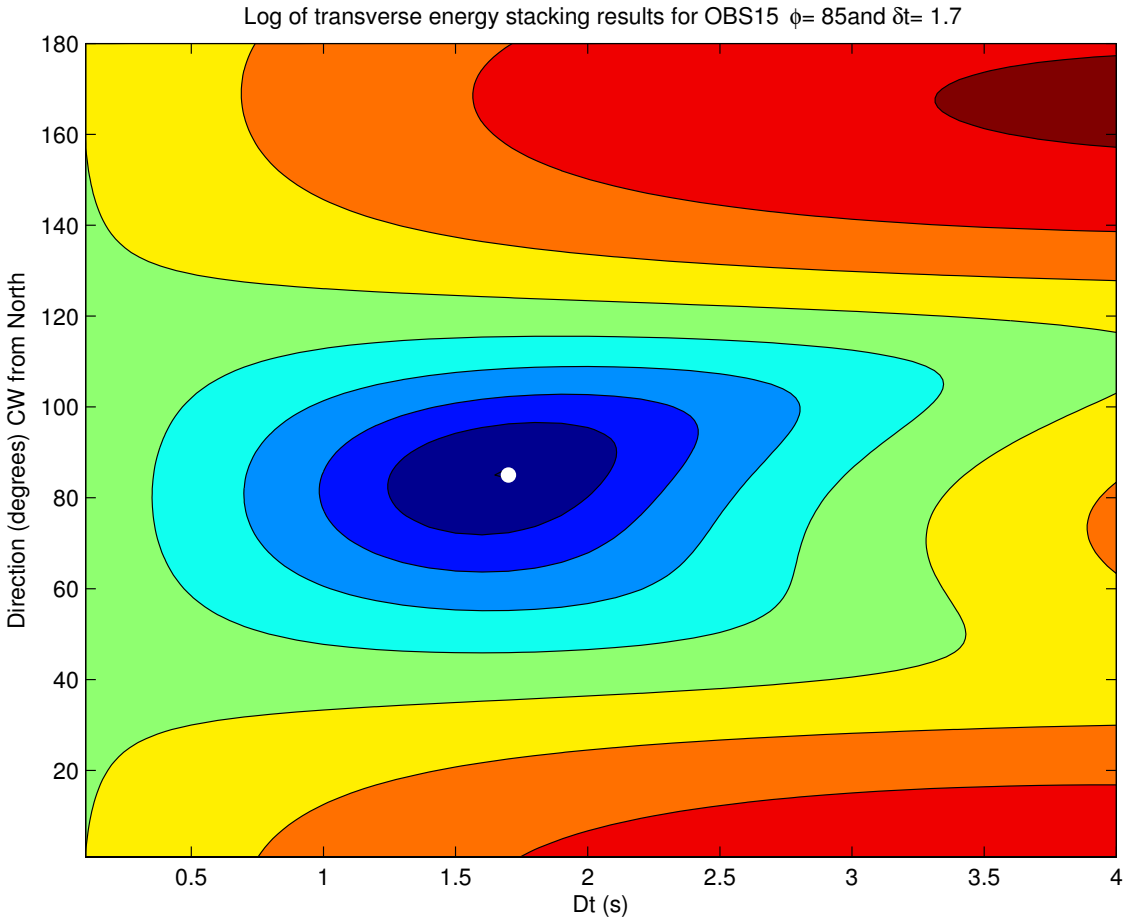

Figure 93: OBS15 Stacked Transverse Energy

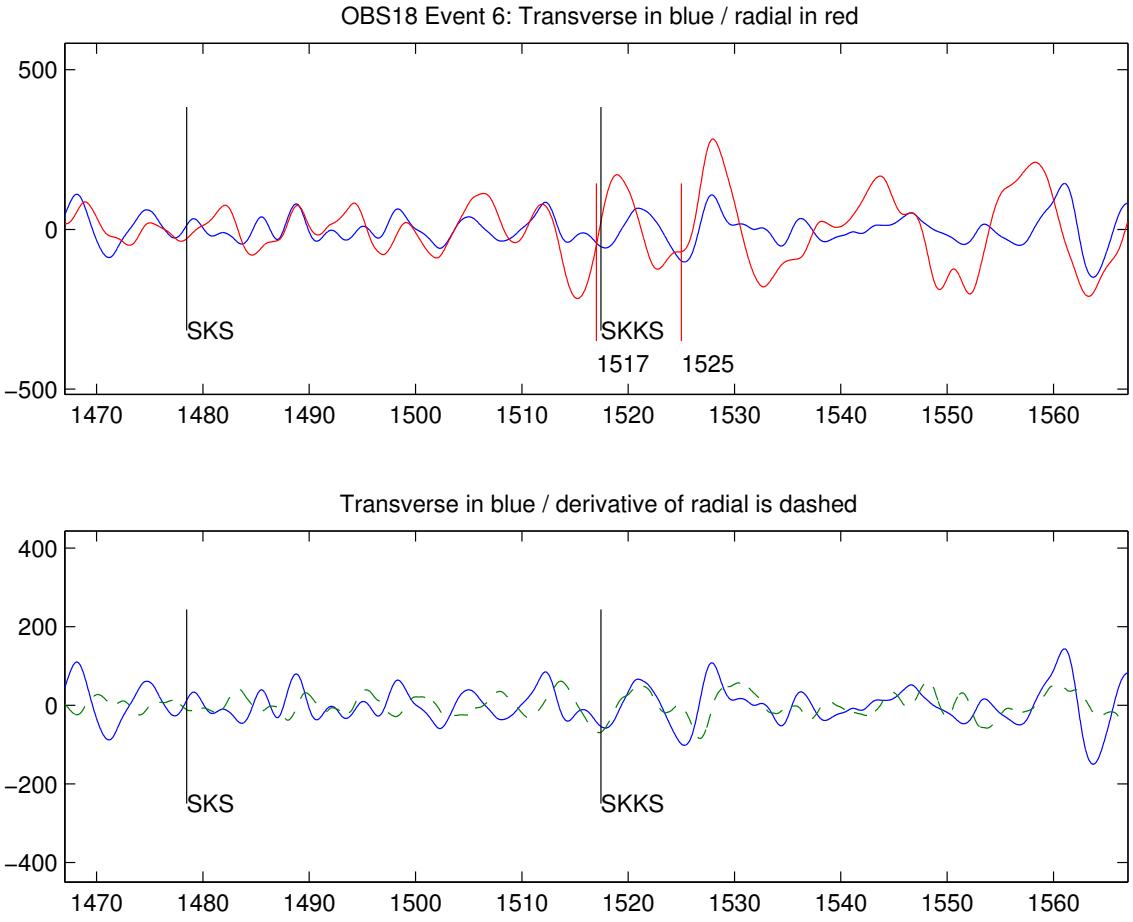

Figure 94: OBS18 Time Window

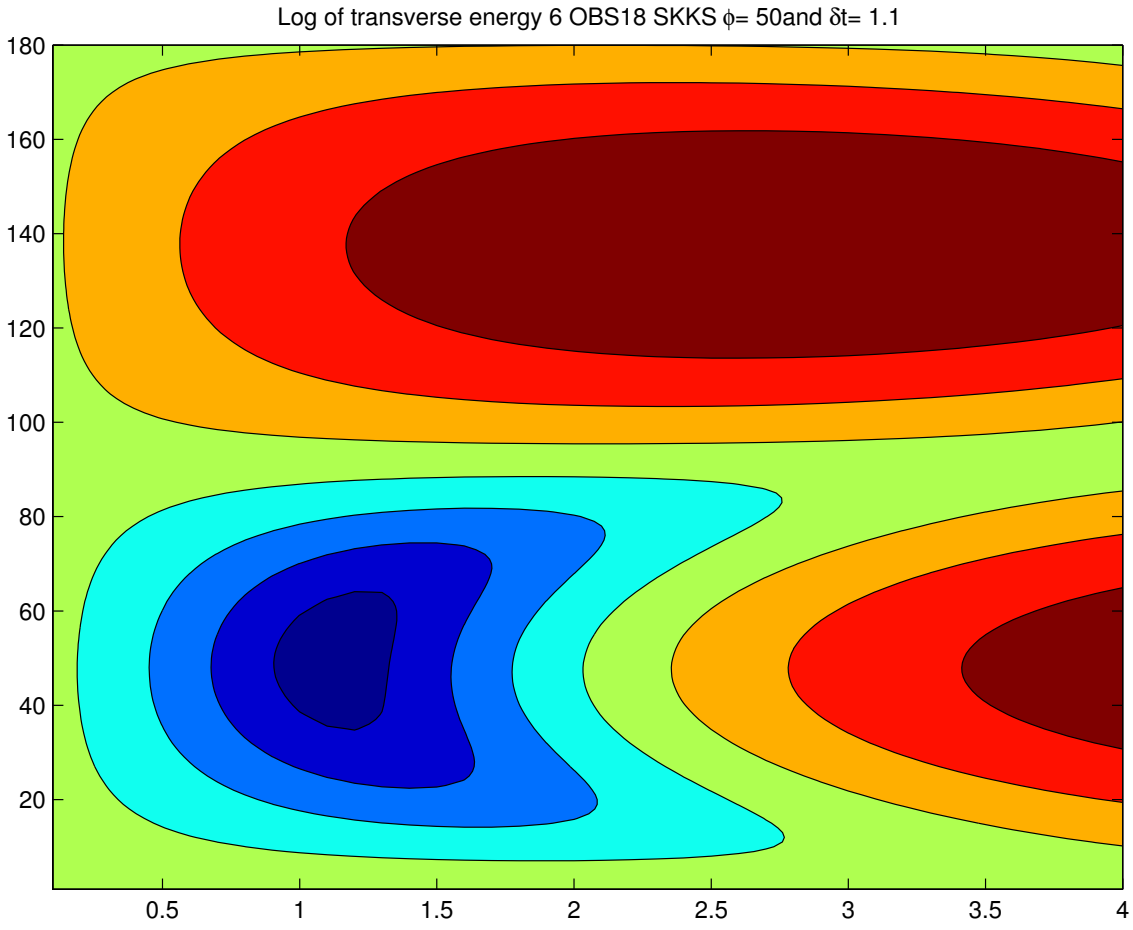

Figure 95: OBS18 Contour

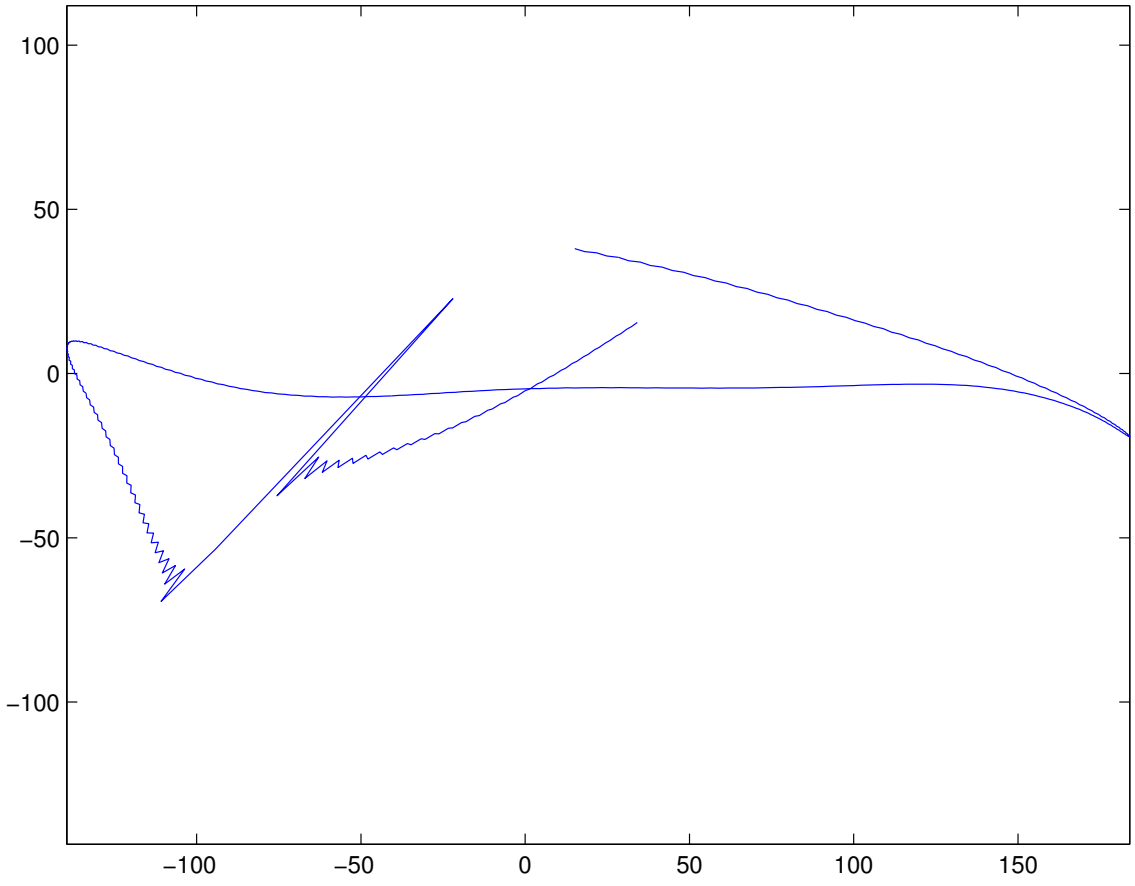

Figure 96: OBS18 Particle Motion

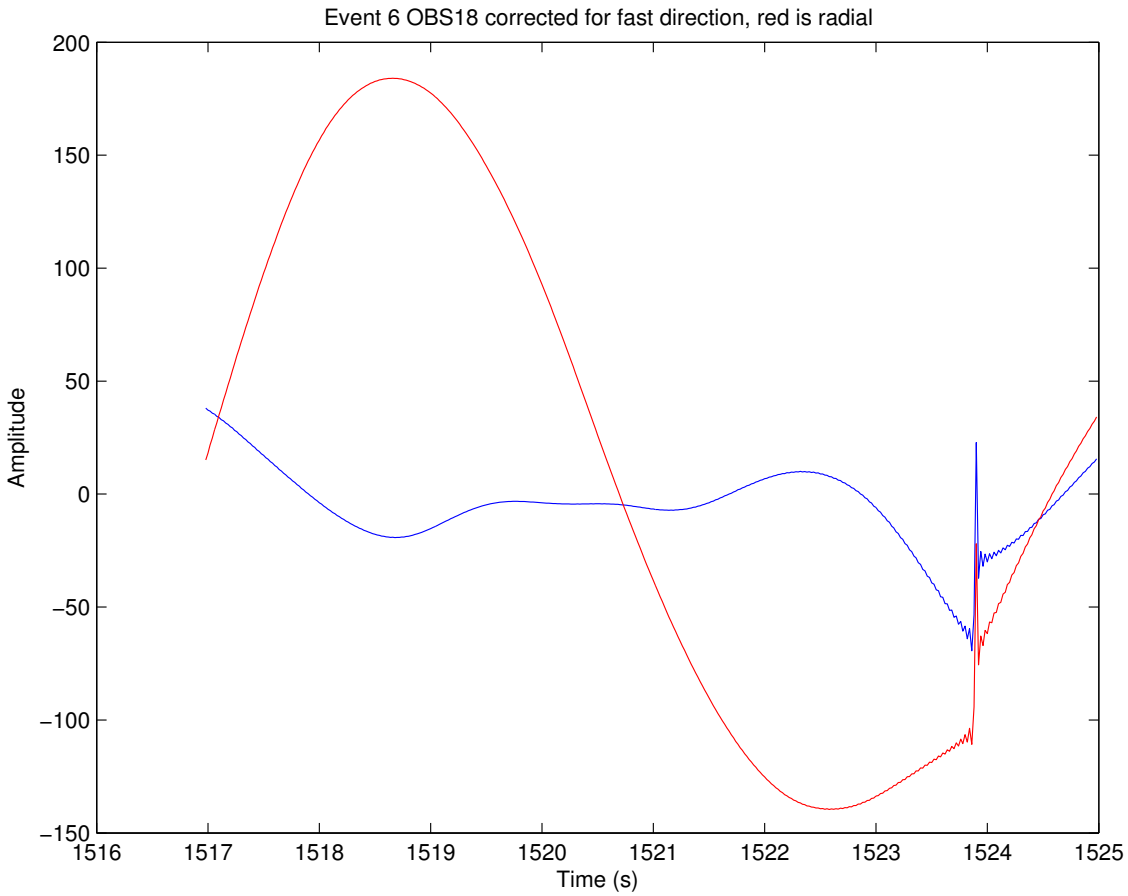

Figure 97: OBS18 Corrected

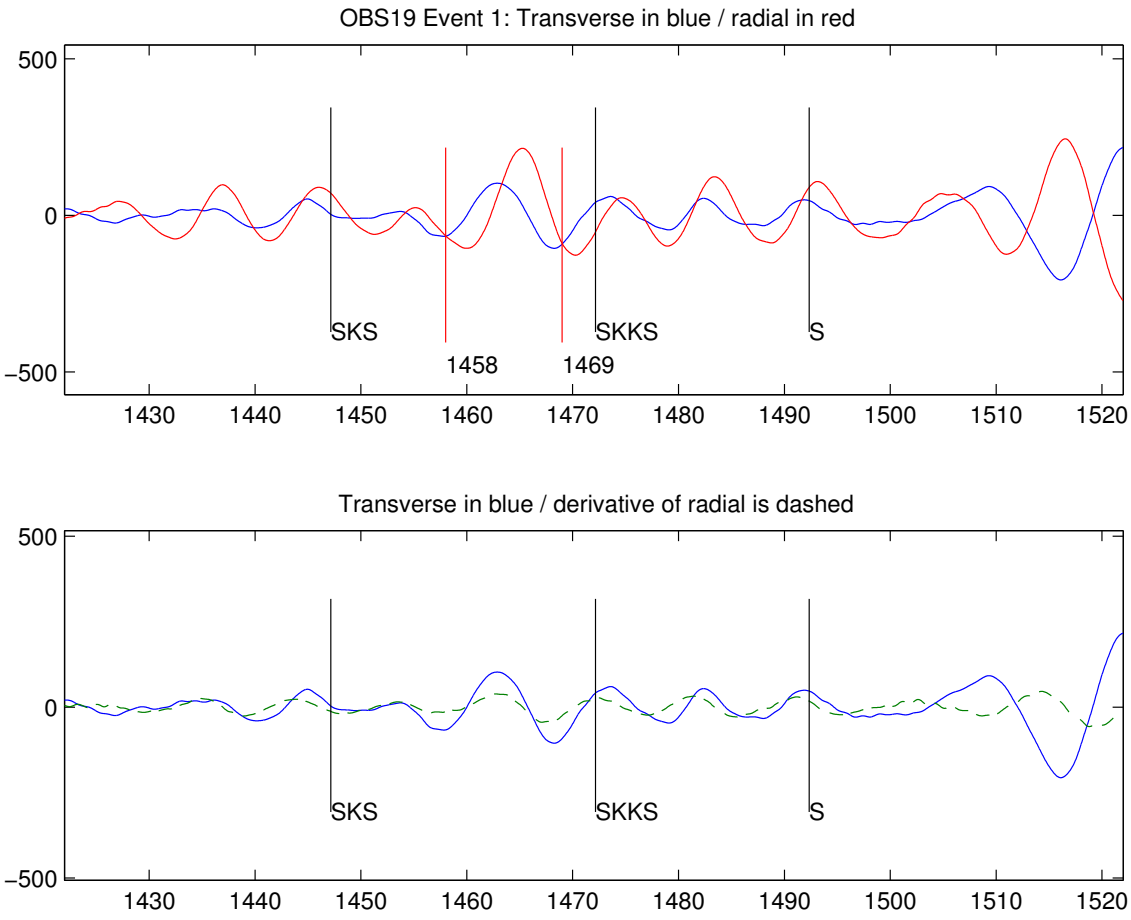

Figure 98: OBS19 Time Window

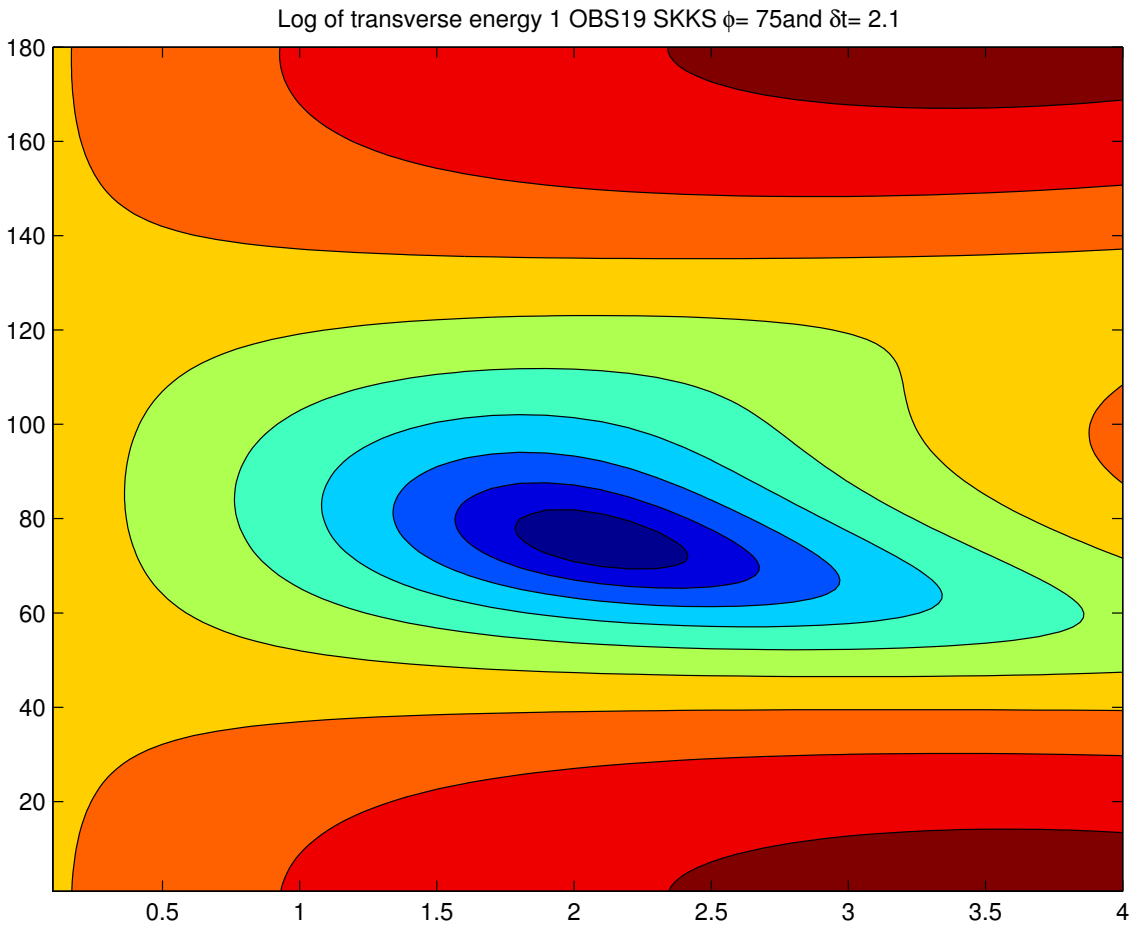

Figure 99: OBS19 Contour

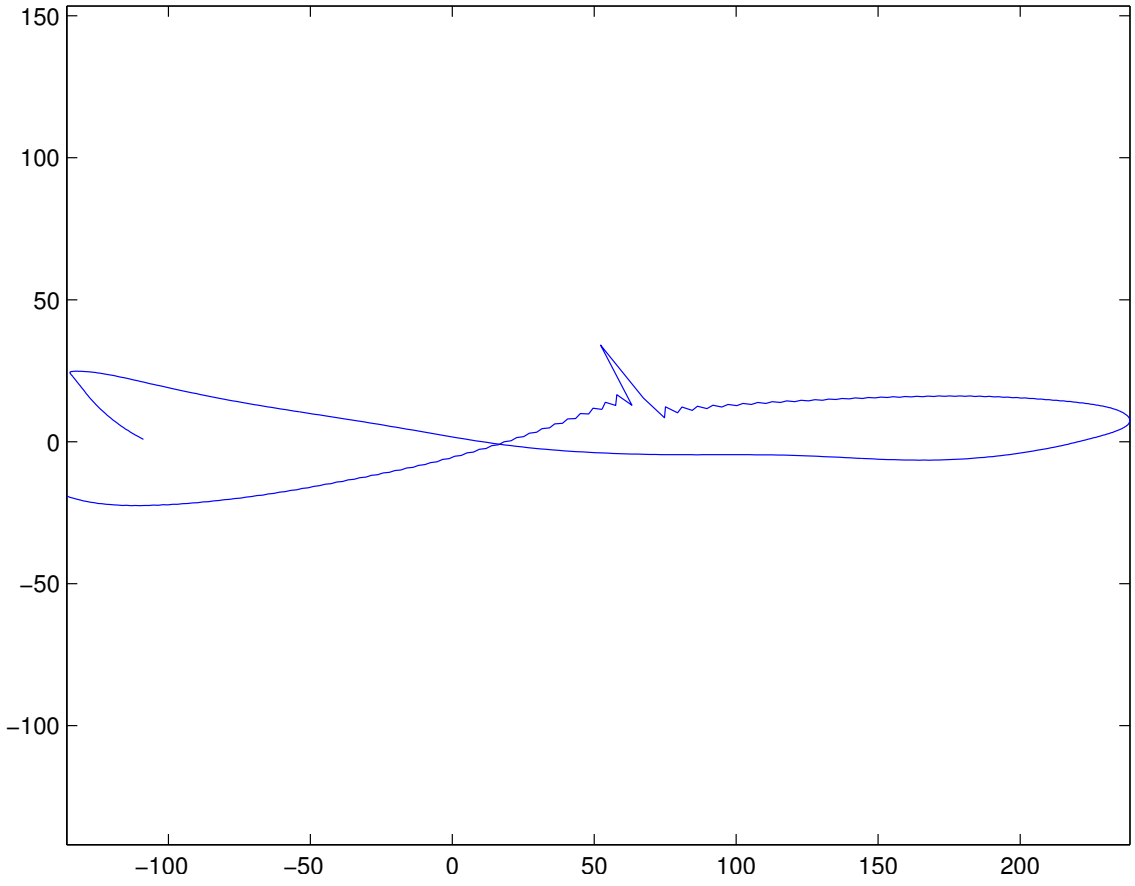

Figure 100: OBS19 Particle Motion

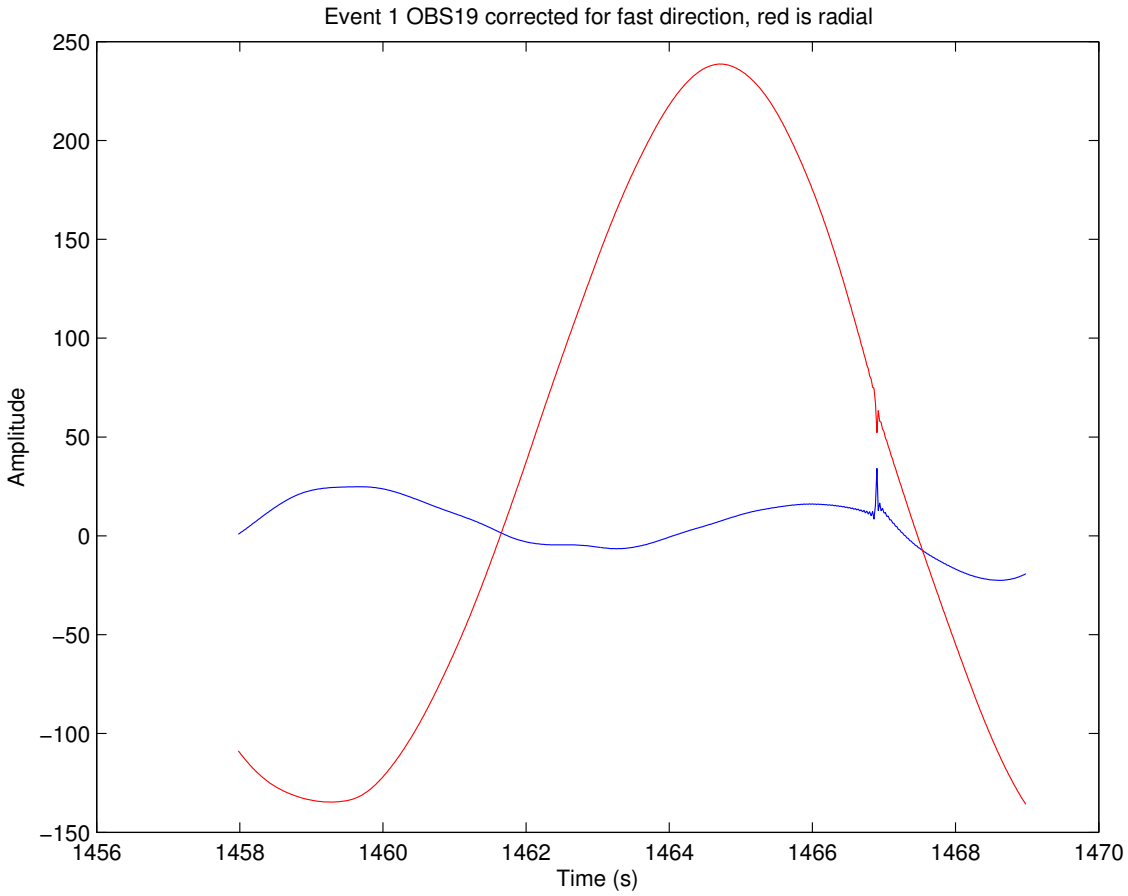

Figure 101: OBS19 Corrected

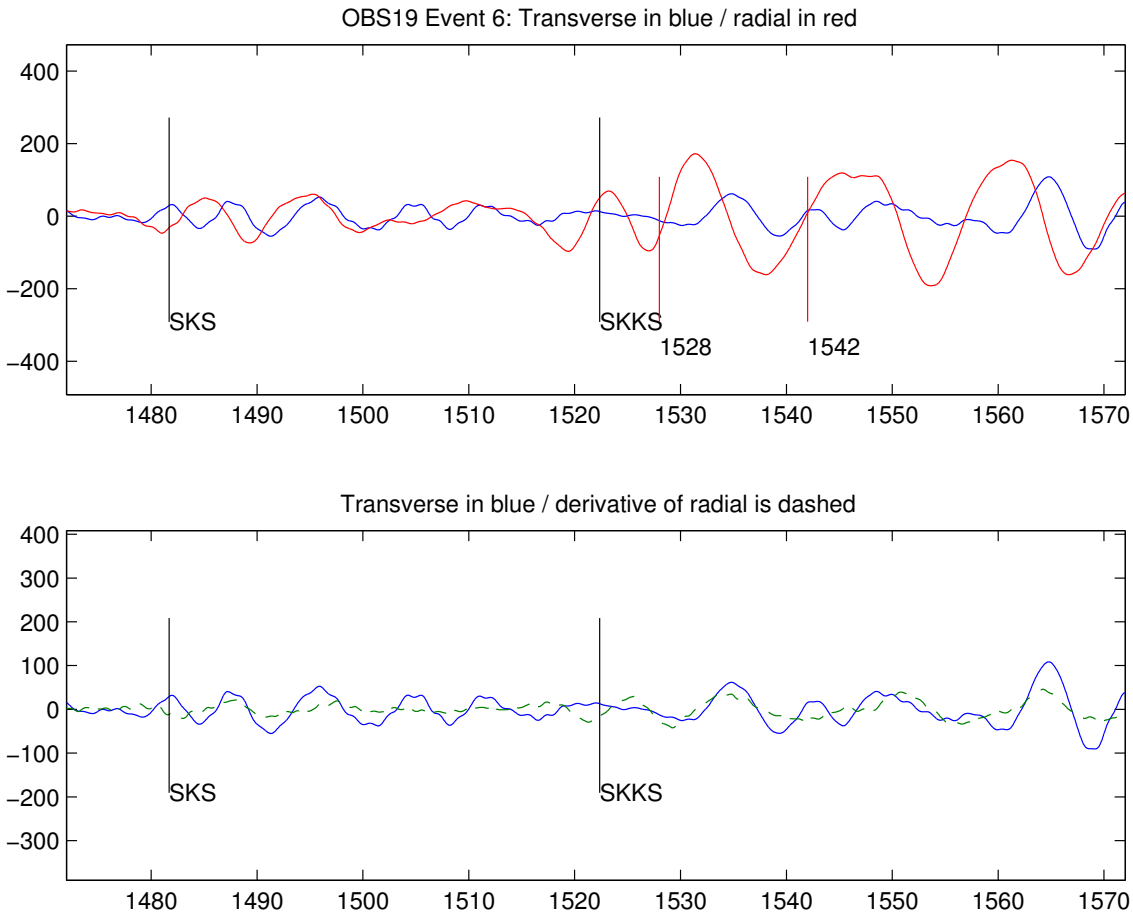

Figure 102: OBS19 Time Window

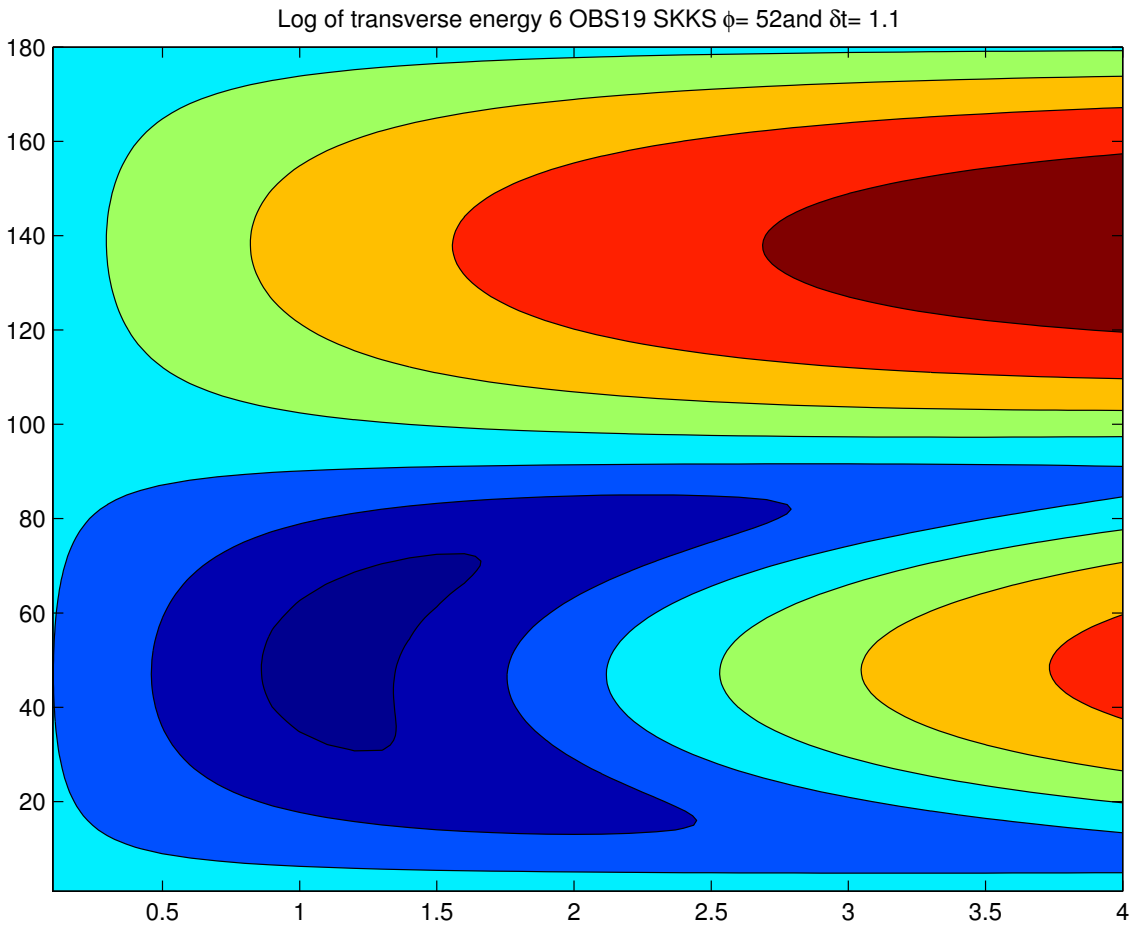

Figure 103: OBS19 Contour

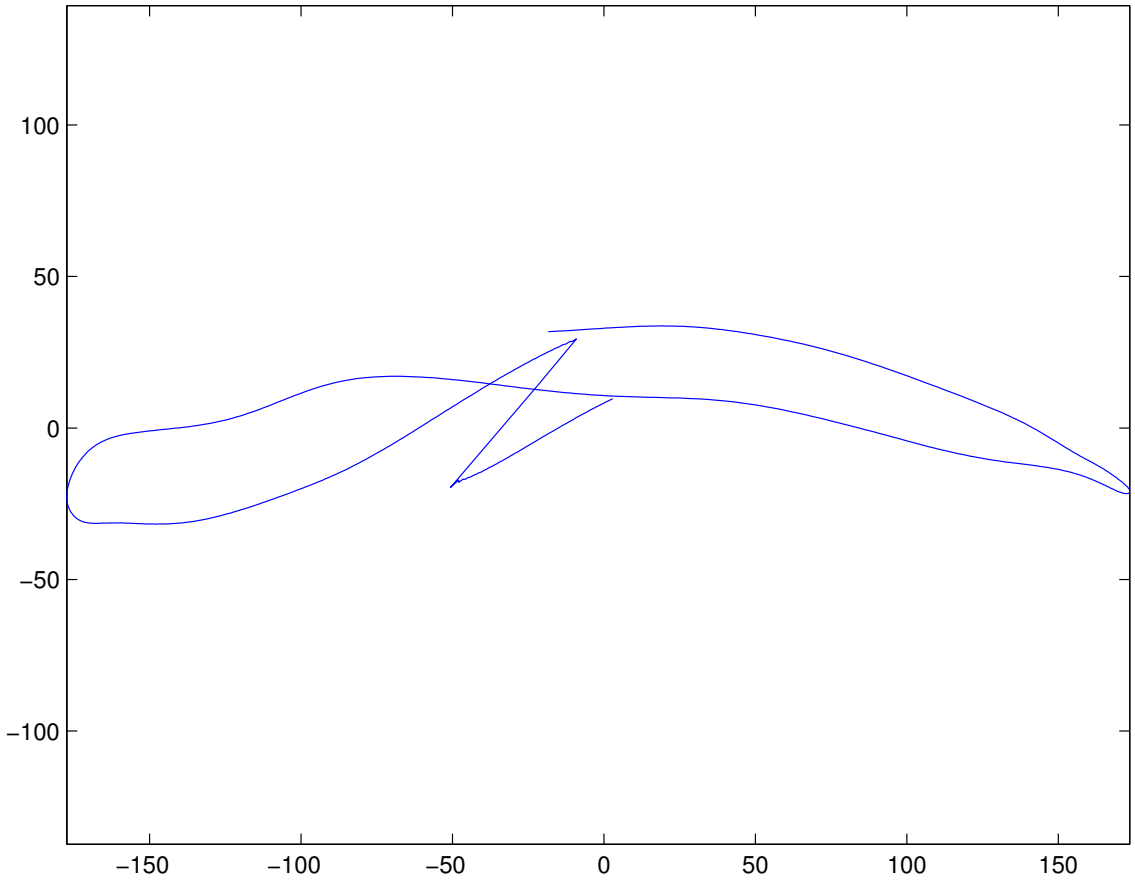

Figure 104: OBS19 Particle Motion

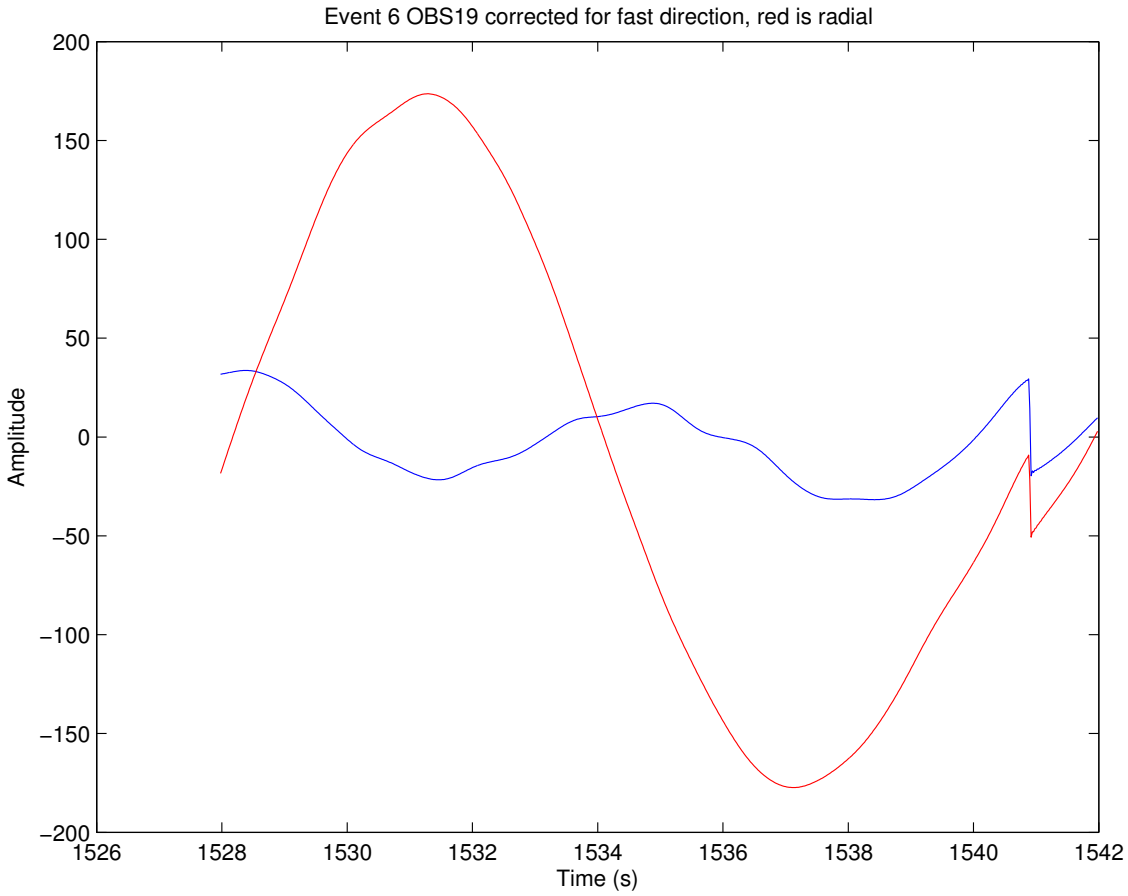

Figure 105: OBS19 Corrected

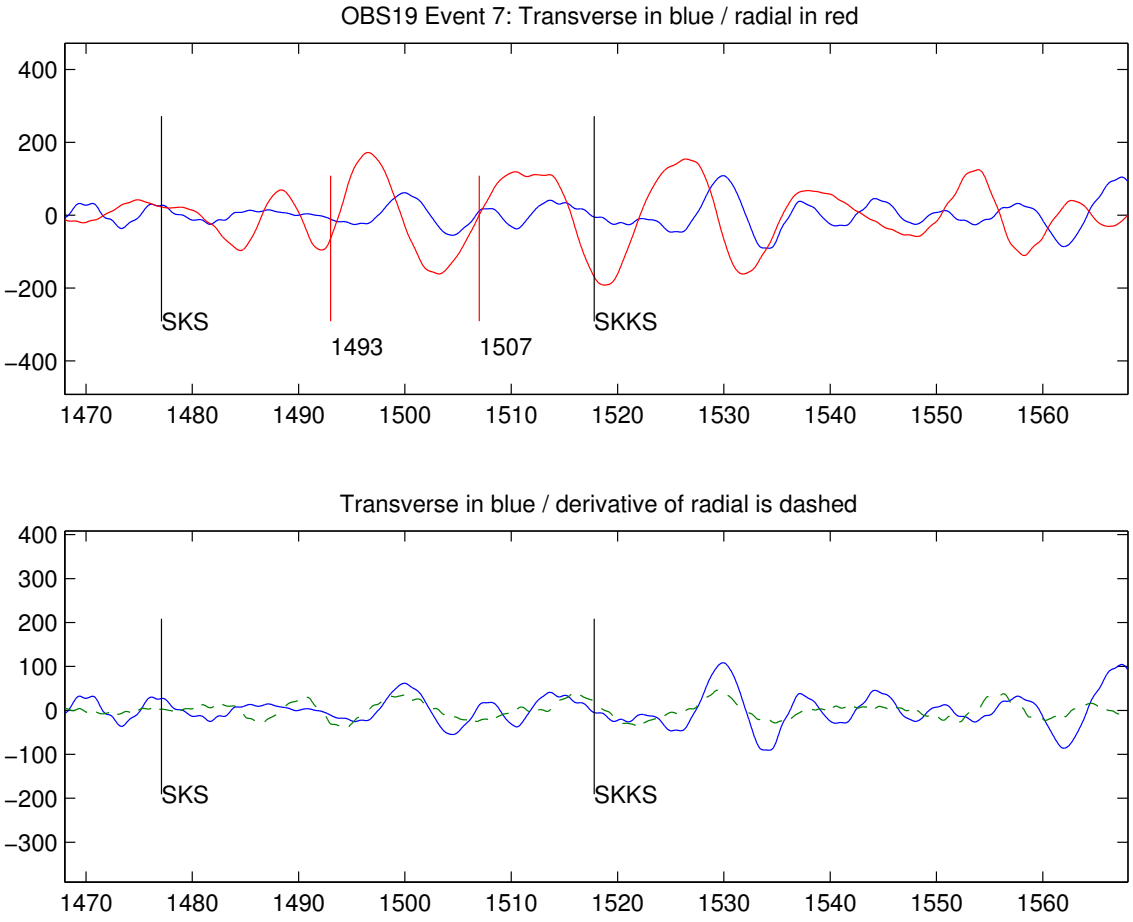

Figure 106: OBS19 Time Window

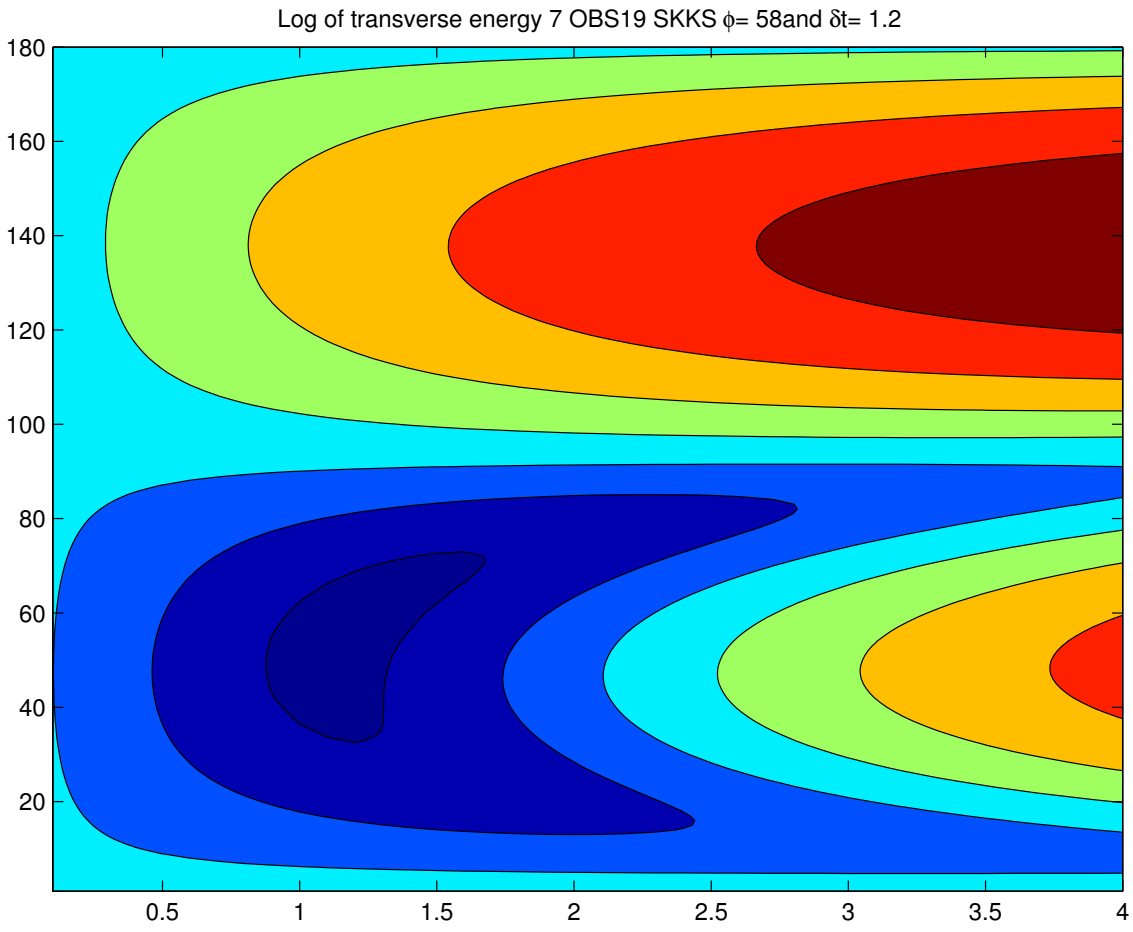

Figure 107: OBS19 Contour

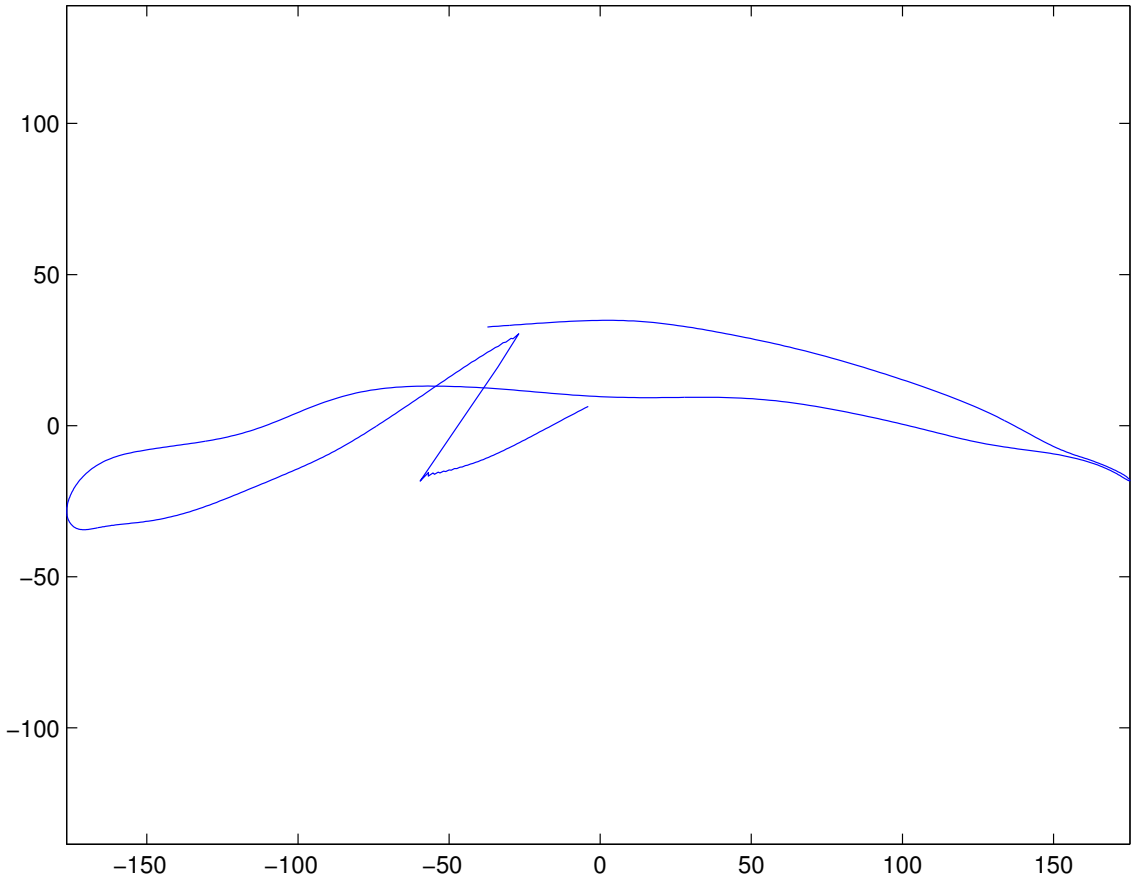

Figure 108: OBS19 Particle Motion

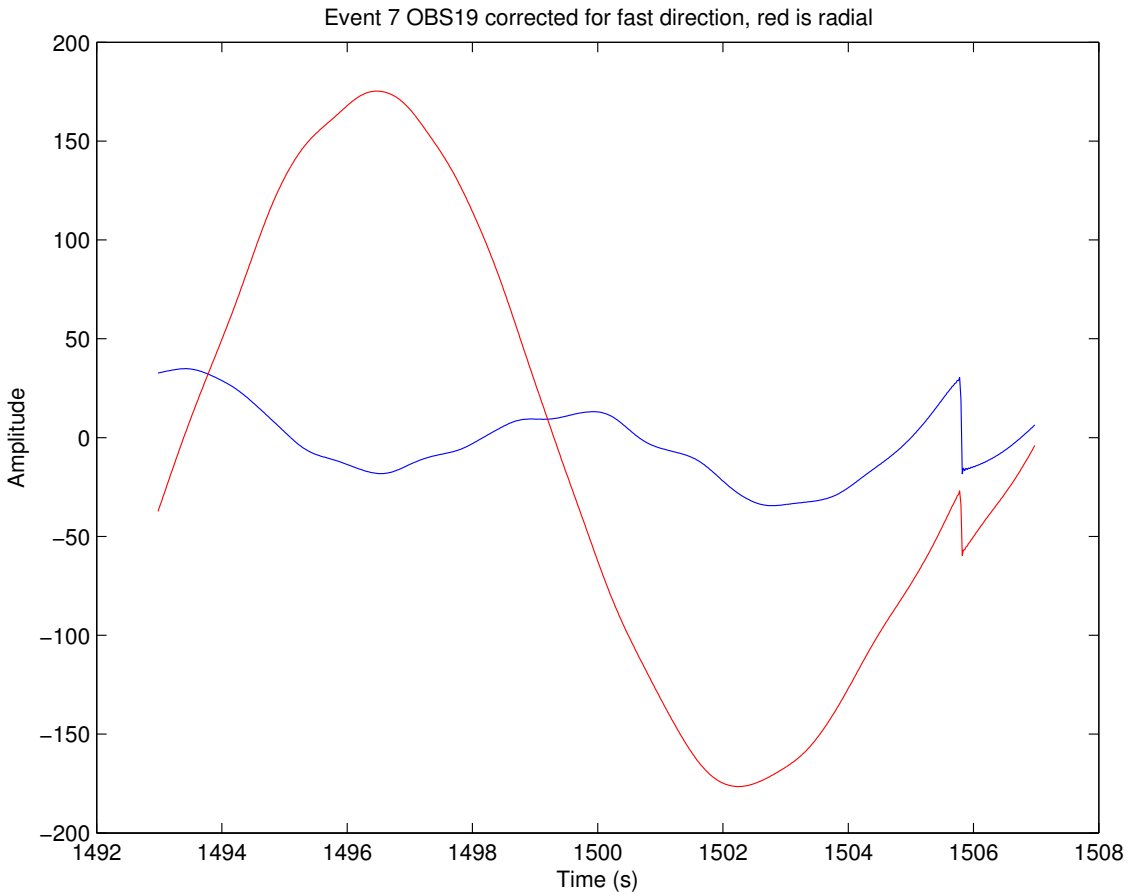

Figure 109: OBS19 Corrected

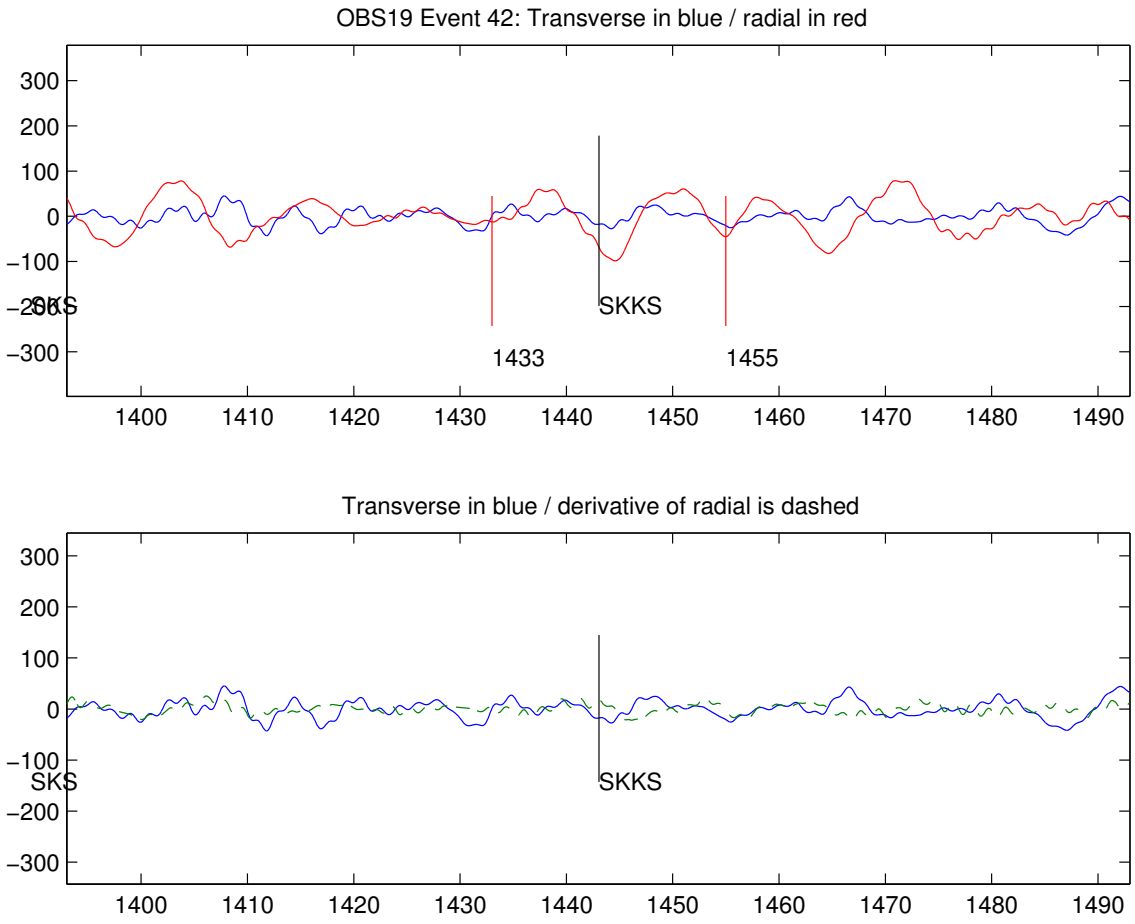

Figure 110: OBS19 Time Window

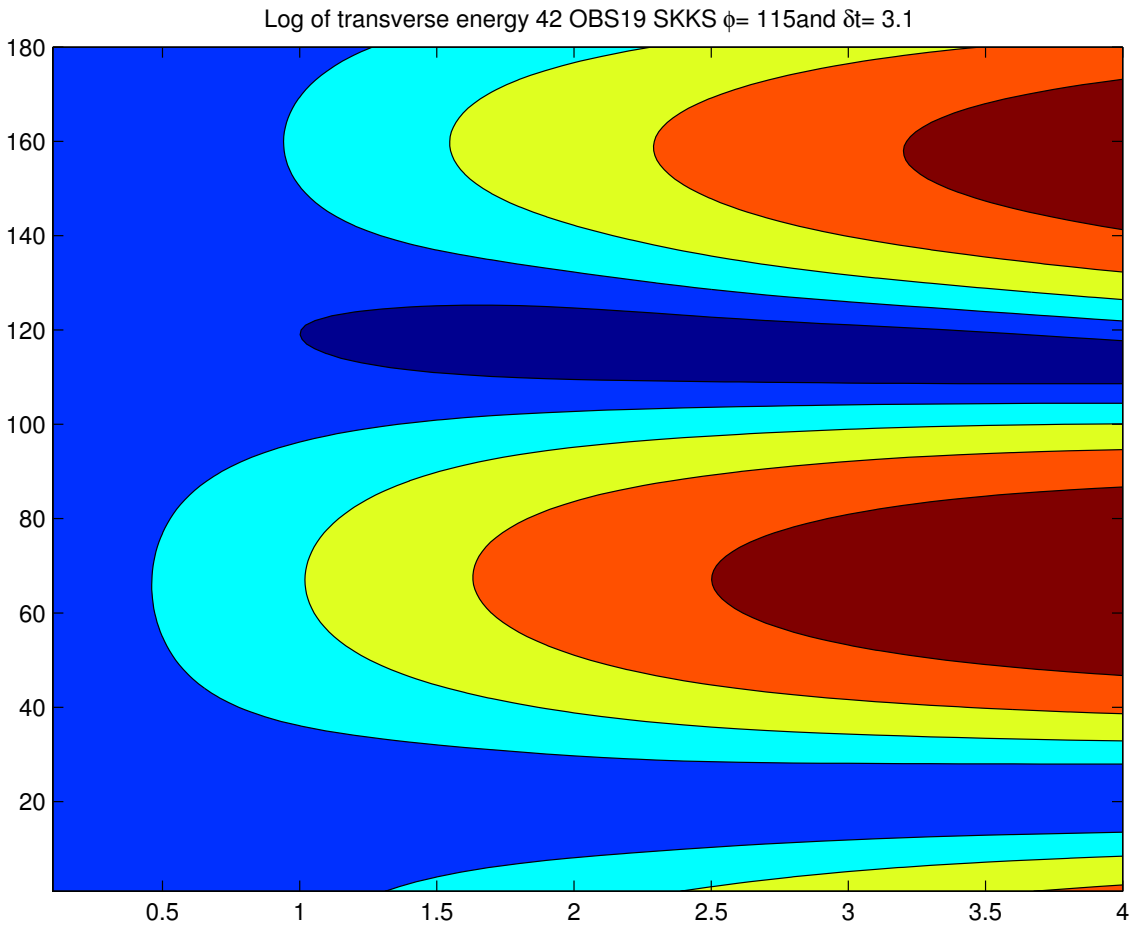

Figure 111: OBS19 Contour

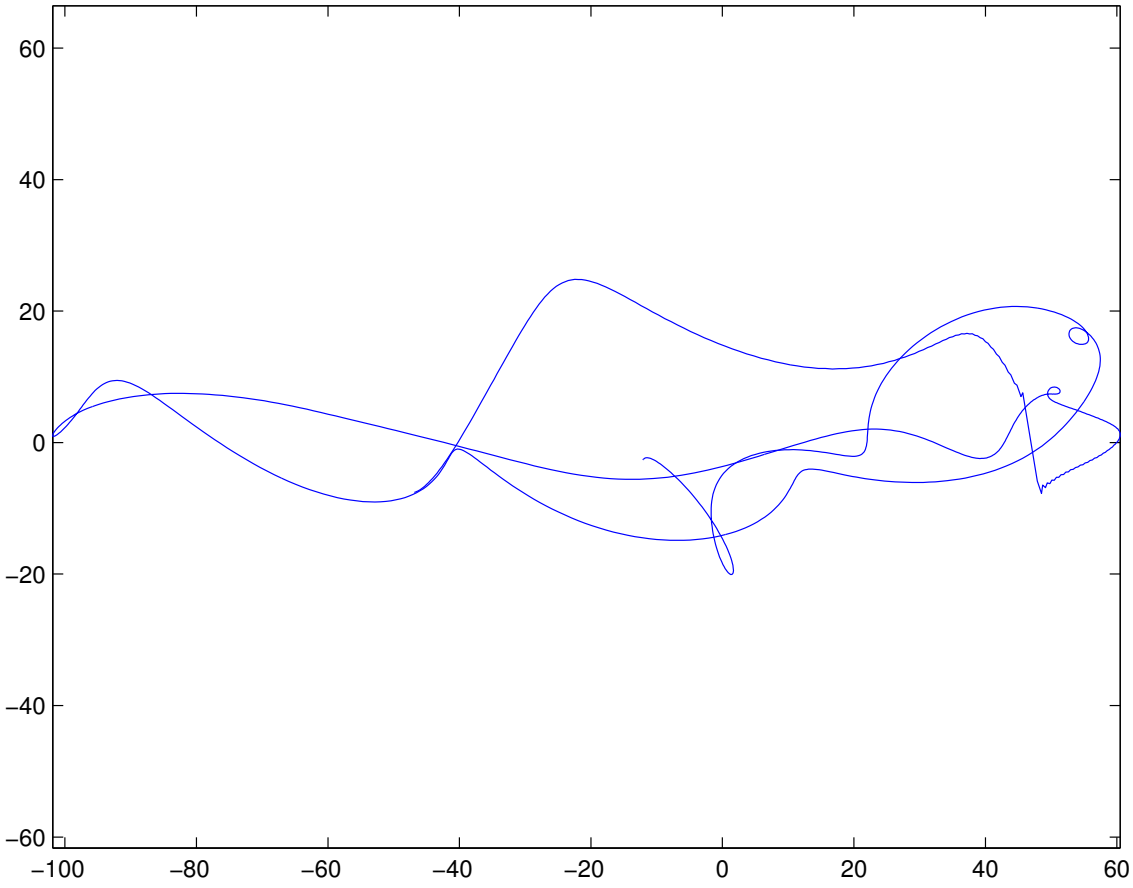

Figure 112: OBS19 Particle Motion

Figure 113: OBS19 Corrected

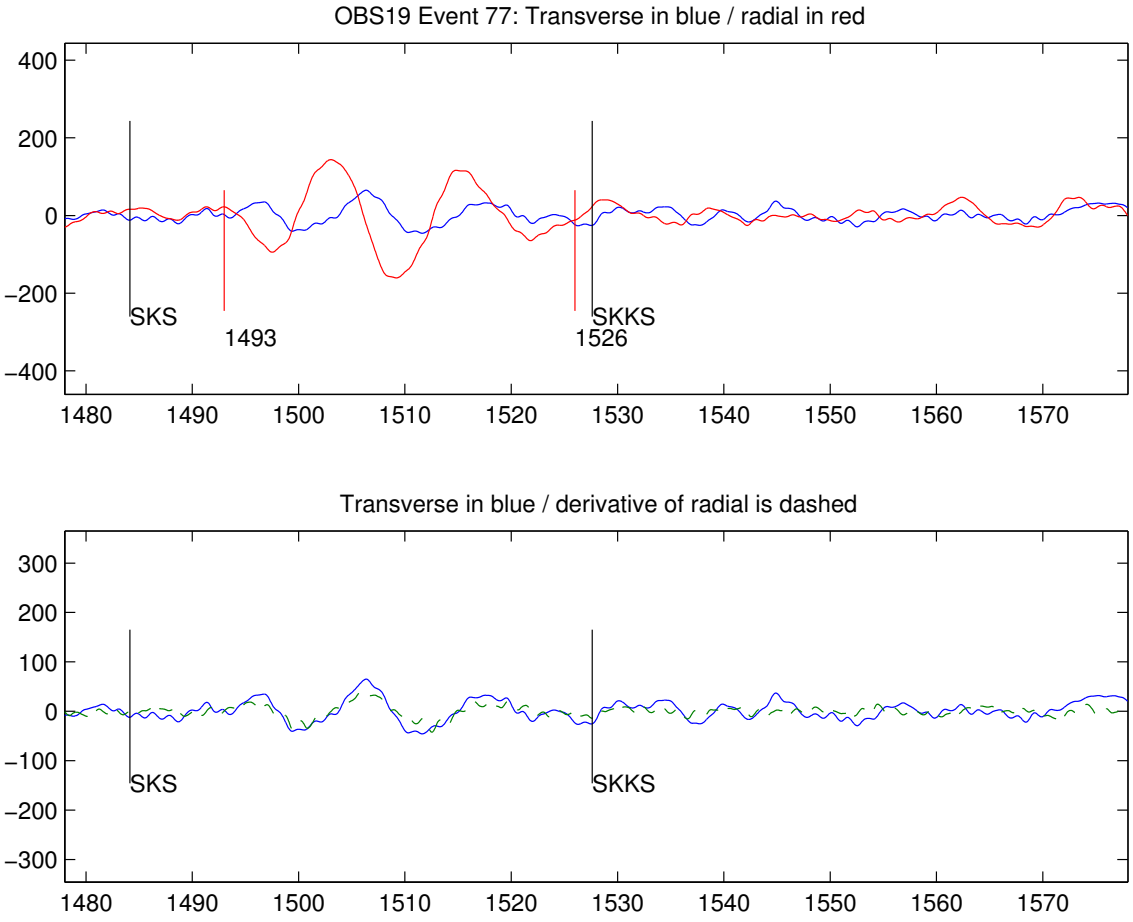

Figure 114: OBS19 Time Window

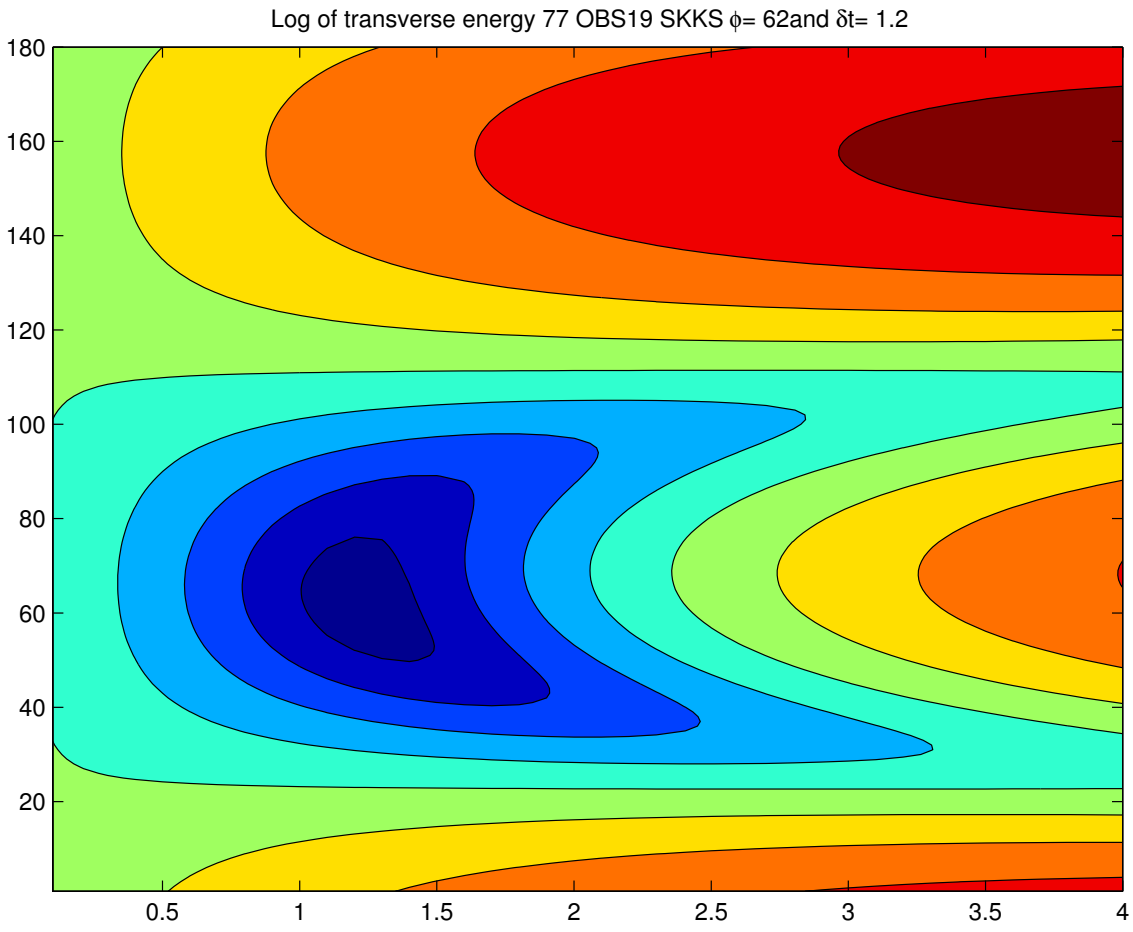

Figure 115: OBS19 Contour

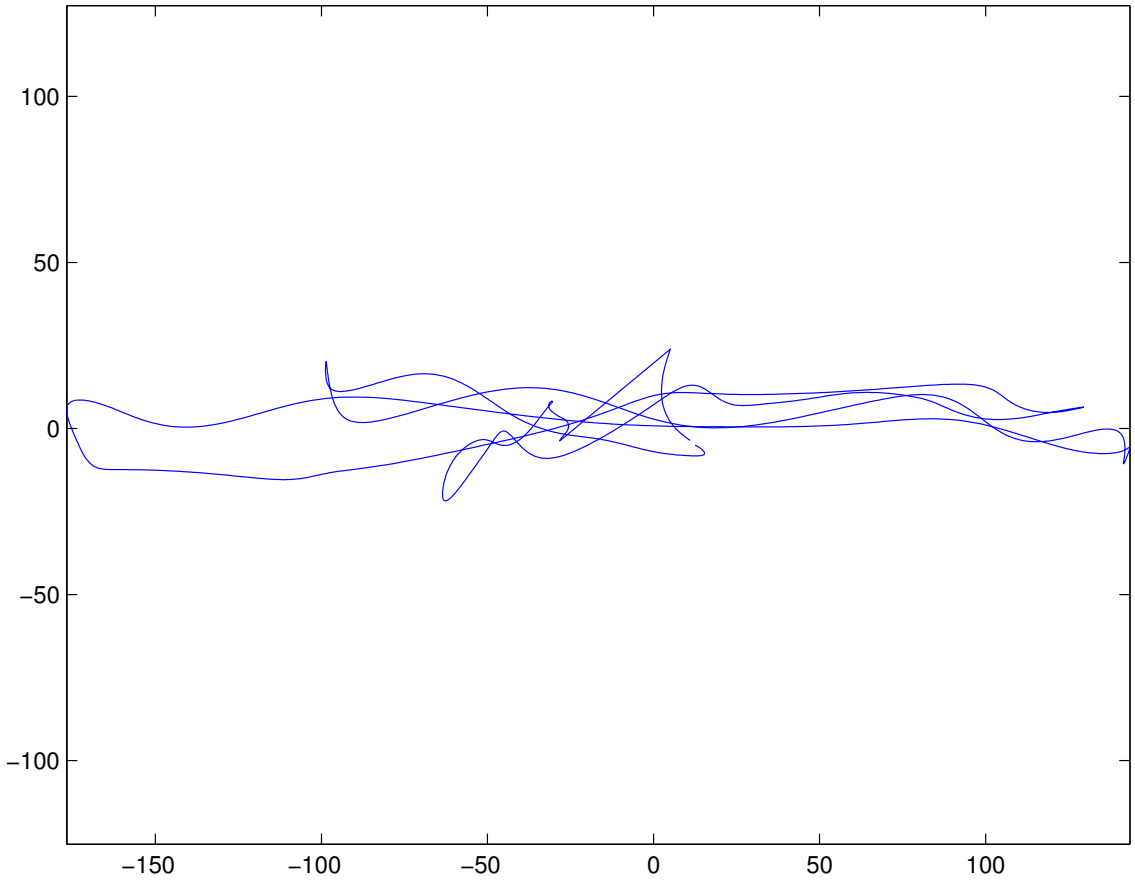

Figure 116: OBS19 Particle Motion

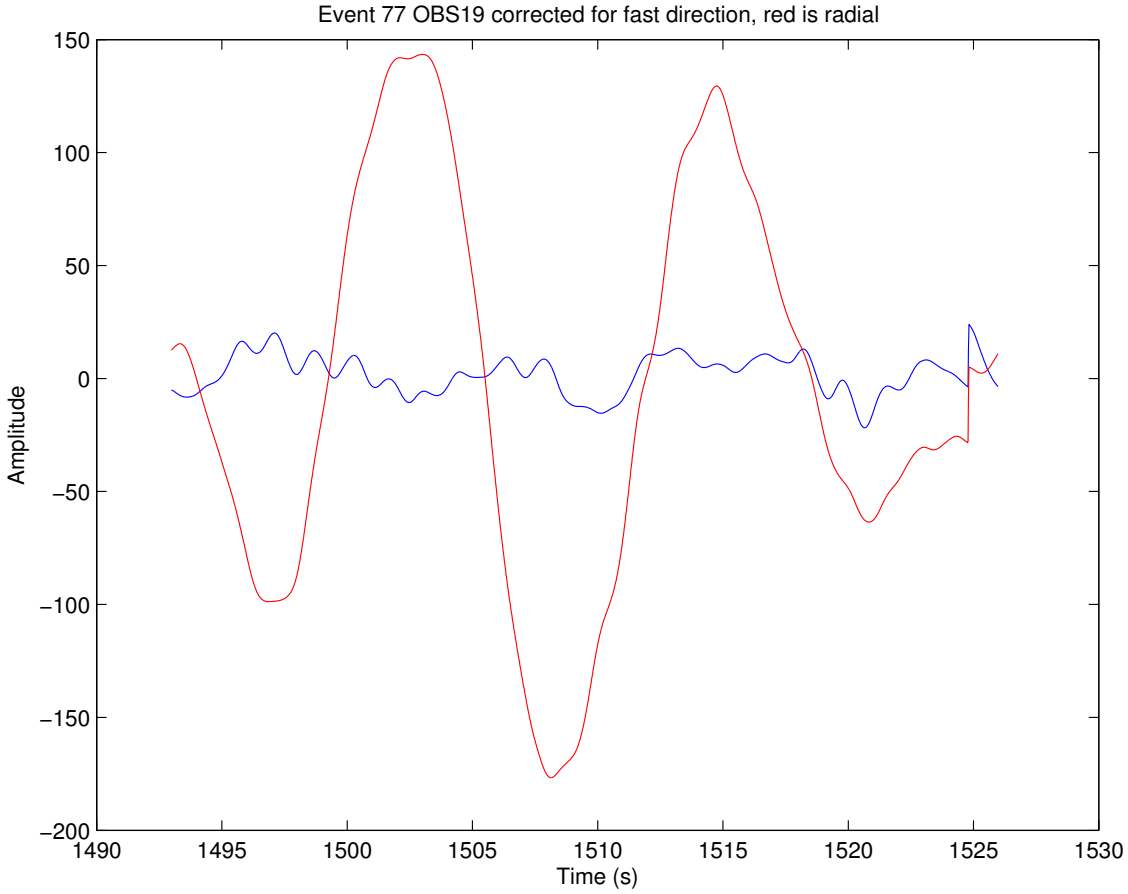

Figure 117: OBS19 Corrected

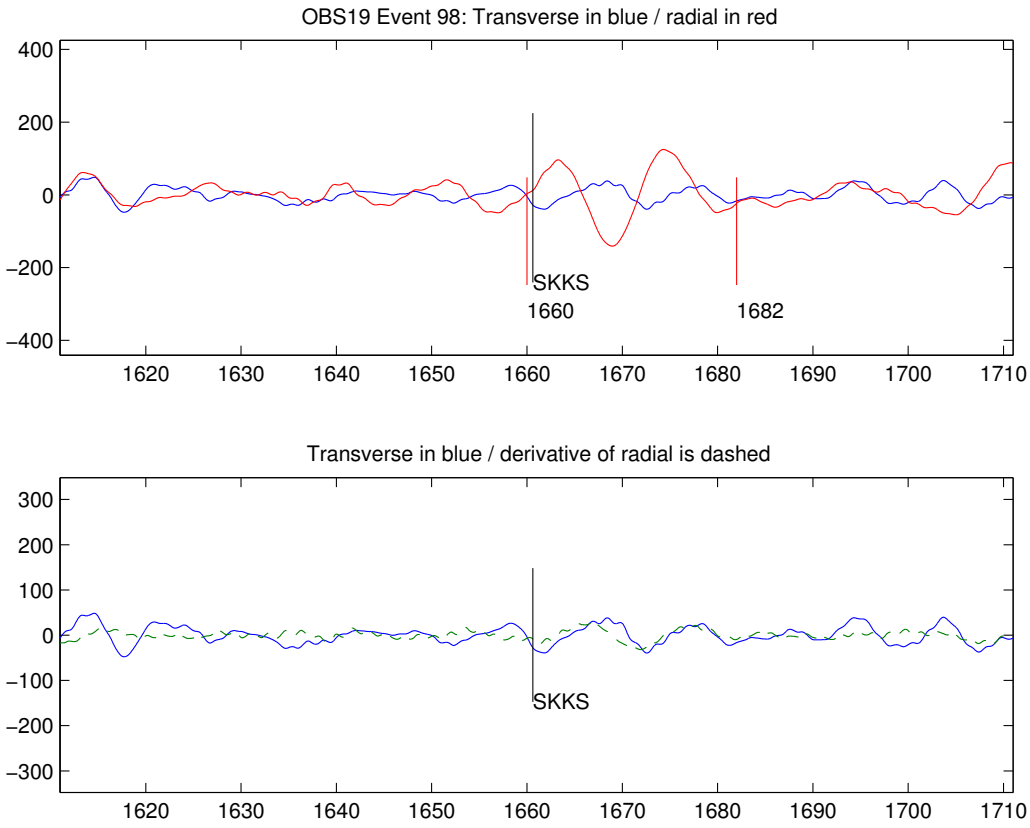

Figure 118: OBS19 Time Window

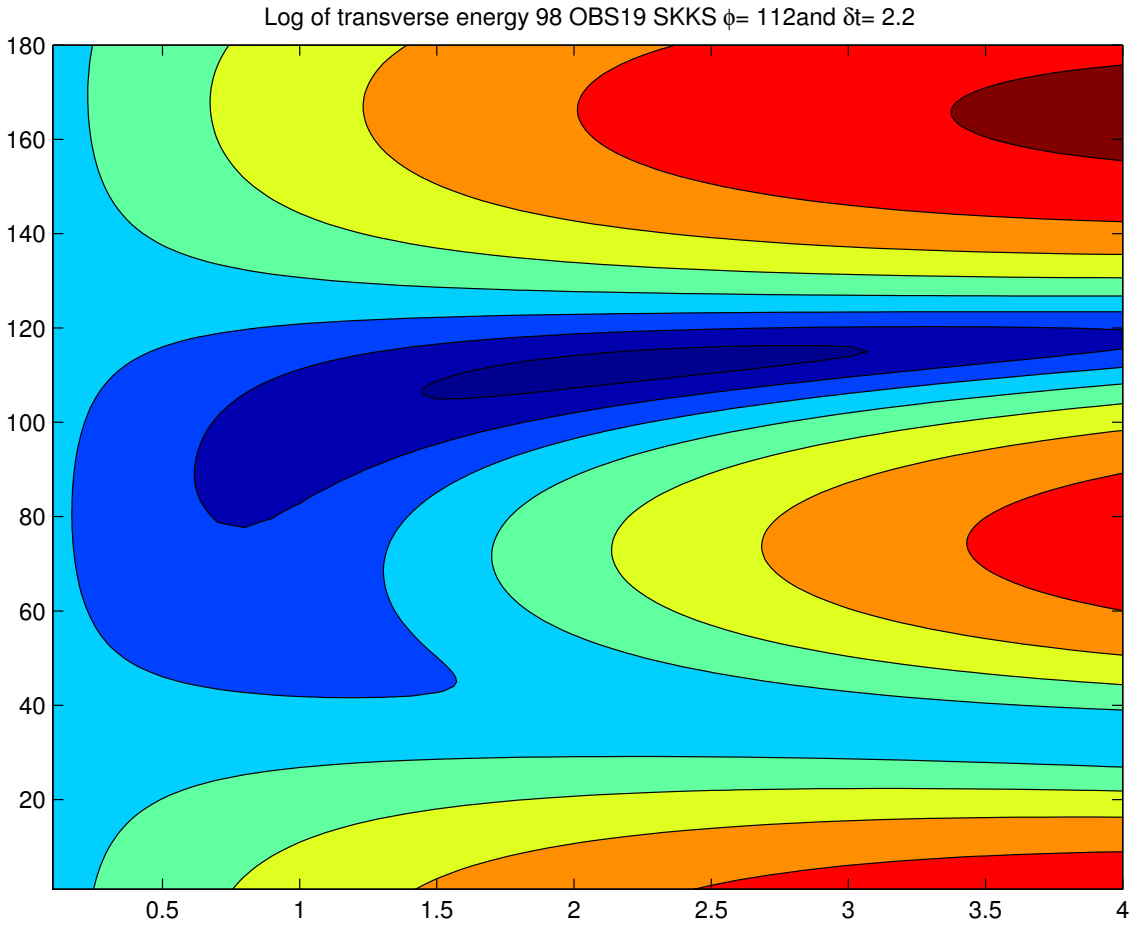

Figure 119: OBS19 Contour

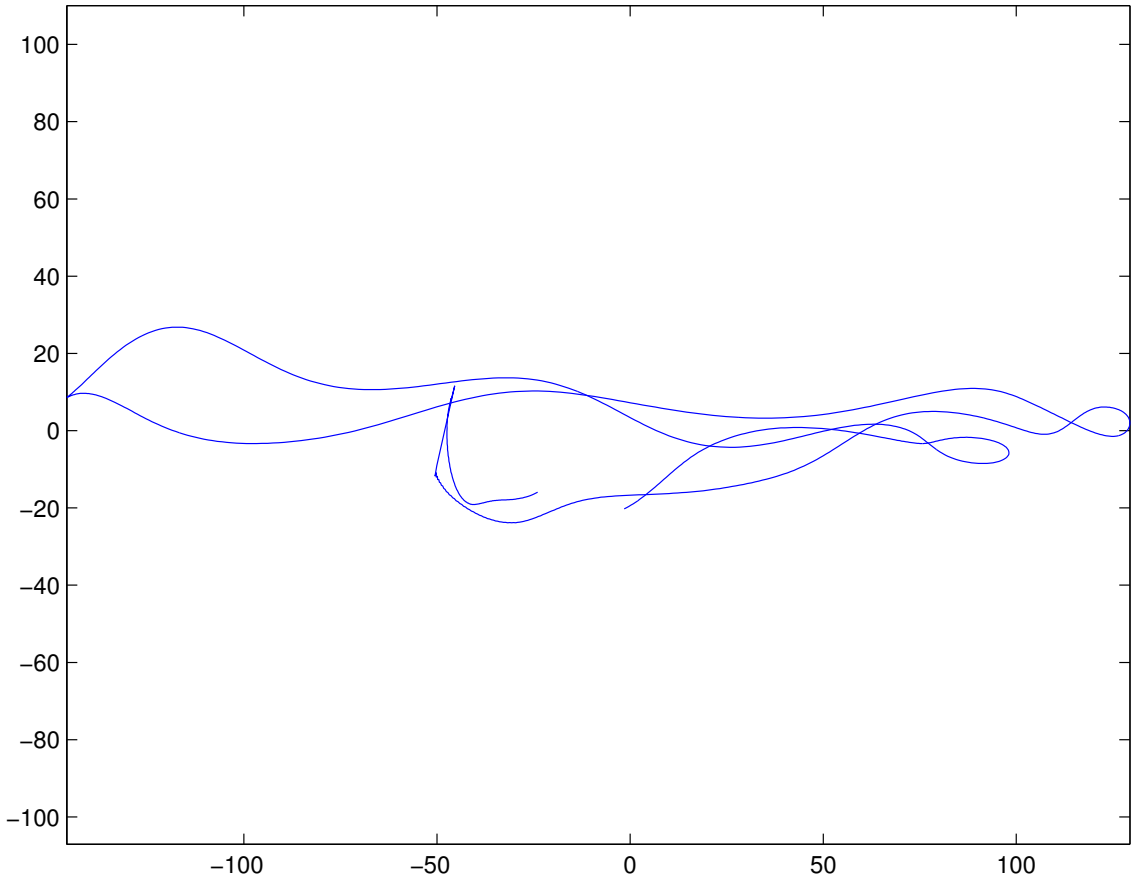

Figure 120: OBS19 Particle Motion

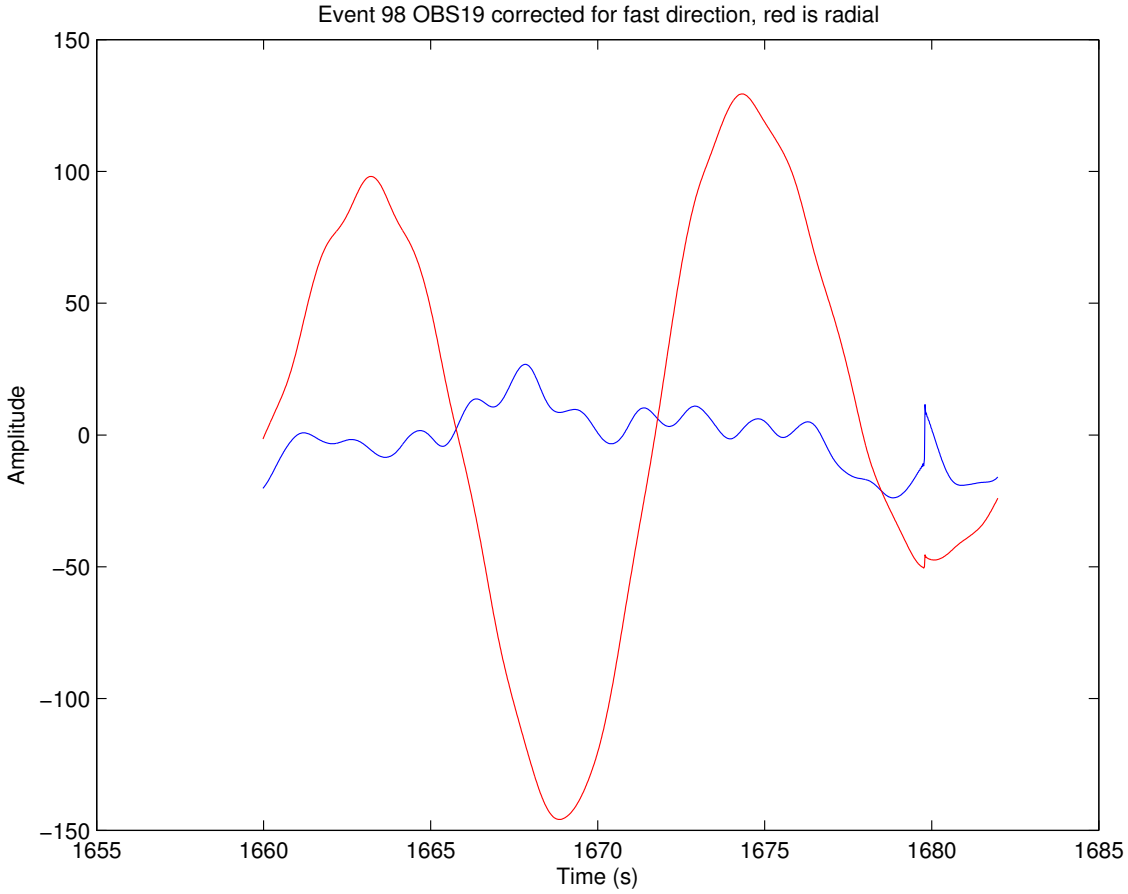

Figure 121: OBS19 Corrected

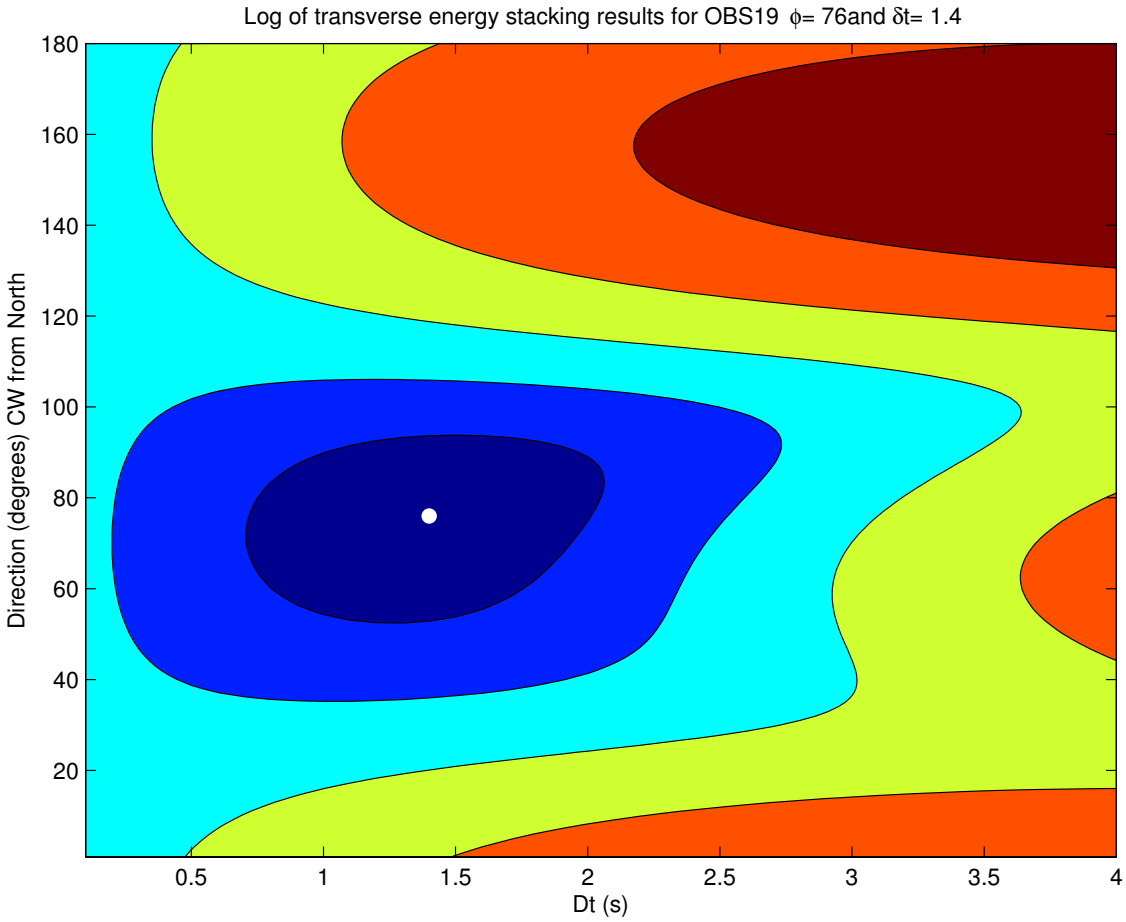

Figure 122: OBS19 Stacked Transverse Energy

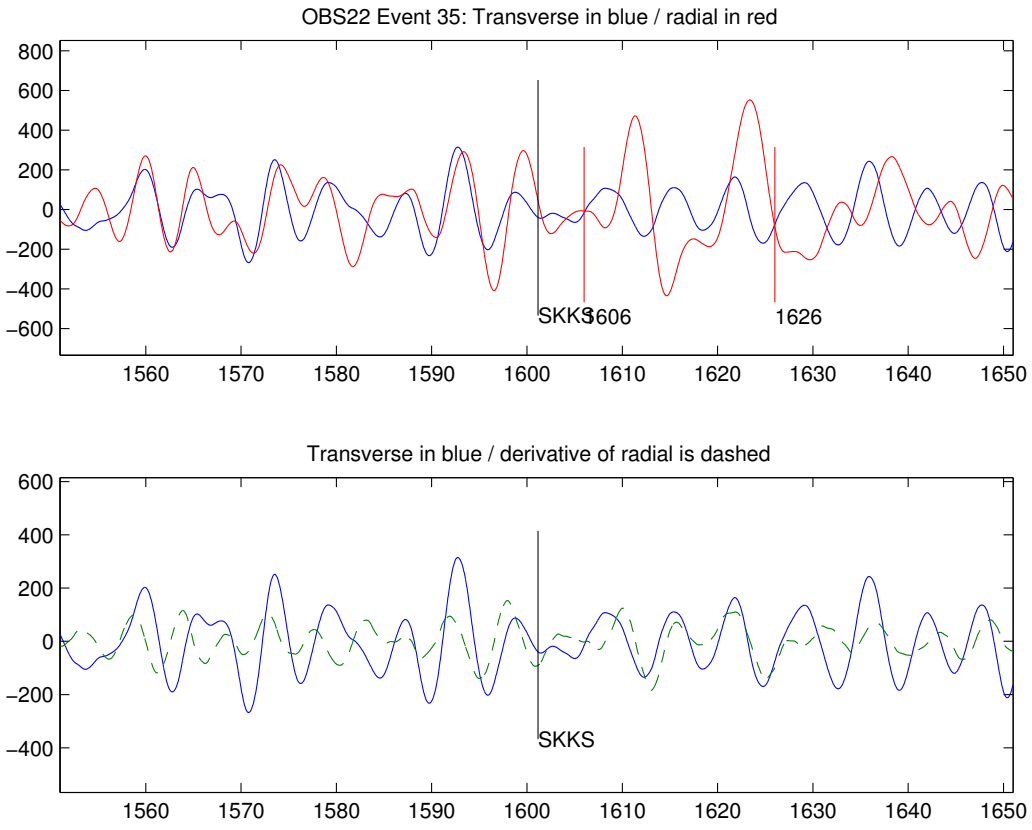

Figure 123: OBS22 Time Window

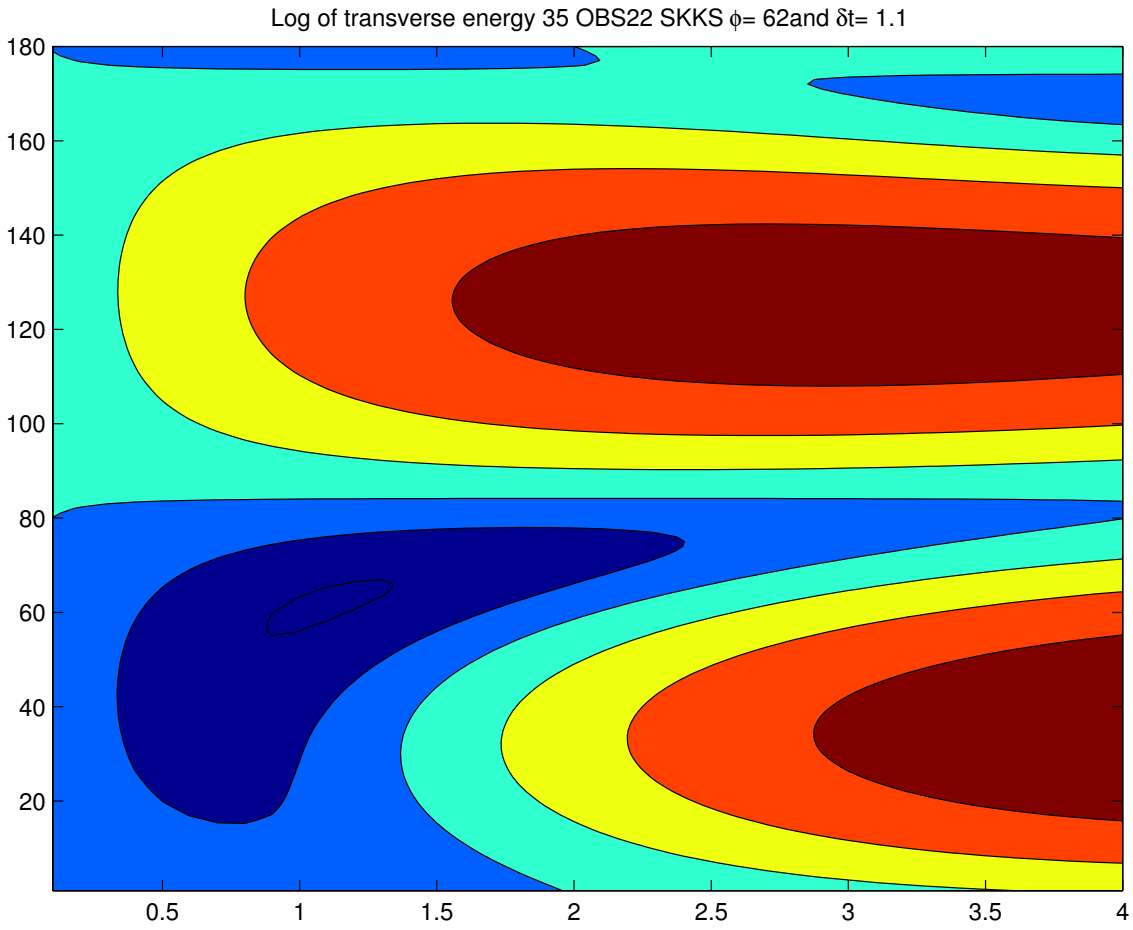

Figure 124: OBS22 Contour

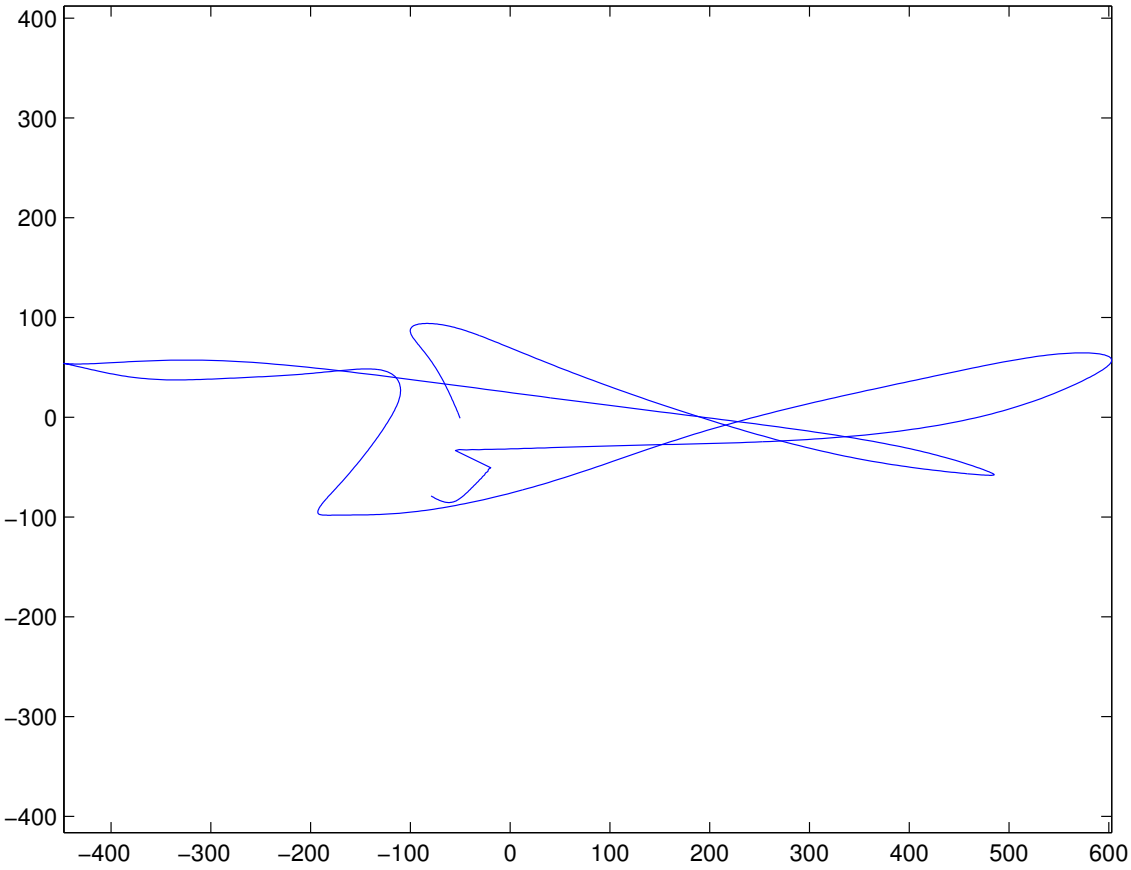

Figure 125: OBS22 Particle Motion

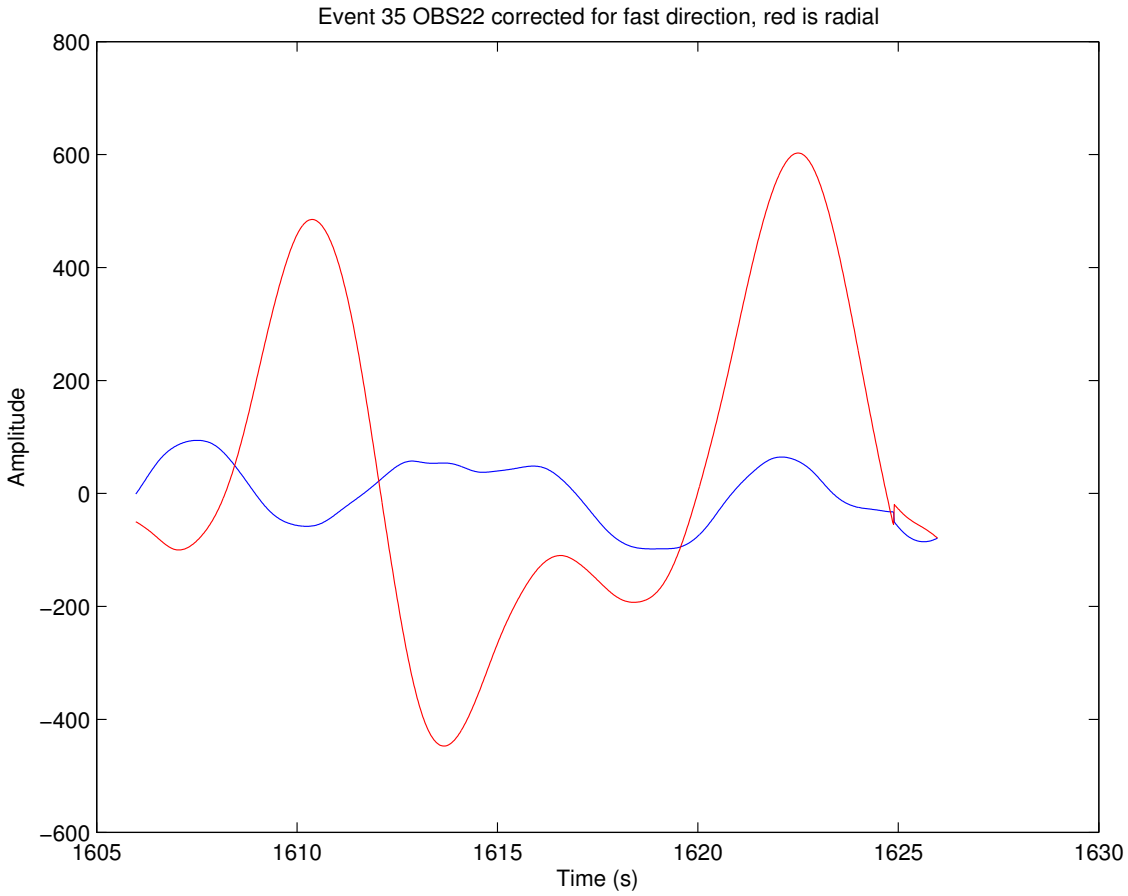

Figure 126: OBS22 Corrected

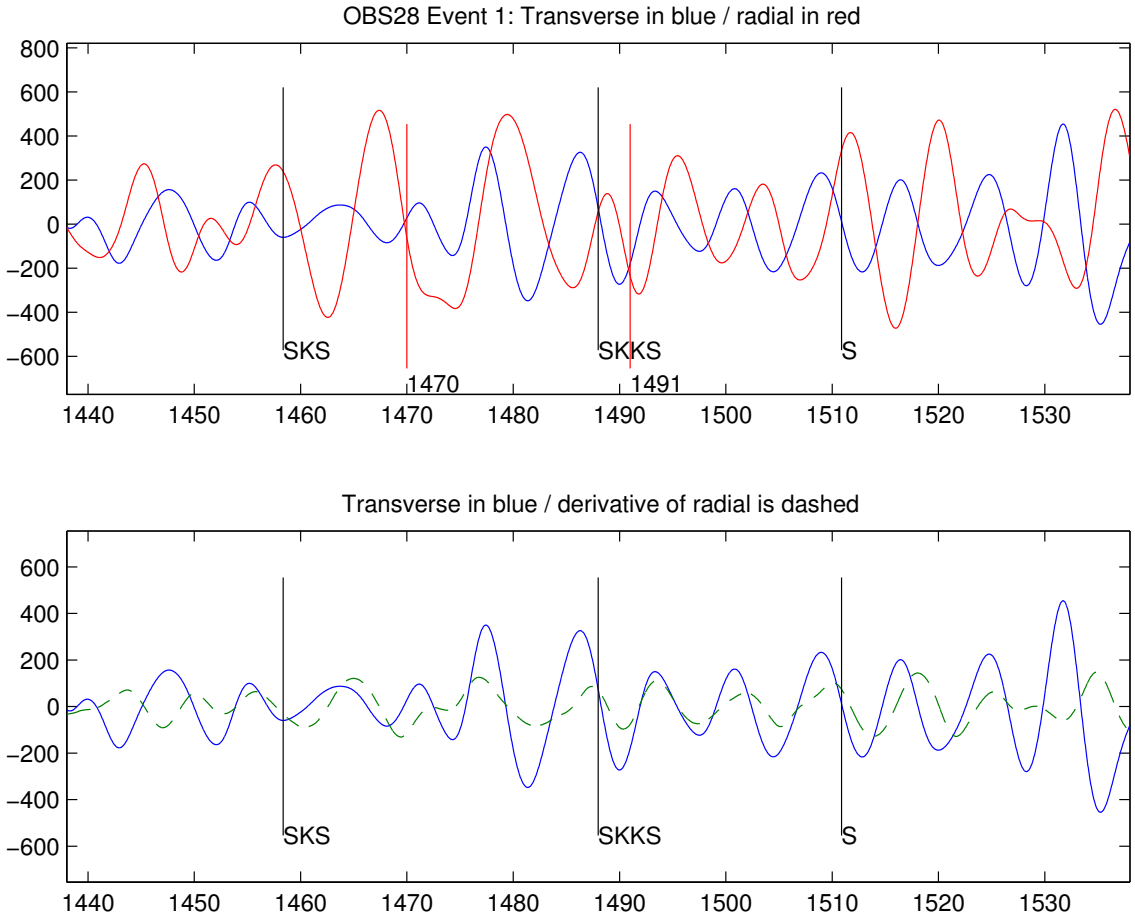

Figure 127: OBS28 Time Window

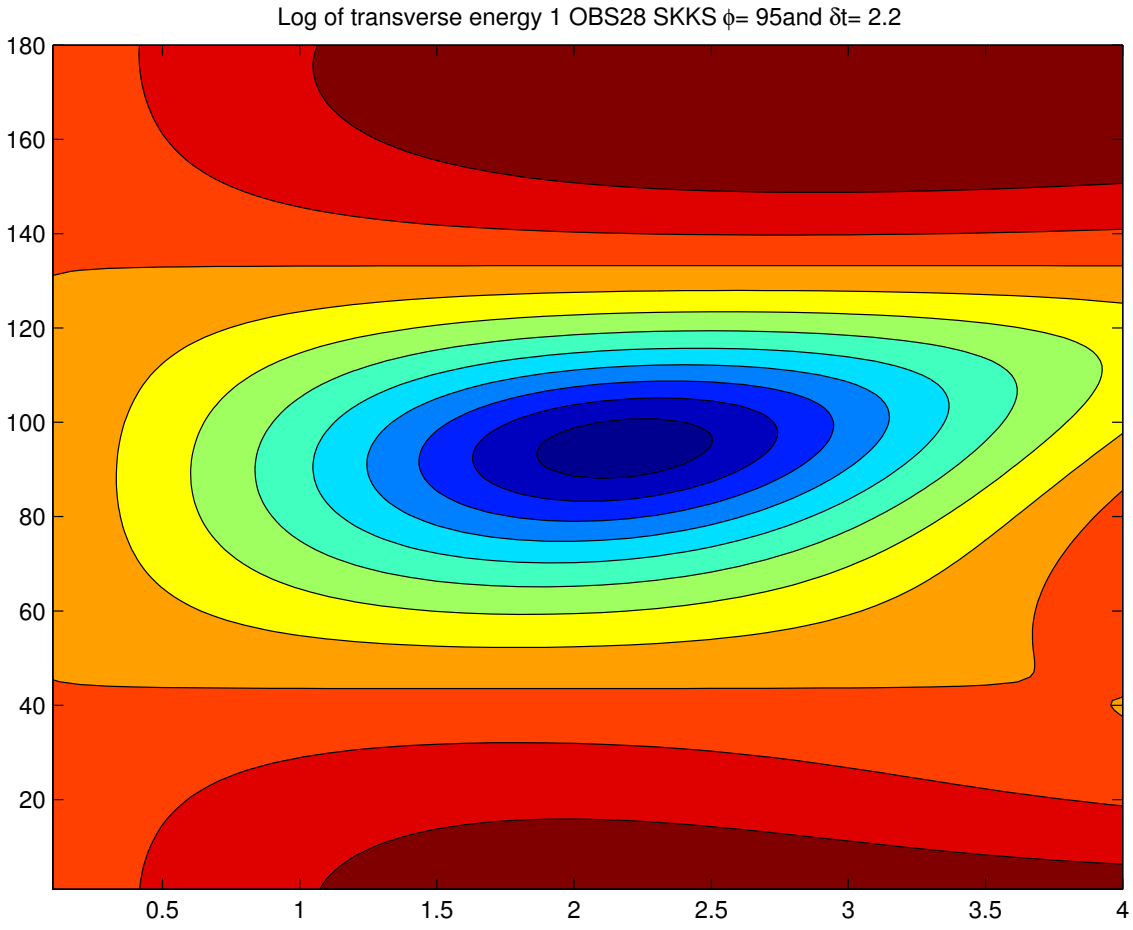

Figure 128: OBS28 Contour

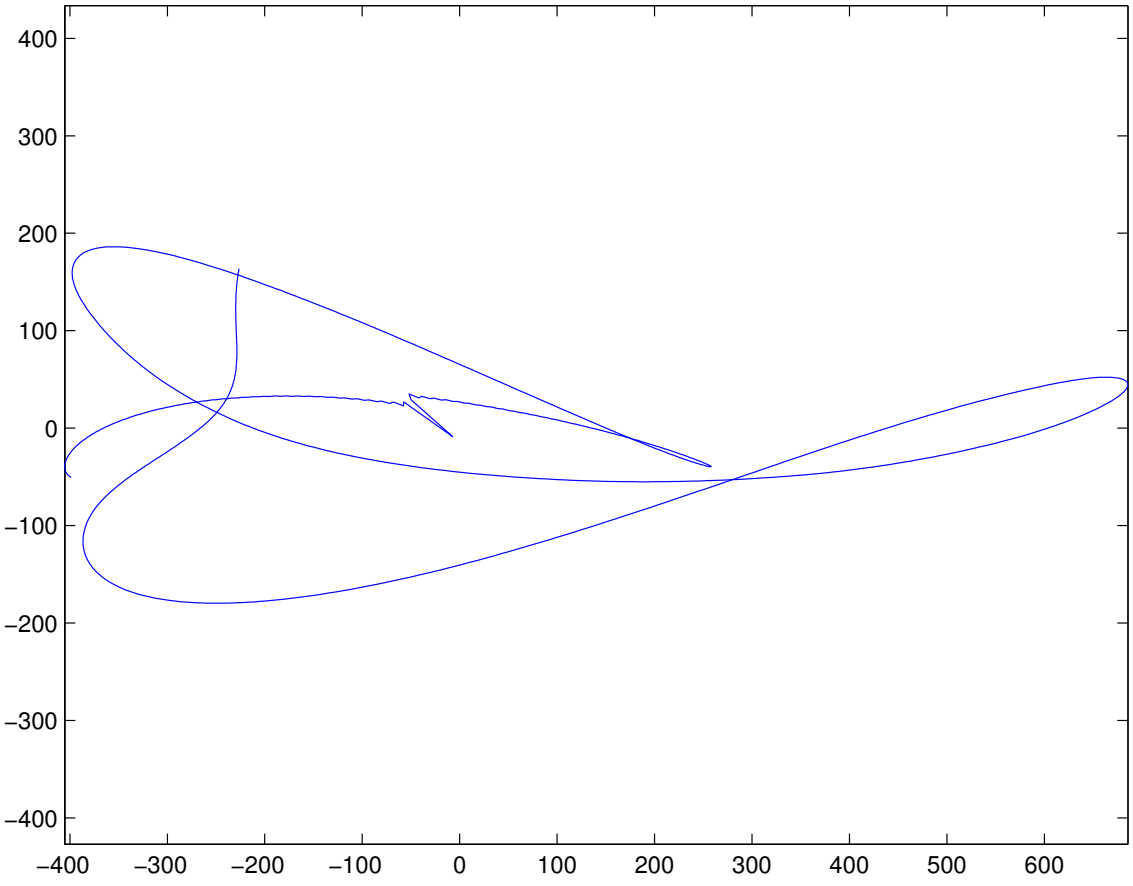

Figure 129: OBS28 Particle Motion

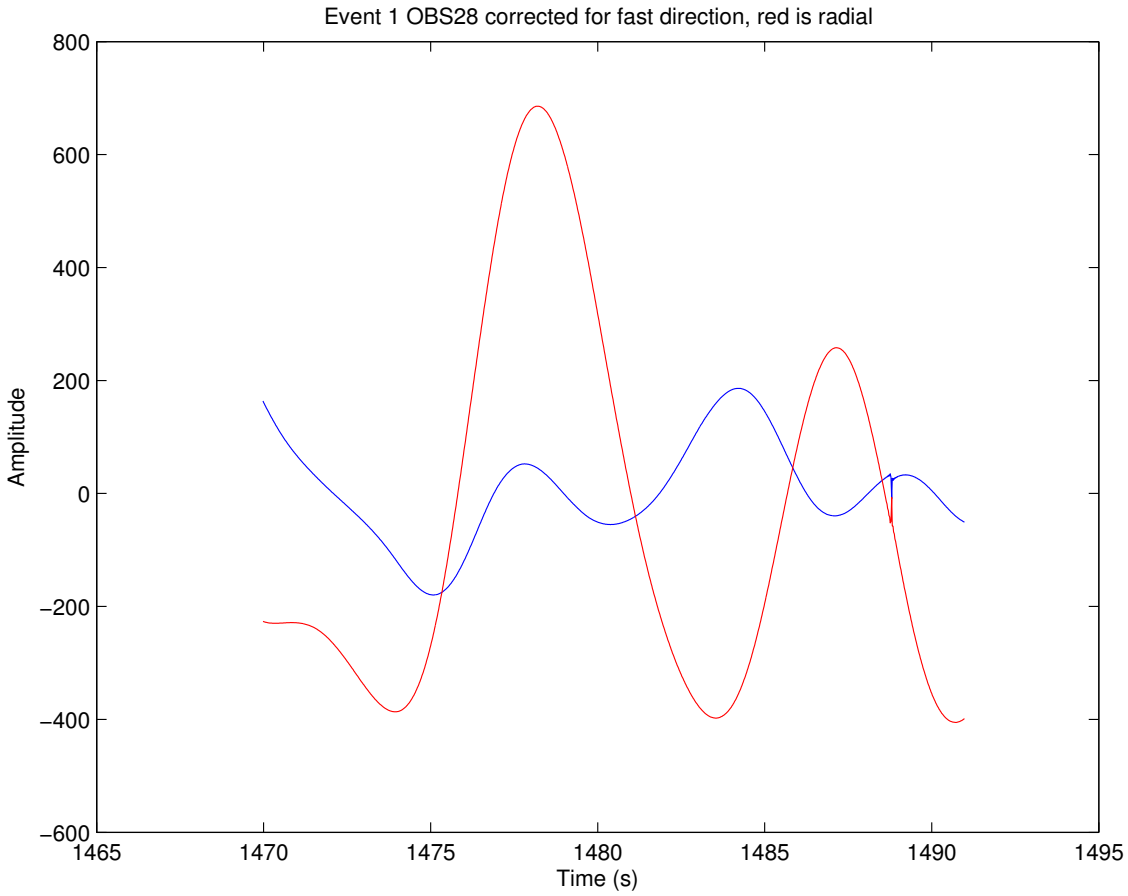

Figure 130: OBS28 Corrected

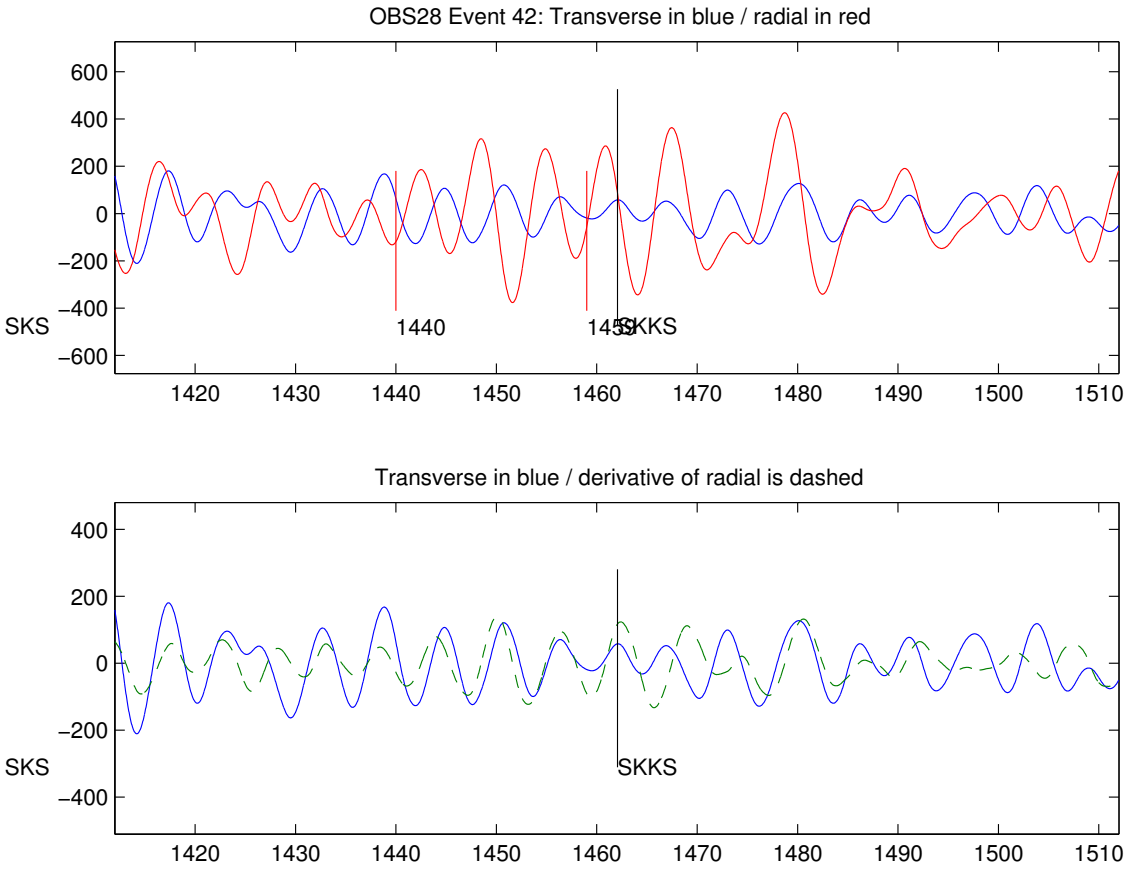

Figure 131: OBS28 Time Window

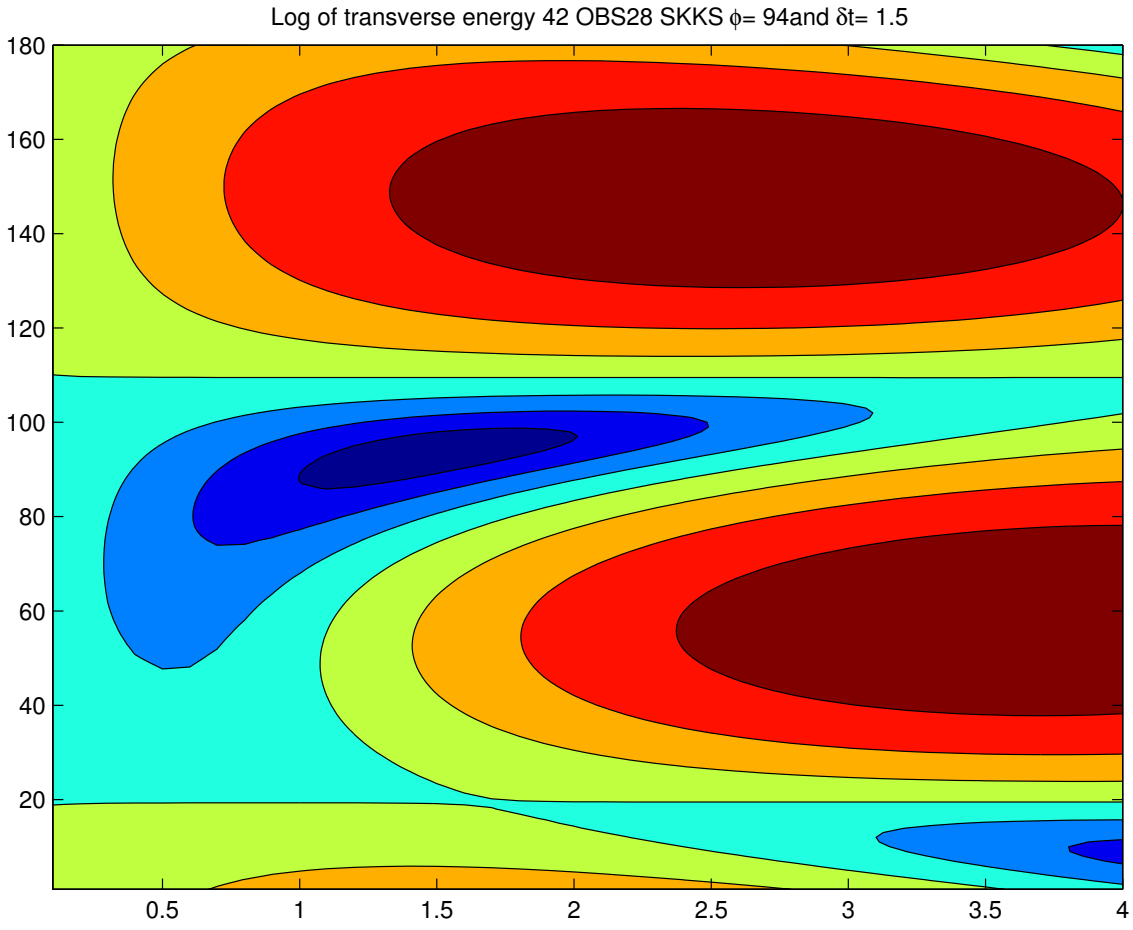

Figure 132: OBS28 Contour

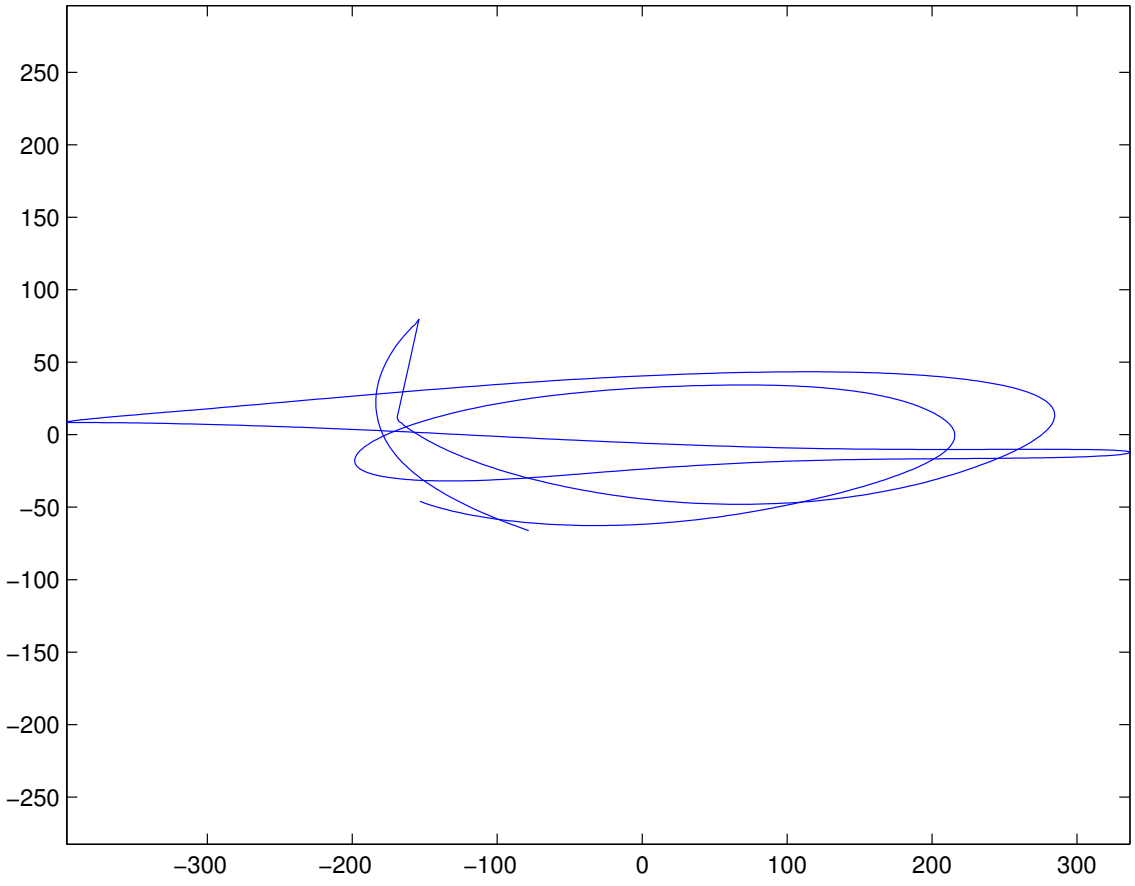

Figure 133: OBS28 Particle Motion

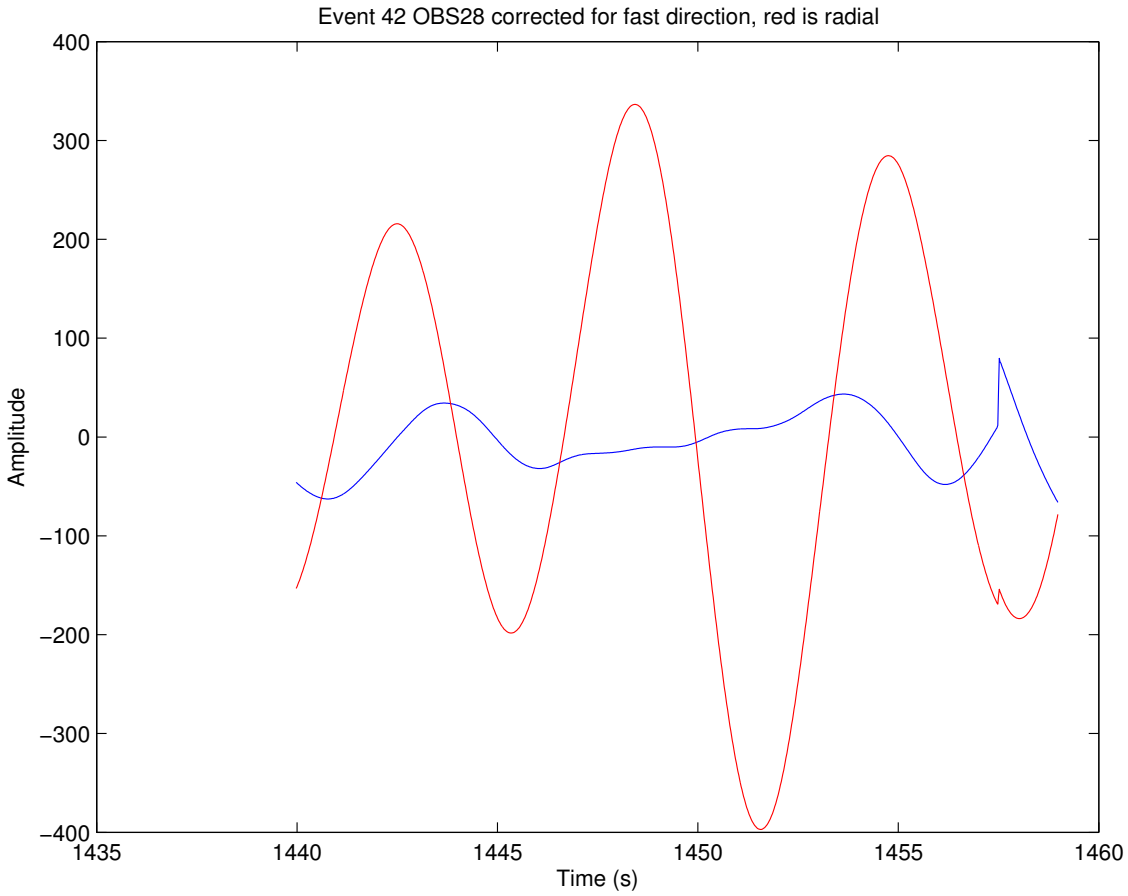

Figure 134: OBS28 Corrected

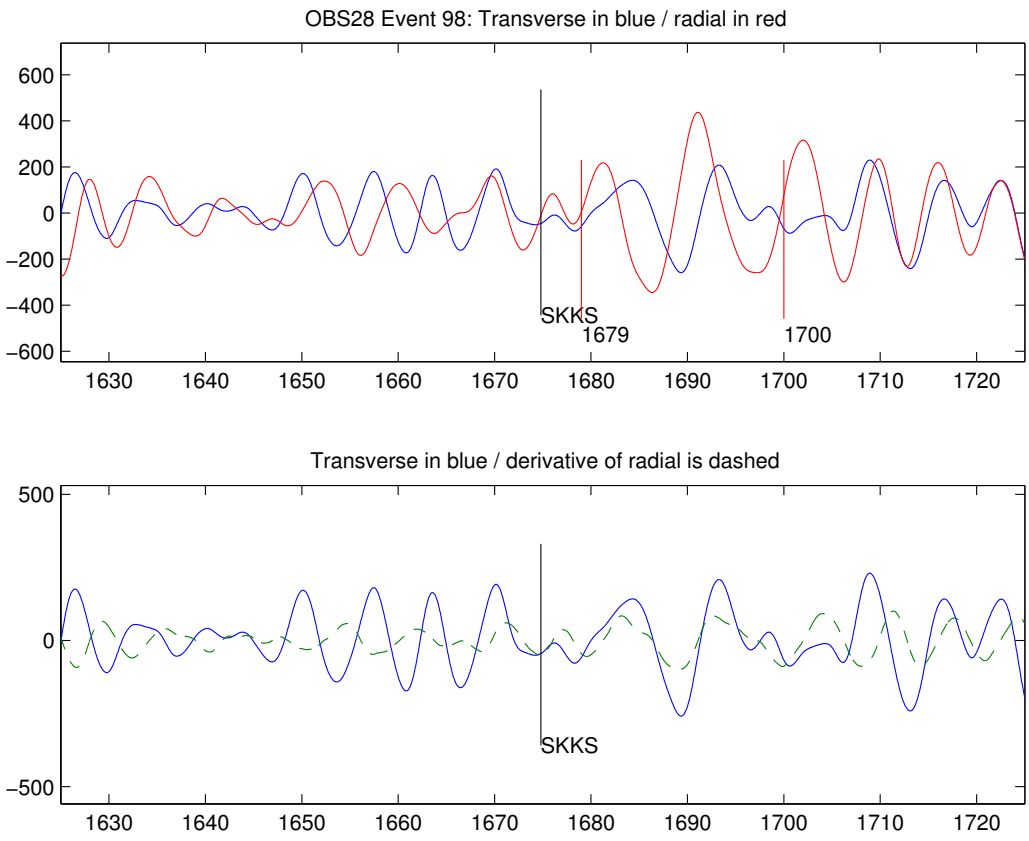

Figure 135: OBS28 Time Window

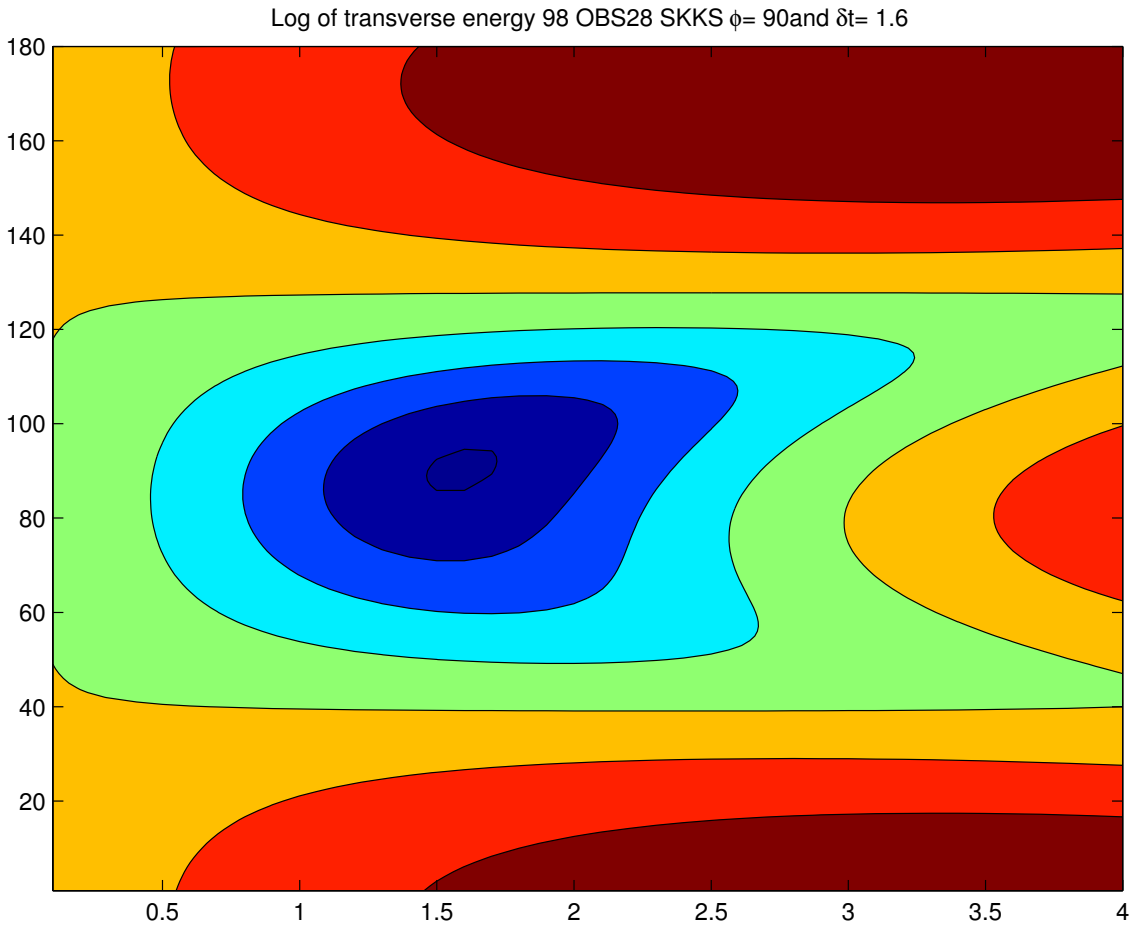

Figure 136: OBS28 Contour

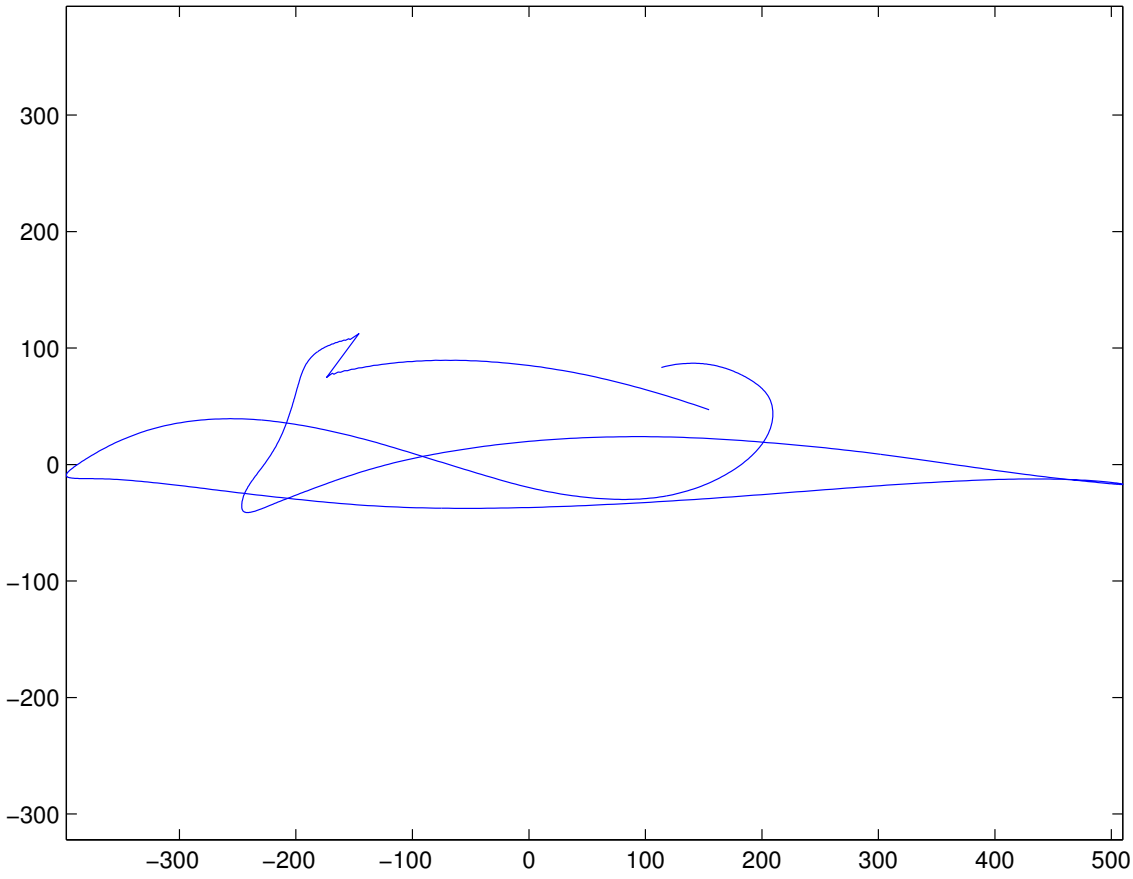

Figure 137: OBS28 Particle Motion

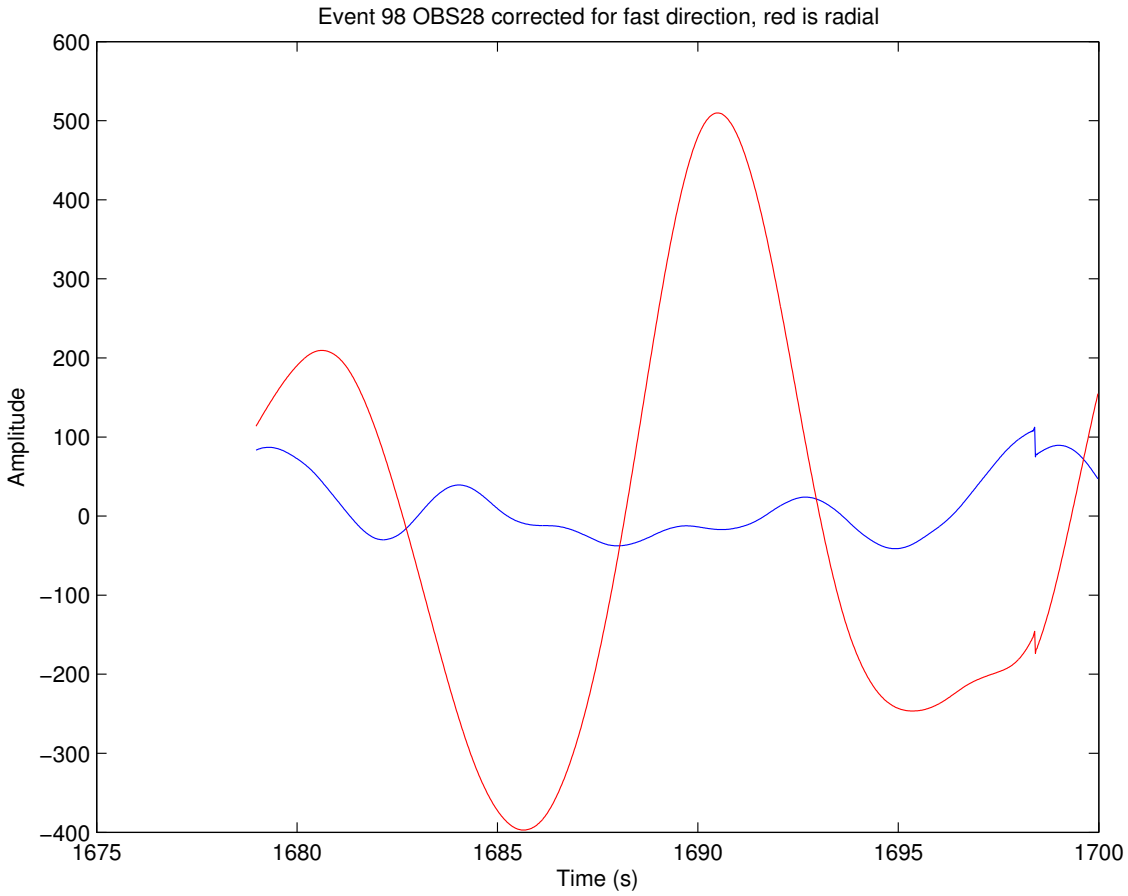

Figure 138: OBS28 Corrected

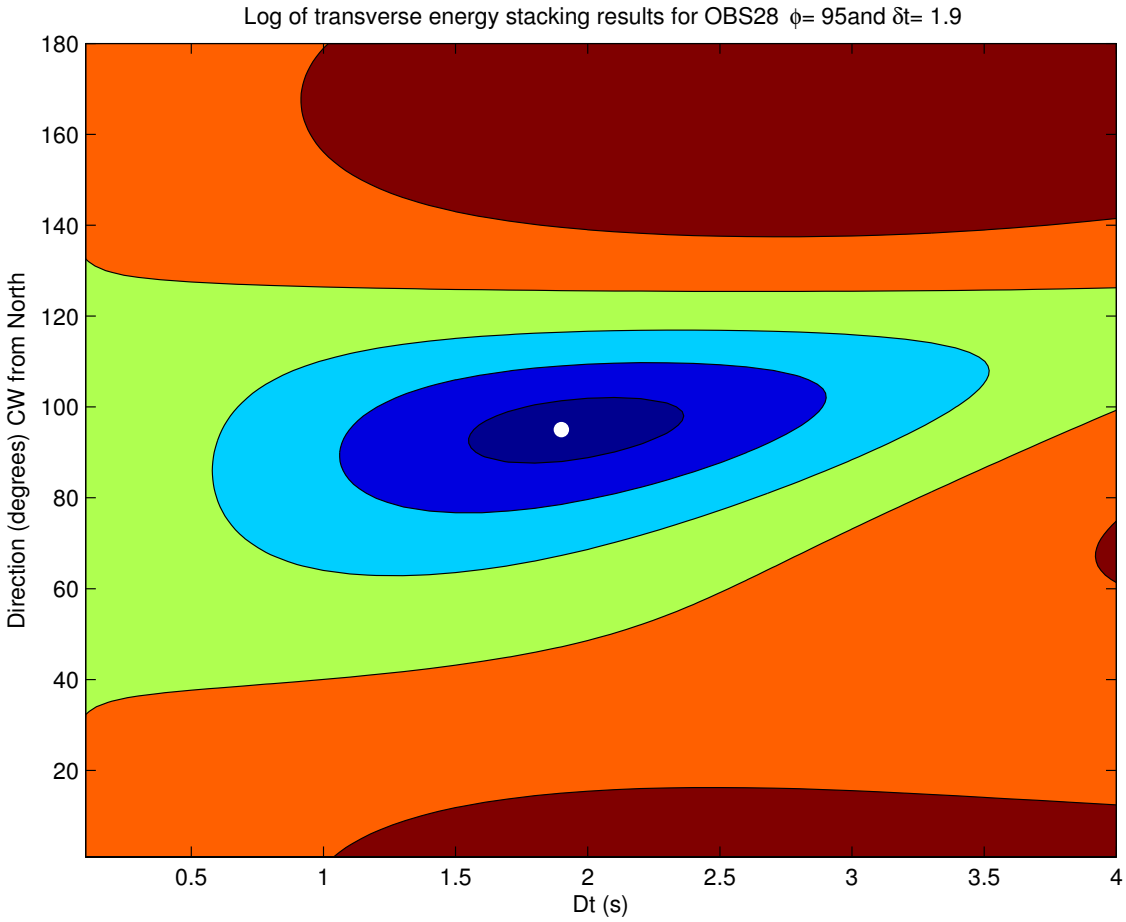

Figure 139: OBS28 Stacked Transverse Energy

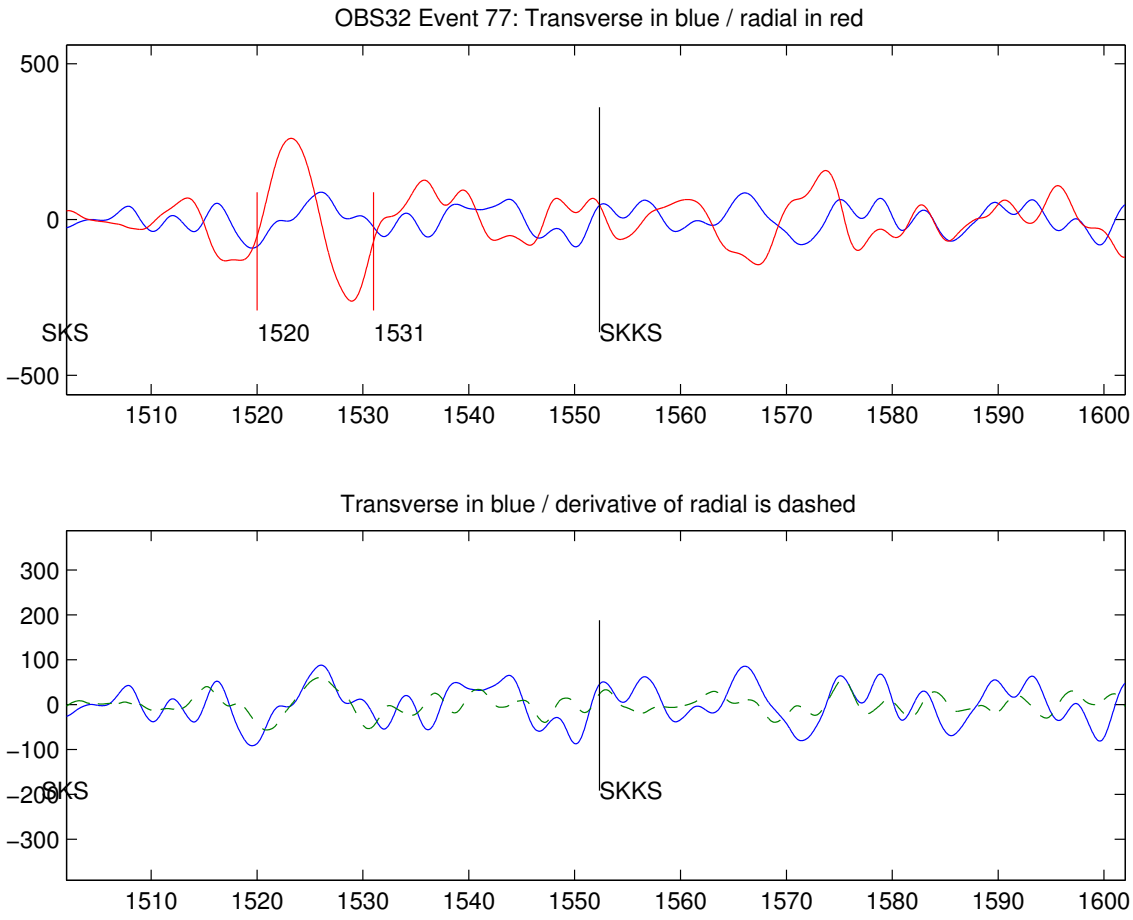

Figure 140: OBS32 Time Window

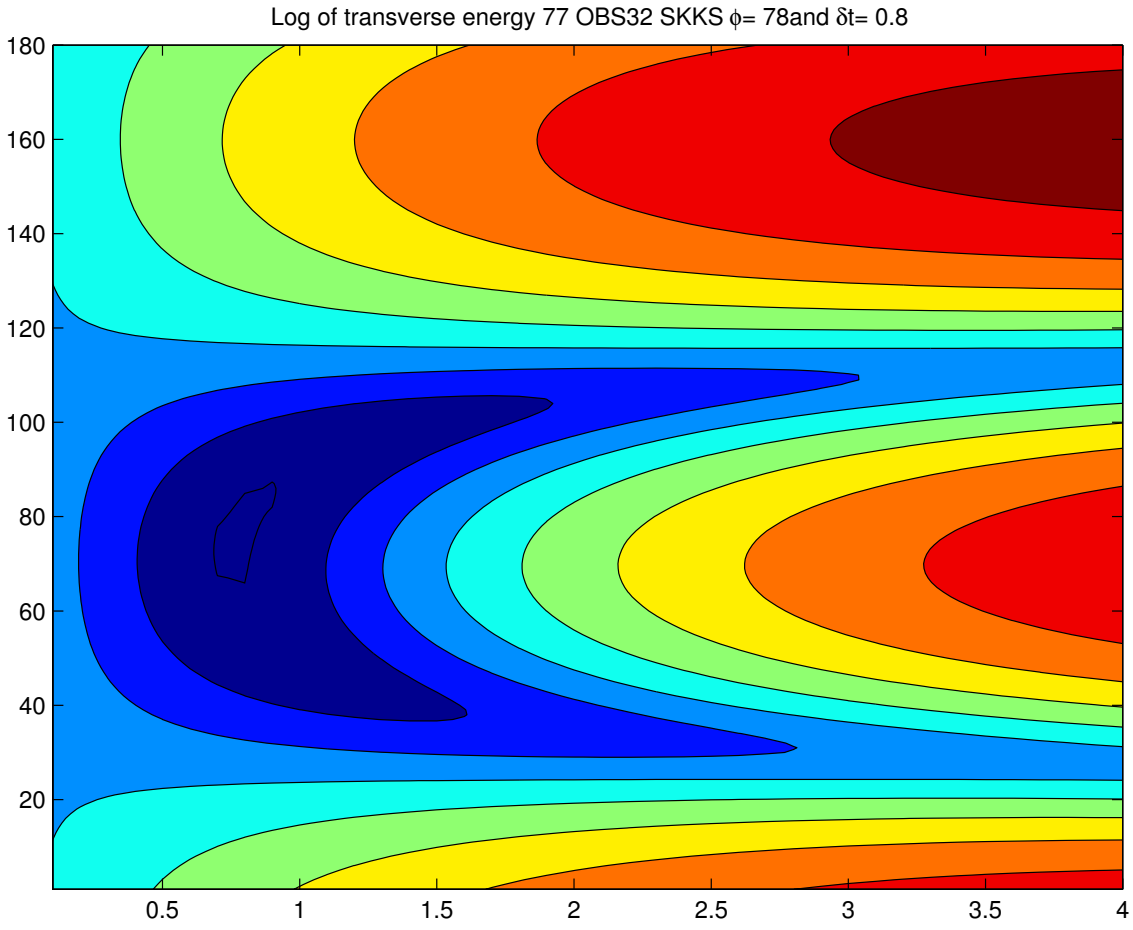

Figure 141: OBS32 Contour

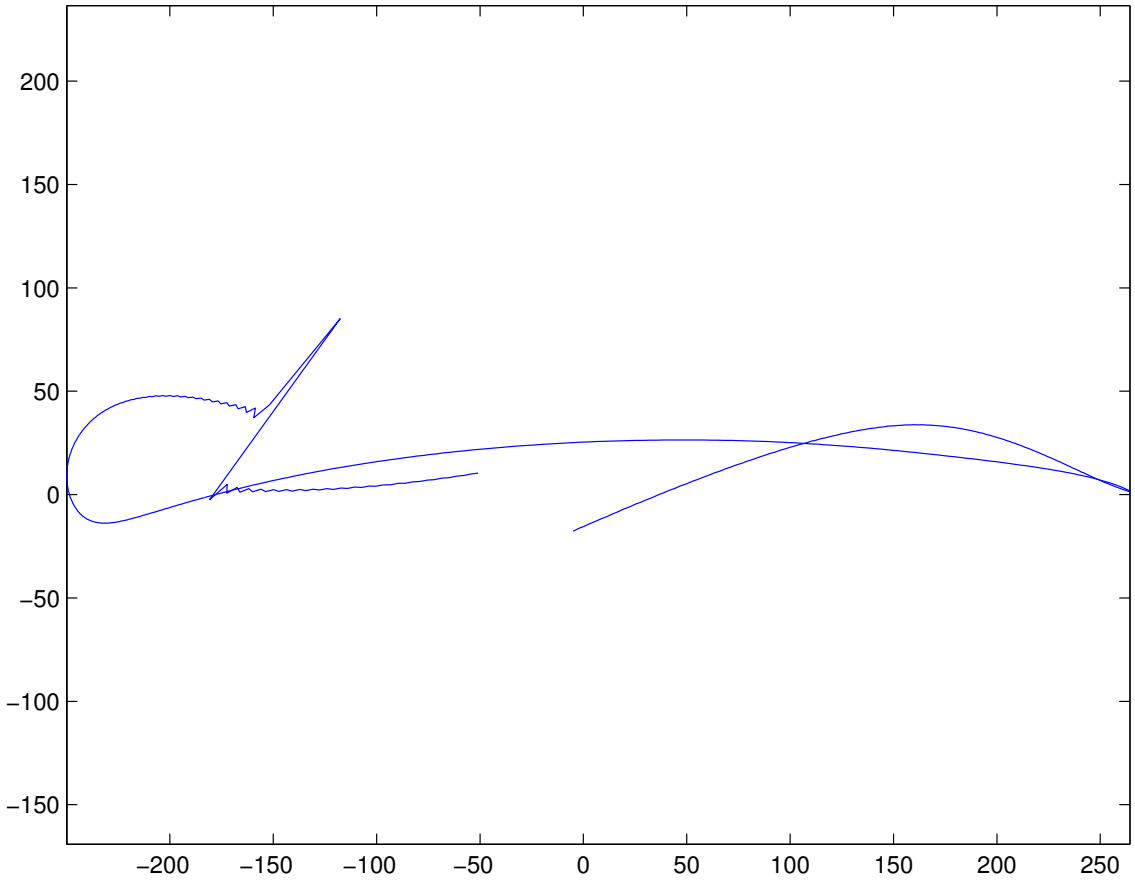

Figure 142: OBS32 Particle Motion

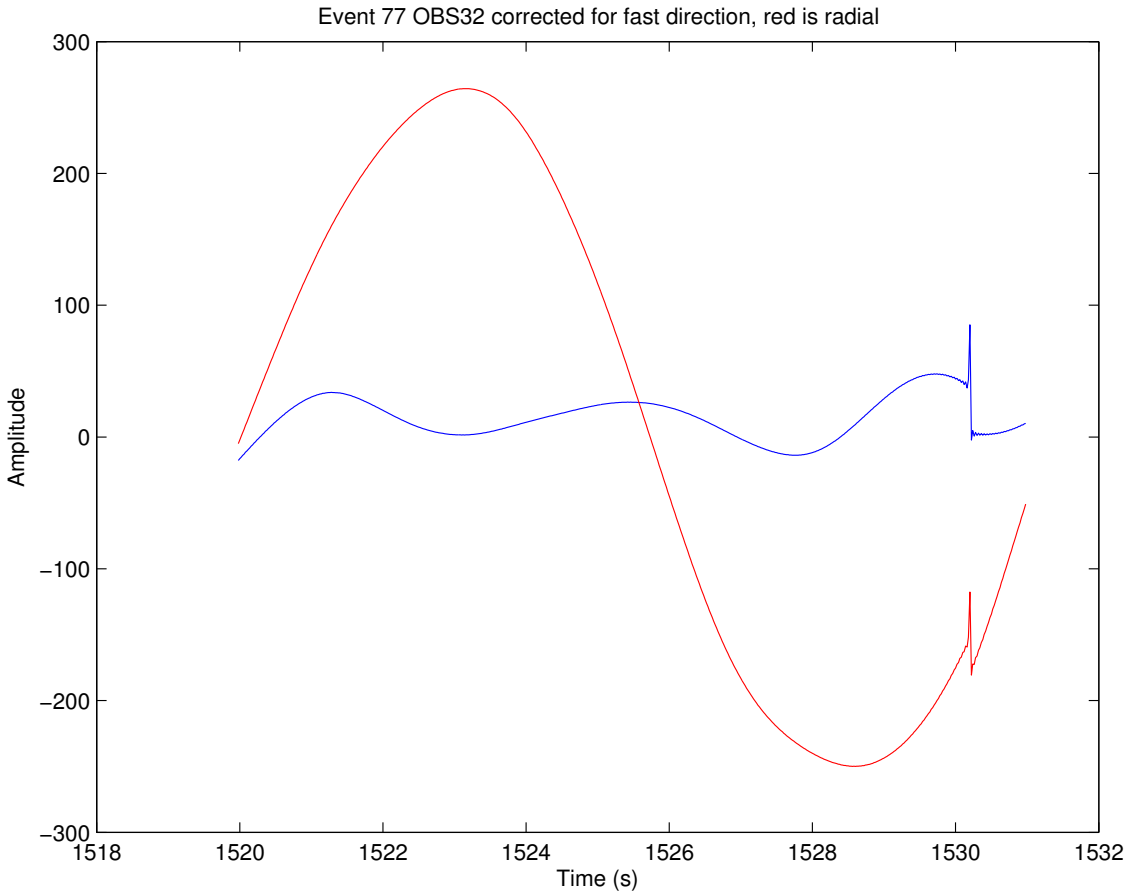

Figure 143: OBS32 Corrected

References

Anderson, Orson L. and Donald G. Isaak. *Elastic Constants of Mantle Minerals at High Temperature*, pages 64–97. American Geophysical Union, 2013.

Barruol, G., D. Suetsugu, H. Shiobara, H. Sugioka, S. Tanaka, G.H.R. Bokelmann, F.R. Fontaine, and D. Reymond. Mapping upper mantle flow beneath french polynesia from broadband ocean bottom seismic observations. *Geophysical Research Letters*, 36(14), 2009.

Becker, Thorsten W., Sebastien Chevrot, Vera Schulte-Pelkum, and Donna K. Blackman. Statistical properties of seismic anisotropy predicted by upper mantle geodynamic models. *Journal of Geophysical Research: Solid Earth*, 111(B8), 2006.

Becker, T.W., S. Lebedev, and M.D. Long. On the relationship between azimuthal anisotropy from shear wave splitting and surface wave tomography. *Journal of Geophysical Research: Solid Earth*, 117(B1), 2012.

Beghein, Caroline, Kaiqing Yuan, Nicholas Schmerr, and Zheng Xing. Changes in seismic anisotropy shed light on the nature of the gutenberg discontinuity. *Science*, 343(6176): 1237–1240, 2014.

Carter, Neville L. Steady state flow of rocks. *Reviews of Geophysics*, 14(3):301–360, 1976.

D. V. Helmberger, X. Ding, L. Wen. Seismic evidence that the source of the iceland hotspot lies at the coremantle boundary, 1998. URL http://www.nature.com/nature/journal/v396/n6708/full/396251a0.html.

DeCourten, Frank. Geology of southern california, 2013. URL http://www.grossmont.edu/garyjacobson/Naural20History20150/Geology20of20Southern20California.pdf.

Etchecopar, A. A plane kinematic model of progressive deformation in a polycrystalline aggregate. *Tectonophysics*, 39(1-3):121 – 139, 1977.

Harmon, Nicholas, Donald W. Forsyth, Karen M. Fischer, and Spahr C. Webb. Variations in shear-wave splitting in young pacific seafloor. *Geophysical Research Letters*, 31(15), 2004.

Kohler, Monica. Albacore obs recovery cruise report, 35 pp., r/v new horizon cruise nh1111, 2012. URL http://goldengate.ce.caltech.edu/~kohler/Offshore/ALBACORE_2011_Cruise_Report.pdf.

Kosarian, Minoo, Paul M. Davis, Toshiro Tanimoto, and Robert W. Clayton. The relationship between upper mantle anisotropic structures beneath california, transpression, and absolute plate motions. *Journal of Geophysical Research: Solid Earth*, 116(B8), 2011.

Long, Maureen D. and Paul G. Silver. The subduction zone flow field from seismic anisotropy: A global view. *Science*, 319(5861):315–318, 2008.

Montagner, Jean-Paul, Daphné-Anne Griot-Pommera, and Jérome Lavé. How to relate body wave and surface wave anisotropy? *Journal of Geophysical Research: Solid Earth*, 105 (B8):19015–19027, 2000.

Ribe, Neil M. and Yang Yu. A theory for plastic deformation and textural evolution of olivine polycrystals. *Journal of Geophysical Research: Solid Earth*, 96(B5):8325–8335, 1991.

Silver, P. G. and W. E. Holt. The mantle flow field beneath western north america. *Science*, 295(5557):1054–1057, 2002.

Silver, P.G. and W.W. Chan. Shear wave splitting and subcontinental mantle deformation. *Journal of Geophysical Research: Solid Earth*, 96(B10):16429–16454, 1991.

Stacey, F.D. *Physics of the earth*. Space science text series. Wiley, 1977.

Stachnik, J.C. Determination of new zealand ocean bottom seismometer orientation via rayleigh-wave polarization. *Seismological Research Letters*, 84:704–713, 2012.

Stubailo, Igor, Caroline Beghein, and Paul Davis. Structure and anisotropy of the mexico subduction zone based on rayleigh-wave analysis and implications for the geometry of the trans-mexican volcanic belt. *Journal of Geophysical Research: Solid Earth*, 117(B5), 2012.

West, John D., Matthew J. Fouch, Jeffrey B. Roth, and Linda T. Elkins-Tanton. Vertical mantle flow associated with a lithospheric drip beneath the great basin, 2009.

Wolfe, Cecily J. and Paul G. Silver. Seismic anisotropy of oceanic upper mantle: Shear wave splitting methodologies and observations. *Journal of Geophysical Research: Solid Earth*, 103(B1):749–771, 1998.

Wolfe, Cecily J. and Sean C. Solomon. Shear-wave splitting and implications for mantle flow beneath the melt region of the east pacific rise. *Science*, 280(5367):1230–1232, 1998.

Yuan, Huaiyu and Barbara Romanowicz. Depth dependent azimuthal anisotropy in the western us upper mantle. *Earth and Planetary Science Letters*, 300(3-4):385 – 394, 2010.

Yuan, Kaiqing and Caroline Beghein. Seismic anisotropy changes across upper mantle phase transitions. *Earth and Planetary Science Letters*, 374(0):132 – 144, 2013.

Zandt, G. and E. Humphreys. Toroidal mantle flow through the western us slab window, 2014. URL http://geology.gsapubs.org/content/36/4/295.full.pdfl.